Modèle de plissement dynamique pour la simulation aux grandes échelles de la combustion turbulente prémelangée

Pedro Stefanin Volpiani

NNT : 2017SACLC005

THÈSE DE DOCTORAT DE L'UNIVERSITÉ PARIS-SACLAY,

préparée à CentraleSupélec.

ÉCOLE DOCTORALE N^{o}579

Sciences Mécaniques et Énergétiques, Matériaux et Géosciences

Spécialité Combustion

Présentée par

Pedro STEFANIN VOLPIANI

Dynamic wrinkling flame model for large eddy simulations of turbulent premixed combustion

Thèse soutenue à Châtenay-Malabry, le 06 février 2017.

Composition du jury:

M. SAGAUT, Pierre	Professeur, Institut Universitaire de France	Président
Mme. DOMINGO, Pascale	Directrice de recherche CNRS, CORIA	Rapporteur
M. SADIKI, Amsini	Professeur, Technische Universitaet Darmstadt	Rapporteur
M. COLIN, Olivier	Ingénieur, IFP Energies nouvelles	Examinateur
M. RICHARD, Stéphane	Ingénieur, Safran Helicopter Engines	Examinateur
M. VERMOREL, Olivier	Chercheur senior, CERFACS	Examinateur
M. VEYNANTE, Denis	Directeur de recherche CNRS, EM2C	Directeur
M. SCHMITT, Thomas	Chargé de Recherche CNRS, EM2C	Encadrant

To my family

Remerciements

J'aimerais remercier non seulement les personnes qui m'ont soutenu lors du déroulement de cette thèse de doctorat mais aussi celles qui ont fait partie de ma vie pendant cette longue période en France remplie de souvenirs inoubliables. Cette partie vous est dédiée !

Mes premiers remerciements vont à mon directeur de thèse M. Denis Veynante qui a joué un rôle essentiel dans le déroulement de ce travail avec ses remarques et conseils toujours pertinents. Je le remercie très sincèrement pour la grande attention fournie et aussi d'avoir partagé avec moi son expérience et ses connaissances en combustion turbulente. Je tiens à remercier également mon encadrant M. Thomas Schmitt qui m'a aidé à de nombreuses occasions : au tout début, lors de la réalisation de mes premiers calculs à hautes performances, mais aussi dans la dernière ligne droite quand il me motivait régulièrement.

De plus, j'exprime ma gratitude à tous les membres du jury pour avoir accepté d'évaluer mon travail. A commencer par M. Pierre Sagaut pour avoir présidé le jury de la soutenance et aussi pour m'avoir donné les notions de turbulence lors de mon master à l'Université Pierre et Marie Curie. Ensuite, les rapporteurs Mme. Pascale Domingo et M. Amsini Sadiki pour leur retour positif et pour avoir accepté de travailler pendant les fêtes de fin d'année à lire les pages de ce manuscrit. Enfin, les examinateurs M. Olivier Colin, M. Stéphane Richard et M. Olivier Vermorel pour les discussions fructueuses avant et pendant la soutenance.

Durant mon séjour au laboratoire, d'autres activités ont été marquantes, notamment les TPs et TDs à Centrale. Je remercie M. Nasser Darabiha avec qui j'ai passé des heures à parler de flammes 1D, moteur HCCI et réacteur parfaitement mélangé (et de séries) et M. Laurent Zimmer et M. Philippe Scouflaire (le plus brésilien des français) pour leurs instructions sur les souffleries.

Il faut souligner que ce travail a donné des excellents résultats non seulement grâce au modèle dynamique mais aussi au super solveur massivement parallèle qui résout les équations de Navier-Stokes tridimensionnelles sur des maillages hybrides non-structurés : AVBP. Un grand merci à l'équipe du CERFACS et IFPEN pour le partage du code et pour l'accueil chaleureux lors de mon séjour

à Toulouse.

Je voudrais aussi remercier tous mes amis qui étaient à mes cotés dans cette belle histoire, pendant les cours, soirées, restos (beaucoup de restos !), pauses café, séances de muscu, randonnés ou même dans un weekend musical au labo pour chanter " My hometown " de Bruce Springsteen. Un merci spécial au bureau de champions, the fantastic 4, the 7 musketeers, la team BRASIL et la meilleure association de Paris Dança Samba ! Et bien évidemment, ma famille parisienne : Mélody Cailler, Adrien Chatelier, Aurélien Genot, Macole Sabat, Maria Luis Castella, Gizem Okay, Mihaela Cirisan, Lúcio Correa, Livia Tardelli, Luiz Bissoto, Diego Silva, Lucas Franceschini, Alejandra Villanueva, Shanshan Geng, Antonin Lefebvre, Yasmin Baggi et tant d'autres. Grâce à vous la vie est plus rose.

Il ne faut pas oublier de mentionner mes professeurs de l'Universidade de Sao Paulo et de l'ENSTA - Paristech qui ont partagé avec moi leurs connaissances dans divers domaines. Je remercie également toute l'équipe du Laboratoire DynFluid, le service MFTA de PSA et le DAFE à l'Onera pour les bons moments passés ensemble et qui ont été essentiels dans ma formation d'ingénieur. Je remercie en particulier vivement M. Xavier Gloerfelt pour m'avoir formé, motivé et inspiré.

Enfin, je voudrais remercier toute ma famille, en particulier mes parents et mon frère Túlio Volpiani pour leur soutien et leurs encouragements. C'est dur de vivre loin de personnes que l'on aime, mais nous avons réussi. Pour finir, un immense merci à Caroline Colombo pour son soutien permanent, pour avoir fait le déplacement pour ma soutenance et avoir partagé avec moi ce moment si important.

Je vous aime tous !

" Un pas, une pierre, un chemin qui chemine ... "

Abstract

Large eddy simulation (LES) is currently applied in a wide range of engineering applications. Actually, designing less polluting engines, reducing costs and development time of a new furnace, or predicting thermo-acoustics instabilities in a gas turbine, is no longer possible without the use of LES. This numerical methodology is based on a low-pass filtering of the Navier-Stokes equations, where only the most energetic structures of the flow are captured by the grid. The effect of small scales structures, responsible for the turbulent energy dissipation, are modeled.
Naturally, the ability to predict realistic systems depends on the accuracy of sub-grid scale models. Classical LES combustion models are based on algebraic expressions and assume equilibrium between turbulence and flame wrinkling which is generally not verified in many circumstances as the flame is laminar at early stages and progressively wrinkled by turbulent motions. In practice, this conceptual drawback has a strong consequence: every computation needs its own set of constants, i.e. any small change in the operating conditions or in the geometry requires an adjustment of model parameters. Possible solutions are then to use more refined models, for instance by solving an additional balance equation for the flame surface density.
Another promising alternative recently developed consists in using a dynamic model to automatically adjust the flame wrinkling factor from the knowledge of resolved scales. Widely used to describe the unresolved turbulent transport, the dynamic approach remains underexplored in combustion despite its interesting potential.
This thesis presents a detailed study of a dynamic wrinkling factor model for large eddy simulation of turbulent premixed combustion. The goal of this thesis is to characterize, unveil pros and cons, apply and validate the global (time dependent model parameter) and local (space and time dependent model parameter) dynamic modeling in different flow configurations. The massively parallel AVBP solver is used to compute the unsteady compressible and reactive multi-species Navier-Stokes equations on unstructured grids. Firstly, a turbulent jet flame is simulated in order to investigate the influence of physical and numerical characteristics of the model. The dynamic model is found to be robust and relatively insensitive to numerical input coefficients to be provided beforehand in the code. Secondly, the model was validated in an aeronautical

burner geometry and it is shown that dynamic models can play an important role in the prediction of combustion instabilities. Finally, simulations of explosion deflagrating flames propagating past repeated obstacles are performed. The local dynamic model is able to capture both, laminar and turbulent, flame regimes simultaneously, handling transient situations very well. Moreover, the additional cost introduced by the dynamic procedure remains limited, around 5-10 % of the total calculation cost, which is perfectly acceptable. We conclude that dynamic models are a very powerful tool, once it can handle academic and industrial configurations, stationary and unsteady flames, steady state and transient regimes very precisely as discussed in this manuscript.

Keywords Dynamic modeling, Turbulent premixed combustion, Large eddy simulation, Thickened flame model, Turbulent jet flame, Swirl burner, Combustion instabilities, PRECCINSTA, Explosion

Contents

Abstract vii

Nomenclature xi

Introduction 1

I General concepts 7

1 Conservation equations for reactive flows 9
1.1 Thermochemical variables 9
1.2 Governing equations 11

2 General features on turbulent combustion 19
2.1 Laminar premixed flames 19
2.2 Turbulent premixed combustion 22

3 Numerical simulations and modeling 27
3.1 Introduction 27
3.2 The LES filtering approach 28
3.3 Filtered equations for reactive flows 31
3.4 LES models for the sub-grid stress tensor 35
3.5 Chemistry modeling in LES 38
3.6 LES models for turbulent premixed combustion 41
3.7 Classical sub-grid term closures 45
3.8 Motivation for a dynamic fractal-like sub-grid term closure . . . 46

4 Dynamic models for LES of turbulent combustion 53
4.1 General concept 53
4.2 State of the art of dynamic models in combustion 54
4.3 Indirect approaches 74
4.4 Comments on the inner cut-off length scale 75

II Validation of the dynamic model in different flow config-

urations **79**

5 A posteriori tests of a dynamic thickened flame model for large eddy simulations of turbulent premixed combustion **83**
5.1 Introduction . . . 84
5.2 Modeling . . . 86
5.3 Numerical set-up . . . 89
5.4 Data processing . . . 92
5.5 Simulation results and discussions . . . 94
5.6 Computational costs . . . 109
5.7 Conclusion . . . 110
5.8 Supplementary material . . . 111

6 Large eddy simulation of a turbulent swirling premixed flame coupling the TFLES model with a dynamic wrinkling formulation **115**
6.1 Introduction . . . 116
6.2 Modeling . . . 118
6.3 The Preccinsta burner . . . 121
6.4 Data processing . . . 125
6.5 Simulations results and discussions . . . 126
6.6 Conclusion . . . 141
6.7 Supplementary material . . . 142

7 Large eddy simulation of explosion deflagrating flames using a dynamic wrinkling formulation **145**
7.1 Introduction . . . 146
7.2 Modeling . . . 148
7.3 Experimental set-up . . . 150
7.4 Chemical scheme . . . 151
7.5 Preliminary results on a two-dimensional configuration . . . 156
7.6 Numerical set-up for the 3D LES . . . 164
7.7 A posteriori tests on the 3D LES of the small-scale experiment 165
7.8 Conclusion . . . 177

General conclusions **179**

A Résumé en français **183**

B Conclusion en français **185**

References **202**

Nomenclature

Latin Characters :

$[X_k]$	Molar concentration of species k $[mol/m^3]$
$\mathcal{F}$	Thickening factor $[-]$
$\mathcal{M}$	Name of species k $[-]$
$\mathcal{Q}_i$	Progress rate of reaction i $[mole/m^3/s]$
a	Strain rate $[1/s]$
A_i	Pre-exponential factor for forward reaction i $[cgs]$
A	Area of the unwrinkled flame surface $[m]$
A_T	Area of the wrinkled flame surface $[m]$
c	Progress variable $[-]$
C_{pk}	Specific heat capacity at constant pressure of species k $[J/Kg/K]$
C_{vk}	Specific heat capacity at constant volume of species k $[J/Kg/K]$
C_p	Specific heat capacity at constant pressure of mixture $[J/Kg/K]$
C_v	Specific heat capacity at constant volume of mixture $[J/Kg/K]$
D	Fractal dimension $[-]$
D_k	Molecular diffusion coefficient of species k $[m/s]$
D_T	Thermal diffusion coefficient $[m/s]$
e_k	Mass energy of species k $[J/kg]$
E	Total non-chemical energy of the mixture $[J/kg]$
E_{ai}	Activation energy for reaction i $[cal/mol]$
h_k	Mass enthalpy of species k $[J/kg]$
H	Total non-chemical enthalpy of the mixture $[J/kg]$
$J_{i,k}$	Component i of the molecular diffusive flux of species k $[kg/m^2/s]$
K^i_{eq}	Equilibrium reaction constant for reaction i $[-]$
K_{fi}	Forward reaction constant for reaction i $[cgs]$
K_{ri}	Reverse reaction constant for reaction i $[cgs]$
ℓ_t	Integral length scale $[m]$
ℓ_t	Turbulent length scale $[m]$
m	Mixture mass $[kg]$
m_k	Mass of species k $[kg]$
n	Number of moles $[mol]$
n_k	Number of moles of species k $[mol]$
P	Pressure $[N/m^2]$
P_k	Partial pressure of species k $[N/m^2]$

q_i	Component i of energy flux $[J/m^2/s]$
R	Perfect gas constant $[J/mol/K]$
s	Mass stoichiometric ratio $[-]$
S_L	Laminar flame speed $[m/s]$
S_T	Turbulent flame speed $[m/s]$
S_a	Absolute speed $[m/s]$
S_c	Consumption speed $[m/s]$
S_d	Displacement speed $[m/s]$
T	Mixture temperature $[K]$
u_i	Component i of velocity vector $[m/s]$
u'	Turbulent velocity fluctuation $[m/s]$
u'_Δ	Sub-grid scale turbulent velocity $[m/s]$
V_i^c	Correction velocity in direction i $[m/s]$
W_k	Molar mass of species k $[kg/mol]$
W	Mean molecular weight of the mixture $[kg/mol]$
X_k	Molar fraction of species k $[-]$
Y_k	Mass fraction of species k $[-]$
Z	Mixture fraction $[-]$

Greek Characters :

β	Model parameter $[-]$
δ_L^0	Thermal flame thickness $[m]$
δ_c	Inner cut-off flame scale $[m]$
δ_{ij}	Component (i,j) of the Kronecker delta $[-]$
Δ_x	Mesh spacing $[m]$
Δ	Combustion filter size $[m]$
$\widehat{\Delta}$	Test filter size $[m]$
$\breve{\Delta}$	Effective test filter size $[m]$
Δ_{avg}	Average filter size $[m]$
η	Kolmogorov length scale $[m]$
γ	Ratio between effective test and combustion filter sizes $[-]$
Γ_Δ	Efficiency function $[-]$
κ	Flame stretch $[1/s]$
$\dot{\omega}_k$	Mass reaction rate of species k $[kg/m^3/s]$
$\dot{\omega}_T$	Heat release due to combustion $[J/m^3/s]$
λ	Heat conduction coefficient $[J/m/K/s]$
μ	Dynamic (shear) viscosity $[kg/m/s]$
ν	Kinematic viscosity $[m^2/s]$
ν_{sgs}	Sub-grid scale turbulent viscosity $[m^2/s]$
ν'_{ki}	Molar stoichiometric coefficient of species k for the forward reaction i $[-]$
ν''_{ki}	Molar stoichiometric coefficient of species k for the backward reaction i $[-]$
ϕ	Equivalence ratio $[-]$
ρ	Mixture density $[kg/m^3]$
ρ_k	Density of species k $[kg/m^3]$
Σ	Surface density $[1/s]$
τ_{ij}	Viscous stress tensor $[N/m^2]$
τ_k	Kolmogorov time scale $[s]$
τ_c	Chemical time scale $[s]$
τ_t	Integral time scale $[s]$
Ξ_Δ	Sub-grid wrinkling factor $[-]$

Non-dimensional numbers :

Da	Damkohler number
Ka	Karlovitz number
Le_k	Lewis number of species k
Pr	Prandtl number
Re	Reynolds number
Re_t	Turbulent Reynolds number
Re_Δ	Sub-grid scale turbulent Reynolds number
Sc_k	Schmidt number of species k

Abbreviations :

CFD	Computational Fluid Dynamics
CPU	Central Processing Unity
DNS	Direct Numerical Simulation
FSD	Flame Surface Density
LES	Large Eddy Simulation
RANS	Reynolds-Averaged Navier-Stokes
SGS	Sub-grid Scale
TFLES	Thickened Flame model for Large Eddy Simulation

Introduction

General context

The number of combustion systems used in power generation and transport industries is growing fast. As a consequence, the total primary energy supply (TPES) has more than doubled since 1971 (Fig. 1(a)). Besides, as depicted in Fig. 1(b), combustion accounts for about 90% of the global energy consumption (International Energy Agency 2016) and will remain at this high level, since it is still the most convenient way to obtain energy. Moreover, in automotive and aeronautical applications, the high energy density of liquid fuels (around 40 MJ kg^{-1} for standard hydrocarbon fuels) facilitates the energy storage. Even if, nowadays, some cars may run with electrical engines, they are still restricted to short distances. To overcome this problem, the automobile manufacturers are investing heavily in new technologies to obtain more efficient batteries. In an aircraft, replacing current gas turbines by an electrical propulsion system is less easy. Furthermore, using electrical vehicles makes sense, only if electricity comes from cleaner, renewable, and less carbon-intensive energy sources. Concerning the power generation in the world, the production of electrical energy relies predominantly on coal burning power plants and gas turbines. The progressively replacement by renewables energies, such as wind turbines or photovoltaic solar panels will reduce the need of having fossil fuel power plants, but this is an extensive and slow process. Additionally, the generation of electricity through these means is extremely low and intermittent (only accessible during a period of the day).
Unfortunately, fossil fuel burning induces pollution and others environmental problems that are critical issues in our society and must be addressed. The emission of carbon monoxide CO, unburned hydrocarbons (UHC), soot and others chemical species is very hazardous for human health. Other products are responsible for the contribution of the greenhouse effect (carbon dioxide, CO_2) or even the acid rain (sulfur and nitrogen oxides - SO_x, NO_x). New environmental norms are becoming more and more severe, encouraging engineers and researchers to develop cleaner combustion devices. The international political response to climate change started at the Rio Convention in 1992, adopting the UN Framework on Climate Change (UNFCCC). This convention set out a framework to stabilize atmospheric concentrations of greenhouse gases

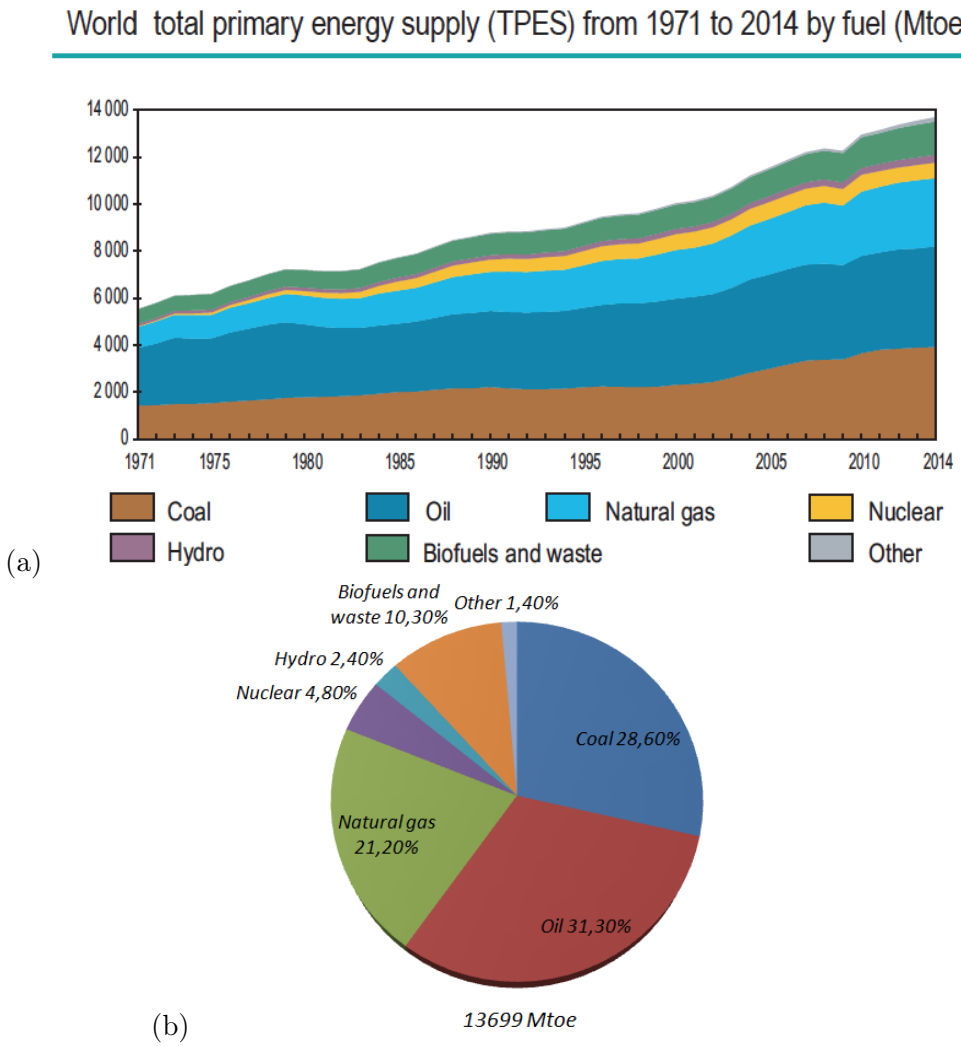

Figure 1: *Total Primary Energy Supply (TPES) in the world shared between different resources: coal/peat, oil, natural gas, nuclear energy, hydraulic power, biofuels and waste, and geothermal/solar/wind energy. TPES is expressed in million tons of oil equivalent (Mtoe). (a) Evolution of global TPES from 1971 to 2014. (b) Share of global TPES in 2014 (International Energy Agency 2016).*

(GHGs). More recently in 2015, COP21 took place in Paris and the result was an historic agreement involving 195 nations to combat climate change and unleash actions and investment towards a low carbon, resilient and sustainable future. The universal agreement's main aim is to keep a global temperature rise this century well below 2 degrees Celsius and to drive efforts to limit the temperature increase even further to 1.5 degrees Celsius above pre-industrial levels. As a result, the improvement of current combustion systems and the development of new technologies seem to be a real need.

Figure 2: *Combustion is very present in our day-to-day life. Examples of combustion systems: gas turbines, piston engines, rockets, airplanes.*

Most practical applications make use of turbulent combustion because turbulence enhances mixing and promotes chemical conversion (Poinsot and Veynante 2011). Piston engines used in land or maritime transportation, gas turbines used in aviation or electric plants, missile ramjets and rockets are some examples of applications in which turbulent combustion occurs (Fig 2). The structure of turbulent flames encountered in these configurations is extremely complex because it results from interactions between turbulence, two phase injection, chemical kinetics, acoustics and radiation. Hence, the description of turbulent flames constitutes a central problem, which requires a wise and well-balanced handling of the complexities of the process.

We need reliable CFD solvers!

Computational fluid dynamics (CFD) is effectively used to improve the design of engineering systems, and today no real progress in design can be made without the use of CFD tools. Because of the large number of degrees of freedom involved in turbulent combustion, a full Direct Numerical Simulation (DNS) of a practical system cannot be performed. Instead, two techniques less expensive than DNS were developed and are used in industries nowadays. The first one consists in solving the averaged flow governing equations; it is the so-called Reynolds Averaged Navier-Stokes (RANS) approach. When the ensemble averaging operator is applied, unknown terms appear and have to be modeled. Basically, it requires a turbulence model to deal with the flow dynamics and a combustion model to describe chemical species conversion and heat release. In the second approach, called Large Eddy Simulations (LES), the large scale

eddies, which are the most energetic structures of the flow, are separated from the small scales, where dissipation occurs by filtering the instantaneous balance equations. LES determines the instantaneous position of a large scale resolved flame front but a sub-grid model, as in RANS, is still required to take into account the effect of small turbulent scales on combustion.
In this thesis, we are interested in the LES approach. Even though LES is more expensive than RANS, there are many advantages attributed to this first method turning it very attractive (Poinsot and Veynante 2011):

- Large structures in turbulent flows are more likely to depend on the system geometry, while small structures are expected to have a more universal behavior;
- Because in RANS simulation, we have only one state (the converged flow), and LES must resolve the flow dynamics in time, this method turns out to be a powerful tool to predict instabilities;
- Large eddy simulations also allow a better description of the turbulence/combustion interactions, once fresh and burnt gas zones where turbulence characteristics are quite different and clearly identified.

One of the key points in combustion problems of large eddy simulations is the sub-grid terms that appear in the filtered balance equations. With the objective of delivering reliable CFD solvers, much work has been devoted to turbulent combustion modeling strategies. Conventional combustion models generally assume an equilibrium hypothesis between turbulent motions and the wrinkling of the flame surface. They can be written using a simple algebraic expression which depends on the known resolved quantities and on parameters that may depend on the configuration and operating conditions and have to be adjusted by hand by the user. Even if the equilibrium hypothesis is acceptable, most of the time it is not verified: a flame is initially laminar and is gradually wrinkled by turbulent structures. Waive this simplification generally implies the resolution of an additional equation, e.g. for flame surface density, where new unclosed terms appear and have to be modeled.
A new alternative is to develop the so-called dynamic combustion models. In this case, the model coefficients, which can now depend on time and space, are automatically adjusted during the calculation, taking advantage of the known resolved scales. Technically, the resolved field is filtered at a second scale, called test filter. The test-filtering leads to an equality that allows the parameter calculation. Highly used to describe the unresolved turbulent transport, this dynamic approach remains underexplored in combustion despite its interesting potential. The goal of this thesis is to characterize, unveil pros and cons, apply and validate the dynamic modeling in different flow configurations.

Structure of this manuscript

This manuscript is organized in two parts. In Part I, general features on turbulent combustion are discussed. In Part II, novel results obtained in the last three years regarding the dynamic combustion model are presented and discussed.

Part I - General concepts

Chapter 1 presents some basic concepts of reactive flows. Firstly, notions of mixture composition and thermo-chemistry are introduced. Then, the balance equations for compressible reactive flows are presented. Premixed laminar and turbulent flames are discussed in chapter 2 and different combustion regimes are identified. The balance equations are extended to the LES method and turbulence and combustion closures are provided in chapter 3. In Chapter 4 the dynamic procedure is detailed and a state of the art concerning the formulations and main results found in the literature is presented.

Part II - Validation of the dynamic model in different flow configurations

In Chapter 5, the dynamic model is used to simulate the turbulent jet flame studied experimentally by Chen et al. (1996). The influence of physical (flame wrinkling inner cut-off length scale) and numerical (averaging procedure, filter widths, filtering frequency) characteristics of a flame wrinkling factor dynamic model for turbulent premixed combustion is investigated in order to characterize the proposed model.
Large Eddy Simulations of the semi-industrial PRECCINSTA burner studied experimentally by Meier et al. (2007) are analyzed in Chapter 6. Two regimes are studied: the quiet and pulsating flames. The dynamic models seem to capture much better the dynamics and instantaneous flame behavior than the ordinary non-dynamic formulation.
In Chapter 7, deflagrating flames propagating past repeated obstacles, typical of an explosion configuration are treated. The idea is to test the dynamic model in a transient configuration, starting from an initial laminar flame kernel in a flow at rest and ending with a turbulent flame propagation. Experimental data are provided by Masri et al. (2012) and his team. The study and understanding of such cases are vital from an industrial, economical and environmental point of view to prevent and mitigate accidental explosions.

Conclusions and perspectives close this manuscript. Note that main results of this thesis have been published and presented in French or international conferences as shown in next sections. This thesis has been financed by the French government and become possible thanks to the HPC resources from GENCI (*Grand Equipement National de Calcul Intensif*) - IDRIS (Turing) and TGCC (Curie).

List of published and submitted articles

- P. S. Volpiani, T. Schmitt, D. Veynante. "A posteriori tests of a dynamic thickened flame model for large eddy simulations of turbulent premixed combustion", *accepted in Combustion and Flame.*

- P. S. Volpiani, T. Schmitt, D. Veynante. "Large eddy simulation of a turbulent swirling premixed flame coupling the TFLES model with a dynamic wrinkling formulation", *accepted in Combustion and Flame.*

- P. S. Volpiani, T. Schmitt, O. Vermorel, P. Quillatre, D. Veynante. "Large eddy simulation of explosion deflagrating flames using a dynamic wrinkling formulation", *submitted to Combust. Flame.*

List of conferences

- P. S. Volpiani, T. Schmitt, D. Veynante, "Analysis of a dynamic wrinkling model for large eddy simulations of a turbulent premixed jet flame". *In 11th European Research Community on Flow, Turbulence and Combustion, ETMM11, Palermo, Italy, September 2016.*

- P. S. Volpiani, T. Schmitt, D. Veynante, "Large eddy simulation of a turbulent swirling flame using the TFLES model coupled with a dynamic wrinkling formulation". *In 11th European Research Community on Flow, Turbulence and Combustion, ETMM11, Palermo, Italy, September 2016.*

- P. S. Volpiani, T. Schmitt, D. Veynante, "Modèle de plissement dynamique pour la simulation aux grandes échelles de la combustion turbulente prémelangée". *In Meeting Annuel du Centre de Recherche sur la Combustion Turbulente, Rueil-Malmaison, France, Mars 2016.*

- P. S. Volpiani, T. Schmitt, D. Veynante, "Analysis of a dynamic thickened flame model for large eddy simulations of turbulent premixed combustion". *In 15th International Conference on Numerical Combustion, Avignon, France, April 2015.*

Part I

General concepts

Chapter 1

Conservation equations for reactive flows

Combustion requires working with multi-species mixtures. Some basic definitions are now presented in order to facilitate the characterization of each species and the global mixture. The Navier-Stokes balance equations for reactive flows are also treated in this chapter. Only the case of ideal gaseous flows is considered.

1.1 Thermochemical variables

First of all, species are characterized through their mass fractions Y_k for $k = 1$ to N where N is the number of species. The mass fractions are defined as

$$Y_k = m_k/m \tag{1.1}$$

where m_k is the mass of species k present in a given volume V and m is the total mass of gas within this volume. The species density is defined as:

$$\rho_k = m_k/V = \rho Y_k \tag{1.2}$$

where ρ is the mixture density.
The molar fraction X_k is defined as the ratio between the number of moles of species k in a volume V and the total number of moles in the same volume:

$$X_k = \frac{n_k}{n} = \frac{W}{W_k} Y_k \tag{1.3}$$

and the molar concentration $[X_k]$ is the number of moles of species k per unit volume:

$$[X_k] = \frac{n_k}{V} = \rho \frac{Y_k}{W_k} = \rho \frac{X_k}{W} \tag{1.4}$$

W_k and W being the molar mass of species k and the mean molecular weight of the mixture respectively.
Its energy (e_k) or enthalpy (h_k) defined as the sum of the sensible and chemical parts:

$$e_k = \underbrace{\int_{T_0}^{T} C_{vk} dT - RT_0/W_k}_{sensible} + \underbrace{\Delta h^0_{f,k}}_{chemical} \tag{1.5}$$

$$h_k = \underbrace{\int_{T_0}^{T} C_{pk} dT}_{sensible} + \underbrace{\Delta h^0_{f,k}}_{chemical} \tag{1.6}$$

where C_{pk} stands for the specific heat capacity at constant pressure and C_{vk} at constant volume.
For a mixture of N species, there are multiple ways to express energy and enthalpy. The different forms are summarized in Table 1.1 (Poinsot and Veynante 2011):

Form	Energy	Enthalpy
Sensible	$e_s = \int_{T_0}^{T} C_v dT - RT_0/W$	$h_s = \int_{T_0}^{T} C_p dT$
Sensible+Chemical	$e = e_s + \sum_{k=1}^{N} \Delta h^0_{f,k} Y_k$	$h = h_s + \sum_{k=1}^{N} \Delta h^0_{f,k} Y_k$
Total Chemical	$e_t = e + \frac{1}{2} u_i u_i$	$h_t = h + \frac{1}{2} u_i u_i$
Total non-Chemical	$E = e_s + \frac{1}{2} u_i u_i$	$H = h_s + \frac{1}{2} u_i u_i$

Table 1.1: *Enthalpy and energy forms used in conservation equations.*

The heat capacities of the mixture are given by the following expressions:

$$C_p = \sum_{k=1}^{N} C_{pk} Y_k \tag{1.7}$$

$$C_v = \sum_{k=1}^{N} C_{vk} Y_k \tag{1.8}$$

Assuming a mixture of N perfect gases, the total pressure is the sum of partial pressures:

$$P = \sum_{k=1}^{N} P_k \quad \text{where} \quad P_k = \rho_k \frac{R}{W_k} T \tag{1.9}$$

where T is the temperature, $R = 8.314 J/(moleK)$ is the perfect gas constant. The state equation is then:

$$P = \sum_{k=1}^{N} P_k = \sum_{k=1}^{N} \rho_k \frac{R}{W_k} T = \rho \frac{R}{W} T \tag{1.10}$$

1.2 Governing equations

The set of conservation equation describing the evolution of a compressible flow with chemical reactions of thermodynamically active scalars are expressed as (Williams 1985):

$$\frac{\partial \rho u_i}{\partial t} + \frac{\partial}{\partial x_j}(\rho u_i u_j) = -\frac{\partial}{\partial x_j}\left[P\delta_{ij} - \tau_{ij}\right] \tag{1.11}$$

$$\frac{\partial \rho E}{\partial t} + \frac{\partial}{\partial x_j}(\rho E u_j) = -\frac{\partial}{\partial x_j}\left[u_i(P\delta_{ij} - \tau_{ij}) + q_j\right] + \dot{\omega}_T \tag{1.12}$$

$$\frac{\partial \rho Y_k}{\partial t} + \frac{\partial}{\partial x_j}(\rho Y_k u_j) = -\frac{\partial}{\partial x_j}\left[J_{j,k}\right] + \dot{\omega}_k \tag{1.13}$$

or in vectorial notation:

$$\frac{\partial \mathbf{w}}{\partial t} + \nabla \cdot \mathbf{F} = \mathbf{s} \tag{1.14}$$

Equations (1.11)-(1.13) correspond to the conservation laws for momentum, total energy and species. Symbols ρ, u_i and E denote respectively the density, the component i of the velocity vector and the total energy per unit mass. Note that the mass balance equation does not need to be computed, if Eq. (1.13) is solved for all species. In fact, the sum of Eq. (1.13) over the N species leads to the mass conservation equation.
The stress tensor τ_{ij}, the diffusive flux of species $J_{j,k}$, the heat flux vector q_j and the source term $\dot{\omega}_k$, in the species transport equations, and $\dot{\omega}_T$, in the total energy equation, must be given to close the system of equations above.

In Eq. (1.14) $\mathbf{w} = (\rho u, \rho v, \rho w, \rho E, \rho Y_k)^T$ is the state vector, $\mathbf{F}$ the flux tensor and $\mathbf{s}$ the source term vector. The flux tensor is usually decomposed into an inviscid and a viscous component:

$$\mathbf{F} = \mathbf{F}^I(\mathbf{w}) + \mathbf{F}^V(\mathbf{w}, \nabla\mathbf{w}) \tag{1.15}$$

1.2.1 Inviscid terms

The three components of the the inviscid flux term $\mathbf{F}^I(\mathbf{w})$ are written as:

$$\mathbf{f}^I = \begin{pmatrix} \rho u^2 + P \\ \rho uv \\ \rho uw \\ (\rho E + P)u \\ \rho Y_k u \end{pmatrix} \tag{1.16}$$

$$\mathbf{g}^I = \begin{pmatrix} \rho uv \\ \rho uv^2 + P \\ \rho vw \\ (\rho E + P)v \\ \rho Y_k v \end{pmatrix} \tag{1.17}$$

$$\mathbf{h}^I = \begin{pmatrix} \rho uw \\ \rho vw \\ \rho w^2 + P \\ (\rho E + P)w \\ \rho Y_k w \end{pmatrix} \tag{1.18}$$

where the hydrostatic pressure P is given by the equation of state (1.10) for a perfect gas.

1.2.2 Viscous terms

For the three components of the viscous flux term $\mathbf{F}^V(\mathbf{w}, \nabla\mathbf{w})$, we have:

$$\mathbf{f}^V = \begin{pmatrix} -\tau_{xx} \\ -\tau_{xy} \\ -\tau_{xz} \\ -(u\tau_{xx} + v\tau_{xy} + w\tau_{xz}) + q_x \\ J_{x,k} \end{pmatrix} \tag{1.19}$$

$$\mathbf{g}^V = \begin{pmatrix} -\tau_{xy} \\ -\tau_{yy} \\ -\tau_{yz} \\ -(u\tau_{xy} + v\tau_{yy} + w\tau_{yz}) + q_y \\ J_{y,k} \end{pmatrix} \tag{1.20}$$

$$\mathbf{h}^V = \begin{pmatrix} -\tau_{xz} \\ -\tau_{yz} \\ -\tau_{zz} \\ -(u\tau_{xz} + v\tau_{yz} + w\tau_{zz}) + q_z \\ J_{z,k} \end{pmatrix} \tag{1.21}$$

where τ_{ij} is the stress tensor, $J_{i,k}$ the diffusive flux of species k in the i-direction and q_i the heat flux vector.

1.2.2.1 Viscous stress tensor

The stress tensor τ_{ij} is given by the following relations for a Newtonian fluid:

$$\tau_{ij} = -\frac{2}{3}\mu\frac{\partial u_k}{\partial x_k}\delta_{ij} + \mu\left(\frac{\partial u_i}{\partial x_j} + \frac{\partial u_j}{\partial x_i}\right) \tag{1.22}$$

where μ is the shear viscosity and δ_{ij} is the Kronecker symbol (if $i = j$, $\delta_{ij} = 1$, otherwise $\delta_{ij} = 0$). Sometimes, the pressure tensor can be gathered with the viscous stress tensor in order to obtain:

$$\sigma_{ij} = \tau_{ij} - p\delta_{ij} = -p\delta_{ij} - \frac{2}{3}\mu\frac{\partial u_k}{\partial x_k}\delta_{ij} + \mu\left(\frac{\partial u_i}{\partial x_j} + \frac{\partial u_j}{\partial x_i}\right) \tag{1.23}$$

1.2.2.2 Species diffusion flux

In multi-species flows the total mass conservation implies that:

$$\sum_{k=1}^{N} Y_k V_{k,i} = 0 \qquad \sum_{k=1}^{N} \dot{\omega}_k = 0 \tag{1.24}$$

where $V_{k,i}$ are the components in the i-direction of the diffusion velocity of species k. They are often expressed as a function of the species gradients using the Hirschfelder-Curtis approximation (Hirschfelder et al. 1954):

$$X_k V_{k,i} = -D_k \frac{\partial X_k}{\partial x_i} \tag{1.25}$$

where X_k is the molar fraction of species k and D_k are the diffusion coefficients for each species k in the mixture. In terms of mass fraction, Eq. (1.25) may be expressed as:

$$Y_k V_{k,i} = -D_k \frac{W_k}{W} \frac{\partial X_k}{\partial x_i} \tag{1.26}$$

The species diffusion due to temperature gradients (Soret effect) and molecular transport due to pressure gradients (Giovangigli 1999) are neglected in this thesis.
Summing Eq. (1.26) for all species, it turns out that the approximation (1.26) does not necessarily comply with Eq. (1.24) that expresses mass conservation. In order to achieve this, a correction diffusion velocity V_i^c is added to the convection velocity to ensure global mass conservation as (Poinsot and Veynante 2011):

$$V_i^c = \sum_{k=1}^{N} D_k \frac{W_k}{W} \frac{\partial X_k}{\partial x_i} \tag{1.27}$$

and computing the diffusive species flux for each species k taking into account this correction, we have:

$$J_{k,i} = \rho Y_k (V_{k,i} + V_i^c) = -\rho \left(D_k \frac{W_k}{W} \frac{\partial X_k}{\partial x_i} - Y_k V_i^c \right) \tag{1.28}$$

1.2.2.3 Heat flux vector

For multi-species flows, an additional heat flux term appears in the diffusive heat flux. This term is due to heat transport by species diffusion. The total heat flux vector then writes:

$$q_i = -\lambda \frac{\partial T}{\partial x_i} + \sum_{k=1}^{N} J_{k,i} h_{sk} \tag{1.29}$$

$$q_i = \underbrace{-\lambda \frac{\partial T}{\partial x_i}}_{\text{conduction}} \quad \underbrace{-\rho \sum_{k=1}^{N} \left(D_k \frac{W_k}{W} \frac{\partial X_k}{\partial x_i} - Y_k V_i^c \right) h_{sk}}_{\text{species diffusion}} \tag{1.30}$$

where λ is the heat conduction coefficient of the mixture. Note that the Dufour effect which takes into account the energy flux due to mass fraction gradients (Giovangigli 1999) are omitted in this work.

1.2.3 Transport coefficients

The dynamic viscosity μ depends on the species concentration, however in most CFD codes the viscosity is assumed to depend only on temperature, as the error induced by such approximation is small (especially for air-fuel combustion in which nitrogen is predominant). The Sutherland's Law (Eq. 1.31) is one of the most used approximations:

$$\mu = \mu_{ref} \left(\frac{T}{T_{ref}} \right)^{3/2} \frac{T_{ref} + S}{T + S} \tag{1.31}$$

where μ_{ref} is the viscosity measured at the reference temperature T_{ref} and S is the Sutherland temperature. In our simulations, we have $T_{ref} = 273$ K, $\mu_{ref} = 1,71 \times 10^{-5}$ kg/m.s and $S = 110,4$ K.
The molecular Prandtl number of the mixture is supposed here constant in time and space, $Pr = 0.68$. The heat conduction coefficient of the gas mixture can then be computed as:

$$\lambda = \frac{\mu C_p}{Pr} \tag{1.32}$$

The thermal diffusion is defined as:

$$D_T = \frac{\mu}{\rho Pr} = \frac{\lambda}{\rho C_p} \tag{1.33}$$

The computation of the species diffusion coefficients D_k is a specific issue. These coefficients are written as a function of the binary coefficients D_{ij} obtained from kinetic theory (Hirschfelder et al. 1954) and are expressed as in Bird et al. (1960):

$$D_k = \frac{1 - Y_k}{\sum_{j \neq k}^{N} X_j / D_{jk}} \tag{1.34}$$

where D_{ij} are complex functions of collision integrals and thermodynamic variables. For a Direct Numerical Simulation (DNS) using complex chemistry, using Eq. (1.34) makes sense. However in most industrial application using Large Eddy Simulations (LES) with reduced chemical schemes, a complex transport description is not necessary. Thus, a simplified approximation is used to determine D_k. The Schmidt numbers Sc_k of the species are assumed to be constant and do not vary in time and space. The diffusion coefficient for each species is computed as:

$$D_k = \frac{\mu}{\rho Sc_k} \tag{1.35}$$

The thermal heat diffusivity D_T and the species diffusion coefficient D_k are linked via the Lewis number Le_k of species k:

$$Le_k = \frac{D_T}{D_k} = \frac{Sc_k}{Pr} \tag{1.36}$$

In simple turbulent models, the Lewis number is usually assumed to be equal to unity, meaning that thermal and molecular diffusivities are equal. In this case, and assuming constant pressure, no heat losses and neglecting the power due to viscous forces, mass and energy balance equation are formally the same.

1.2.4 Source terms

The source term $\mathbf{s}$ on the right hand side of Eq. (1.14) writes:

$$\mathbf{s} = \begin{pmatrix} 0 \\ 0 \\ 0 \\ \dot{\omega}_T \\ \dot{\omega}_k \end{pmatrix} \tag{1.37}$$

where $\dot{\omega}_T$ is the rate of heat release and $\dot{\omega}_k$ the reaction rate of species k. Consider N species $\mathcal{M}_k$ reacting through M reactions as:

$$\sum_{k=1}^{N} \nu_{ki}^{'} \mathcal{M}_k \rightleftharpoons \sum_{k=1}^{N} \nu_{ki}^{''} \mathcal{M}_k, \qquad i = 1, ..., M \tag{1.38}$$

$\nu_{ki}^{'}$ and $\nu_{ki}^{''}$ are the molar stoichiometric coefficients of species k for reaction i. The total reaction rate of species k, $\dot{\omega}_k$ is the sum of rates $\dot{\omega}_{ki}$ produced by all M reactions:

$$\dot{\omega}_k = \sum_{i=1}^{M} \dot{\omega}_{ki} = W_k \sum_{i=1}^{M} \nu_{ki} \mathcal{Q}_i \tag{1.39}$$

where $\nu_{ki} = \nu_{ki}^{''} - \nu_{ki}^{'}$ and $\mathcal{Q}_i$ is the rate progress of reaction i and is written:

$$\mathcal{Q}_i = K_{fi} \prod_{k=1}^{N} \left(\frac{\rho Y_k}{W_k} \right)^{\nu_{ki}^{'}} - K_{ri} \prod_{k=1}^{N} \left(\frac{\rho Y_k}{W_k} \right)^{\nu_{ki}^{''}} \tag{1.40}$$

K_{fi} and K_{ri} are the forward and reverse rates of reaction i. They are commonly modeled using the empirical Arrhenius law:

$$K_{fi} = A_i T^{\beta_i} \exp\left(-\frac{E_{ai}}{RT} \right) \tag{1.41}$$

Information about the pre-exponential constant A_i, the temperature exponent β_i and the activation energy E_{ai} of reaction i must be provided. The reverse rates K_{ri} are computed from the forward rates and the equilibrium constants K_{eq}^i:

$$K_{ri} = \frac{K_{fi}}{K_{eq}^i} \tag{1.42}$$

The K_{eq}^i terms depend only on the temperature and the thermodynamic data of the system and are written as (Kuo 1986):

$$K_{eq}^i = \left(\frac{p_{atm}}{RT}\right)^{\sum_{k=1}^{N} \nu_{ki}} \exp\left(\frac{S_i^0}{R} - \frac{H_i^0}{RT}\right) \tag{1.43}$$

H_i^0 and S_i^0 are respectively the enthalpy and the entropy changes when passing from reactants to products for reaction i.
The heat release is calculated as:

$$\dot{\omega}_T = -\sum_{k=1}^{N} \dot{\omega}_k \Delta h_{f,k}^0 \tag{1.44}$$

where $\Delta h_{f,k}^0$ is the mass enthalpy of formation of species k at temperature $T_0 = 0$ K.
The source term linked to radiation effects is not taken into account in this manuscript.

Chapter 2

General features on turbulent combustion

Before studying turbulent flames and turbulent combustion models for large eddy simulations, a good knowledge of laminar flames is essential. Firstly, because the understanding of turbulent combustion phenomena is impossible without a prior description of the laminar flames properties and secondly, because most theories developed for turbulent flames are based on concepts derived from laminar flames studies. For this reason, indispensable notions concerning premixed laminar flames are briefly presented. Then, turbulent combustion regimes are discussed.

2.1 Laminar premixed flames

The structure of a laminar premixed flame is shown in Fig. 2.1. The flame front can be decomposed into two zones: the preheating and the reaction zone. While the preheating zone is dominated by species diffusion, the reaction zone is controlled by chemical effects.
The equivalence ratio ϕ is used to determine the combustion regime ($\phi < 1$ for lean combustion; $\phi > 1$ for rich combustion). In premixed flames the local equivalence ratio has a homogeneous spatial distribution and can be associated to the mass fractions of fuel and oxidizer by the following relation:

$$\phi = s\frac{Y_F^u}{Y_O^u} \tag{2.1}$$

where s is the mass stoichiometric ratio. For a generic reaction $\nu_F F + \nu_O O \longrightarrow \nu_P P$, with ν_F and ν_O being the molar stoichiometric coefficients, we have:

$$s = \frac{\nu_O W_O}{\nu_F W_F} \tag{2.2}$$

where W_F and W_O are the molecular weights of fuel and oxidizer respectively.

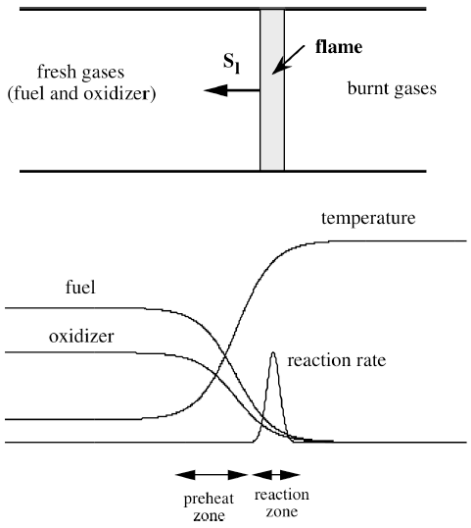

Figure 2.1: *Structure of a one-dimensional laminar premixed flame (Veynante and Vervisch 2002).*

Assuming a simple one-step irreversible chemical scheme, the evolution of the thermochemical quantities through the front of a premixed flame is described by the progress variable c which is a standardized reactive scalar. It can be defined using intensive (temperature) or extensive quantities (mass fractions) and is defined as $c = 0$ in the fresh gases, wherein the reaction is not yet initiated, and $c = 1$ in the fully burnt ones:

$$c = \frac{T - T^u}{T^b - T^u} \quad \text{or} \quad c = \frac{Y_F - Y_F^u}{Y_F^b - Y_F^u} \tag{2.3}$$

where T, T^u, and T^b are respectively the local, the unburnt gas and the burnt gas temperatures. Y_F, Y_F^u, and Y_F^b are respectively the local, the unburnt gas and the burnt gas fuel mass fractions. For unity Lewis numbers (identical molecular and thermal diffusivities), without heat losses (adiabatic combustion) and neglecting compressibility effects, the two definitions of Eq. (2.3) are equivalent and mass and low Mach number energy balance equations reduce to a single balance equation for the progress variable:

$$\frac{\partial \rho c}{\partial t} + \nabla.(\rho \mathbf{u} c) = \nabla.(\rho D \nabla c) + \dot{\omega} \tag{2.4}$$

The flame propagation speed is a crucial point in the theory of combustion. Three definitions of flame speeds are now introduced: displacement S_d, absolute S_a and consumption S_c speeds.

The previous Eq. (2.4) may be recast in a propagative form, introducing the displacement speed S_d of the iso-c surface (Veynante and Vervisch 2002):

$$\frac{\partial c}{\partial t} + \mathbf{u}.\nabla c = \underbrace{\frac{1}{\rho}\left[\frac{\nabla.(\rho D \nabla c) + \dot{\omega}}{|\nabla c|}\right]}_{\text{displacement speed}} |\nabla c| = S_d \, |\nabla c| \tag{2.5}$$

Eq. (2.5) describes the displacement of an iso-c surface with the displacement speed S_d measured relative to the flow.
The absolute speed S_a is the flame front speed relative to a fixed reference frame. It is written as:

$$S_a = \mathbf{u} + S_d \, \mathbf{n} \tag{2.6}$$

$\mathbf{n}$ is the unit vector normal to the flame front pointing towards the fresh gases, expressed as a function of the local gradient of the progress variable: $\mathbf{n} = -\nabla c / |\nabla c|$.
The consumption speed S_c is the speed at which the reactants are consumed. It can be estimated from the mass conservation of fuel, for instance:

$$S_c = \frac{\int_{-\infty}^{+\infty} \dot{\omega}_F dx}{\rho^u (Y_F^b - Y_F^u)} \tag{2.7}$$

For a laminar planar unstretched freely propagating one-dimensional flame, the displacement and consumption speed are equal and simply referred to as "the laminar flame speed" denoted S_L in the following ($S_L = S_d = S_c$). It is the reference speed for all combustion studies.
For a stretched flame, the different flame speeds (S_d, S_a and S_c) are modified and their evaluation is not straightforward. The flame stretch κ defined as the fractional rate of change of a flame surface element A (Williams 1985):

$$\kappa = \frac{1}{A}\frac{dA}{dt} \tag{2.8}$$

can be decomposed into strain and curvature terms (Candel and Poinsot 1990). Asymptotic theories show that if these terms are small, the displacement and consumption speeds have a linear response to stretch (Bush and Fendell 1970; Clavin 1985):

$$\frac{S_d}{S_L} = 1 - \mathcal{L}_a^d \frac{\kappa}{S_L} \qquad \text{and} \qquad \frac{S_c}{S_L} = 1 - \mathcal{L}_a^c \frac{\kappa}{S_L} \tag{2.9}$$

where $\mathcal{L}_a^d$ and $\mathcal{L}_a^c$ are Markstein lengths. Many expressions for these terms are available in the literature (see Clavin and Joulin (1983) for instance).

The thermal flame thickness is another key variable for the dynamic description of premixed flames and there are many ways to define it. A classical way is to link this parameter to the temperature gradient as:

$$\delta_L^0 = \frac{T^b - T^u}{\left|\frac{\mathrm{d}T}{\mathrm{d}x}\right|_{\max}} \tag{2.10}$$

One can define a second thermal thickness δ_L^1 corresponding to the temperature jump of 98% of the temperature difference between fresh and burnt products. A typical flame thickness is about $0.1 - 1$ mm and for the laminar flame speed of $0.1 - 1$ m/s. These two parameters are related to the Reynolds number of the flame by the following relationship derived from the theory of Zeldovitch / Franck-Kamenetski (Veynante and Vervisch 2002):

$$Re_f = \frac{S_L \delta_L^1}{\nu} \approx 4 \qquad \text{for } 0.01 \leq c \leq 0.99 \tag{2.11}$$

In practice δ_L^1 is always larger than δ_L^0 and since definition (2.10) measures temperature gradient, it is more convenient to determine the mesh resolution.

2.2 Turbulent premixed combustion

Turbulent combustion involves various lengths, velocity and time scales describing turbulent flow field and chemical reactions. The Damköhler number compares turbulent (τ_t) and chemical (τ_c) time scales. For turbulent premixed flames, the chemical time scale may be estimated as the ratio of the thickness δ_L^0 and the propagation speed S_L of the laminar flame. The turbulent time is estimated from the turbulent integral scales:

$$Da = \frac{\tau_t}{\tau_c} = \frac{\ell_t / u'(\ell_t)}{\delta_L^0 / S_L} \tag{2.12}$$

In the limit of high Damköhler numbers ($Da \gg 1$), the chemical time is short compared to the turbulent one, corresponding to a thin reaction zone distorted and convected by the flow field. The internal structure of the flame is not strongly affected by turbulence and may be described as a laminar flame element called "flamelet". The turbulent structures wrinkle and strain the flame surface. On the other hand, a low Damköhler number ($Da \ll 1$) corresponds to a slow chemical reaction. Reactants and products are rapidly mixed by turbulence as the reaction progresses slowly. As a result, turbulent motions becomes sufficiently strong to affect the whole flame structure so that the flame front

is no longer distinguishable. This is the case of the perfectly stirred reactor (Libby and Williams 1980).
According to the criterion of Klimov-Williams (Klimov 1988; Williams 1976), even for $Da > 1$, the small structures associated with the Kolmogorov scales, η, can penetrate the flame front and change its topological structure. This observation motivated the introduction of another parameter to characterize the flame topology. The Karlovitz number (Ka) completes the description of the different flame regimes. It compares the chemical time to the time associated with the smallest turbulent structures (Peters 1986):

$$Ka = \frac{\tau_c}{\tau_k} = \frac{u'(\eta)/\eta}{S_L/\delta_l^0} = \left(\frac{\delta_L^0}{\eta}\right)^2 \tag{2.13}$$

τ_k being the Kolmogorov characteristic time scale.
The Karlovitz number takes into account possible interactions between these small structures and the flame itself. Several authors, including Borghi (1985); Peters (1986); Borghi and Destriau (1998); Peters (1999) among others, used Re, Da and Ka numbers to discuss various flame regimes in the case of premixed reactants and classified them in a diagram similar to the one shown in Fig. 2.2.

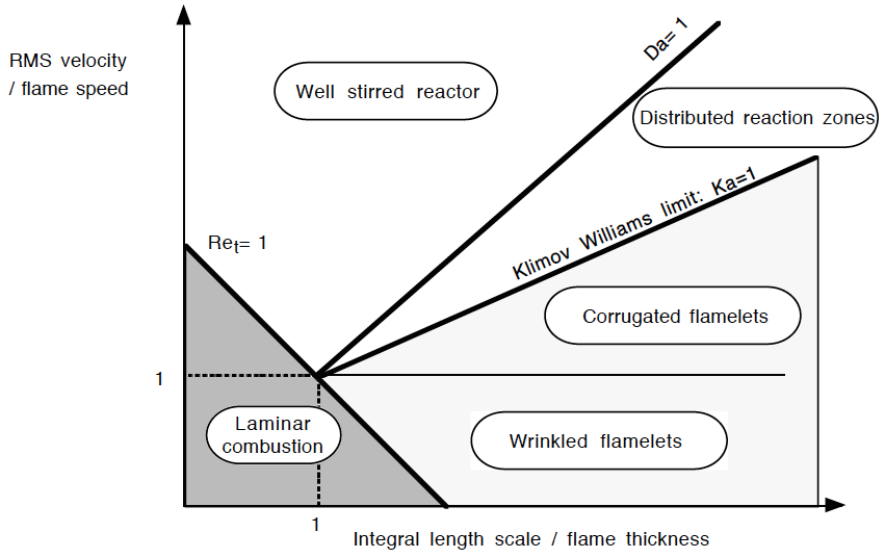

Figure 2.2: *Turbulent premixed combustion diagram: combustion regimes are identified in terms of length (ℓ_t/δ_L^0) and velocity (u'/S_L) ratios using a log-log scale (Poinsot and Veynante 2011).*

The following turbulent premixed flame regimes are proposed (Peters 1999):

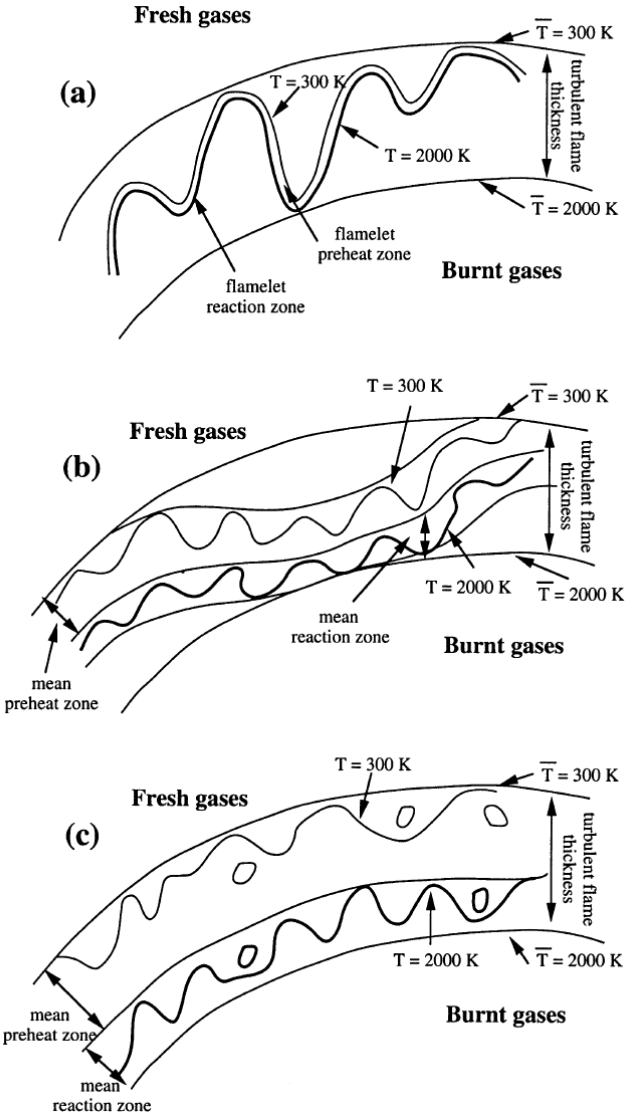

Figure 2.3: *Turbulent premixed combustion regimes proposed by Borghi and Destriau (1998). (a) flamelet (thin wrinkled flame), (b) thickened wrinkled flame regime and (c) thickened flame regime (Veynante and Vervisch 2002).*

1. $Ka < 1$ ($Da > 1$): Flamelet regime or thin wrinkled flame regime (Fig. 2.3-a). In this regime, the flame front is thin, has an inner structure close to a laminar flame and is wrinkled by turbulent structures. Two subdivisions may be proposed depending on the velocity ratio u'/S_L:

    - $(u'/S_L) < 1$: wrinkled flame. As u' may be viewed as the rotation speed of the larger turbulent motions, turbulent structures are unable to wrinkle the flame surface up to flame front in-

teractions. The laminar propagation is predominant and turbulence/combustion interactions remain limited.

- $(u'/S_L) > 1$: wrinkled flame with pockets ("corrugated flames"). In this situation, larger structures become able to induce flame front interactions leading to pockets.

2. $Ka > 1$ and $Da > 1$: Thickened wrinkled flame regime or thin reaction zone. In this case, turbulent motions are able to affect and to thicken the flame preheat zone, but cannot modify the reaction zone which remains thin and close to a laminar reaction zone (Fig. 2.3-b).

3. $Da < 1$: Thickened flame regime or well-stirred reactor. In this situation, preheat and reaction zones are strongly affected by turbulent motions and no laminar flame structure may be identified (Fig. 2.3-c).

The line separating corrugated flamelets and thickened wrinkled flame regimes corresponds to the condition $Ka = 1$ and is known as the Klimov-Williams criterion. It is important to remember that combustion diagrams are based on qualitative variables and simplifying assumptions. However, even if those limits are not exact, this flame regime diagram allowed the formulation of several combustion models for different applications.

When fresh gases are turbulent, the premixed flame propagates faster. Of course there is a practical interest to determine the flame speed in a turbulent flow, but the problem here is much more complex than in the laminar case. In the flamelet regime, the turbulent flame front can be modeled locally as a laminar premixed flame which is stretched and deformed by turbulence. The main effect of turbulence on combustion is the flame front wrinkling by the largest turbulent structures, increasing the total flame surface A_T. Consequently, the reactant consumption rate increases, augmenting the propagation speed of the mean flame front. In the flamelet regime, the turbulent flame front propagates with a turbulent flame speed S_T equal to the laminar flame speed S_L weighted by the ratio of the wrinkled instantaneous front area A_T and the area of the mean flame surface A (Fig. 2.4):

$$S_T = S_L \frac{A_T}{A} \tag{2.14}$$

Various expressions have been proposed in the literature to estimate the turbulent flame speed and it is still an open problem of major interest in the context of numerical simulations of turbulent reactive flows, as it is an essential parameter to many models that aims to reproduce the effect of turbulence on the flame. This subject is treated more deeply in the next chapters.

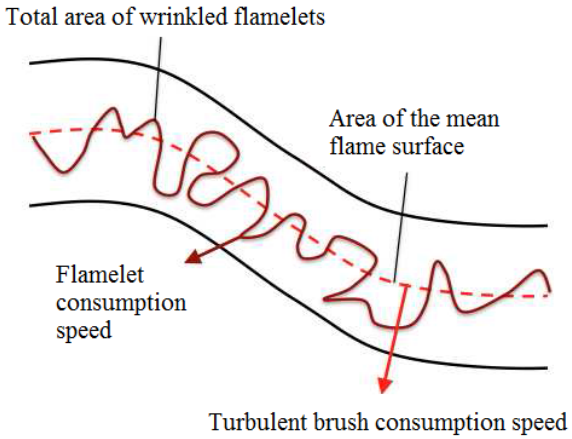

Figure 2.4: *Sketch of the total wrinkled area A_T and the mean flame surface A. The flamelet consumption speed S_L and the turbulent brush local consumption speed S_T are also labeled (Driscoll 2008).*

Chapter 3

Numerical simulations and modeling

Nowadays, running full-resolved simulations of highly turbulent reactive flows typical from industrial combustion systems is a practically impossible task. Large eddy simulation, based on the filtering of Navier-Stokes equations, is a widespread technique able to overcome this difficulty. In LES, the biggest structures of the flow are captured by the grid while the effect of the small ones is modeled. In this chapter, the LES concept and several sub-grid models are discussed.

3.1 Introduction

Solving the unsteady Navier-Stokes equations requires taking into account all space and time scales of the solution. Therefore, the discretization has to be fine enough to represent numerically all scales of the flow. It means that space (Δx) and time (Δt) steps of the simulation must be smaller, respectively, than the characteristic length and the characteristic time associated with the smallest dynamically active scale of the exact solution. This criterion turns out to be extremely restrictive when the solution of the exact problem contains scales of very different sizes, which is the case of turbulent flows. For example, considering a statistically homogeneous and isotropic turbulent flow, it is easy to show that the ratio between the characteristic length of the most energetic scale, ℓ_t, and that of the smallest dynamically active scale (called the Kolmogorov scale), η, is evaluated by the relation:

$$\frac{\ell_t}{\eta} = \mathcal{O}\left(Re^{3/4}\right) \tag{3.1}$$

in which Re is the Reynolds number, which is a measure of the ratio of the forces of inertia and the molecular viscosity effects. Thus, we need $\mathcal{O}\left(Re^{9/4}\right)$ degrees of freedom in order to be able to represent all scales in a cubic volume of size

ℓ_t. In addition, the use of explicit time-integration algorithm leads to a linear dependency of the time step with respect to the mesh size (Pope 2000). Thus, in order to calculate the evolution of the solution in a volume ℓ_t^3 for a duration equal to the characteristic time of the most energetic scale, the Navier-Stokes equations must be solved numerically $\mathcal{O}\left(Re^3\right)$ times!
High Reynolds numbers typically found in aeronautical applications ($Re \approx 10^8$) requires computer resources much greater than currently available supercomputer capacities. Therefore this prohibitive numerical cost makes impracticable the use of direct numerical simulations (DNS) for industrial applications. For this reason, we do not have access to the exact solution but different methods have been developed in order to obtain in a coarser level the description of the fluid system (Sagaut 2002).
This comes down to picking out certain scales that will be represented directly in the simulation while others will not be. The non-linearity of the Navier-Stokes equations reflects the dynamic coupling that exists among all the scales of the solution, which implies that these scales cannot be calculated independently of each other. So, a good representation of scales that are resolved in the simulation must consider their interactions with scales that are missing. To model these interactions, additional terms are introduced in the equations governing the evolution of the resolved scales.
In Reynolds averaged Navier-Stokes simulation (RANS), the artifice used to reduce the number of degrees of freedom is the separation of the flow variable into mean (ensemble-averaged) and fluctuating components. In this case, a turbulence model is used to describe the behavior of the fluctuations.
In large eddy simulation (LES), a low-pass filtering operation is applied to the Navier-Stokes equations to eliminate small scales of the solution. In this way, the large scale eddies, which contain the energy of the flow are separated from the small scales where dissipation occurs. One more time, a model is necessary to take into account the effects of small structures. Since this model reflect the global (or average) action of a large number of small scales with those that are resolved, LES makes sense only in a statistical approach. Therefore, instantaneous filtered quantities are not supposed to be directly compared to experimental flow fields (Pope 2000; Pope 2004).
Figure 3.1 illustrates the difference between RANS, LES and DNS using the example of the turbulent kinetic energy spectrum (E), which is plotted as a function of the inverse length scale of the turbulent structures.

3.2 The LES filtering approach

The cut off between the structures of a turbulent flow that are resolved and the ones that are modeled, is done by spatially filtering the balance equations. This procedure can be interpreted as the convolution of a quantity of interest

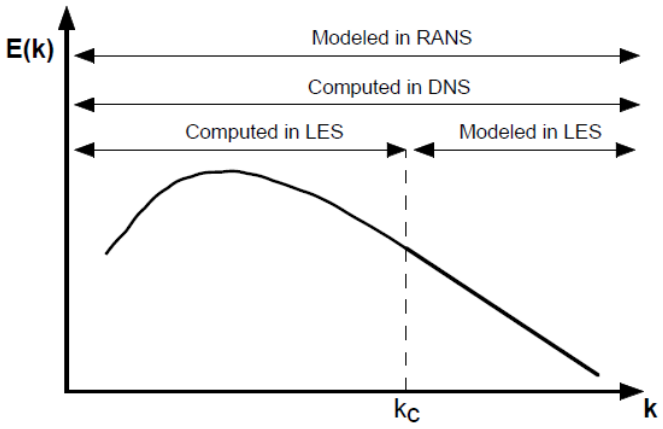

Figure 3.1: *Turbulence energy spectrum plotted as a function of wave numbers (proportional to the inverse of the length scales). RANS, LES and DNS are summarized in terms of spatial frequency range. k_c is the cut-off wave number used in LES (log-log diagram) (Poinsot and Veynante 2011).*

with a low-pass filter function G (Leonard 1974). Mathematically this yields:

$$\overline{\phi}(\mathbf{x}) = \int G(\mathbf{x} - \mathbf{x}')\phi(\mathbf{x}')d\mathbf{x}' \tag{3.2}$$

In general, G is chosen as a box filter or a Gaussian filter (Sagaut 2002). These filters are written in the physical space as:

- Box filter

$$G(\mathbf{x}) = \begin{cases} 1/\Delta^3 & \text{if } |\mathbf{x}| \leq \Delta/2 \\ 0 & \text{otherwise} \end{cases} \tag{3.3}$$

  This filter corresponds to an averaging over a cubic box of size Δ.

- Gaussian filter

$$G(\mathbf{x}) = \left(\frac{6}{\pi\Delta^2}\right)^{3/2} \exp\left[-\frac{6}{\Delta^2}(x^2 + y^2 + z^2)\right] \tag{3.4}$$

The filtered quantity, denoted using an overbar ($\overline{\phi}$), represents the resolved turbulent structures (large eddies). All structures smaller than the filter width are denoted as:

$$\phi'(\mathbf{x}, t) = \phi(\mathbf{x}, t) - \overline{\phi(\mathbf{x}, t)} \tag{3.5}$$

In order to account for density fluctuations when applying filtering to the compressible balance equations, density weighted Favre-filtering (Favre 1969) can

be applied. The tilde ($\widetilde{\phi}$) denotes the variable in consideration. By this means, the occurrence of sub-grid scale terms in the mass balance equation can be avoided. A Favre filtered quantity is defined as follows:

$$\overline{\rho}\widetilde{\phi}(\mathbf{x}) = \int G(\mathbf{x}-\mathbf{x}')\rho\phi(\mathbf{x}')d\mathbf{x}' \quad \text{or} \quad \widetilde{\phi} = \frac{\overline{\rho\phi}}{\overline{\rho}} \tag{3.6}$$

3.2.1 Fundamental Properties

In order to be able to manipulate the filtered Navier-Stokes equations, the filter has to verify the three following properties:

- Conservation of constants:

$$\overline{a} = a \longleftrightarrow \int_{-\infty}^{+\infty} G(\mathbf{x}')d\mathbf{x}' = 1 \tag{3.7}$$

- Linearity:

$$\overline{\phi+\psi} = \overline{\phi} + \overline{\psi} \tag{3.8}$$

- Commutation with derivation:

$$\overline{\frac{\partial\phi}{\partial x_i}} = \frac{\partial\overline{\phi}}{\partial x_i} \quad ; \quad \overline{\frac{\partial\phi}{\partial t}} = \frac{\partial\overline{\phi}}{\partial t} \tag{3.9}$$

Note that the filtering operation is not based on a Reynolds operator. Thus, a priori:

$$\overline{\overline{\phi}} \neq \overline{\phi} \quad \text{and} \quad \overline{\phi'} \neq 0 \tag{3.10}$$

While properties (3.7) and (3.8) are performed without difficulty for an isotropic filter, for an inhomogeneous or anisotropic filter, the third property is more difficult to be verified. Thus, spatial commutation errors occur when the filter is inhomogeneous, especially when the domain is bounded by walls or when the mesh size is not uniform. These terms resulting from the non-commutation with derivation are often considered to be included in the sub-grid models.
Ghosal and Moin (1995) proposed a class of filters with variable cut-off length for bounded or unbounded domains. They presented an alternative definition of the filtering operation based on the mapping function of the non-uniform grid and showed that the introduced commutation error was of order Δ^2 (Second order commuting filter - SOCF). Thus, if the numerical scheme is also of order 2, we can say that the filtering operation commutes with the derivation, once the error introduced by the filtering is not bigger than the one introduced by the second-order finite difference scheme. The authors emphasize that if

the numerical scheme is of a higher order, the commutation error cannot be neglected.
Van der Ven (1995) constructed a family of filters developed for LES with non-uniform filter widths that commute with differentiation up to any given order. However, this family of filters is applicable only for infinite domains. In order to overcome this issue, Vasilyev et al. (1998) have extended the previous studies for the generic case of a bounded domain, i.e. non-periodic boundary conditions.
In practice, the filter used in most of the codes is the so-called implicit filter, typical of the mesh. Actually, the explicit filter is used only in simple cases simulated with finite difference codes with regular meshes. In the majority of industrial cases, the separation between the resolved and modeled scales is in fact dictated by the size of the grid cells. As the mesh is refined, the resolved scales become finer and the modeling of small scales is less critical. Thus, when the mesh size tends to the Kolmogorov scale, the resolution of the LES approaches to the DNS resolution.

3.3 Filtered equations for reactive flows

The balance equations for large eddy simulations are obtained by filtering the instantaneous balance equations (1.11), (1.12) and (1.13).

$$\frac{\partial \overline{\rho}\widetilde{u}_i}{\partial t} + \frac{\partial}{\partial x_j}(\overline{\rho}\widetilde{u}_i\widetilde{u}_j) + \frac{\partial}{\partial x_j}\overline{\rho}(\widetilde{u_i u_j} - \widetilde{u}_i\widetilde{u}_j) = -\frac{\partial \overline{P}\delta_{ij}}{\partial x_j} + \frac{\partial \overline{\tau}_{ij}}{\partial x_j} \tag{3.11}$$

$$\frac{\partial \overline{\rho}\widetilde{E}}{\partial t} + \frac{\partial}{\partial x_j}(\overline{\rho}\widetilde{u}_j\widetilde{E}) + \frac{\partial}{\partial x_j}\overline{\rho}(\widetilde{u_j E} - \widetilde{u}_j\widetilde{E}) = -\frac{\partial}{\partial x_j}\left[\overline{u_i(P\delta_{ij} - \tau_{ij})} + \overline{q}_j\right] + \overline{\dot{\omega}}_T \tag{3.12}$$

$$\frac{\partial \overline{\rho}\widetilde{Y}_k}{\partial t} + \frac{\partial}{\partial x_j}(\overline{\rho}\widetilde{Y}_k\widetilde{u}_j) + \frac{\partial}{\partial x_j}\overline{\rho}(\widetilde{u_j Y_k} - \widetilde{u}_j\widetilde{Y_k}) = -\frac{\partial}{\partial x_j}\left[\overline{J}_{j,k}\right] + \overline{\dot{\omega}}_k \tag{3.13}$$

or in vectorial notation

$$\frac{\partial \overline{\mathbf{w}}}{\partial t} + \nabla \cdot \overline{\mathbf{F}} = \overline{\mathbf{s}} \tag{3.14}$$

with $\overline{\mathbf{w}} = \left(\overline{\rho}\widetilde{u}, \overline{\rho}\widetilde{v}, \overline{\rho}\widetilde{w}, \overline{\rho}\widetilde{E}, \overline{\rho}\widetilde{Y}_k\right)^T$ being the state vector and $\overline{\mathbf{s}}$ representing the filtered source terms. $\overline{\mathbf{F}}$ is the flux tensor and it can be divided in three parts: the resolved inviscid part $\overline{\mathbf{F}}^I$, the viscous part $\overline{\mathbf{F}}^V$ and the sub-grid scale turbulent part $\overline{\mathbf{F}}^{SGS}$.

When we separate the resolved part of the field, which represents the "large" eddies, and the unresolved part, which represents the "small scales", unknown terms appear in the filtered equations. The effect of unresolved scales on the resolved field is included through the sub-grid scale (SGS) models. In this set of equations, the following quantities must be modeled:

- **Unresolved Reynolds stresses** $\overline{\tau}_{ij}^{sgs} = \overline{\rho}(\widetilde{u_i u_j} - \widetilde{u}_i \widetilde{u}_j)$, which represents the impact of the unresolved flow motions on the resolved momentum.
- **Unresolved species fluxes** $\overline{J}_{j,k}^{sgs} = \overline{\rho}(\widetilde{u_i Y_k} - \widetilde{u}_i \widetilde{Y_k})$.
- **Unresolved energy fluxes** $\overline{q}_j^{sgs} = \overline{\rho}(\widetilde{u_i E} - \widetilde{u}_i \widetilde{E})$.
- **Filtered laminar diffusion fluxes** $\overline{J}_{j,k}$ in the especies equation and $\overline{q}_j$ in the energy equation.
- **Filtered chemical reaction rates** $\overline{\dot{\omega}}_k$

3.3.1 Inviscid terms

The three spatial components of the inviscid flux tensor are the same as in DNS but based on the filtered quantities:

$$\overline{\mathbf{f}}^I = \begin{pmatrix} \overline{\rho}\widetilde{u}^2 + \overline{P} \\ \overline{\rho}\widetilde{u}\widetilde{v} \\ \overline{\rho}\widetilde{u}\widetilde{w} \\ \overline{\rho}\widetilde{E}\widetilde{u} + \overline{Pu} \\ \overline{\rho}\widetilde{Y}_k\widetilde{u} \end{pmatrix} \tag{3.15}$$

$$\overline{\mathbf{g}}^I = \begin{pmatrix} \overline{\rho}\widetilde{u}\widetilde{v} \\ \overline{\rho}\widetilde{u}\widetilde{v}^2 + \overline{P} \\ \overline{\rho}\widetilde{v}\widetilde{w} \\ \overline{\rho}\widetilde{E}\widetilde{v} + \overline{Pv} \\ \overline{\rho}\widetilde{Y}_k\widetilde{v} \end{pmatrix} \tag{3.16}$$

$$\overline{\mathbf{h}}^I = \begin{pmatrix} \overline{\rho}\widetilde{u}\widetilde{w} \\ \overline{\rho}\widetilde{v}\widetilde{w} \\ \overline{\rho}\widetilde{w}^2 + \overline{P} \\ \overline{\rho}\widetilde{E}\widetilde{w} + \overline{Pw} \\ \overline{\rho}\widetilde{Y}_k\widetilde{w} \end{pmatrix} \tag{3.17}$$

3.3.2 Viscous terms

The components of the viscous flux tensor take the form:

$$\overline{\mathbf{f}}^V = \begin{pmatrix} -\overline{\tau}_{xx} \\ -\overline{\tau}_{xy} \\ -\overline{\tau}_{xz} \\ -(\overline{u\tau}_{xx} + \overline{v\tau}_{xy} + \overline{w\tau}_{xz}) + \overline{q}_x \\ \overline{J}_{x,k} \end{pmatrix} \tag{3.18}$$

$$\overline{\mathbf{g}}^V = \begin{pmatrix} -\overline{\tau}_{xy} \\ -\overline{\tau}_{yy} \\ -\overline{\tau}_{yz} \\ -(\overline{u\tau}_{xy} + \overline{v\tau}_{yy} + \overline{w\tau}_{yz}) + \overline{q}_y \\ \overline{J}_{y,k} \end{pmatrix} \tag{3.19}$$

$$\overline{\mathbf{h}}^V = \begin{pmatrix} -\overline{\tau}_{xz} \\ -\overline{\tau}_{yz} \\ -\overline{\tau}_{zz} \\ -(\overline{u\tau}_{xz} + \overline{v\tau}_{yz} + \overline{w\tau}_{zz}) + \overline{q}_z \\ \overline{J}_{z,k} \end{pmatrix} \tag{3.20}$$

The filtered diffusion terms for non-reacting flows are modeled as follows:

3.3.2.1 Laminar filtered stress tensor $\overline{\tau}_{ij}$

$$\overline{\tau}_{ij} = \overline{2\mu\left(S_{ij} - \frac{1}{3}\delta_{ij}S_{ll}\right)} \approx 2\overline{\mu}\left(\widetilde{S}_{ij} - \frac{1}{3}\delta_{ij}\widetilde{S}_{ll}\right) \tag{3.21}$$

with $\overline{\mu} \approx \mu(\widetilde{T})$ and

$$\widetilde{S}_{ij} = \frac{1}{2}\left(\frac{\partial \widetilde{u}_j}{\partial x_i} + \frac{\partial \widetilde{u}_i}{\partial x_j}\right) \tag{3.22}$$

3.3.2.2 Diffusive species flux $\overline{J}_{i,k}$

$$\overline{J}_{i,k} = -\overline{\rho\left(D_k\frac{W_k}{W}\frac{\partial X_k}{\partial x_i} - Y_k V_i^c\right)} \approx -\overline{\rho}\left(\overline{D}_k\frac{W_k}{W}\frac{\partial \widetilde{X}_k}{\partial x_i} - \widetilde{Y}_k\widetilde{V}_i^c\right) \tag{3.23}$$

with $\overline{D}_k = \overline{\mu}/(\overline{\rho}Sc_k)$ and

$$\widetilde{V}_i^c = \sum_{k=1}^{N}\overline{D}_k\frac{W_k}{W}\frac{\partial \widetilde{X}_k}{\partial x_i} \tag{3.24}$$

3.3.2.3 Heat flux $\overline{q}_i$

$$\overline{q}_i = -\overline{\lambda\frac{\partial T}{\partial x_i}} + \sum_{k=1}^{N}\overline{J_{i,k}h_{sk}} \approx -\overline{\lambda}\frac{\partial \widetilde{T}}{\partial x_i} + \sum_{k=1}^{N}\overline{J}_{i,k}\widetilde{h}_{sk} \tag{3.25}$$

with $\overline{\lambda} \approx \overline{\mu}\overline{C_p}(\widetilde{T})/Pr$.

3.3.3 Sub-grid scale turbulent terms

Filtering the balance equations leads to unclosed quantities, which need to be modeled. The components of the turbulent sub-grid scale flux take the form:

$$\overline{\mathbf{f}}^{SGS} = \begin{pmatrix} \overline{\tau}_{xx}^{sgs} \\ \overline{\tau}_{xy}^{sgs} \\ \overline{\tau}_{xz}^{sgs} \\ \overline{q}_{x}^{sgs} \\ \overline{J}_{x,k}^{sgs} \end{pmatrix} \tag{3.26}$$

$$\overline{\mathbf{g}}^{SGS} = \begin{pmatrix} \overline{\tau}_{xy}^{sgs} \\ \overline{\tau}_{yy}^{sgs} \\ \overline{\tau}_{yz}^{sgs} \\ \overline{q}_{y}^{sgs} \\ \overline{J}_{y,k}^{sgs} \end{pmatrix} \tag{3.27}$$

$$\overline{\mathbf{h}}^{SGS} = \begin{pmatrix} \overline{\tau}_{xz}^{sgs} \\ \overline{\tau}_{yz}^{sgs} \\ \overline{\tau}_{zz}^{sgs} \\ \overline{q}_{z}^{sgs} \\ \overline{J}_{z,k}^{sgs} \end{pmatrix} \tag{3.28}$$

These different terms are modeled as:

3.3.3.1 Reynolds tensor $\overline{\tau}_{ij}^{sgs}$

$$\overline{\tau}_{ij}^{sgs} = \overline{\rho}\left(\widetilde{u_i u_j} - \widetilde{u}_i\widetilde{u}_j\right) \approx -2\overline{\rho}\nu_{sgs}\left(\widetilde{S}_{ij} - \frac{1}{3}\delta_{ij}\widetilde{S}_{kk}\right) \tag{3.29}$$

where ν_{sgs} is the so called SGS turbulent viscosity. Its modeling is one of the main issues in LES and is presented in Section 3.4.

3.3.3.2 Sub-grid scale diffusive species flux vector

$$\overline{J}_{i,k}^{sgs} = \overline{\rho}\left(\widetilde{u_i Y_k} - \widetilde{u}_i\widetilde{Y}_k\right) \approx -\overline{\rho}\left(D_k^{sgs}\frac{W_k}{W}\frac{\partial \widetilde{X}_k}{\partial x_i} - \widetilde{Y}_k\widetilde{V}_i^{c,t}\right) \tag{3.30}$$

with $D_k^{sgs} = \nu_{sgs}/Sc_k^t$. Usually, the turbulent Schmidt number $Sc_k^t = 0.6$ is the same for all species. The correction diffusion velocities are written as:

$$\widetilde{V}_i^c + \widetilde{V}_i^{c,t} = \sum_{k=1}^{N}\left(\frac{\overline{\mu}}{\overline{\rho}Sc_k} + \frac{\mu_{sgs}}{\overline{\rho}Sc_k^t}\right)\frac{W_k}{W}\frac{\partial \widetilde{X}_k}{\partial x_i} \tag{3.31}$$

3.3.3.3 Sub-grid scale heat flux vector

$$\overline{q}_i^{sgs} = \overline{\rho}\left(\widetilde{u_i E} - \widetilde{u}_i\widetilde{E}\right) \approx -\lambda_{sgs}\frac{\partial \widetilde{T}}{\partial x_i} + \sum_{k=1}^{N}\overline{J}_{i,k}^{sgs}\widetilde{h}_{sk} \tag{3.32}$$

with $\lambda_{sgs} = \mu_{sgs}\overline{C_p}(\widetilde{T})/Pr^t$. The turbulent Prandtl number is set $Pr^t = 0.6$.

3.4 LES models for the sub-grid stress tensor

The filtered compressible Navier-Stokes equations exhibit sub-grid scale (SGS) tensors and vectors describing the interaction between the resolved and non-resolved structures. The influence of the SGS on the resolved motion is commonly taken into account by a SGS model based on the introduction of a turbulent viscosity, ν_{sgs}. Such an approach assumes the effect of the SGS field on the resolved field to be purely dissipative. Boussinesq (1877) hypothesis is essentially valid within the cascade theory of turbulence of Kolmogorov (1941). Eddy-viscosity models are written in the following form:

$$\overline{\tau}_{ij}^{sgs} = -\overline{\rho}\nu_{sgs}\left(\frac{\partial \widetilde{u}_i}{\partial x_j} + \frac{\partial \widetilde{u}_j}{\partial x_i} - \frac{2}{3}\delta_{ij}\frac{\partial \widetilde{u}_k}{\partial x_k}\right) = -2\overline{\rho}\nu_{sgs}\left(\widetilde{S}_{ij} - \frac{1}{3}\delta_{ij}\widetilde{S}_{kk}\right) \tag{3.33}$$

$\widetilde{S}_{ij}$ being the strain rate of the resolved structures. The problem is closed when the sub-grid scale viscosity is specified. The three eddy viscosity models presented herein represent only a small variety of what is available in the literature. The objective is not to do an extensive description of sub-grid scale models but to describe the ones used in this manuscript. For more information on the topic, the reader is invited to refer to Sagaut (2002); Garnier et al. (2009).

3.4.1 Smagorinsky model and its filtered form

The pioneer work introduced by Smagorinsky (1963) was firstly developed for meteorological applications. Posteriorly, it has been extensively employed in other flow conditions. The turbulent viscosity is written:

$$\nu_{sgs} = (C_S\Delta)^2 \left(2\widetilde{S}_{ij}\widetilde{S}_{ij}\right)^{1/2} = (C_S\Delta)^2 \left|\widetilde{S}\right| \tag{3.34}$$

where Δ denotes the filter characteristic length evaluated as $\Delta = (\Delta x \Delta y \Delta z)^{1/3}$, C_S is the model constant set to 0.18 but can vary between 0.1 and 0.18 depending on the flow configuration. Giving the correct amount of dissipation in the case of a homogeneous isotropic turbulence, this model is known to be over predictive as soon as the flow becomes anisotropic, e.g. close to solid boundaries and mixing layers.
Ducros et al. (1996) improved the previous model by computing the resolved strain rate tensor from a high pass filtered velocity field.

$$\nu_{sgs} = (C_F\Delta)^2 \sqrt{2HP(\widetilde{S}_{ij})HP(\widetilde{S}_{ij})} \tag{3.35}$$

Transition is better predicted and locality is in general better preserved with the Filtered Smagorinsky model. In AVBP, $C_F = 0.37$.

3.4.2 Dynamic Smagorinsky model

The standard Smagorinsky model and the dynamic version proposed by Germano et al. (1991) differ in such a way that the model parameter C_d is no longer fixed *a priori* by the user but it is evaluated during the simulation. The objective is to estimate the small scale dissipation from the knowledge of the resolved eddies. The determination of C_d is based on the Germano identity and follows Lilly (1992)'s procedure. A test filter, $\widehat{\phi}$, of width $\widehat{\Delta} > \Delta$ is introduced. Numerical tests show that an optimal value for the test filter width is $\widehat{\Delta} = 2\Delta$ (Spyropoulos and Blaisdell 1996). Consider the following Germano identity (Fig. 3.2):

$$\mathcal{L}_{ij} = T_{ij} - \widehat{\tau}_{ij}^{sgs} \tag{3.36}$$

in which

$$T_{ij} = \widehat{\overline{\rho u_i u_j}} - \widehat{\overline{\rho u}}_i \widehat{\overline{\rho u}}_j / \widehat{\overline{\rho}} \tag{3.37}$$

$$\mathcal{L}_{ij} = \widehat{\overline{\rho}\widetilde{u}_i\widetilde{u}_j} - \widehat{\overline{\rho}\widetilde{u}}_i\widehat{\overline{\rho}\widetilde{u}}_j/\widehat{\overline{\rho}} \tag{3.38}$$

τ_{ij}^{sgs} is the sub-grid stress term, T_{ij} is the sub-grid stress term at the test level and $\mathcal{L}_{ij}$ is the resolved turbulent stress.

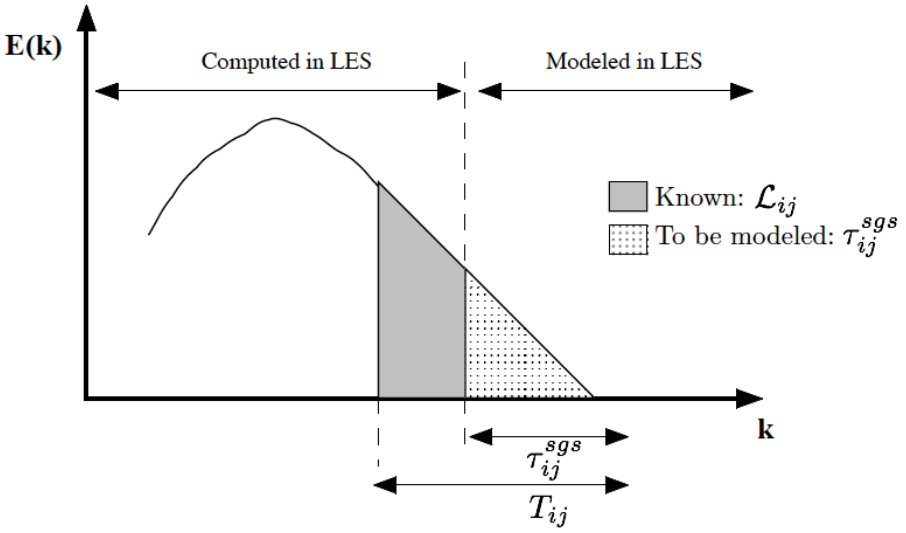

Figure 3.2: *Graphical representation of the Germano identity (3.36) in the energy spectrum. The unknown unresolved Reynolds stresses at the filter level (τ_{ij}^{sgs}) and at the test filter level (T_{ij}) are related through $\mathcal{L}_{ij}$ which is the LES resolved part of the unresolved Reynolds stresses T_{ij} (Poinsot and Veynante 2011).*

We now assume that the two sub-grid tensors τ_{ij}^{sgs} and T_{ij} can be modeled by the same constant C_d for both filter levels. If one considers the Smagorinsky model, this is expressed as:

$$\tau_{ij}^{sgs} - \frac{\delta_{ij}}{3}\tau_{kk}^{sgs} = -2C_d\Delta^2|\widetilde{S}|\left(\widetilde{S}_{ij} - \frac{1}{3}\delta_{ij}\widetilde{S}_{kk}\right) = C_d\beta_{ij} \tag{3.39}$$

$$T_{ij} - \frac{\delta_{ij}}{3}T_{kk} = -2C_d\widehat{\Delta}^2|\widehat{\widetilde{S}}|\left(\widehat{\widetilde{S}}_{ij} - \frac{1}{3}\delta_{ij}\widehat{\widetilde{S}}_{kk}\right) = C_d\alpha_{ij} \tag{3.40}$$

where C_d is the parameter to determine and the tensors α_{ij} and β_{ij} are introduced to simplify the notations. The Germano identity is finally written as:

$$\mathcal{L}_{ij}^d = \mathcal{L}_{ij} - \frac{\delta_{ij}}{3}\mathcal{L}_{kk} = C_d\alpha_{ij} - \widehat{C_d\beta_{ij}} \tag{3.41}$$

Making the hypothesis that the parameter C_d is constant over the interval at least equal to the test filter width, $\widehat{C_d\beta_{ij}} = C_d\widehat{\beta_{ij}}$. The model parameter can be computed in such a way to minimize the error:

$$E_{ij} = \mathcal{L}_{ij}^d - C_d\alpha_{ij} + C_d\widehat{\beta_{ij}} \tag{3.42}$$

This definition consists of six independent relations, which in theory makes it possible to compute six values of the constant. In order to compute a single

value, Lilly (1992) proposed to calculate the constant C_d by a least-squares method, in which the model constant is solution of:

$$\frac{\partial E_{ij} E_{ij}}{\partial C_d} = 0 \tag{3.43}$$

resulting in

$$C_d = \frac{M_{ij} \mathcal{L}_{ij}^d}{M_{kl} M_{kl}} \tag{3.44}$$

with $M_{ij} = \alpha_{ij} - \widehat{\beta_{ij}}$.
Averaging the denominator and numerator separately or locally in space or time are common procedures to ensure numerical stability. Clipping the constant value in order to impose $\nu_{sgs} + \nu \geq 0$ is also a regular practice.

3.4.3 WALE model

The Wall-Adapting Local Eddy-viscosity model (Nicoud and Ducros 1999), was developed for wall bounded flows with the objective to recover the scaling laws at the wall.

$$\nu_{sgs} = (C_W \Delta)^2 \frac{(s_{ij}^d s_{ij}^d)^{3/2}}{(\widetilde{S}_{ij} \widetilde{S}_{ij})^{5/2} + (s_{ij}^d s_{ij}^d)^{5/4}} \tag{3.45}$$

The parameter $C_W = 0.5$ is the model constant and s_{ij}^d being the traceless symmetric part of the square of the velocity gradient tensor computed as:

$$s_{ij}^d = \frac{1}{2} \left(\frac{\partial \widetilde{u}_i}{\partial x_l} \frac{\partial \widetilde{u}_l}{\partial x_j} + \frac{\partial \widetilde{u}_j}{\partial x_l} \frac{\partial \widetilde{u}_l}{\partial x_i} \right) - \frac{1}{3} \left(\frac{\partial \widetilde{u}_m}{\partial x_l} \frac{\partial \widetilde{u}_l}{\partial x_m} \delta_{ij} \right) \tag{3.46}$$

This model can only be used in 3D configurations, once the sub-grid viscosity vanishes when the flow is two-dimensional.

3.5 Chemistry modeling in LES

Detailed chemical kinetic mechanisms are employed to describe the transformation of reactants into products at the molecular level. Its aim is to explain the chemical reaction paths the most precise as possible. Therefore, they involve numerous intermediate species. The GRI mechanism used for methane/air chemistry (Smith et al. 1999) presents 53 transported species and 325 reactions. For larger hydrocarbons chains, this number can increase rapidly: Dagaut and

Cathonnet (2006)'s mechanism for kerosene/air is composed of 209 species and 1673 reversible reactions. The use of detailed chemistry is restricted to simple phenomena such as auto-ignition, premixed or non-premixed planar flames. Its application in 3D calculations of industrial configurations is not feasible, not only because it would require to solve the balance equations for an important number of species, but also because it would need a large number of grid points in the flame front to correctly capture all intermediate and radicals species with stiff profiles. Moreover, it is still unclear how to couple detailed kinetic mechanisms with turbulent combustion models to run large eddy simulations.
Skeletal schemes are constructed from detailed mechanisms by explicitly removing species and corresponding reactions, which have a negligible contribution to the phenomena of interest. To perform this operation, a set of targets is chosen. They correspond to chemical features that the reduced mechanism is expected to reproduce over a predefined range of physical conditions. Several methods exist to determine which species have a negligible contribution to these targets (Turanyi 1990; Tomlin et al. 1997; Lu and Law 2005; Massias et al. 1999). Even if information of redundant species is ignored, the reaction rates of the relevant ones remain practically unaffected and combustion phenomena are correctly described. Unfortunately, skeletal mechanisms are still too expensive to be used in realistic configurations. For instance, Luche et al. (2004)'s skeletal scheme for kerosene/air combustion accounts for 134 species and 1220 reactions.
Analytical mechanisms use the quasi-steady state approximation (QSS) for some species and partial equilibrium assumption for some reactions. Only the remaining species are explicitly transported while the QSS species reaction rates are deduced from the composition of the transported species. As for the skeletal scheme, a set of targets must be specified to determine the QSS species in the analytical scheme. Peters (1985); Lu and Law (2008) are examples of analytical schemes.
Contrarily to previous methods, reduced schemes present a very limited number of species (generally around 6) and of reactions (generally 2 to 4) (Jones and Lindstedt 1988; Franzelli et al. 2010). Reactions do not correspond to elementary reactions but to global reactions, based on Arrhenius-like expressions, calibrated to reproduce specific features of the flame (usually the laminar flame speed and the burnt gas state) at a given range of operating conditions (fresh gas temperature, pressure, equivalence ratio). When increasing the number of species and reactions, more details are introduced about the flame structure and its response to stretch. From an industrial point of view, only a few species are of interest and taking into account a large set of species is usually not required. In gas turbines for example, being able to predict the chamber efficiency (which requires a correct prediction of fuel reaction rates), the outlet temperature, CO and NO composition is sufficient for a large part of the design process. Moreover, with simple adjustments, reduced schemes can predict the evolution of flame quantities such as laminar flame speed, adiabatic

flame temperature or ignition delay over a wide range of operating conditions (pressure, temperature, dilution) making them very suitable for LES (Franzelli et al. 2010). Finally, thanks to their affordable CPU costs, simplified schemes are widely used in LES of industrial configurations.

A classical approach used to take into account detailed chemistry effects in realistic LES keeping the CPU cost relatively low makes use of tabulated chemistry. Tabulated chemistry methods assume that chemical evolutions in the composition space can be parameterized and tabulated by a reduced set of variables, generally, combinations of species mass fractions: $\psi_l = \sum_{k=1}^{N} \alpha_{lk} Y_k$, where α_{lk} are constant numbers. Knowing the variables ψ_l in a simulation, all thermo-chemical variables ψ can be estimated using the chemical database $\psi^{tab}(\psi_1; ...; \psi_n)$. Among these tabulation techniques, we can mention ILDM (Maas and Pope 1992), FPI (Gicquel et al. 2000), FGM (Oijen and Goey 2000), REDIM (Bykov and Maas 2007) or ICE-PIC (Ren et al. 2006) methods. In these methods, instead of solving one balance equation for each chemical species involved in the detailed elementary reactions, only few equations for the reduced set of variables are solved. In the perfectly premixed case, all species profiles $Y_k(x)$ are extracted from the laminar premixed flamelet solution and expressed as a function of a progress variable c. Mixture fraction is added by computing flamelets at different equivalence ratio. An extension to non-adiabatic flames introduces the enthalpy as a new dimension of the database (Fiorina et al. 2003). A major issue associated to tabulation techniques is their extension to cases where the number of controlling variables is drastically increased. Generating and handling a lookup table can be difficult in such situations. For instance, having a lookup table with several inputs can lead to memory problems on massively parallel machines, where the table must be duplicated on each core. Additionally, determining the most adequate flame prototype in a combustor, where the combustion regime is unknown, is a very complicated task.

The principle of classical reduction methods is to decrease the number of species and reactions to achieve a certain agreement with the reference mechanism. A recently developed strategy goes the other way round: it gradually increases the dimensionality of the kinetic scheme, in order to capture accurately the quantities of interest (Cailler et al. 2016). The virtual optimized mechanism (VOM) method relies on both the optimization of species properties and kinetic rate parameters to retrieve temperature and/or other species profiles and laminar flame speeds of a collection of premixed and/or non-premixed flames generated with a detailed kinetic mechanism. Even if this strategy seems very promising, more tests are needed to validate the methodology.

All cases treated in this manuscript consider perfectly premixed combustion. Reduced mechanisms are chosen to model chemistry and are used to run the LES, but tabulated chemistry or even the recently developed virtual optimized mechanism could also be retained. In the coming decades, with the constant improvement of computational power, more precise and expensive mechanisms,

such as analytical schemes, will also be used.

3.6 LES models for turbulent premixed combustion

In this section, the main models for premixed turbulent combustion are reviewed. For general discussion, consider the filtered balance equation for the progress variable c:

$$\frac{\partial \overline{\rho}\widetilde{c}}{\partial t} + \frac{\partial \overline{\rho}\widetilde{u}_i\widetilde{c}}{\partial x_i} + \frac{\partial}{\partial x_i}\left(\overline{\rho}\widetilde{u_i c} - \overline{\rho}\widetilde{u}_i\widetilde{c}\right) = \frac{\partial}{\partial x_i}\left(\overline{\rho D \frac{\partial c}{\partial x_i}}\right) + \overline{\dot{\omega}}_c \tag{3.47}$$

3.6.1 Level-set formalism: the G-equation

In the G-equation formalism, the flame thickness is viewed as an infinitely thin propagating surface. The key idea is to track the position of the flame front using a field variable G. The flame surface is associated to a given iso-level $G = G^*$. Since only the propagating surface is modeled, the flame structure is neglected and, as a result, the details on the reaction rates and species diffusion can be ignored (Kim et al. 1999). The G-field does not have to follow the gradients of the progress variable c and can be smoothed out to be resolved on the LES mesh (Poinsot and Veynante 2011). The G-equation is written as (Kerstein et al. 1988):

$$\frac{\partial \overline{\rho}\widetilde{G}}{\partial t} + \frac{\partial \overline{\rho}\widetilde{u}_i\widetilde{G}}{\partial x_i} = \rho_u S_T \left|\frac{\partial \widetilde{G}}{\partial x_i}\right| \tag{3.48}$$

The challenge is to propose a model for the sub-grid scale turbulent flame speed S_T. The closure is often based on Eq. (3.49):

$$\frac{S_T}{S_L} = 1 + \alpha\left(\frac{u'_\Delta}{S_L}\right)^p \tag{3.49}$$

The constants α and p have to be specified by the user, u'_Δ is the sub-grid scale turbulence level.

3.6.2 Flame surface density approach

This approach developed by Boger et al. (1998) is based on the filtering of the balance equation for the progress variable using a LES filter larger than the mesh size. Equation (3.47) can be recast in the following form:

$$\frac{\partial \overline{\rho}\widetilde{c}}{\partial t} + \frac{\partial \overline{\rho}\widetilde{u}_i\widetilde{c}}{\partial x_i} + \frac{\partial}{\partial x_i}\left(\overline{\rho}\widetilde{u_i c} - \overline{\rho}\widetilde{u}_i\widetilde{c}\right) = \overline{\rho S_d \left|\nabla c\right|} \tag{3.50}$$

where S_d is the local displacement speed and $\overline{\rho S_d \left|\nabla c\right|}$ corresponds to the flame front displacement. This latter term may be modeled as in Boger et al. (1998):

$$\overline{\rho S_d \left|\nabla c\right|} \approx \rho_u S_L \Sigma = \rho_u S_L \Xi_\Delta |\nabla \overline{c}| \tag{3.51}$$

where ρ_u and S_L are the fresh gases density and the laminar flame speed respectively. Σ is the sub-grid scale flame surface density (the flame surface density per unit volume at the sub-grid scale level) and Ξ_Δ the sub-grid scale flame wrinkling factor (the sub-grid flame surface divided by the projected surface in the propagating direction) and must be modeled.
Boger et al. (1998) has proposed an algebraic model for Σ and Ξ_Δ similar to the Bray-Moss-Libby formulation widely used in RANS simulations. They founded their study on the DNS database of a laminar premixed flame interacting with a homogeneous and isotropic flow field developed by Boughanem and Trouvé (1998). They estimated $|\nabla \overline{c}|$ by filtering one-dimensional laminar premixed flame and approximated the result by a progress variable parabolic shape, leading to:

$$\Sigma = 4\Xi_\Delta \sqrt{\frac{6}{\pi}} \frac{\widetilde{c}(1-\widetilde{c})}{\Delta} \tag{3.52}$$

Boger and Veynante (2000) extended the previous study and proposed an adapted model for the unresolved progress variable transport $(\overline{\rho \widetilde{u_i c}} - \overline{\rho}\widetilde{u}_i\widetilde{c})$ writing Eq. (3.50) as:

$$\frac{\partial \overline{\rho}\widetilde{c}}{\partial t} + \frac{\partial \overline{\rho}\widetilde{u}_i\widetilde{c}}{\partial x_i} = \frac{\partial}{\partial x_i}\left(\rho_u \frac{S_L \Xi_\Delta \Delta}{16\sqrt{6/\pi}} \frac{\partial \widetilde{c}}{\partial x_i}\right) + 4\rho_u S_L \Xi_\Delta \sqrt{\frac{6}{\pi}} \frac{\widetilde{c}(1-\widetilde{c})}{\Delta} \tag{3.53}$$

Boger et al. (1998) also derived a balance equation for Σ:

$$\frac{\partial \Sigma}{\partial t} + \nabla \cdot \left[\langle \mathbf{u} \rangle_s \Sigma\right] = \langle \nabla \cdot \mathbf{u} - \mathbf{nn} : \nabla \mathbf{u} \rangle_s \Sigma - \nabla \cdot \left[\langle w\mathbf{n} \rangle_s \Sigma\right] + \langle w \nabla \cdot \mathbf{n} \rangle_s \Sigma \tag{3.54}$$

where $\mathbf{n} = -\nabla c / \left|\nabla c\right|$ is the unit vector normal to the iso-c surface pointing toward the fresh gases. $\nabla \cdot \mathbf{n}$ denotes the iso-surface curvature. The two first terms on the RHS correspond respectively to the strain rate acting on the c-surfaces and to the normal front displacement. The last term combines propagation and curvature effects.
As a matter of fact, Eq. (3.54) is formally identical to the balance equation for flame surface density used in the RANS context (Trouvé and Poinsot 1994; Vervisch et al. 1995). Hawkes and Cant (2000) and Richard et al. (2007) modeled the unclosed terms presented in the transport equation for the filtered flame surface density, Σ. Weller et al. (1998) presented a model for the reaction rate based on the transport equation of Ξ_Δ.

3.6.3 F-TACLES approach

A common approach to address fluid/chemistry interactions at a reduced computational cost consists in tabulating the chemistry as a function of a reduced set of variables. Two classical methods are the Flame Prolongation of ILDM (FPI) (Gicquel et al. 2000) or the Flamelet Generated Manifold (FGM) (Oijen and Goey 2000) when treating premixed flames. Both techniques assemble one-dimensional laminar premixed flames in a database and suppose that all thermo-chemical quantities ψ are related to a single progress variable c, which evolves monotonically between fresh and burnt gases. A thermochemical table $\psi^{tab}(c)$ is obtained for a specific element composition and a specific enthalpy and pressure.
The principle of the Filtered Tabulated Chemistry for Large Eddy Simulation is to tabulate the unresolved terms of the progress variable balance equation by filtering one-dimension laminar flames.
The sub-grid scale transport term $\nabla\cdot(\overline{\rho\mathbf{u}c}-\overline{\rho}\widetilde{\mathbf{u}}\widetilde{c})$, the filtered laminar diffusion term $\nabla\cdot\left(\overline{\rho D\nabla c}\right)$ and the filtered source term $\overline{\dot{\omega}}_c$ in Eq. (3.47) have to be modeled. These terms are directly stored as a function of $\widetilde{c}$ and Δ in a filtered chemical database:

$$\overline{\dot{\omega}}_c = \Xi_\Delta\,\overline{\dot{\omega}}^{tab}\left[\widetilde{c},\Delta\right] \tag{3.55}$$

$$\nabla\cdot\left(\overline{\rho D\nabla c}\right) = \nabla\cdot\left(\alpha_c^{tab}\left[\widetilde{c},\Delta\right]\overline{\rho}D\nabla\widetilde{c}\right) \tag{3.56}$$

$$-\nabla\cdot(\overline{\rho\mathbf{u}c}-\overline{\rho}\widetilde{\mathbf{u}}\widetilde{c}) = (\Xi_\Delta-1)\nabla\cdot\left[\alpha_c^{tab}\left[\widetilde{c},\Delta\right]\overline{\rho}D\nabla\widetilde{c}\right]+\Xi_\Delta\Omega_c^{tab}\left[\widetilde{c},\Delta\right] \tag{3.57}$$

where the superscript ^{tab} denotes quantities extracted from one-dimensional filtered laminar premixed flames. $\Omega_c^{tab}\left[\widetilde{c},\Delta\right]$ corresponds to the unresolved progress variable transport linked to thermal expansion and $\alpha_c^{tab}\left[\widetilde{c},\Delta\right]$ is a correction parameter.
Finally, the final filtered equation for the progress variable can be expressed in the following form:

$$\frac{\partial\overline{\rho}\widetilde{c}}{\partial t}+\frac{\partial}{\partial x_i}(\overline{\rho}\widetilde{\mathbf{u}}\widetilde{c}) = \Xi_\Delta\frac{\partial}{\partial x_i}\left[\alpha_c^{tab}\left[\widetilde{c},\Delta\right]\widetilde{\rho}D\nabla\widetilde{c}\right]+\Xi_\Delta\Omega_c^{tab}\left[\widetilde{c},\Delta\right]+\Xi_\Delta\,\overline{\dot{\omega}}^{tab}\left[\widetilde{c},\Delta\right] \tag{3.58}$$

3.6.4 Artificially thickened flames: TFLES

One of the challenges encountered in combustion problems of large eddy simulations is the fact that the flame front cannot be resolved on the computational mesh. A common procedure to overcome this problem is to artificially thicken the flame by a factor $\mathcal{F}$ keeping the same burning laminar velocity (Butler and O'Rourke 1977; O'Rourke and Bracco 1979). Following simple theories of laminar premixed flames (Williams 1985), the flame speed S_L and the flame thickness δ_L^0 may be expressed as:

$$S_L \propto \sqrt{D_T \dot{\omega}}\,, \quad \delta_L^0 \propto \frac{D_T}{S_L} \tag{3.59}$$

where D_T is the thermal diffusivity and $\dot{\omega}$ the mean reaction rate. Then, an increase of the flame thickness δ_L^0 by a factor $\mathcal{F}$ with a constant flame speed S_L is easily achieved substituting D_T by $\mathcal{F}D_T$ and $\dot{\omega}$ by $\dot{\omega}/\mathcal{F}$.
Unfortunately, when the flame is thickened from δ_L^0 to $\mathcal{F}\delta_L^0$, the interaction between turbulence and chemistry is affected. The Damköhler number, comparing turbulent, $\tau_t = l_t/u'(l_t)$ and chemical, $\tau_c = S_L/\delta_L^0$ time scales is divided by $\mathcal{F}$. This point has been investigated using DNS by Angelberger et al. (1998) and Colin et al. (2000). To account for this effect, an efficiency function, corresponding to a sub-grid scale wrinkling factor is introduced (Colin et al. 2000; Charlette et al. 2002a). In practical applications, the molecular and thermal diffusivities are replaced by $\Xi_\Delta \mathcal{F} D$ and $\Xi_\Delta \mathcal{F} D_T$ respectively, and the reaction rate replaced by $\Xi_\Delta\, \overline{\dot{\omega}}_c/\mathcal{F}$. The equation for the progress variable (3.47) takes the following form:

$$\frac{\partial \overline{\rho}\widetilde{c}}{\partial t} + \frac{\partial \overline{\rho}\widetilde{u}_i\widetilde{c}}{\partial x_i} + \frac{\partial}{\partial x_i}\left(\overline{\rho u_i c} - \overline{\rho}\widetilde{u}_i\widetilde{c}\right) = \frac{\partial}{\partial x_i}\left(\mathcal{F}\Xi_\Delta \overline{\rho D \frac{\partial c}{\partial x_i}}\right) + \Xi_\Delta \frac{\overline{\dot{\omega}}_c}{\mathcal{F}} \tag{3.60}$$

The Thickened Flame model for LES adopted in this thesis is used together with reduced chemical mechanisms and is not based on a single progress variable approach. The final set of equations solved when performing LES of reacting flows jointly with the TFLES model reads:

$$\frac{\partial \overline{\rho}\widetilde{u}_i}{\partial t} + \frac{\partial}{\partial x_j}(\overline{\rho}\widetilde{u}_i\widetilde{u}_j) = -\frac{\partial}{\partial x_j}\left[\overline{P}\delta_{ij} - 2(\overline{\mu} + \mu_{sgs})\left(\widetilde{S}_{ij} - \frac{\delta_{ij}}{3}\widetilde{S}_{kk}\right)\right] \tag{3.61}$$

$$\begin{aligned}\frac{\partial\overline{\rho}\widetilde{E}}{\partial t}+\frac{\partial}{\partial x_j}(\overline{\rho}\widetilde{E}\widetilde{u}_j) = &-\frac{\partial}{\partial x_j}\left[\widetilde{u}_i\overline{P}\delta_{ij}-2\widetilde{u}_i\overline{\mu}\left(\widetilde{S}_{ij}-\frac{\delta_{ij}}{3}\widetilde{S}_{kk}\right)\right]\\ &+\frac{\partial}{\partial x_j}\left[\overline{C}_p\Xi_\Delta\mathcal{F}\left(\frac{\overline{\mu}}{Pr}+\frac{\mu_{sgs}}{Pr^t}\right)\frac{\partial\widetilde{T}}{\partial x_j}\right]\\ &+\frac{\partial}{\partial x_j}\left\{\sum_{k=1}^{N}\left[\Xi_\Delta\mathcal{F}\left(\frac{\overline{\mu}}{Sc_k}+\frac{\mu_{sgs}}{Sc_k^t}\right)\frac{W_k}{W}\frac{\partial\widetilde{X}_k}{\partial x_j}\right]\widetilde{h}_{sk}\right\}\\ &-\frac{\partial}{\partial x_j}\left\{\sum_{k=1}^{N}\left[\widetilde{Y}_k\sum_{k=1}^{N}\Xi_\Delta\mathcal{F}\left(\frac{\overline{\mu}}{Sc_k}+\frac{\mu_{sgs}}{Sc_k^t}\right)\frac{W_k}{W}\frac{\partial\widetilde{X}_k}{\partial x_j}\right]\widetilde{h}_{sk}\right\}\\ &+\Xi_\Delta\frac{\overline{\dot{\omega}}_T}{\mathcal{F}}\end{aligned} \tag{3.62}$$

$$\begin{aligned}\frac{\partial\overline{\rho}\widetilde{Y}_k}{\partial t}+\frac{\partial}{\partial x_j}(\overline{\rho}\widetilde{Y}_k\widetilde{u}_j) = &+\frac{\partial}{\partial x_j}\left[\Xi_\Delta\mathcal{F}\left(\frac{\overline{\mu}}{Sc_k}+\frac{\mu_{sgs}}{Sc_k^t}\right)\frac{W_k}{W}\frac{\partial\widetilde{X}_k}{\partial x_j}\right]\\ &-\frac{\partial}{\partial x_j}\left[\widetilde{Y}_k\sum_{k=1}^{N}\Xi_\Delta\mathcal{F}\left(\frac{\overline{\mu}}{Sc_k}+\frac{\mu_{sgs}}{Sc_k^t}\right)\frac{W_k}{W}\frac{\partial\widetilde{X}_k}{\partial x_j}\right]+\Xi_\Delta\frac{\overline{\dot{\omega}}_k}{\mathcal{F}}\end{aligned} \tag{3.63}$$

3.7 Classical sub-grid term closures

All previous combustion models presented in the previous sections describe the flame/turbulence interactions in terms of wrinkling factor or sub-grid scale turbulent flame speed $S_T = \Xi_\Delta S_L$ and are within the flamelet assumption (see Chapter 2). Following Charlette et al. (2002b), the generic form of the filtered reaction rate $\overline{\dot{\omega}}$ of Eq. (3.47) can be recast as:

$$\overline{\dot{\omega}} = \Xi_\Delta\frac{W_\Delta(\widetilde{Q})}{\Delta} \tag{3.64}$$

where $W_\Delta(\widetilde{Q})/\Delta$ corresponds to the resolved reaction rate, estimated from filtered quantities. $\widetilde{Q}$ stands for any known filtered quantity entering the reaction rate expression. Δ is the LES filter size. Table 3.1 summarizes $\overline{\dot{\omega}}$ and W_Δ expressions for the four combustion models presented.

Several expressions are available in the literature to close the sub-grid wrinkling factor term, Ξ_Δ. Table 3.2 shows some examples found in the literature, but the list is not exhaustive. The limitation of models presented in Table 3.2

Table 3.1: *Generic reaction rate expressions according to Eq. (3.64) for four turbulent premixed combustion LES models (Veynante and Moureau 2015).*

Model	$\overline{\dot{\omega}}$	W_Δ
Level set/G-equation	$\rho_u S_L \Xi_\Delta \left\lvert \nabla \widetilde{G} \right\rvert$	$\rho_u S_L \Delta \left\lvert \nabla \widetilde{G} \right\rvert$
FSD (Boger et al. 1998)	$4\rho_u S_L \Xi_\Delta \sqrt{\frac{6}{\pi}} \frac{\widetilde{c}(1-\widetilde{c})}{\Delta}$	$4\rho_u S_L \sqrt{\frac{6}{\pi}} \widetilde{c}(1-\widetilde{c})$
F-TACLES	$\Xi_\Delta \overline{\dot{\omega}}^{tab}[\widetilde{c}, \Delta]$	$\Delta\, \overline{\dot{\omega}}^{tab}[\widetilde{c}, \Delta]$
TFLES	$\Xi_\Delta \dot{\omega}_c / \mathcal{F}$	$\delta_L^0 \dot{\omega}_c$

is to assume equilibrium between turbulence motions and flame surface and consequently they cannot handle transient situations (Richard et al. 2007). Besides, the model coefficients do not exhibit an universal behavior and must be adjusted by hand case-by-case, a very fastidious and time-consuming task. The advantage of the dynamic formalism is that the model coefficient is computed on the fly and adjusted automatically based on the known resolved fields.

3.8 Motivation for a dynamic fractal-like sub-grid term closure

Driven by the successful application of fractal theory to several complex natural phenomena (Mandelbrot 1975; Mandelbrot 1977; Mandelbrot 1983; Sreenivasan and Meneveau 1986), experimental and numerical analysis indicate that premixed flames also display fractal behavior (Peters 1986; Gouldin 1987; Gouldin et al. 1989; Gülder 1991; Gülder and Smallwood 1995; Smallwood et al. 1995; North and Santavicca 1990; Chatakonda et al. 2013). Fractal theory provides a method of characterizing geometries that cannot be described by conventional methods of Euclidean geometry. It is particularly useful to describe natural geometries presenting a wide range of self-similar shapes and forms. A self-similar object is composed of smaller pieces, each of which is a replica of the whole. A key characteristic of fractal geometries is that the measured size of a fractal object (L for a curve and A for a surface) varies with the measurement scale, ε, by a power law relationship. For a fractal curve, this dependence is written as:

$$L(\varepsilon) \propto \varepsilon^{1-D} \text{ , with } 1 < D \leq 2 \tag{3.65}$$

Table 3.2: *Some examples of closures for the sub-grid wrinkling factor term found in the literature.*

SGS combustion model	Formula for the wrinkling factor, Ξ_Δ	Constants
Colin et al. (2000)	$\Xi_\Delta = 1 + \alpha \frac{2\ln 2}{3c_{ms}(Re_t^{1/2}-1)} \Gamma_\Delta \frac{u'_\Delta}{S_L}$ with $\Gamma_\Delta = 0.75 \exp\left[-\frac{1.2}{(u'_\Delta/S_L)^{0.3}}\right] \left(\frac{\Delta}{\delta_L^0}\right)^{2/3}$	$\alpha \approx 1$; $c_{ms} = 0.28$
Flohr and Pitsch (2000)	$\Xi_\Delta = 1 + a(Re_\Delta Pr)^{1/2} Da_\Delta^{-1/4}$	$a = 0.52$
Kim and Menon (2000)	$\Xi_\Delta^\gamma = \left(\frac{S_L^*}{S_L}\right)^\gamma + \beta \left[\frac{u'_\Delta}{S_L}\left(1 - \left(\frac{A\nu}{Pr\Delta S_L}\frac{S_L^*}{S_L}\right)\right)^{1/2}\right]^\gamma$ with $\frac{S_L^*}{S_L} = f\left(1.5^{1.2} c_v \left(\frac{A}{Pr}\frac{u'_\Delta}{S_L}\right)^{4/3} Re_\Delta^{-1/3}\right)$	$\beta = 1; \gamma = 2$; $A = 6, c_v = 0.05$
Charlette et al. (2002a)	$\Xi_\Delta = \left(1 + \min\left[\frac{\Delta}{\delta_l^0}, \Gamma_\Delta \frac{u'_\Delta}{S_L}\right]\right)^\beta$ $\Gamma_\Delta = \left[\left(\left(f_u^d + f_\Delta^{-d}\right)^{-1/d}\right)^{-1.4} + f_{Re}^{-1.4}\right]^{-1/1.4}$ $f_u = 4\left(\frac{27C_k}{110}\right)^{1/2}\left(\frac{18C_k}{55}\right)\left(\frac{u'_\Delta}{S_L}\right)^2$ $f_{Re} = \left[\frac{9}{55}\exp\left(\frac{3}{2}C_k\pi^{4/3}Re_\Delta^{-1}\right)\right]^{1/2} \times Re_\Delta^{1/2}$ $d = 0.6 + 0.2\exp\left(-0.1\frac{u'_\Delta}{S_L}\right) - 0.2\exp\left(-0.01\frac{\Delta}{\delta_L^0}\right)$	$\beta = 0.5$
Pitsch and De Lageneste (2002)	$\Xi_\Delta = 1 + \frac{u'_\Delta}{S_L} b_3 \left[\left(\frac{Da_\Delta}{Sc_\Delta}\right) / \left(1 + \frac{b_3^2}{b_1^2 Sc_\Delta} Da_\Delta\right)\right]^{1/2}$	$b_1 = 2; b_3 = 1$

while for a fractal surface, we have:

$$A(\varepsilon) \propto \varepsilon^{2-D} \text{ , with } 2 < D \leq 3 \tag{3.66}$$

where D is the fractal dimension of the curve/surface. The larger D, the more space filling the surface will be. In the following, discussion is done only for the three-dimensional case. Equation (3.66) holds at a given range bounded by cut-off length scales imposed by physical limits. These small and large limits are referred to as inner (δ_c) and outer (ε_o) cut-offs, respectively. These quantities are illustrated in Fig. 3.3, which is a log-log plot of the variation of observed surface versus measurement scale. As indicated in Eq. (3.66), the slope of the length versus ε is $\beta = 2 - D$, while the points of deviation from this constant slope region are the inner and outer cut-offs.

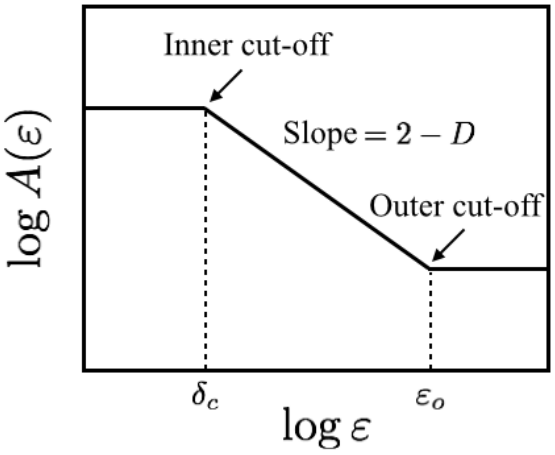

Figure 3.3: *Graphical description of the area versus measurement resolution relationship for a fractal surface. D is the fractal dimension.*

Experimental (Smallwood et al. 1995; Chen and Mansour 1999; Battista et al. 2015) and numerical (Chatakonda et al. 2013; Battista et al. 2015) studies have been carried out in order to analyze the fractal nature of the flames. Smallwood et al. (1995) accomplished a detailed experimental investigation of the fractal scaling properties of turbulent premixed flame fronts. The fractal dimension and cut-off scales were determined for several turbulent flames for different equivalence ratios and turbulence intensities. Figure 3.4 shows the experimental determination of the mean fractal parameters using the caliper (Mandelbrot 1983) method to measure the length of the outline of the flame boundary. The fractal behavior is notable, with distinct inner and outer cut-offs. Additionally, the outer cut-off is an order of magnitude greater than the inner cut-off length scale. They also show that the fractal dimension is not constant and they plotted a probability density function of the fractal slope derived from individual flame images (Fig. 3.5).

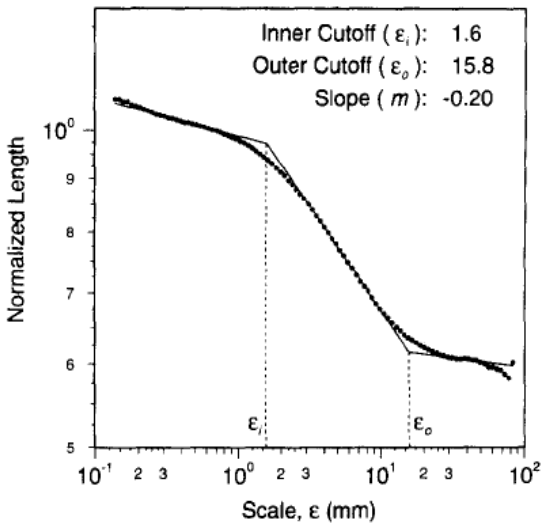

Figure 3.4: *Normalized length as a function of scale for average of 366 images for the CH_4/air flame at $\phi = 0.7$, mean bulk velocity $\overline{u} = 5$ m/s and $u'/S_L = 1.22$. Best-fit three linear segments are shown along with slope and inner and outer cut-offs (Smallwood et al. 1995).*

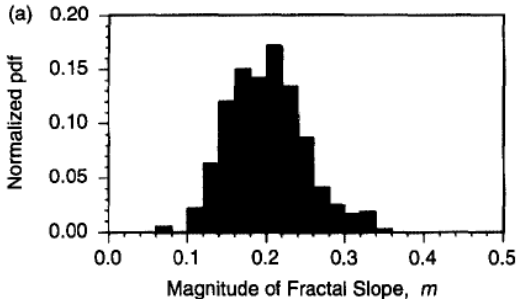

Figure 3.5: *Histogram of the magnitude of fractal slope from 366 individual flame images for the CH_4/air flame at $\phi = 0.7$, mean bulk velocity $\overline{u} = 5$ m/s and $u'/S_L = 1.22$ (Smallwood et al. 1995).*

Battista et al. (2015) used experimental and DNS data to extract fractal features of turbulent flames. Experiments consisted of methane/air premixed flames using two different jet-burners: a cylindrical Bunsen burner and a bluff-body stabilized burner. Different equivalence ratios and Reynolds numbers based on the mean bulk velocity and burner inner diameter have been reported. Three DNS of premixed Bunsen jets have also been performed to replicate the main characteristics of premixed methane/air flames in conditions comparable to the experiments. Differently from Smallwood et al. (1995), they evaluated the fractal characteristics of their experimental and numerical dataset based on the box-counting technique, which consists in enumerating the squared boxes of size L necessary to entirely cover the flame front. They show that the fractal

dimension is substantially constant and around $D = 2.23$.
Chatakonda et al. (2013) used direct numerical simulations to evaluate the fractal nature of the flames. Hydrogen-air turbulent premixed plane-jet flames with detailed chemistry and thermonuclear flames in type Ia supernovae have been investigated. A three-dimensional box counting method was used to investigate fractal dimension of the flame surface, characterizing the self-similarity of flame fronts. Figure 3.6 shows the progress variable contours at different stages of the flame development for the hydrogen flames while entering the temporally developing planar-jet of premixed reactants. The authors claimed that the fractal dimension evolves in time taking values between 2.1 and 2.7 for the cases reported in Fig. 3.6.

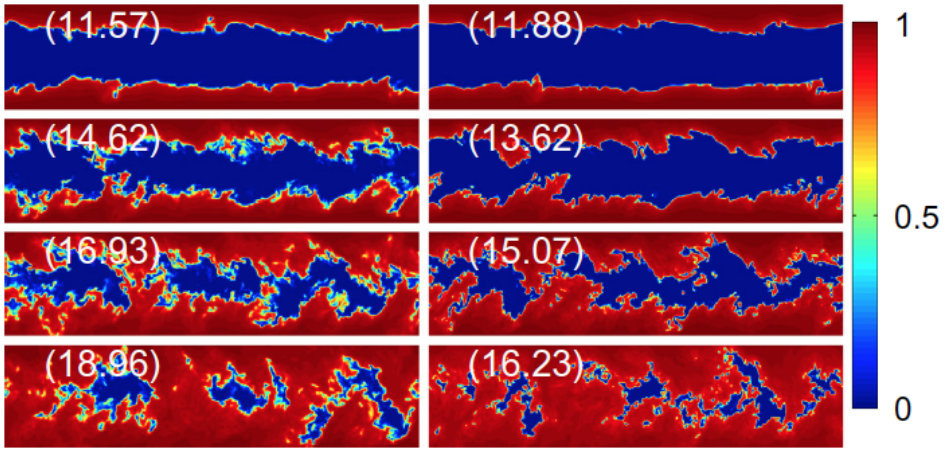

Figure 3.6: *Contours of progress variable at different times for simulations using two Damköhler numbers (the white numbers are times normalized by jet time) (Chatakonda et al. 2013).*

Until now, researches were concerned to find a global fractal dimension for the whole flame. Chen and Mansour (1999) studied turbulent premixed jet flames experimentally and planar images of Rayleigh scattering and laser induced OH-fluorescence (OH-LIPF) have been employed for fractal analysis. They examined the spatial dependence of fractal dimension in Bunsen-type flames, finding a nearly linear increase with downstream distance which correlated well with the increasing flame-brush thickness, as shown in Fig. 3.7. The authors explain that the axial jet development with increasing large-scale wrinkling is responsible for the streamwise increase of fractal dimension.
Results obtained by Chen and Mansour (1999); Chatakonda et al. (2013) are very challenging for combustion models and indicates that the fractal dimension may be time and space dependent. This fact motivates the development of a dynamic fractal-like wrinkling factor model for LES of turbulent premixed combustion.

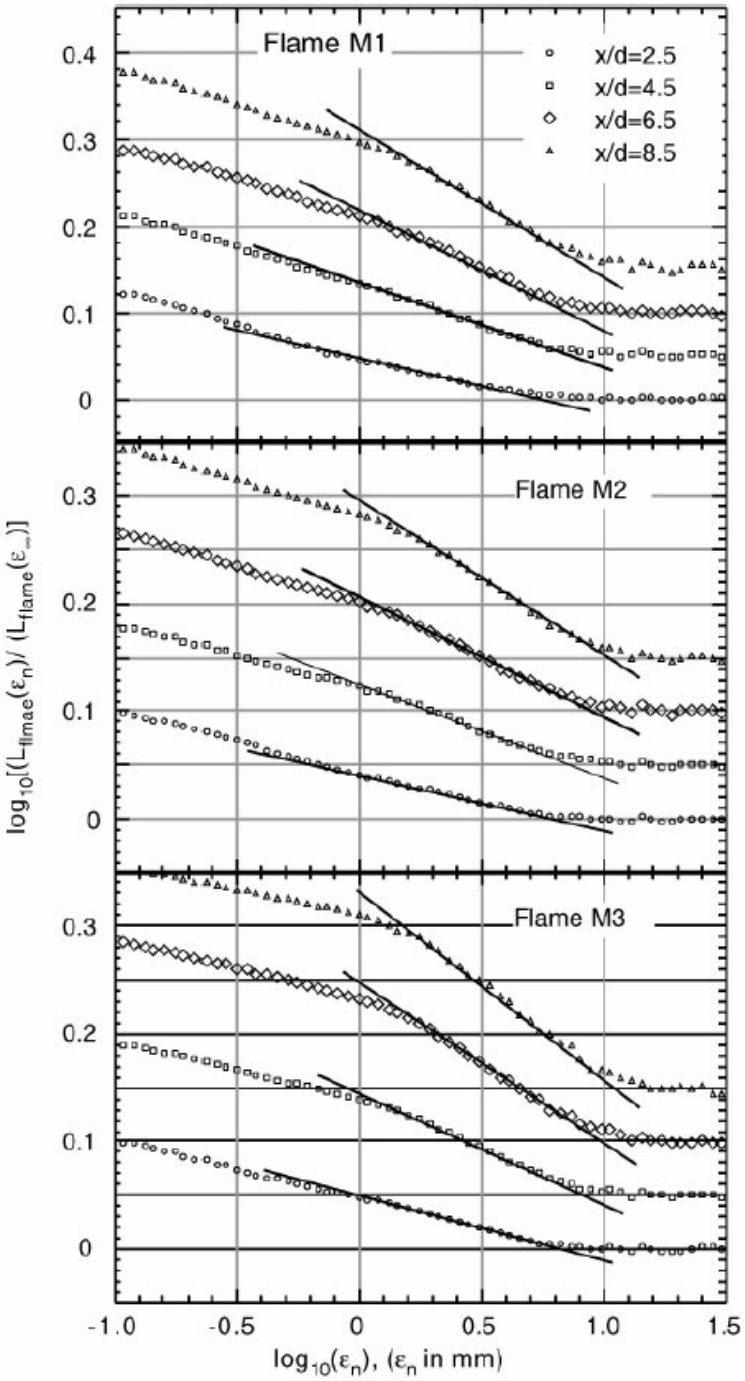

Figure 3.7: *Log-log plot of the normalized, ensemble-average length from the iso-temperature contours for the three investigated flames, denoted M1, M2 and M3, at different axial stations. For clarity, an offset of 0.05 in the vertical axis is given between each profile. The solid lines indicate the region where a constant slope can be approximated (Chen and Mansour 1999).*

Chapter 4

Dynamic models for LES of turbulent combustion

The methodology employed in this thesis follows the Germano-like procedure described in Section 3.4.2, and was extended for large eddy simulation of turbulent premixed combustion by Charlette et al. (2002b). The final goal of this approach is to compute the model parameter on the fly without adjusting it by hand for each set of configurations studied. The general concept is first described. Then, a state of the art section concerning dynamic models for large eddy simulation of turbulent combustion is presented. The determination of the model parameter is done using different sub-grid scale models, including the fractal-like sub-grid closure. A short review regarding the inner cut-off length scale closes this chapter.

4.1 General concept

The generic form of the filtered reaction rate, Eq. (3.64), is considered to develop a more universal formulation. The principle is to compare the test-filtered resolved reaction rate to the reaction rate estimated at the test-filter level (Charlette et al. 2002b):

$$\widehat{\overline{\dot{\omega}}} = \widehat{\frac{\Xi_\Delta}{\Delta} W_\Delta(\widetilde{Q})} = \frac{\Xi_{\gamma\Delta}}{\gamma\Delta} W_\Delta(\widehat{\widetilde{Q}}) \tag{4.1}$$

where the hat symbol denotes a test-filter operation. Combining two Gaussian filters of size Δ and $\widehat{\Delta}$, the effective filter size of the test filter is $\breve{\Delta} = \gamma\Delta$, with $\gamma = [1 + (\widehat{\Delta}/\Delta)^2]^{1/2}$. Charlette et al. (2002a) proposed a weak formulation of Eq. (4.1) by averaging it over a domain ($\langle\cdot\rangle$ operator) meaning that the total reaction rate over this domain should be the same when estimated from

resolved and test-filtered fields. Then:

$$\left\langle \overline{\frac{\Xi_\Delta}{\Delta} W_\Delta(\widetilde{Q})} \right\rangle = \left\langle \frac{\Xi_{\gamma\Delta}}{\gamma\Delta} W_\Delta(\widehat{\widetilde{Q}}) \right\rangle \tag{4.2}$$

Assuming the model parameter constant on the averaging domain, as done by Germano et al. (1991), to get it out of the operator $\langle\cdot\rangle$, Eq. (4.2) may be solved for a given parameter (see Table 3.2 for example).
Averaging over the entire computational domain provides a spatially uniform model parameter evolving only with time (global formulation). When a small local volume is chosen, the model parameter evolves both with time and space coordinates (local formulation).
In explicit compressible solvers, such as AVBP, the time step Δt is limited by the Courant-Friedrich-Levy (CFL) criterion, linked to the propagation speed of acoustic waves and the mesh size. On the other hand, parameters of dynamic models are more likely to evolve with the convective time of the flow turbulence motions. As subsonic flows are considered here, this time is larger than the acoustic time Δt by one or two orders of magnitude. Then, Eq. (4.2) does not need to be solved every time step, saving computational cost due to the filtering operation. Thus, the model parameters only need to be updated at time steps $n.\Delta t$ with n larger than unity. Note that this technique cannot be employed when dealing with an implicit incompressible solver.
It is important to emphasize that Eq. (4.2) does not depend on the model used for $W_\Delta(\widetilde{Q})$ and can be used in the context of different LES models of premixed combustion in which a wrinkling factor is needed. Some examples are now discussed.

4.2 State of the art of dynamic models in combustion

In this section, a state of the art concerning dynamic models for large eddy simulation of turbulent combustion is carefully discussed and major results found in the literature are shown. Table 4.1 summarizes the main works dealing with dynamic models for LES of turbulent premixed combustion.

Table 4.1: *Main works dealing with dynamic modeling.*

Work	Model	Configuration	Formulation	Parameter
Im et al. (1997)	Level-set	Academic test case	Global	$\alpha(t)$
Charlette et al. (2002b)	TFLES	Academic test case	Global/Semi-local	$\beta(t)/\beta(t,y,z)$
Knikker et al. (2004)	FSD	A priori analysis	Global	$D(t)$
Knudsen and Pitsch (2008)	Level-set	Jet flame	Local	$\alpha(t,x,y,z)$
Wang et al. (2011)	TFLES	Jet flame	Global	$\beta(t)$
Gubba et al. (2011)	FSD	Deflagrating flame	Global	$D(t)$
Wang et al. (2012)	FSD	Flame kernel	Global	$\beta(t)$
Schmitt et al. (2013)	F-TACLES	Turbulent swirl burner	Global/Semi-local	$\beta(t)/\beta(t,x)$
Schmitt et al. (2015)	F-TACLES	Jet flame	Global/Local	$\beta(t)/\beta(t,x,y,z)$
Veynante and Moureau (2015)	FSD	Turbulent swirl burner	Local	$\beta(t,x,y,z)$
Mouriaux et al. (2016)	FSD	Piston engine	Local	$\beta(t,x,y,z)$

4.2.1 Charlette et al. (2002b) formulation

The classical relationship between sub-grid turbulent flame velocity and wrinkling factor proposed by Charlette et al. (2002b) is written as:

$$\Xi_\Delta \equiv \frac{S_T}{S_L} = \left(1 + \min\left[\frac{\Delta}{\delta_L^0}, \Gamma_\Delta \frac{u'_\Delta}{S_L}\right]\right)^\beta \tag{4.3}$$

In Eq. (4.3), u'_Δ is the characteristic turbulent velocity at scale Δ, the effect of flame stretch on the local flame velocity are directly integrated in the efficiency function Γ_Δ defined in Table 3.2. Equation (4.2) can be recast in the following form:

$$\overline{\left\langle \left(1 + \min\left[\frac{\Delta}{\delta_L^0}, \Gamma_\Delta \frac{u'_\Delta}{S_L}\right]\right)^\beta \frac{W_\Delta(\widetilde{Q})}{\Delta} \right\rangle} = \left\langle \left(1 + \min\left[\frac{\gamma\Delta}{\delta_L^0}, \Gamma_{\gamma\Delta} \frac{u'_{\gamma\Delta}}{S_L}\right]\right)^\beta \frac{W_{\gamma\Delta}(\widehat{\widetilde{Q}})}{\gamma\Delta} \right\rangle \tag{4.4}$$

A few assumptions are needed to solve Eq. (4.4) for the unknown exponent β. Assuming that (i) wrinkling factors Ξ_Δ and $\Xi_{\gamma\Delta}$ are uniform within the averaging volume and (ii) u'_Δ and $W_\Delta(\widetilde{Q})$ are uncorrelated, Eq. (4.4) gives:

$$\beta = \frac{\log\left(\gamma \widehat{\langle W_\Delta(\widetilde{Q})\rangle} / \langle W_{\gamma\Delta}(\widehat{\widetilde{Q}})\rangle\right)}{\log\left(\dfrac{1 + \min\left[\gamma\Delta/\delta_L^0, \Gamma_{\gamma\Delta}\langle u'_{\gamma\Delta}\rangle/S_L\right]}{1 + \min\left[\Delta/\delta_L^0, \Gamma_\Delta\langle u'_\Delta\rangle/S_L\right]}\right)} \tag{4.5}$$

Charlette et al. (2002b) validated the dynamic methodology coupled with the TFLES model simulating 3D premixed flames in decaying isotropic turbulence. They compared their results with DNS and the estimate of the overall turbulent speed was fairly accurate for various LES runs, as displayed in Fig. 4.1. The temporal evolution of the global model parameter for the same runs is shown in Fig. 4.2. They discuss the possibility to have an exponent parameter that depends on space as well. They also tested a semi-local dynamic approach by applying an averaging in the x-direction (approximately normal to the flame brush), obtaining an exponent β, function of time, y- and z-coordinates.

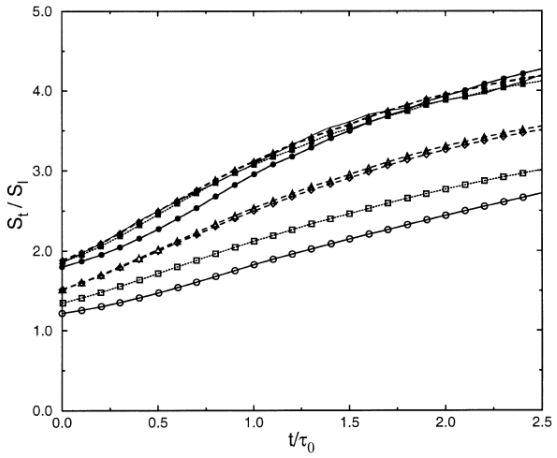

Figure 4.1: *Time evolution of the turbulent flame speed. Time is made non-dimensional by the initial turbulent eddy turn-over-time τ_0. Thick solid line: DNS;* •, ○ $\mathcal{F} = 6.6$*;* ■, □ $\mathcal{F} = 4.0$*;* ⧫, ◇, $\mathcal{F} = 2.8$ - $\gamma = 2$*;* ▲, △ $\mathcal{F} = 2.8$ - $\gamma = 3$*. The empty symbols are for the resolved turbulent speed (computing the reaction rate without wrinkling factor), plain symbols are for the total turbulent speed (with wrinkling factor) (Charlette et al. 2002b).*

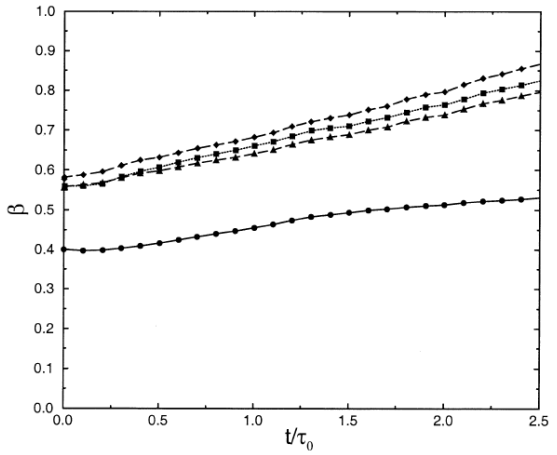

Figure 4.2: *Time evolution of the dynamic exponent β.* • $\mathcal{F} = 6.6$*;* ■ $\mathcal{F} = 4.0$*;* ⧫, $\mathcal{F} = 2.8$ - $\gamma = 2$*;* ▲ $\mathcal{F} = 2.8$ - $\gamma = 3$ *(Charlette et al. 2002b).*

4.2.2 Wang et al. (2011) formulation

As presented in Chapter 2, Damköhler (1940) suggested that the ratio of the turbulent to the laminar flame speed should be proportional to the ratio of the instantaneous flame surface area A_T of the turbulent flame to the cross-sectional area A of the flow. The fractal formalism gives (Gouldin 1987; Gouldin et al.

1989; Gülder 1991):

$$\frac{S_T}{S_L} = \frac{A_T}{A} = \left(\frac{\varepsilon_o}{\delta_c}\right)^{2-D} \tag{4.6}$$

In LES, $\varepsilon_o = \Delta$, where Δ is the combustion filter size. The inner cut-off is more difficult to model and requires additional experimental or DNS information, but a common practice is to assume it proportional to the laminar flame thickness δ_L^0. Finally, the fractal-like wrinkling factor expression becomes much simpler than the ones presented in Table 3.2 and is given by:

$$\Xi_\Delta = \left(\frac{\Delta}{\delta_c}\right)^{\beta} \tag{4.7}$$

In order to retrieve the fractal model (Eq. 4.7) for large turbulence intensities, Wang et al. (2011) proposed to modify Charlette et al. (2002a) expression (Eq. 4.3) as:

$$\Xi_\Delta \equiv \frac{S_T}{S_L} = \left(1 + \min\left[\frac{\Delta}{\delta_L^0} - 1, \Gamma_\Delta \frac{u'_\Delta}{S_L}\right]\right)^{\beta} \tag{4.8}$$

with $\Delta \geq \delta_L^0$. However, a reliable estimation of the turbulence intensity at both filter (u'_Δ) and test-filter ($u'_{\gamma\Delta}$) scales from the known resolved fields is not straightforward. To avoid the determination of these variables, the parameter β is computed in the limiting case of large turbulence intensities:

$$\lim_{u'_\Delta \to \infty} \Xi_\Delta = \left(\frac{\Delta}{\delta_L^0}\right)^{\beta} \tag{4.9}$$

$$\lim_{u'_{\gamma\Delta} \to \infty} \Xi_{\gamma\Delta} = \left(\frac{\gamma\Delta}{\delta_L^0}\right)^{\beta} \tag{4.10}$$

As a matter of fact, this hypothesis is found to be valid most of the time as shown by Veynante and Moureau (2015) using direct numerical simulations. In this case, Charlette et al. (2002a) expression is said saturated.
Finally, Wang et al. (2011) propose to solve:

$$\left\langle \widehat{\left(\frac{\Delta}{\delta_L^0}\right)^{\beta} \frac{W_\Delta(\widetilde{Q})}{\Delta}} \right\rangle = \left\langle \left(\frac{\gamma\Delta}{\delta_L^0}\right)^{\beta} \frac{W_{\gamma\Delta}(\widehat{\widetilde{Q}})}{\gamma\Delta} \right\rangle \tag{4.11}$$

leading to

$$\beta = 1 + \frac{\log(\langle \widehat{W_\Delta(\widetilde{Q})} \rangle / \langle W_{\gamma\Delta}(\widehat{\widetilde{Q}}) \rangle)}{\log \gamma} \tag{4.12}$$

The wrinkling factor Ξ_Δ is then computed, using Eq. (4.8), where the sub-grid scale turbulence intensity u'_Δ enters.
Wang et al. (2011) focused in computing a global β value, depending only on time: the averaging volume being the entire computational domain. Note, however, that the wrinkling factor is still a local variable. Their choice was based on two reasons: (i) reduced computational cost if comparable to a local approach and (ii) ease to implement, as it was the first work where the dynamic procedure was employed in parallel machines using unstructured meshes. Test filtering and the parameter calculation were done by a dedicated solver, while the AVBP code computed the flow balance equations. A Gaussian test filter was used:

$$G(\mathbf{x}) = \left(\frac{6}{\pi\widehat{\Delta}}\right) \exp\left[-\frac{6}{\widehat{\Delta}^2}(x^2+y^2+z^2)\right] \tag{4.13}$$

For each node i in the unstructured mesh, the test filtered quantities were calculated from filtered quantities $\overline{\phi}$ at nodes j by a discrete convolution operator:

$$\widehat{\overline{\phi}}_i = \frac{\sum_{j\in\mathcal{D}} \overline{\phi}_j . V_j . w_{i,j}}{\sum_{j\in\mathcal{D}} V_j . w_{i,j}} \tag{4.14}$$

where V_i denotes the cell volume linked to node j, $\mathcal{D}$ the filter cut-off domain and $w_{i,j}$ the Gaussian weight of node j to i given by a lookup table set prior to computation to avoid the repetition of expensive floating-point calculations of Eq. (4.13).
Finally, Wang et al. (2011) employed the TFLES model to simulate the turbulent Bunsen flames studied experimentally by Chen et al. (1996) over three different operating conditions. However, thickening a flame is not equivalent to filtering a flame following the standard LES definitions. The authors introduced a calibration factor to express an equivalent TFLES filter width as $\Delta = \alpha\mathcal{F}\delta_L^0$, with $\alpha = 2.2$ and to retrieve $\beta = 0$ and $\Xi_\Delta = 0$ for an unstretched laminar flame.
They observed that the global model parameter depends on the flame Reynolds number. For case F3 ($\mathrm{Re} \approx 23,000$), β stabilizes around a mean value of about $\beta \approx 0.2$, corresponding to a steady-state flow regime (Fig. 4.3). On the other hand, for case F2 ($\mathrm{Re} \approx 40,000$), the steady-state value jumps to $\beta \approx 0.4$ leading to a higher sub-grid scale wrinkling factor. Average fields were also in excellent agreement with experimental data when using the dynamic model. The non-dynamic flame wrinkling factor model provided good results, only when the empirical parameter β was properly estimated, i.e. set to the value found by the dynamic model.

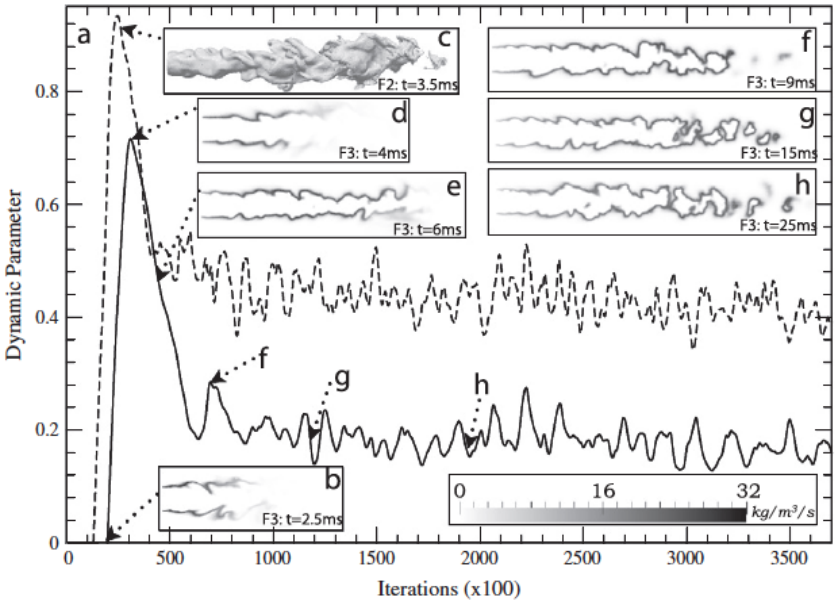

Figure 4.3: *Time evolution, in terms of number of iterations, of the dynamic parameter β and the flow field for LES of Chen et al. (1996) F2 and F3 jet flames. (a) β evolutions for F3 (solid line) and F2 (dashed line) flame; (b) chemical reaction term ($\times 8$); (d − h) chemical reaction term; (c) iso-surface of $\widetilde{Y}_{CH_4} = 0.011$ (Wang et al. 2011).*

4.2.3 Wang et al. (2012) formulation

Wang et al. (2012) applied the fractal-like dynamic model in the context of the Flame Surface Density model with Boger et al. (1998) formulation. The expression for the parameter β is similar to the one presented in Eq. (4.12). For $W_\Delta(\widetilde{c}) = 4\rho_u S_L \sqrt{6/\pi}\, \widetilde{c}(1-\widetilde{c})$, obtaining Eq. (4.15) is straightforward:

$$\beta = 1 + \frac{\log(\langle \widehat{\widetilde{c}(1-\widetilde{c})} \rangle / \langle \widehat{\widetilde{c}}(1-\widehat{\widetilde{c}}) \rangle)}{\log \gamma} \tag{4.15}$$

Unfortunately, Eqs. (4.12) and (4.15) generally does not recover $\beta = 0$ (i.e. $\Xi_\Delta = 1$) when the flame wrinkling is fully resolved in the simulation. In order to satisfy this condition, it is more appropriate to recast Eq. (4.2) in terms of flame surfaces (Hawkes and Cant 2000; Veynante and Vervisch 2002) $\overline{\dot{\omega}} = \rho_u s_L^0 \Sigma$ with ρ_u being the fresh gas density, S_L the laminar flame speed and $\Sigma = \overline{|\nabla c|} = \Xi_\Delta |\nabla \overline{c}|$ the flame surface density, i.e the available flame surface area per unit volume:

$$\langle \widehat{\Xi_\Delta |\nabla \overline{c}|} \rangle = \langle \Xi_{\gamma\Delta} |\nabla \widehat{\overline{c}}| \rangle \tag{4.16}$$

Using the fractal formalism, Eq. (4.16) becomes:

$$\left\langle \widehat{\left(\frac{\Delta}{\delta_c}\right)^{\beta} |\nabla \overline{c}|} \right\rangle = \left\langle \left(\frac{\gamma\Delta}{\delta_c}\right)^{\beta} \left|\nabla \widehat{\overline{c}}\right| \right\rangle \tag{4.17}$$

$|\nabla \overline{c}|$, $\Xi_\Delta |\nabla \overline{c}|$, $|\nabla \widehat{\overline{c}}|$ and $\Xi_{\gamma\Delta} |\nabla \widehat{\overline{c}}|$ measure resolved and total flame surface densities at combustion and test filter scales, respectively.
Hence, solving Eq. (4.17) for β, yields :

$$\beta = \frac{\log(\langle \widehat{|\nabla \overline{c}|} \rangle / \langle |\nabla \widehat{\overline{c}}| \rangle)}{\log \gamma} \tag{4.18}$$

Unfortunately, Eq. (4.17) involves unweighted quantities instead of Favre (or mass-weighted) ones. However, for infinitely thin flame fronts, one has $\overline{\rho \widetilde{c}} = \overline{\rho c} = \rho_b \overline{c}$ and $\widehat{\overline{\rho}\widetilde{\overline{c}}} = \widehat{\overline{\rho c}} = \rho_b \widehat{\overline{c}}$, where ρ_b is the burnt gas density.
Wang et al. (2012) used this dynamic version with Boger et al. (1998) flame surface density algebraic model to reproduce the growth of a flame kernel in a homogeneous and isotropic turbulent flow field. Two- and three-dimensional simulations were carried out (see Fig. 4.4 for the 3D case). They indicate that the β parameter, and accordingly the wrinkling factor Ξ_Δ, is not constant along time and increases with the progressive wrinkling of the flame kernel by the turbulent flow field (Fig. 4.5). Figure 4.5 also illustrates that the higher the initial turbulence intensity, the faster the model parameter increases. Moreover, for the laminar case ($u' = 0$ m/s), β tends toward zero as expected. Numerical results were also compared to experimental data from Renou (1999). Figure 4.6 compares the total flame radius[1] R_p as predicted by the present dynamic model, the fractal model (Eq. 4.7) with a constant $\beta = 0.35$ and the Charlette et al. (2002a) non-dynamic model ($\beta = 0.5$), starting from the same initial spherical resolved flame front. The dynamic model behaves significantly better than the non-dynamic models. Actually, as explained in Wang et al. (2012), non-dynamic models assume equilibrium between flame surface and turbulence motions and predict constant values of the wrinkling factor for a given set of turbulence characteristics. The constant fractal model predicts the correct evolution of the total flame radius but overestimates the experimental values because the wrinkling factor is too large at the early stages when the flame has not yet reach equilibrium with turbulence. On the contrary, Charlette et al. (2002a) non-dynamic model reproduces quite well the initial flame development because of a lower wrinkling factor due to a low turbulence intensity u'. Yet, it underestimates the total flame surface posteriorly.

[1]The total flame radius was defined as the radius of the spherical flame having the same total surface $R_p = [S_t(t)/4\pi]^{1/2}$, where S_t is the total flame surface $S_t(t) = \int \Xi_\Delta |\nabla \overline{c}| d\mathcal{V}$.

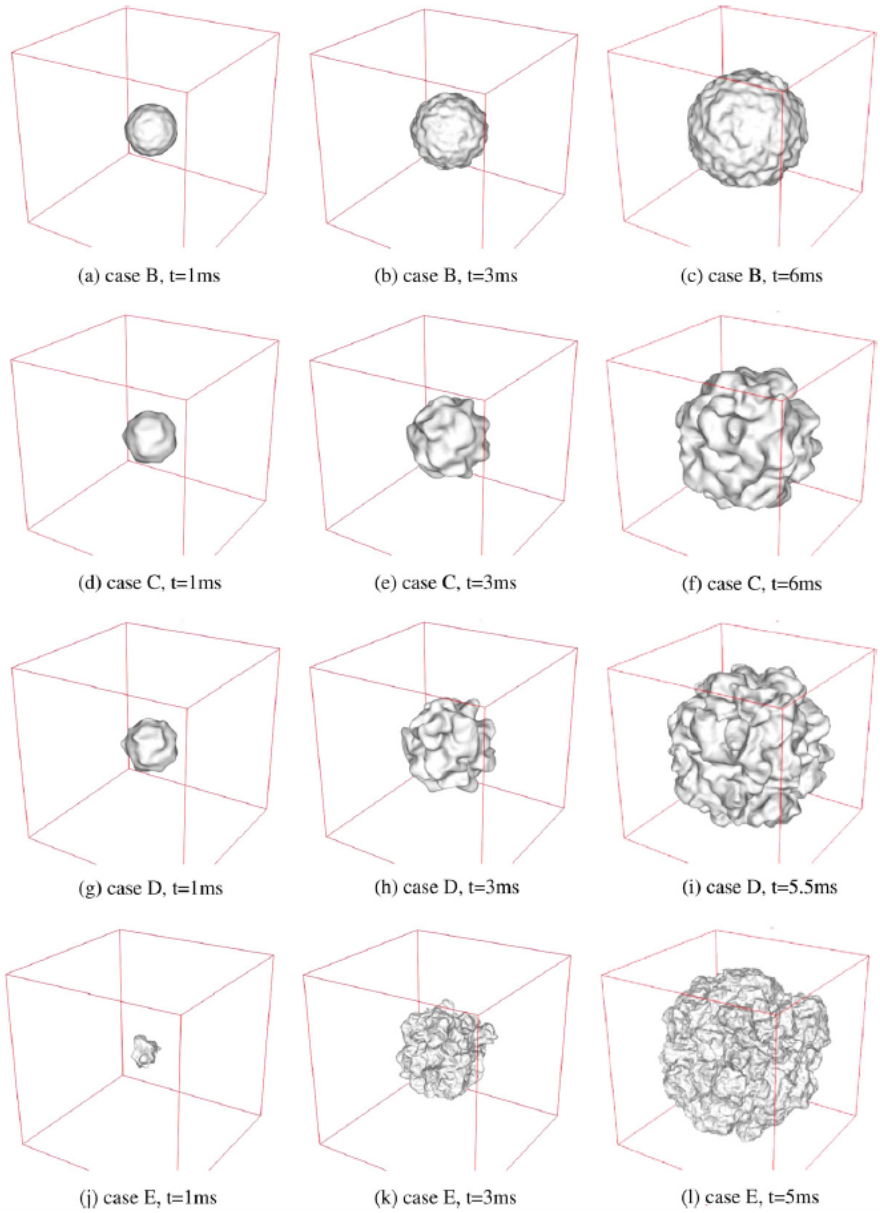

Figure 4.4: *Iso-surfaces of the* $\widetilde{c} = 0.5$ *resolved progress variables for flame kernels growing in different turbulent environments (RMS turbulent velocities* u' *and integral length scales* L*). Case A: laminar case,* $u' = 0$ *(not shown). Case B:* $u' = 0.18$ *m/s;* $L = 3.0$ *mm. Case C:* $u' = 0.34$ *m/s;* $L = 6.5$ *mm. Case D:* $u' = 0.51$ *m/s;* $L = 6.0$ *mm. Case E:* $u' = 3.0$ *m/s;* $L = 10.0$ *mm. The length of computational domain is 60 mm for the low turbulence cases B to D, and 120 mm for the high turbulence case E. Filter size* $\Delta = 7\Delta_x$ *(Wang et al. 2012).*

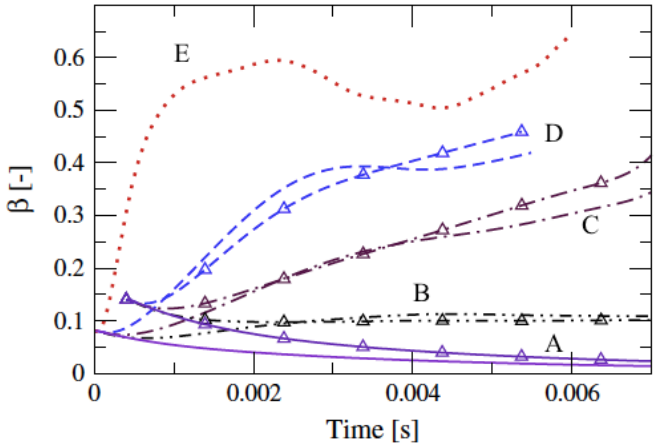

Figure 4.5: *Dynamic evolution of the model parameter β for different initial turbulence intensities u' and two LES filter sizes of $\Delta = 7\Delta_x$ (without symbols) and $\Delta = 10\Delta_x$ (with symbols). Initial turbulence conditions are the same than in Fig. 4.4 (Wang et al. 2012).*

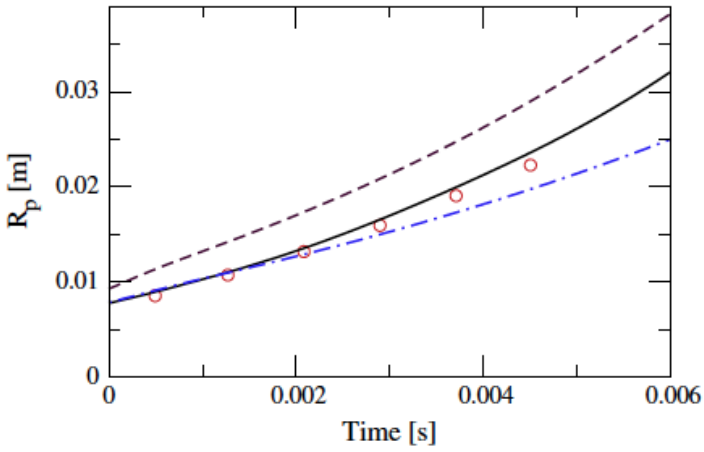

Figure 4.6: *Evolution of the total flame radius R_p using dynamic model (solid line), non-dynamic fractal model with a constant $\beta = 0.35$ value (dashed line) and Charlette et al. (2002a) model with $\beta = 0.5$ (dotted-dashed line). Symbols denote experimental data shifted by 3.3 ms in time to fit initial conditions. The filter size is $\Delta = 7\Delta_x$. Case C. (Wang et al. 2012).*

4.2.4 Veynante and Moureau (2015) formulation

Veynante and Moureau (2015) carried out detailed a priori analyzes in the lean-premixed PRECCINSTA burner, using the DNS results of Moureau et al. (2011). The grid employed in their simulation counted 2.6 billions cells, with a homogeneous mesh size of 85 micrometers in the flame region. They showed

using a priori analysis that Eq. (4.18) can be approximated by

$$\beta \approx \frac{\log\left(\left\langle\widehat{|\nabla\widetilde{c}|}\right\rangle / \left\langle\left|\nabla\widehat{\widetilde{c}}\right|\right\rangle\right)}{\log\gamma} \tag{4.19}$$

Note that the saturated form of Charlette et al. (2002a) expression, Eq. (4.8) retrieves the fractal model, Eq. (4.7). However, a constant fractal dimension would correspond to a uniform wrinkling factor over the flow field, which is generally not verified. In fact, Eq. (4.7) with space and time dependent dynamic β values is more general than a usual fractal model and the saturated form of Eq. (4.8) as this equation is easily recast as:

$$\Xi_\Delta = \left(\frac{\Delta}{\delta_c}\right)^{\beta'} \tag{4.20}$$

with

$$\beta' = \beta\frac{\log\left(1+\min\left[\frac{\Delta}{\delta_c}-1, \Gamma_\Delta\left(\frac{\Delta}{\delta_L^0}, \frac{u'_\Delta}{s_L^0}, Re_\Delta\right)\frac{u'_\Delta}{s_L^0}\right]\right)}{\log\left(\frac{\Delta}{\delta_c}\right)} \tag{4.21}$$

A significant improvement concerning the numerical implementation is achieved replacing the test and averaging operator by a Gaussian filtering, written as unsteady diffusion operators, making use of standard finite-difference or finite-volume schemes (Moureau et al. 2011). This technique is easier to implement when using unstructured meshes and/or a parallel solver (Veynante and Moureau 2015). Actually, to compute a regular average over a given volume, corresponding to a top hat filtering operation, or a filtering operation using lookup tables as done by Wang et al. (2011), involve a large number of distributed grid points and consequently MPI process. Thereby, the numerical performance is considerably increased when this procedure is applied. In the present work, formulation (4.19) is retained with the new filtering computation. Preliminary a posteriori tests were also presented proving the robustness of the dynamic model. Figure 4.7 compares an instantaneous field of the progress variable iso-surface colored by the value of the model parameter β computed a priori and a posteriori. They highlighted the fact that large eddy simulations should be extensively performed to assess the behavior of the model in a large range of conditions and to investigate the possible influence of various numerical parameters on results and on flame dynamics.

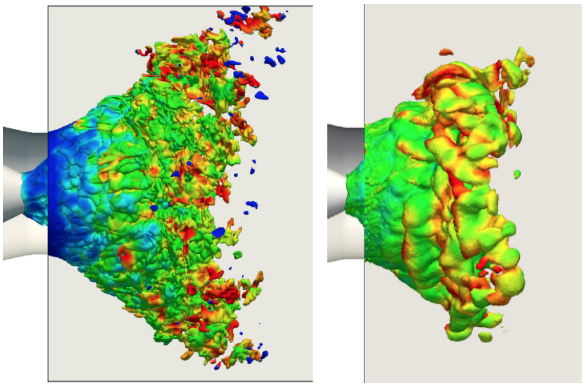

Figure 4.7: *An instantaneous flame surface obtained from the DNS is colored by the value of the model parameter β computed a priori (left). The resolved flame surface obtained from the LES is colored by the value of the model parameter β computed a posteriori (right) (Veynante and Moureau 2015).*

4.2.5 Schmitt et al. (2015) formulation

Schmitt et al. (2013); Schmitt et al. (2015) adopted a similar strategy coupled with the tabulated chemistry F-TACLES method. In the F-TACLES context, the dynamic computation for the β parameter leads to:

$$\beta = \frac{\log(\langle \widehat{\dot{\omega}^{tab}(\widetilde{c},\Delta)}\rangle / \langle \dot{\omega}^{tab}(\widehat{\widetilde{c}},\gamma\Delta)\rangle)}{\log\gamma} \tag{4.22}$$

In their early work, they simulated the Tecflam turbulent swirl burner (Schneider et al. 2005; Gregor et al. 2009), firstly, assuming that the parameter is global and spatially independent, and then assuming that it also depends on the downstream distance from the injector. In both cases, using a dynamic determination of the exponent instead of using the value suggested by Charlette et al. (2002a) improves the accuracy of the simulation. More recently, Schmitt et al. (2015) simulated turbulent Bunsen flames (Chen et al. 1996) over three different operating conditions using three different approaches: (i) a global parameter based on reaction rate (GPRR, Eq. 4.22), global parameter based on flame surfaces (GPC, Eq. 4.19) and local parameter based on flame surfaces (LPC, Eq. 4.19). When using the LPC model, the dynamic formulation is able to distinguish zones where the model parameter is close to zero (near the injector) and zones where it takes higher values due to turbulence motions.
A pulsating flame was also studied in order to characterize the model behavior. They highlighted that the development of the large coherent structures induced by the flow modulation is similar in both, GPC and LPC, situations. However, the amplitude of the reaction rate variations is larger when using the local approach since maximum reaction rate values are located in the highly wrinkled regions of the vortices as illustrates Fig. 4.8. They indicate that dynamic

procedures might affect the overall flame dynamics and instantaneous flame behavior and, as a result, they might play an important role in the prediction of combustion instabilities when strong unsteady motions develop.

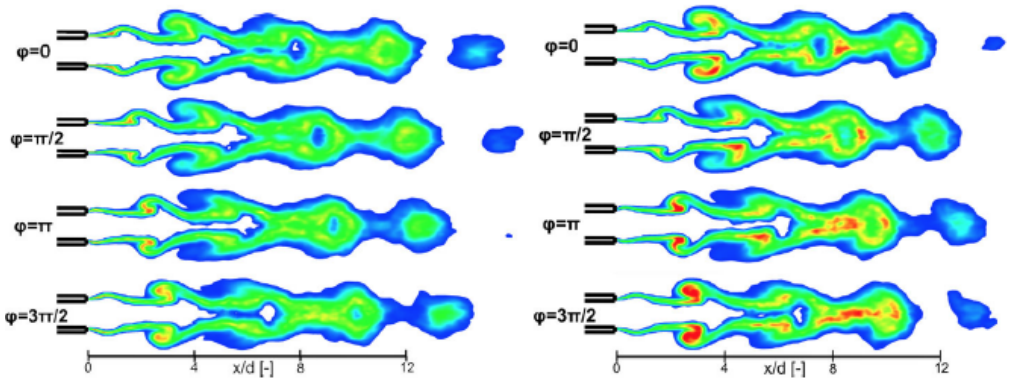

Figure 4.8: *Phase averaged filtered progress variable reaction rate fields when using global (left) and local (right) model approaches for four phases of the pulsation cycle (from top to bottom) (Schmitt et al. 2015).*

4.2.6 Mouriaux et al. (2016) improvements

Mouriaux et al. (2016) improved and validated the dynamic model in an engine configuration. They emphasized that interaction of flame fronts and interaction with solid boundaries can be problematic, once they induce large unphysical β values. They explain that contrary to flames at atmospheric condition (such as the ones considered in this manuscript), the ratio Δ/δ_c can be extremely important and difficult to treat numerically. In piston engines, the flame front is very thin ($\approx 10\mu$m), the ratio Δ/δ_c is very high (≈ 200), leading to high unexpected values of Ξ_Δ when $\beta > 0.9$. Based on 1D laminar flames, two model adaptations were proposed.

4.2.6.1 Interaction of flame fronts with solid boundaries

When the resolved flame front is close to boundaries ($d < \widehat{\Delta}$), the filter operator is truncated, as a consequence, filtering and derivative operators do not commute anymore:

$$\widehat{\nabla\widetilde{c}} \neq \nabla\widehat{\widetilde{c}} \tag{4.23}$$

Hence, the model erroneously predicts wrinkling factors larger than unity for a 1D laminar flame (Fig. 4.9), due to the fact that $\Sigma_1 = \widehat{|\nabla\widetilde{c}|}$ is larger than $\Sigma_2 = |\nabla\widehat{\widetilde{c}}|$. This numerical difficulty is overcome assuming that norm and filter operators commute everywhere and, thus, replacing $\Sigma_2 = |\nabla\widehat{\widetilde{c}}|$ by $\Sigma_{2,mod} = |\widehat{\nabla\widetilde{c}}|$ in Eq. (4.19) to compute β_{mod}.

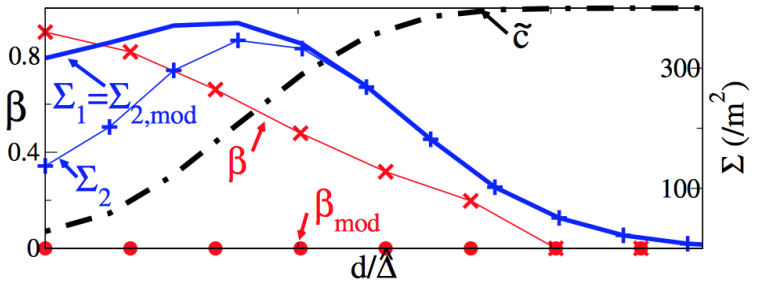

Figure 4.9: *Axial profiles of a 1D flame propagating toward the boundary of the computational domain at a distance $d < \widehat{\Delta}$ from the boundary (Mouriaux et al. 2016).*

4.2.6.2 Flame front interactions

When flame fronts interact at scale $\widehat{\Delta}$, $|\widehat{\nabla \tilde{c}}|$ may become zero, as confirmed by Fig. 4.10 that show two interacting 1D flames separated by a distance d. When $d < \widehat{\Delta}$, at point I, $\Sigma_2(I) = 0$ and $\Sigma_1 \geq 0$, leading to an ill-posed problem. The authors proposed to correct the flame surface Σ_2 as:

$$\Sigma_{2,corr} = (1 - \widehat{\zeta})\,\Sigma_2 + \widehat{\zeta}\,\Sigma_3 \tag{4.24}$$

where $\widehat{\zeta} > 0$ when fronts interact and zero elsewhere. Flag ζ is defined as $\zeta = 1$ when $\mathbf{N}.\mathbf{n} < 0.9$ and zero elsewhere, with $\mathbf{n} = -\nabla\tilde{c}/|\nabla\tilde{c}|$ and $\mathbf{N} = -\widehat{\nabla\tilde{c}}/|\widehat{\nabla\tilde{c}}|$. Then, variable ζ is test-filtered. Σ_3 is expressed as $\Sigma_3 = \widehat{\mathbf{N}.\mathbf{n}|\nabla\tilde{c}|}$, close to $\Sigma_2 = \mathbf{N}.\widehat{\mathbf{n}|\nabla\tilde{c}|}$, but when there are front interactions, Σ_3 does not approach zero like Σ_2. This formulation enables to $\Sigma_\Delta \approx 1$ for interactions of two 1D

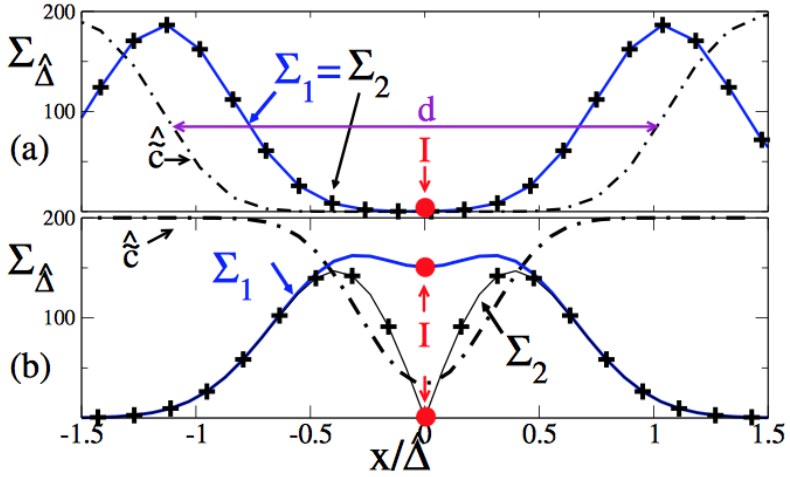

Figure 4.10: *Two interacting one-dimensional planar flame fronts at a distance d. (a) $d > \widehat{\Delta}$ (b) $d < \widehat{\Delta}$. $\Sigma_1 = \widehat{|\nabla\tilde{c}|}$; $\Sigma_2 = |\widehat{\nabla\tilde{c}}|$ (Mouriaux et al. 2016).*

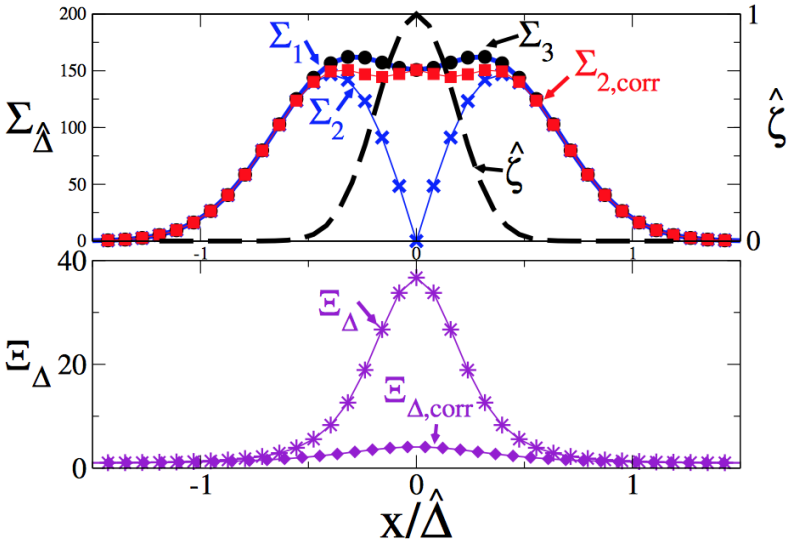

Figure 4.11: *Effect of corrections for 1D flame interactions (Mouriaux et al. 2016).*

flames, as illustrated in Fig. 4.11. This *ad hoc* correction is not used in this work, as front interactions did not engender numerical problems.

4.2.7 Dynamic formulation using Colin et al. (2000) model

The dynamic procedure can be applied using other wrinkling factor formulations. Consider, for instance, Colin et al. (2000) model:

$$\Xi_\Delta = 1 + \alpha \Gamma'_\Delta \frac{u'_\Delta}{S_L} \tag{4.25}$$

where α is the model parameter and Γ'_Δ is Colin et al. (2000) efficiency function, which describes the ability of vortices to effectively wrinkle the flame front. Combining Eq. (4.25) with Eq. (4.16) gives:

$$\left\langle \overbrace{\left[1 + \alpha \Gamma'_\Delta \frac{u'_\Delta}{S_L}\right] |\nabla \overline{c}|} \right\rangle = \left\langle \left[1 + \alpha \Gamma'_{\gamma\Delta} \frac{u'_{\gamma\Delta}}{S_L}\right] |\nabla \widehat{\overline{c}}| \right\rangle \tag{4.26}$$

Charlette et al. (2002b) pointed out that solving Eq. (4.26) leads to an ill-posed problem, if sub-grid scales turbulence intensities are much larger than unity. In this way, the model parameter cancels from each side of Eq. (4.26) and the determination of α is no longer possible. However, with practical meshes available today, typical flame surface wrinkling factors remain relatively low (around $1 - 4$) and unity is not negligible anymore. Assuming that wrinkling

factor and resolved surfaces are uncorrelated gives:

$$\alpha = \frac{\langle|\widehat{\nabla \overline{c}}|\rangle - \langle|\nabla \widehat{\overline{c}}|\rangle}{\Gamma'_{\gamma\Delta}\langle u'_{\gamma\Delta}\rangle/S_L\langle|\nabla \widehat{\overline{c}}|\rangle - \Gamma'_{\Delta}\langle u'_{\Delta}\rangle/S_L\langle|\widehat{\nabla \overline{c}}|\rangle} \tag{4.27}$$

As stated by Veynante and Moureau (2015), Eq. (4.27) may lead to practical difficulties and may deteriorate the robustness of a numerical code. First, because numerator and denominator tend towards zero when sub-grid scale turbulence vanishes and when the flame front wrinkling is fully resolved at both filter and test filter scales. Second, the numerator in Eq. (4.27) is expected to be positive, but the behavior of the denominator is unknown a priori. Moreover, inaccuracies of $\langle u'_{\Delta}\rangle$ and Γ'_{Δ} and numerical uncertainties can affect adversely the dynamic procedure, leading to unforeseen division by zero, large or negative α values. For these reasons, formulation presented in Subsection 4.2.4 is preferred.

4.2.8 Knikker et al. (2004) formulation

The similarity assumption was firstly suggested by Bardina et al. (1980) to describe unresolved momentum transport. Knikker et al. (2002) extended this notion to reactive flows to compute the SGS flame surface density, assuming that the unresolved scales behave like those slightly larger than the cut-off scale. Knikker et al. (2004) proposed a dynamic version of their similarity model and validated it from a priori tests performed on experimental data. The flame surface density, Σ, can be split into a resolved and unresolved contribution:

$$\Sigma = \overline{|\nabla c|} = \Xi_{\Delta}|\nabla \overline{c}| = \underbrace{|\nabla \overline{c}|}_{resolved} + \underbrace{[\overline{|\nabla c|} - |\nabla \overline{c}|]}_{unresolved} \tag{4.28}$$

The unresolved contribution is modeled as being proportional to the known flame surface between LES and test filter scales:

$$\Sigma = \overline{|\nabla c|} = \Xi_{\Delta}|\nabla \overline{c}| = |\nabla \overline{c}| + K_s[\widehat{|\nabla \overline{c}|} - |\nabla \widehat{\overline{c}}|] \tag{4.29}$$

The coefficient K_s is determined by identifying the SGS flame surface as a fractal surface:

$$\widehat{|\nabla \overline{c}|} = \widehat{\Sigma}\left(\frac{\Delta}{\delta_c}\right)^{-\beta} \tag{4.30}$$

$$|\nabla \widehat{\overline{c}}| = \widehat{\Sigma}\left(\frac{\gamma\Delta}{\delta_c}\right)^{-\beta} \tag{4.31}$$

giving

$$K_s = \frac{1}{1-\gamma^{-\beta}}\left[\left(\frac{\Delta}{\delta_c}\right)^{\beta} - 1\right] \tag{4.32}$$

The flame surface conservation at the cut-off scales Δ and $\gamma\Delta$ over a given volume leads to Eq. (4.17). Finally, the model parameter β can be computed on the fly as in Eq. (4.18).
Knikker et al. (2004) validated their model with experimental data obtained by OH- radical laser induced fluorescence in a turbulent premixed propane/air flame. The drawback of their model is that a filtering operation is required not only to compute the model parameter, but also the reaction rate (terms in square brackets in Eq. 4.29). Therefore, a filtering operation is needed every iteration and is likely to be very expensive from a numerical point of view. Still, Gubba et al. (2011) employed the FSD model formulated by Knikker et al. (2004) to study the propagation of a turbulent premixed flame through obstacles in a laboratory scale combustion chamber investigated experimentally by Masri et al. (2012). They obtained very good results in terms of flame dynamics and overpressure inside the chamber. Figure 4.12 shows a sequence of

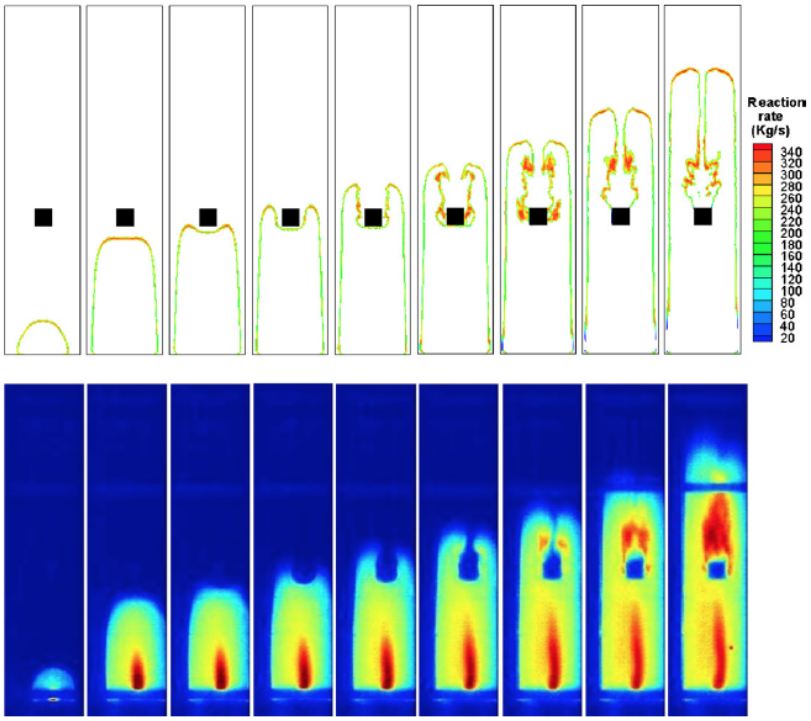

Figure 4.12: *Series of flame images at 6.0, 12.0, 12.5, 13.0, 13.5, 14.0, 14.5, 15.0, 15.5 ms respectively after ignition (top) LES (bottom) experimental video images (false color) (Gubba et al. 2011).*

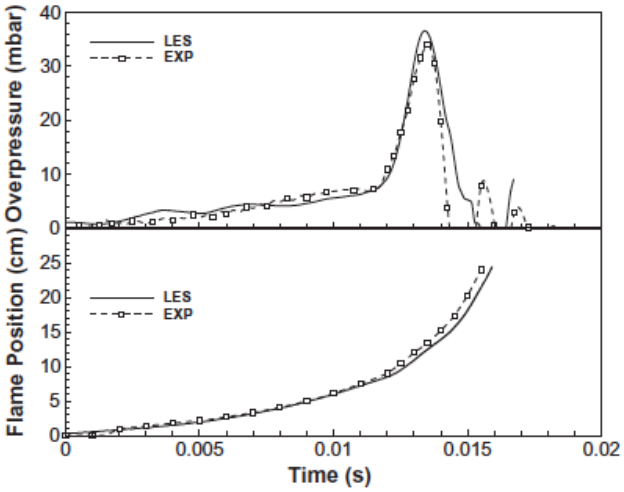

Figure 4.13: *Time histories of overpressure and flame position for the base case presented in Fig. 4.12 (Gubba et al. 2011).*

images for the calculated reaction rate contours compared to the measured high speed video images at various times after ignition for the base case (the small square obstacle is present without any baffle plate). The temporal evolution of the overpressure and flame position from LES are plotted against experimental measurements in Fig. 4.13 for the same geometry. The authors concluded that large eddy simulation is capable of reproducing turbulent flame structure and the overpressure with a high level of accuracy.
The same combustion chamber with different obstructions was studied in this thesis and is the subject of Chapter 7.

4.2.9 Im et al. (1997) formulation

Im et al. (1997) proposed a dynamic sub-grid scale model in the context of the G-equation formalism. In their study, the sub-grid scalar flux term is modeled by an eddy diffusivity model to avoid the formation of cusps and improve the numerical stability. The constant of sub-grid flux term is computed dynamically using Germano et al. (1991) identity. For the filtered modulus term, $|\overline{\nabla G}|$ a dynamic approach is also employed and is succinctly discussed here. The latter term can be decomposed as:

$$|\overline{\nabla G}| = |\nabla \overline{G}| + [|\overline{\nabla G}| - |\nabla \overline{G}|] \tag{4.33}$$

$$= |\nabla \overline{G}| + v \tag{4.34}$$

The same term at the test-filter level becomes:

$$|\widehat{\overline{\nabla G}}| = |\nabla\widehat{\overline{G}}| + [|\widehat{\overline{\nabla G}}| - |\nabla\widehat{\overline{G}}|] \tag{4.35}$$

$$= |\nabla\widehat{\overline{G}}| + V \tag{4.36}$$

Using Germano et al. (1991) identity, the following expression is easily derived:

$$V - \widehat{v} = |\widehat{\overline{\nabla G}}| - |\nabla\widehat{\overline{G}}| \tag{4.37}$$

where the right-hand side can be computed from the grid-level solution. If now v and V are modeled as:

$$|\nabla\overline{G}| + v = \frac{S_T}{S_L}|\nabla\overline{G}| \tag{4.38}$$

$$|\nabla\widehat{\overline{G}}| + V = \frac{\widehat{S}_T}{S_L}|\nabla\widehat{\overline{G}}| \tag{4.39}$$

with S_T/S_L given by Eq. (3.49) reminded below:

$$\frac{S_T}{S_L} = 1 + \alpha\left(\frac{u'_\Delta}{S_L}\right)^p$$

we obtain

$$\alpha[\langle(u'_{\gamma\Delta})^p|\nabla\widehat{\overline{G}}|\rangle - \langle\widehat{(u'_\Delta)^p|\nabla\overline{G}|}\rangle] = (S_L)^p[\langle|\widehat{\overline{\nabla G}}|\rangle - \langle|\nabla\widehat{\overline{G}}|\rangle] \tag{4.40}$$

from which the unknown constant α is easily determined for a constant value of p. The brackets denotes a volume averaging as done in other studies.
They conducted a priori tests based on direct numerical simulations of forced homogeneous isotropic turbulence and a posteriori tests for large eddy simulations in similar configurations. Three formulations have been proposed for the sub-grid flame velocity. The first one is based on the Laplacian of the strain rate tensor: $u'_\Delta \approx \Delta(2\widetilde{S}_{ij}\widetilde{S}_{ij})^{1/2}$ (Model 1). In the second, the sub-grid term is computed as $u'_\Delta(\overline{k}) = \int_{\overline{k}}^{\infty} E(k)dk$ where $E(k) = C_k k^{-m}$ is appropriate in the inertial zone (Model 2A) and $E(k) = C_k \exp(-mk)$ appropriate in the dissipation zone (Model 2B), where C_k and m are constants. The last formulation is based on the scale similarity model, proposed by Bardina et al. (1980) (Model 3). Within the studied cases, model 2B is the most accurate. The authors also highlighted that the p parameter has a big influence on the results. Note that expression (4.40) may lead to numerical problems, similarly to the dynamic formulation based on Colin et al. (2000) model, described in Sub-section 4.2.7.

4.2.10 Knudsen and Pitsch (2008) formulation

Knudsen and Pitsch (2008) developed a dynamic model that describes the turbulent burning velocity in the context of the G-equation formalism for LES of turbulent premixed combustion. They also introduced a new approach to write the filtered flame front equation that is consistent with standard LES filtering. The terms that describe subfilter influences on the turbulent burning velocity are prescribed using information that comes directly from the flame front. For conciseness, only one simple case is considered. In the limit of corrugated flamelet regime, neglecting convective and curvature effects and assuming that differences between the filtered and test-filtered density are small, one can writes:

$$\widehat{S_T|\nabla\overline{G}|} = \widehat{S}_T|\nabla\widehat{\overline{G}}| \tag{4.41}$$

Note that Eq. (4.41) can be seen as an enforcement of a constant rate of flame mass consumption, independent of the filter being used.
The authors expressed $|\nabla\overline{G}|$ using the area of the filtered flame front that passes through the local filter volume, A_Δ, and the filter volume itself, V_Δ, as:

$$|\nabla\overline{G}| \approx A_\Delta/V_\Delta \tag{4.42}$$

They modeled the burning speed based on Peters (2000):

$$\frac{S_T - S_L}{u'_\Delta} = -\zeta Da_\Delta + [(\zeta Da_\Delta)^2 + \zeta\alpha Da_\Delta]^{1/2} \tag{4.43}$$

where α and ζ are model constants and Da_Δ is the Damköhler number associated with the filter width. Finally, combining Eqs. (4.41)-(4.43), the dynamic equation takes the following form:

$$\begin{aligned}\left\{S_L + u'_\Delta\left[-\zeta Da_\Delta + \left((\zeta Da_\Delta)^2 + \zeta\alpha Da_\Delta\right)^{1/2}\right]\frac{A_\Delta}{V_\Delta}\right\}^\wedge = \\ S_L + u'_{\gamma\Delta}\left[-\zeta Da_{\gamma\Delta} + \left((\zeta Da_{\gamma\Delta})^2 + \zeta\alpha Da_{\gamma\Delta}\right)^{1/2}\right]\frac{A_{\gamma\Delta}}{V_{\gamma\Delta}}\end{aligned} \tag{4.44}$$

Two weaknesses arise from this formulation. First, if one seeks to compute α dynamically, the unknown parameters ζ and the subfilter velocity fluctuation at both scales, u'_Δ and $u'_{\gamma\Delta}$ must be estimated. Second, an iterative procedure such as Newton's method is needed to solve Eq. (4.44) for α locally. This procedure requires information from local and surrounding cells that are used in the test-filtering operation and is likely to be very expensive.

Finally, Knudsen and Pitsch (2008) performed simulations where the model parameter depends on both time and space coordinates. Figure 4.14 shows a single snapshot from the LES of Chen et al. (1996)'s F3 jet flame. The local influence of the dynamic model can be seen in the coloring of the flame front. This coloring shows the ratio of the filtered and test-filtered flame areas, on a per-test-filter-volume basis. In the flat, planar regions of the flame, this ratio is nearly one (blue color). In regions of the flame where turbulence has produced a large amount of wrinkling, the ratio increases to 1.15 (red color).

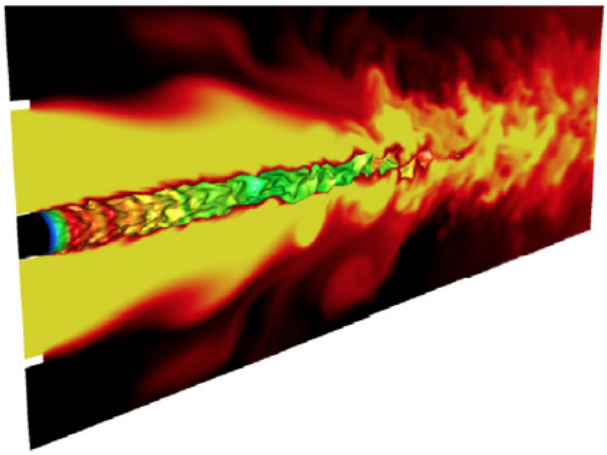

Figure 4.14: *Instantaneous snapshot from an LES of the F3 flame. The cut plane shows a contour plot of temperature, which ranges from 300 K (black) to 2200 K (bright yellow). The premixed flame is colored according to the ratio of the filtered and test-filtered flame areas, on a per-test-filter-volume basis (Knudsen and Pitsch 2008).*

4.3 Indirect approaches

In large eddy simulation of non-premixed combustion, instead of solving transport equations for all of the numerous species in a typical chemical mechanism and modeling the unclosed chemical source terms, the detailed chemical processes can be simplified to a reduced system of tracking scalars. Typically, two scalars are considered: a mixture fraction variable, which tracks the mixing of fuel and oxidizer, and a progress variable, which tracks the global extent of reaction of the local mixture (Pierce and Moin 2004). Accurate prediction of non-premixed turbulent combustion using LES requires detailed modeling of the mixing between fuel and oxidizer at scales finer than the LES filter resolution. In flamelet models of non-premixed combustion, the small scale mixing process is quantified by two parameters: the subfilter scalar variance and the subfilter scalar dissipation rate (Kaul et al. 2013). Thus, the dynamic formalism has also been employed to compute these sub-grid quantities, that enter non-premixed combustion models (Réveillon and Vervisch 1998; Pierce and Moin 1998; Pierce

and Moin 2004; Balarac et al. 2008; Kaul et al. 2013). These procedures can be denoted "indirect approaches", to differ from the previous one that involve directly reaction rate terms.
Réveillon and Vervisch (1998) have proposed extensions of the PDF method to LES and a dynamic approach was used to close the turbulent micro-mixing term in the PDF transport equation.
Pierce and Moin (1998) proposed a simple scaling relation for the sub-grid scale variance where the scaling coefficient was computed dynamically. The variance dissipation rate was also obtained using a dynamic procedure assuming equilibrium with the local variance production rate. Based on their previous work, Pierce and Moin (2004) simulate a methane-fuelled coaxial jet combustor and captured the unsteady, lifted flame dynamics observed in the experiment, and obtained good agreement with the experimental data.
Balarac et al. (2008) carried out a priori tests based on 512^3 direct numerical simulation data of forced homogeneous isotropic turbulence and evaluate several subfilter variance models for the mixture fraction. They proposed a new dynamic procedure that improve the predictive accuracy.
Kaul et al. (2013) developed a dynamic non-equilibrium model for variance and dissipation rate, based on a scale similarity assumption, and simulated a turbulent lifted ethylene flame. They concluded that the use of the dynamic procedure increase the accuracy of the non-equilibrium modeling approach.

4.4 Comments on the inner cut-off length scale

The inner cut-off represents the smallest scale of wrinkling present in the flame. A good estimate for this physical parameter is a prerequisite to determine correctly the turbulent flame surface and speed, since it enters Eq. (4.6). Note that this physical parameter, cannot be determined using a dynamic procedure as it corresponds to scales lost in the filtering process ($\delta_c < \Delta$). There are several expressions in the literature that relate the inner cut-off to the Kolmogorov length scale, the laminar flame thickness and even the Gibson scale.
Over the years, many research teams tried to provide general expressions for the inner cut-off length scale based on experimental data, numerical simulations or physical reasoning. The argument that the smallest scale of wrinkling corresponds to the Kolmogorov scale, η, neglects some basic flame/turbulence interaction considerations. Indeed, such scales do not carry enough energy to affect the flame front (Poinsot et al. 1991). Peters (1986) suggested that the Gibson scale, $L_G = L(S_L/u')^3$ should be used as the inner cut-off. He defined it as the length scale of eddies whose characteristic velocity is equal to the laminar flame speed. Unfortunately, the Gibson scale concept does not appear to predict properly the inner cut-off (North and Santavicca 1990; Gülder and Smallwood 1995).
Physical arguments indicate that it is impossible for an object to have wrinkles,

Table 4.2: *Summary of inner cut-off expressions (Gülder and Smallwood 1995).*

Reference	δ_c/δ_L
Peters (1986)	Ka^{-2}
Gouldin (1987)	$\mathrm{f}(u'/S_L;\mathrm{Re})\mathrm{Ka}^{-2}$
Murayama and Takeno (1989)	10-15
Poinsot et al. (1991)	$0.74+16.4\mathrm{Ka}^{-1/3}$
Gülder (1991)	$712\ \mathrm{Re}^{-3/4}\ \mathrm{Ka}^{-1/2}$
Mantzaras (1992)	$\mathrm{f}(u'/S_L)\mathrm{Ka}^{-2}$
Roberts et al. (1993)	$7\ \mathrm{Ka}^{-1/2}$

Abbreviations: δ_c = inner cut-off; $\delta_L = \nu/S_L$; ν = kinematic viscosity of the unburned premixed gases; S_L = laminar burning velocity; Ka $= (u'/S_L)^{3/2}(L/\delta_L)^{-1/2}$; u' = rms velocity fluctuations; L = integral length scale; Re = Reynolds number based on L.

which are smaller than its thickness. Under such conditions, the laminar flame thickness would be a more judicious choice for the inner cut-off. Murayama and Takeno (1989) have shown that the inner cut-off is close to δ_L^0, which was an order of magnitude greater than η for the lean methane/air premixed flames studied.

Gülder and Smallwood (1995) gathered expressions found in the literature for the inner cut-off length scale and compared with numerical and experimental data. They showed that the non-dimensional inner cut-off scales well with the Karlovitz number, $\mathrm{Ka}^{-1/2}$. These formulations are organized in Table 4.2.

Gülder et al. (2000) investigated the characteristics of the flame front surfaces in turbulent premixed propane/air flames for different Reynolds numbers and turbulence intensities. They used laser-induced fluorescence (LIF) of OH and Mie scattering on two Bunsen-type burners of 11.2 mm and 22.4 mm diameters. The caliper technique was used to extract fractal parameters (dimension, inner and outer cut-offs) of the flame front. While fractal dimensions derived from OH and Mie scattering images are practically identical, inner and outer cut-offs are higher when using the former method. Table 4.3 presents a summary of experimental conditions and results for the burner of 22.4 mm diameter. Note that inner cut-off scale is always greater than the laminar flame thickness

Table 4.3: *Summary of experimental conditions and results for the burner of 22.4 mm diameter (Gülder et al. 2000).*

Data set	ϕ	L [mm]	u'/S_L	Re	D	δ_c [mm]	ϵ_o [mm]
MIE1	1	1.51	0.9	39	2.16 (0.03)	1.10 (0.28)	12.39 (2.34)
OH10					2.18 (0.03)	1.58 (0.39)	14.48 (2.40)
MIE4	1	1.78	1.12	57	2.16 (0.02)	1.12 (0.23)	12.64 (2.21)
OH14					2.16 (0.02)	1.43 (0.23)	13.75 (2.50)
MIE7	1	1.58	1.13	51	2.19 (0.03)	1.18 (0.26)	13.42 (2.40)
OH11					2.19 (0.03)	1.59 (0.32)	13.83 (2.40)
MIE6	1	2.28	1.48	97	2.24 (0.04)	1.09 (0.27)	13.82 (4.17)
OH15					2.25 (0.05)	1.60 (0.38)	16.26 (5.40)

Abbreviations: ϕ = fuel-air equivalence ratio; L = integral legth scale; u' = rms velocity fluctuations; S_L = laminar burning velocity (0.43 m/s at $\phi = 1$); Re = Reynolds number based on L; D = fractal dimension; δ_c = inner cut-off; ϵ_o = outer cut-off; $\delta_L^0 = 0.34$ mm at $\phi = 1$.

($\delta_L^0 = 0.34$ mm at $\phi = 1$) independently on the employed method. They also claim that the caliper method is more accurate than the circle method (also called the Minkowski sausage (Mandelbrot 1983)), used in other studies (Mantzaras et al. 1989; North and Santavicca 1990; Yoshida et al. 1994).
Curiously, Gülder et al. (2000); Cintosun et al. (2007) show that the fractal approach is not able to predict the estimated turbulent burning rates. The fundamental assumption that S_T/S_L is proportional to the ratio of the wrinkled flame surface area, A_T, to the flow reference area A may not be appropriate for the turbulent premixed flames in the flamelet regime. Ronney and Yakhot (1992) proposed that scales smaller than the laminar flame thickness affect the turbulent flame propagation for most flames at sufficiently high turbulence intensities.
In another study (Battista et al. 2015), the inner cut-off length shows a clear scaling with the Kolmogorov scales and the Karlovitz number as indicates Fig. 4.15.

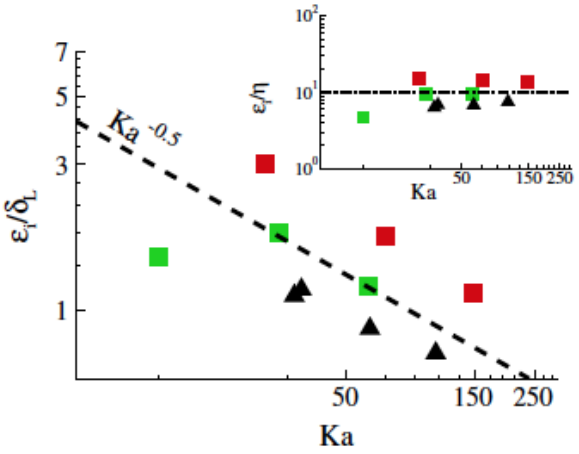

Figure 4.15: *Inner cut-off δ_c/δ_L^0 vs Karlovitz number Ka. Only experimental values are reported. Dotted line represents the scaling $\delta_c/\delta_L^0 \propto Ka^{-1/2}$. In the inset the inner cut-off length normalized by the Kolmogorov scale, δ_c/η, is reported against Karlovitz number. The dash-dotted line represent the constant fitting value $\delta_c/\eta = 10$ (Battista et al. 2015).*

The hypothesis that $\delta_c \propto \delta_L^0$ seems acceptable, although too coarse, and is used for convenience in this manuscript. Nonetheless, this short review proves that research is still needed and modeling the inner cut-off length scale remains an open question.

Part II

Validation of the dynamic model in different flow configurations

This part comprises three chapters based on journal articles:

- *The article* ***"A posteriori tests of a dynamic thickened flame model for large eddy simulations of turbulent premixed combustion"*** *by P. S. Volpiani, T. Schmitt and D. Veynante accepted in Combustion and Flame is reported in Chapter 5.*

- *The article* ***"Large eddy simulation of a turbulent swirling premixed flame coupling the TFLES model with a dynamic wrinkling formulation"*** *by P. S. Volpiani, T. Schmitt and D. Veynante accepted in Combustion and Flame is reported in Chapter 6.*

- *The article* ***"Large eddy simulation of explosion deflagrating flames using a dynamic wrinkling formulation"*** *by P. S. Volpiani, T. Schmitt, O. Vermorel, P. Quillatre, and D. Veynante submitted to Combustion and Flame is reported in Chapter 7.*

Chapter 5

A posteriori tests of a dynamic thickened flame model for large eddy simulations of turbulent premixed combustion

Dynamic models where model parameters are automatically adjusted from known resolved fields are a very attractive formulation for large eddy simulations. Now widely used for unresolved momentum transport, this approach remains rather marginal to describe filtered reaction rates despite of very promising results. Global and local dynamic formulations for the flame wrinkling factor are combined with the Thickened Flame (TFLES) model to simulate the F3 pilot stabilized jet flame studied experimentally by Chen and coworkers. The influence of physical (flame wrinkling inner cut-off length scale) and numerical (test filter width, averaging procedure, updating frequency) characteristics of a flame wrinkling factor dynamic model for turbulent premixed combustion is investigated. Numerical results are discussed in terms of mean flow fields as well as dynamical behaviors. It is shown that the dynamic model is robust and relatively insensitive to the numerical input coefficients to be provided beforehand in the code. This finding indicates that the model parameter does not need to be adjusted any more. However, a model for the inner cut-off scale of flame wrinkles, lost in the filtering process, is required.

5.1 Introduction

Progress in gas turbines or automotive engines is directly linked to the capacity of computational fluid dynamics (CFD) tools to predict correctly the behavior of these complex systems. Large eddy simulation (LES) is now routinely used to improve the design of such combustion devices (Pitsch 2006; Gicquel et al. 2012; Poinsot and Veynante 2011). In LES, the largest structures of the flow are captured by the grid while the effects of the small ones are modeled.
One of the challenges in combustion problems of large eddy simulations is the fact that the flame front is too thin to be resolved on the computational mesh. To overcome this difficulty, several approaches have been developed. Examples include flame front tracking techniques, such as the G equation (Kerstein et al. 1988; Pitsch 2005), the use of filters larger than the mesh size (Boger et al. 1998; Poinsot and Veynante 2011) and the TFLES approach in which diffusion and pre-exponential factors are modified in order to artificially thicken the flame (Butler and O'Rourke 1977; Colin et al. 2000; Charlette et al. 2002a). This last strategy is adopted in this work.
Another major topic that draws attention is the modeling of the sub-grid terms that appear in filtered balance equations. Thus, unresolved flame/turbulence interaction is a crucial point and a good model for the sub-grid turbulent flame speed (Pitsch 2006; Poinsot and Veynante 2011), directly related to the flame front wrinkling factor (Colin et al. 2000; Charlette et al. 2002a), or to the sub-grid scale flame surface density (Boger et al. 1998) is mandatory. However, usual algebraic models assume equilibrium between turbulence motions and flame surface and consequently they cannot handle transient situations (Richard et al. 2007). This is the case of a flame kernel growth or even a jet flame initially laminar during the early stages of the flame development and then progressively wrinkled by turbulence motions. One way to overcome this problem is to solve a balance equation for the filtered surface density (Hawkes and Cant 2000; Richard et al. 2007) or for the wrinkling factor (Weller et al. 1998) but new unclosed terms appear.
An alternative is to develop dynamic combustion models. Dynamic modeling is based on the filtering of the instantaneous resolved fields at a test filter scale larger than the original LES filter. The model is then assumed to hold at both scales and the model parameter can be obtained by solving a "Germano-like" equation (Germano et al. 1991). This strategy has been successfully applied by Charlette et al. (2002b) and Wang et al. (2011) in the context of the TFLES model. Charlette et al. (2002b) carried out 3D simulations of premixed flames in decaying isotropic turbulence and comparisons between DNS and LES showed that the dynamic procedure allows the LES to reproduce the total reaction rate of the DNS quite well. Wang et al. (2011) improved the procedure and simulated the turbulent Bunsen flames studied experimentally by Chen et al. (1996) over three different operating conditions and results were in good agreement with the experimental data.

In the Flame Surface Density (FSD) context, Knikker et al. (2002); Knikker et al. (2004) proposed a model based on a fractal analysis (Gouldin 1987; Gülder 1991) and a similarity assumption (Bardina et al. 1980). The model was validated *a priori* from experimental data obtained by OH-radical laser induced fluorescence in a turbulent premixed propane/air flame. Gubba et al. (2011) retained this approach to investigate the propagation of a turbulent premixed flame through obstacles in a laboratory scale combustion chamber. Wang et al. (2012) implemented a dynamic version of Boger et al. (1998) flame surface density algebraic model to reproduce the growth of a flame kernel in a homogeneous and isotropic turbulent flow field. Two- and three-dimensional simulations were carried out and results were compared with the experimental data from Renou (1999).

Im et al. (1997) and Knudsen and Pitsch (2008) also developed dynamic models in the G-equation framework. Im et al. (1997) tested their model in a forced homogeneous and isotropic turbulence case, while Knudsen and Pitsch (2008) chose the F3 jet flame investigated experimentally by Chen et al. (1996).

More recently, dynamical modeling has also been combined with tabulated chemistry techniques (Fiorina et al. 2010). Schmitt et al. (2013) obtained very good preliminary results for the Tecflam burner configuration Schneider et al. (2005); Gregor et al. (2009) using a dynamic local formulation. Mercier et al. (2015) simulated the Cambridge stratified swirl burner (SwB) (Sweeney et al. 2011; Sweeney et al. 2011) using different heat losses and SGS flame wrinkling models, including the dynamic formulation.

Other authors applied the dynamic formalism to compute variances and scalar dissipation rates of a mixture fraction, that enter non-premixed combustion models (Réveillon and Vervisch 1998; Pierce and Moin 1998; Pierce and Moin 2004; Balarac et al. 2008; Kaul et al. 2013). These procedures can be denoted "indirect approaches", to differ from the previous ones that involves directly the reaction rate term.

However, many points remain unclear and not yet investigated, in particular the influence of physical (flame wrinkling inner cut-off length scale) and numerical (test filter width, averaging procedure, updating frequency) characteristics of the model. In the present paper, global and local formulations (Veynante et al. 2012; Veynante and Moureau 2015) are analyzed in the framework of the TFLES model. In the next section, the basic concepts of the TFLES combustion model are briefly discussed and the dynamic procedure is presented based on the previous *a priori* and *a posteriori* works (Charlette et al. 2002b; Wang et al. 2011; Veynante et al. 2012; Veynante and Moureau 2015; Schmitt et al. 2015). Subsequently, the turbulent jet flame configuration investigated by Chen et al. (1996) is described together with computational details. Global and local saturated formulations are analyzed as well as the influence of the model coefficients that must be specified beforehand in the code. Conclusions are drawn.

5.2 Modeling

5.2.1 The thickened flame model (TFLES)

Flames are artificially thickened to be resolved on numerical grids by multiplying diffusion and dividing reaction rates by a thickening factor $\mathcal{F}$. The modified flame front of thickness $\mathcal{F}\delta_L^0$ propagates at the same laminar flame speed S_L as the original flame of thickness δ_L^0 (Butler and O'Rourke 1977; O'Rourke and Bracco 1979). However, when the flame is thickened, the interaction between turbulence and chemistry is modified and the flame becomes less sensitive to turbulence motions (Colin et al. 2000). An efficiency function has been derived to counteract this effect by increasing the flame propagation velocity (Colin et al. 2000; Charlette et al. 2002a). Charlette et al. (2002a) introduce a sub-grid scale wrinkling factor, Ξ_Δ that measures the ratio of the total flame surface to the resolved flame surface in the filter volume and directly related to the sub-grid scale flame surface lost because of the thickening process. The balance equations for filtered species mass fractions $\widetilde{Y}_k$ are written as:

$$\frac{\partial \overline{\rho}\widetilde{Y}_k}{\partial t} + \nabla \cdot (\overline{\rho}\widetilde{\mathbf{u}}\widetilde{Y}_k) = -\nabla \cdot (\Xi_\Delta \mathcal{F}\overline{\rho \mathbf{V}_k}\widetilde{Y}_k) + \frac{\Xi_\Delta}{\mathcal{F}}\dot{\omega}_k(\widetilde{Q}) \tag{5.1}$$

where ρ is the density, $\mathbf{u}$ the velocity vector, $\mathbf{V_k}$ the diffusion velocity of species k, expressed here using the Hirschfelder and Curtiss approximation (Poinsot and Veynante 2011; Hirschfelder et al. 1954) and $\dot{\omega}_k$ the reaction rate of species k, estimated from Arrhenius law. Q denotes any quantity entering the computation of the reaction rate, such as species mass fractions or temperature. $\overline{Q}$ and $\widetilde{Q}$ denotes filtered and mass-weighted filtered quantities, respectively ($\overline{\rho}\widetilde{Q} = \overline{\rho Q}$). By construction, Eq. (5.1) propagates a flame front of thickness $\mathcal{F}\delta_L^0$ at the sub-grid scale turbulent flame speed $\Xi_\Delta S_L$. Charlette et al. (2002a) modeled the wrinkling factor with a power-law relationship. Wang et al. (2011) slightly modified the initial expression and wrote:

$$\Xi_\Delta = \left(1 + \min\left[\frac{\Delta}{\delta_c} - 1, \Gamma_\Delta\left(\frac{\Delta}{\delta_L^0}, \frac{u'_\Delta}{S_L}, Re_\Delta\right)\frac{u'_\Delta}{S_L}\right]\right)^\beta \tag{5.2}$$

δ_c is the inner cut-off length scale (i.e. the smallest scale for the interaction of turbulent eddies with the premixed flame front) assumed equal to the laminar flame thickness δ_L^0. The efficiency function Γ_Δ measures the ability of vortices to effectively wrinkle the flame front, u'_Δ and $Re_\Delta = u'_\Delta \Delta/\nu$ are the sub-grid scale turbulence intensity and Reynolds number, respectively, ν being the fresh gas kinematic viscosity. β is the model parameter to be specified.
However, direct numerical simulations (Veynante et al. 2012; Veynante and Moureau 2015) showed that Eq. (5.2) is often saturated, i.e. the minimum

term is usually controlled by the $(\Delta/\delta_c - 1)$ contribution. Therefore, Eq. (5.2) reduces to:

$$\Xi_\Delta = \left(\frac{\Delta}{\delta_c}\right)^\beta \tag{5.3}$$

Equation (5.3) corresponds to a fractal model (Gouldin 1987; Gouldin et al. 1989; Gülder 1991), where $D = \beta + 2$ is the fractal dimension of the flame surface. Note that this expression no longer requires the modeling of the sub-grid scale turbulence intensity, u'_Δ. However, a constant fractal dimension would correspond to a uniform wrinkling factor over the flow field which is generally not verified. In fact, Eq. (5.3) with space and time dependent dynamic β values is more general than a usual fractal model and the saturated form of Eq. (5.2) as this equation is easily recast as:

$$\Xi_\Delta = \left(\frac{\Delta}{\delta_c}\right)^{\beta'} \tag{5.4}$$

with

$$\beta' = \beta \frac{\log\left(1 + \min\left[\frac{\Delta}{\delta_c} - 1, \Gamma_\Delta\left(\frac{\Delta}{\delta_L^0}, \frac{u'_\Delta}{S_L}, Re_\Delta\right)\frac{u'_\Delta}{S_L}\right]\right)}{\log\left(\frac{\Delta}{\delta_c}\right)} \tag{5.5}$$

The thickened flame model is retained in this work that focuses on the dynamic determination of the flame wrinkling factor Ξ_Δ. This wrinkling factor enters also other models such as algebraic flame surface density (Boger et al. 1998) or F-TACLES (Fiorina et al. 2010). All these models will provide similar results at least as long as the flamelet assumption holds, as confirmed in practice.

5.2.2 Dynamic formulation

The exponent β of the power law model given by Eq. (5.3) can be estimated dynamically following a Germano-like procedure. The principle is to compare the progress variable source term computed from test-filtered variables and the test filtered progress variable source term (Charlette et al. 2002b; Wang et al. 2011). The procedure may also be applied in terms of flame surfaces (Wang et al. 2012; Veynante et al. 2012; Veynante and Moureau 2015; Schmitt et al. 2015), writing the filtered progress variable reaction rate as (Veynante and Vervisch 2002):

$$\overline{\dot{\omega}}_c = \rho_u S_L \Sigma \tag{5.6}$$

where ρ_u is the fresh gas density, S_L the laminar flame speed and $\Sigma = \overline{|\nabla c|} = \Xi_\Delta |\nabla \overline{c}|$ the flame surface density, i.e the available flame surface area per unit volume, and c a progress variable increasing from $c = 0$ in fresh gases to $c = 1$ in burnt gases. This last technique, which correctly predicts unity-wrinkling factors ($\Xi_\Delta = 1$ and $\beta = 0$) for mono-dimensional laminar flames, is adopted in this study. Then, equating averaged flame surfaces over a given domain $\langle \cdot \rangle$ when computed at filter and test-filter scales gives (Veynante and Moureau 2015):

$$\left\langle \widehat{\Xi_\Delta |\nabla \overline{c}|} \right\rangle = \left\langle \Xi_{\gamma\Delta} \left| \nabla \widehat{\overline{c}} \right| \right\rangle \tag{5.7}$$

where the hat symbol denotes a test-filter operation (filter width $\widehat{\Delta}$). The effective filter width when combining two Gaussian filters of width Δ and $\widehat{\Delta}$ is $\breve{\Delta} = \gamma\Delta$, with $\gamma = [1 + (\widehat{\Delta}/\Delta)^2]^{1/2}$. Quantities $|\nabla \overline{c}|$, $\Xi_\Delta |\nabla \overline{c}|$, $|\nabla \widehat{\overline{c}}|$ and $\Xi_{\gamma\Delta} |\nabla \widehat{\overline{c}}|$ measure resolved and total flame surface densities at filter and test filter scales, respectively. Averaging over all the computational domain provides a spatially uniform model parameter evolving only with time (global formulation). When a small local volume is chosen, the model parameter evolves both with time and space coordinates (local formulation). In this latter case, this operation can be replaced by a Gaussian filtering of size Δ_{avg}, easier to implement when using unstructured meshes and/or a parallel solver (Veynante et al. 2012; Veynante and Moureau 2015).
Combining Eqs (5.3) and (5.7) and assuming that wrinkling factors are uniform over the averaging volume $\langle \cdot \rangle$ gives:

$$\beta = \frac{\log\left(\left\langle \widehat{|\nabla \overline{c}|} \right\rangle / \left\langle \left| \nabla \widehat{\overline{c}} \right| \right\rangle \right)}{\log \gamma} \tag{5.8}$$

Unfortunately, Eq. (5.8) involves unknown unweighted filtered progress variables instead of Favre (or mass-weighted) ones. However, as discussed in Ref. (Veynante and Moureau 2015), the model parameter may be estimated from known filtered progress variable fields as:

$$\beta \approx \frac{\log\left(\left\langle \widehat{|\nabla \overline{c}|} \right\rangle / \left\langle \left| \nabla \widehat{\overline{c}} \right| \right\rangle \right)}{\log \gamma} \tag{5.9}$$

The effective combustion filter size Δ is unknown *a priori*, because thickening a flame as done in the TFLES approach is not strictly equivalent to filtering a flame front following the standard LES definitions. An equivalent TFLES filter width Δ is then estimated by equating maximum progress variable gradients to Gaussian filtered solutions of a mono-dimensional stoichiometric CH_4/air laminar flame. Wang et al. (2011) also introduced a calibration factor for the

same reasons. A good approximation is found to be $\Delta = 1.4\mathcal{F}\delta_L^0$ for thickening factors $\mathcal{F} > 4$. Test, effective test and averaging filter widths may be expressed as a function of the combustion filter size Δ (see Table 5.1).

Symbol	Meaning	Expression
Δ	combustion filter size	$\alpha\mathcal{F}\delta_L^0$
$\widehat{\Delta}$	test filter size	$c_1\Delta$
$\breve{\Delta}$	effective test filter size	$\gamma\Delta$
Δ_{avg}	average filter size	$c_2\Delta$

Table 5.1: *Table of model parameters. α, γ, c_1 and c_2 are imposed coefficients.*

5.3 Numerical set-up

AVBP developed at CERFACS and IFPEN is a parallel CFD code that solves explicitly the three-dimensional compressible Navier-Stokes equations on unstructured and hybrid meshes (Schonfeld and Rudgyard 1999). This solver specially designed to simulate unsteady reacting flows is used in this study to reproduce the F3 methane/air jet flame investigated experimentally by Chen et al. (1996). This configuration corresponds to a Reynolds number of about $23,000$ and is characterized by a bulk velocity and a centerline turbulent kinetic energy of $U_0 = 30$ m/s and $k_0 = 3.83$ m^2/s^2, respectively. The injector diameter of the main jet is $d = 12$ mm.
The computational domain is composed by three inlets, one outlet, the duct and outer walls (Fig. 5.1). In the fresh gas inlet, velocity and turbulence intensity profiles are imposed from experimental data. The inlet turbulence signal is constructed using the Random Flow Generation technique (Van Kalmthout and Veynante 1998; Smirnov et al. 2001), computing the fluctuating velocity components by synthesizing a divergence-free velocity-vector field from the summation of Fourier harmonics. The turbulence integral length scale is set to $d/3 = 4$ mm. The inlet temperature of the main fuel-air jet is specified as 298 K. A secondary flow of burnt gases, assumed to be issued from a complete combustion and composed of nitrogen, water and carbon dioxide, is injected through a perforated plate of outer diameter 68 mm surrounding the jet nozzle. In our simulations, the pilot flame bulk velocity is set to 1.5 m/s, estimated by conservation of the total mass flow rate (Herrmann 2006), and the gas temperature is set to 1810 K, assuming about 20% of heat losses in the pilot flame due to

the water cooling at the burner surface (Lindstedt and Vaos 2006; Pitsch and De Lageneste 2002; De and Acharya 2009). The ambient air co-flow is specified to an inlet velocity of 0.22 m/s to mimic the air entrainment with a temperature of 298 K. Adiabatic and no-slip conditions were imposed in the pipe walls while the lateral boundaries far-away from the flame are set as slip walls. A constant pressure condition is specified for the outlet.

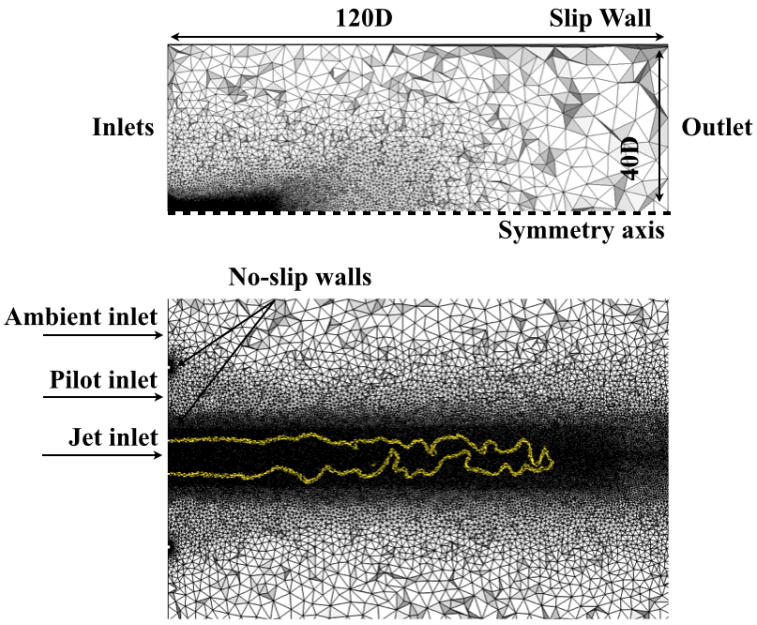

Figure 5.1: *Longitudinal half-section of the cylindrical numerical domain (top) and zoom on the mesh (bottom). Isolines of equivalence ratio* $\phi = 0.5$ *and* $\phi = 0.8$ *are superimposed.*

The computational domain extends to $120d$ downstream, $0.07d$ upstream of the nozzle and $40d$ in the radial direction. The mesh contains 8.5M cells/1.5M nodes approximately and the typical cell size of the reacting zone is $\Delta_x \approx 0.4$ mm.

The third-order finite element TTCG scheme (Colin and Rudgyard 2000) is used. Boundary conditions are prescribed using the Navier-Stokes Characteristic Boundary Conditions (NSCBC) (Poinsot and Lele 1992). The filtered Smagorinsky turbulence model closes the unresolved shear stress tensor (Ducros et al. 1996). This model has been chosen to allow direct comparisons with Wang et al. (2011) but in the future a dynamic model will also be used for sub-grid scale transport.

The Gaussian filtering operation is based on a truncation of the moments of

the filter:

$$\widehat{\widetilde{\phi}}(\mathbf{x}) \approx \widetilde{\phi}(\mathbf{x}) + \frac{\widehat{\Delta}^2}{24}\frac{\partial^2 \widetilde{\phi}(\mathbf{x})}{\partial x_i^2} \tag{5.10}$$

This diffusion-like equation is computed explicitly using a series of sub-steps in order to alleviate the pseudo Fourier condition (Moureau et al. 2011) and is very convenient for unstructured meshes. According to Eq. (5.9), the model parameter is defined only when the gradient of the test-filtered progress variable, $\nabla\widehat{\widetilde{c}}$, is non-zero. In practice, β is estimated from Eq. (5.9) when $0.01 \leq \widehat{\widetilde{c}} \leq 0.99$ and sets to $\beta = 0$ ($\Xi_\Delta = 1$) elsewhere. These threshold values have no sensible influence on results as reaction rates are negligible outside this range.
A two-step reduced chemical mechanism for the methane oxidation including six major species (CH_4, O_2, H_2O, CO_2, CO, $N2$) is considered here (Selle et al. 2004):

$$CH_4 + 1.5O_2 \longrightarrow CO + 2H_2O \tag{5.11}$$
$$CO + 0.5O_2 \longleftrightarrow CO2 \tag{5.12}$$

The corresponding reaction rate expressions are given by:

$$q_1 = A_1 \exp\left(\frac{-E_{a1}}{RT}\right)\left(\frac{\rho Y_{CH_4}}{W_{CH_4}}\right)^{n^1_{CH_4}}\left(\frac{\rho Y_{O_2}}{W_{O_2}}\right)^{n^1_{O2}} \tag{5.13}$$

$$q_2 = A_2 \exp\left(\frac{-E_{a2}}{RT}\right)\left[\left(\frac{\rho Y_{CO}}{W_{CO}}\right)^{n^2_{CO}}\left(\frac{\rho Y_{O_2}}{W_{O_2}}\right)^{n^2_{O2}} - \frac{1}{K_e}\left(\frac{\rho Y_{CO_2}}{W_{CO_2}}\right)^{n^2_{CO_2}}\right] \tag{5.14}$$

where pre-exponential factors, activation energies and model exponents are summarized in Table 6.2. K_e is the equilibrium constant for the second reaction.

Reaction	Coefficients	A_n	E_{an}
1	$n^1_{CH_4} = 0.9$ $n^1_{O_2} = 1.1$	$2.0\,10^{15}$	$3.5\,10^4$
2	$n^2_{CO} = 1.0$ $n^2_{O_2} = 0.5$ $n^2_{CO_2} = 1.0$	$2.0\,10^9$	$1.2\,10^4$

Table 5.2: *Two-step reduced chemical mechanism for $CH_4 - Air$. Coefficients for the Arrhenius formulation (Selle et al. 2004). Activation energies are in cal/mol and pre-exponential constants in cgs units.*

5.4 Data processing

In Section 5.5, numerical simulations will be analyzed in terms of velocity and species mass fractions statistics, resolved and total flame surfaces and model parameter distributions. Corresponding quantities of interest are now defined and summarized in Table 5.3.

5.4.1 Velocity and mass fraction statistics

Large eddy simulations give access to local instantaneous mass-weighted filtered quantities $\widetilde{Q}$. They can be directly averaged over time, leading to "quasi-Reynolds" averages:

$$\left[\widetilde{Q}\right](\mathbf{x}) = \frac{1}{T}\int_0^T \widetilde{Q}(\mathbf{x},t)\mathrm{d}t \tag{5.15}$$

where T is the averaging period and $\mathbf{x}$ the spatial location. One can use also a mass-weighted Favre average defined as:

$$\left\{\widetilde{Q}\right\}(\mathbf{x}) = \frac{\left[\overline{\rho}\widetilde{Q}\right](\mathbf{x})}{[\overline{\rho}](\mathbf{x})} = \frac{\int_0^T \overline{\rho}(\mathbf{x},t)\widetilde{Q}(\mathbf{x},t)\mathrm{d}t}{\int_0^T \overline{\rho}(\mathbf{x},t)\mathrm{d}t} \tag{5.16}$$

which seems more appropriate when dealing with variable density flows. Veynante and Knikker (2006) showed that $\{\widetilde{Q}\}$ provides a good estimation of the local mass-weighted average $\{Q\}$, as long as mean flow length scales are larger than the filter size Δ. On the other hand, a simple average $[\widetilde{Q}]$ (Eq. 5.15) corresponds neither to Reynolds nor Favre averages, at least in the approximation of infinitely thin flame front. However, most works performing LES in variable density flows use the quasi-Reynolds definition because $[\widetilde{Q}]$ is closer to $[Q]$ than $\{\widetilde{Q}\}$.
Time averaged statistics are performed here over about 30 ms physical time once the statistically steady-state regime is established. This time corresponds to 6 convective times $\tau_c = L_f/U_0$, where $L_f \approx 0.15$ m is the flame length and U_0 the inlet bulk velocity.

5.4.2 Flame surface statistics

The time evolution of resolved (S_r) and total (S_t) flame surfaces over all the computational domain $\mathcal{V}$ provides information on the flame dynamics and are estimated here as (Veynante and Vervisch 2002):

$$S_r(t) = \int_{\mathcal{V}} |\nabla\widetilde{c}|\, d\mathcal{V} \tag{5.17}$$

$$S_t(t) = \int_{\mathcal{V}} \Xi_\Delta \left|\nabla \widetilde{c}\right| d\mathcal{V} \tag{5.18}$$

The evolution of the mean resolved and total flames as a function of the downstream $x-$coordinate are expressed as:

$$S_r^s(x) = \int_{S(x)} \left[\left|\nabla \widetilde{c}\right|\right] dS \tag{5.19}$$

$$S_t^s(x) = \int_{S(x)} \left[\Xi_\Delta \left|\nabla \widetilde{c}\right|\right] dS \tag{5.20}$$

where $S(x)$ denotes the plane normal to the downstream axis at the x location and [.] a time average operator.

5.4.3 Model parameter statistics

Behaviors of local model parameters are characterized in terms of mean temporal and downstream evolutions. The time evolution of the mean parameter over the flame volume is defined as:

$$\overline{\beta}(t) = \frac{\int_{\mathcal{V}_f} \beta(x,y,z,t) d\mathcal{V}}{\int_{\mathcal{V}_f} d\mathcal{V}} \tag{5.21}$$

where $\mathcal{V}_f$ denotes the flame volume defined as the volume where $\varepsilon \leq \widetilde{c} \leq 1-\varepsilon$, with $\varepsilon = 0.05$. The corresponding rms is given by:

$$\beta'(t) = \sqrt{\overline{\beta^2}(t) - \left(\overline{\beta}(t)\right)^2} \tag{5.22}$$

The downstream evolution of the mean parameter, conditioned on the flame surface, is defined as:

$$\beta_{avg}^s(x) = \frac{\int_{S(x)} \left[\beta(x,y,z,t) \left|\nabla \widetilde{c}\right|\right] dS}{\int_{S(x)} \left[\left|\nabla \widetilde{c}\right|\right] dS} \tag{5.23}$$

and the corresponding rms by:

$$\beta_{rms}^s(x) = \sqrt{\frac{\int_{S(x)} \left[\left(\beta(x,y,z,t)\right)^2 \left|\nabla \widetilde{c}\right|\right] dS}{\int_{S(x)} \left[\left|\nabla \widetilde{c}\right|\right] dS} - \left(\beta_{avg}^s(x)\right)^2} \tag{5.24}$$

Variable	Integration over volume	Integration over time and normal surface
β	$\overline{\beta}(t) = \frac{\int_{\mathcal{V}_f} \beta \, d\mathcal{V}}{\int_{\mathcal{V}_f} d\mathcal{V}}$	$\beta^s_{avg}(x) = \frac{\int_{S(x)} [\beta \, \lvert\nabla \widetilde{c}\rvert] \, dS}{\int_{S(x)} [\lvert\nabla \widetilde{c}\rvert] \, dS}$
	$\beta'(t) = \sqrt{\overline{\beta^2} - \overline{\beta}^2}$	$\beta^s_{rms}(x) = \sqrt{\frac{\int_{S(x)} [\beta^2 \, \lvert\nabla \widetilde{c}\rvert] \, dS}{\int_{S(x)} [\lvert\nabla \widetilde{c}\rvert] \, dS} - \left(\beta^s_{avg}(x)\right)^2}$
Resolved surface	$S_r(t) = \int_{\mathcal{V}} \lvert\nabla \widetilde{c}\rvert \, d\mathcal{V}$	$S^s_r(x) = \int_{S(x)} [\lvert\nabla \widetilde{c}\rvert] \, dS$
Total surface	$S_t(t) = \int_{\mathcal{V}} \Xi_\Delta \lvert\nabla \widetilde{c}\rvert \, d\mathcal{V}$	$S^s_t(x) = \int_{S(x)} [\Xi_\Delta \lvert\nabla \widetilde{c}\rvert] \, dS$

Table 5.3: *Summary of basic definitions.* $[\cdot]$ *denotes a time average operator while* $\mathcal{V}_f$ *corresponds to the flame volume defined as* $\varepsilon \leq \widetilde{c} \leq 1 - \varepsilon$ *(here* $\varepsilon = 0.05$*).* $S(x)$ *is the plane intersecting the downstream direction at the location* x*.*

5.5 Simulation results and discussions

Discussion is organized as follows: first, few observations about the dynamic model and the fractal behavior are drawn. Mean fields are presented in terms of "quasi-Reynolds" and Favre quantities. A mesh refinement is performed to validate numerical results. Then global and local formulations are compared. The parameters of the model, such as filter sizes, inner cut-off length scale and updating frequency are varied to characterize the model behavior. Table 5.4 summarizes the different cases studied.

5.5.1 General comments

Figure 5.2 displays a typical instantaneous field of the progress variable $\widetilde{c} = 0.5$ iso-surface colored by the local model parameter $\beta(\mathbf{x}, t)$. The progress variable $\widetilde{c}$ is computed here from fuel resolved mass fractions and not temperature because hot burnt gases are also injected from the pilot stream. As expected, the model parameter is small in the initial flame region and increases downstream while the flame is progressively wrinkled by turbulence motions, in agreement with previous findings (Schmitt et al. 2015).
Figure 5.3 displays snapshots of the instantaneous LES resolved fields and the corresponding test filtered and average filtered quantities illustrating the dynamic procedure to determine the model parameter. The gradient (Fig. 5.3b) of the progress variable $\widetilde{c}$ (Fig. 5.3a) is filtered twice at the test (Fig. 5.3c) and average (Fig. 5.3e) length scales. The gradient of the filtered progress variable components (Fig. 5.3d) is also filtered (Fig. 5.3f). Then, Eq. (5.9) is applied,

Simulation	Approach	δ_c	$\widehat{\Delta}$	Δ_{avg}
$L^{1.5\Delta}_{3.0\Delta}$ (ref.)	Local	δ^0_L	1.5Δ	3.0Δ
$L^{1.5\Delta}_{6.0\Delta}$	Local	δ^0_L	1.5Δ	6.0Δ
$L^{3.0\Delta}_{3.0\Delta}$	Local	δ^0_L	3.0Δ	3.0Δ
$G^{1.5\Delta}$ (ref.)	Global	δ^0_L	1.5Δ	–
$G^{3.0\Delta}$	Global	δ^0_L	3.0Δ	–
$L_{2\delta^0_L}$	Local	$2\delta^0_L$	1.5Δ	3.0Δ
$G_{2\delta^0_L}$	Global	$2\delta^0_L$	3.0Δ	–

Table 5.4: *Summary of simulated cases. L and G correspond to local and global formulations, respectively. Superscript α_1 and subscript α_2 in $L^{\alpha_1}_{\alpha_2}$ denote test and averaging filter sizes, respectively. The subscript α_3 in L_{α_3} stands for the inner cut-off length scale. The combustion filter size is set to $\Delta = 1.4\mathcal{F}\delta^0_L$, where $\delta^0_L = 0.4$ mm is the thermal flame thickness. The thickening factor is constant and set to $\mathcal{F} = 4$ for all cases.*

obtaining the β-field displayed in Fig. 5.3g.

5.5.2 Fractal behavior

One of the main assumptions of the current model is that the wrinkling factor Ξ_Δ scales as an exponent of the filter width Δ (Eq. 5.3). Resolved flame surfaces at filter (S_r) and test-filter ($\widehat{S}_r$) scales are related through the conservation of the total flame surface, $\Xi_\Delta S_r = \Xi_{\gamma\Delta}\widehat{S}_r$, leading to:

$$\frac{\widehat{S}_r}{S_r} = \frac{\Xi_\Delta}{\Xi_{\gamma\Delta}} = \left(\frac{\gamma\Delta}{\Delta}\right)^{-\beta} = \gamma^{-\beta} \tag{5.25}$$

Accordingly, the normalized filtered surface flame, $\widehat{S}_r/S_r$, is expected to follow a straight line of slope $-\beta$ when displayed as a function of the ratio γ of filter sizes in log-scale as confirmed by Fig. 5.4. The test filter width was varied from Δ to 9Δ. The filtered flame surface $\widehat{S}_r$ was computed in two different ways: *(i)* as the $\hat{\tilde{c}} = 0.5$ iso-surface (Fig 5.5) and *(ii)* from the norm of the filtered progress variable gradient integrated over the total volume, $\widehat{S}_r = \int_\mathcal{V} |\nabla \widehat{\tilde{c}}| d\mathcal{V}$

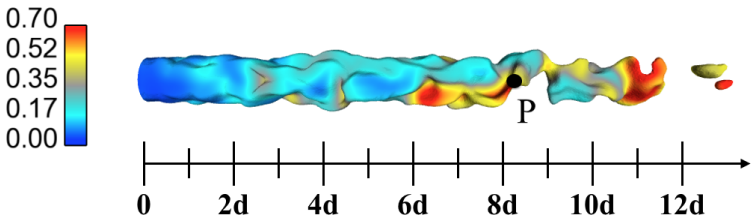

Figure 5.2: *Instantaneous field of the progress variable $\tilde{c} = 0.5$ iso-surface colored by the local model parameter for the F3 turbulent jet flame. Snapshot corresponds to simulation $L^{1.5\Delta}_{3.0\Delta}$. Point P indicates a probe position used later (Fig. 5.18).*

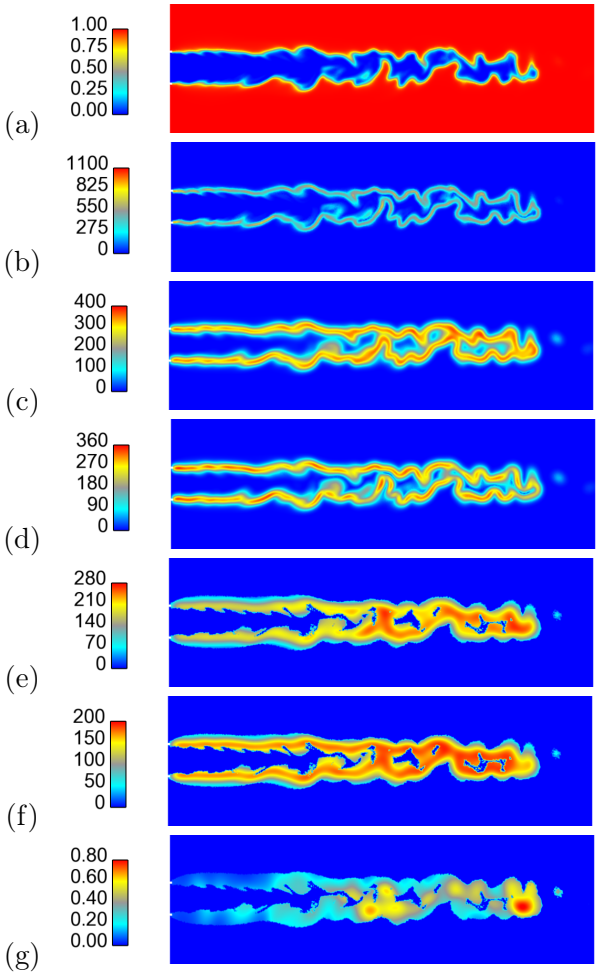

Figure 5.3: *Instantaneous LES resolved fields and corresponding test-filtered quantities for the F3 flame. (a) $\widetilde{c}$; (b) $|\nabla\widetilde{c}|$; (c) $|\widehat{\nabla\widetilde{c}}|$; (d) $|\nabla\widehat{\widetilde{c}}|$; (e) $\langle|\widehat{\nabla\widetilde{c}}|\rangle$; (f) $\langle|\nabla\widehat{\widetilde{c}}|\rangle$; (g) β-field. Snapshots corresponds to simulation $L^{1.5\Delta}_{3.0\Delta}$.*

(dashed line). The latter method is found less sensitive to the test filter size but both definitions give close results at least for small test filter sizes. For larger

test filters, a rapid drop in the flame surface is observed in the iso-surface case due to front interactions: when two flame fronts are present in the test-filtering volume, the $\hat{\tilde{c}} = 0.5$ iso-surface may disappear. This phenomenon is more accentuated at the end of the flame ($8 < x/d < 12$) and can be visualized in Fig. 5.5 as the test filter is increased. The curves generated using the whole domain (Fig. 5.4 left) correspond to the global formulation, while the others take into consideration three different portions of the flame. The scaling of resolved flame surfaces as a function of the filter width (Eq. 5.25) is confirmed disregarding the front interaction problem. The slope of the global curve gives $\beta = 0.35$ while β values of $0.22, 0.37$ and 0.58 are found for the initial, middle and final flame regions respectively, showing a very good agreement between theory and numerical results. Furthermore, the fractal dimension depends also on the space coordinates, evidencing the need of a local formulation. Last but not least, these results show that the model parameter β does not depend on the test filter width, as long as its value remains sufficiently small to avoid flame front interactions. Taking into consideration the geometry of the burner, we recommend here a maximum value for the test filter size of $d/2$, corresponding to $\widehat{\Delta} < 2.7\Delta$. Problems, as already mentioned, may appear for higher values and are discussed later on.

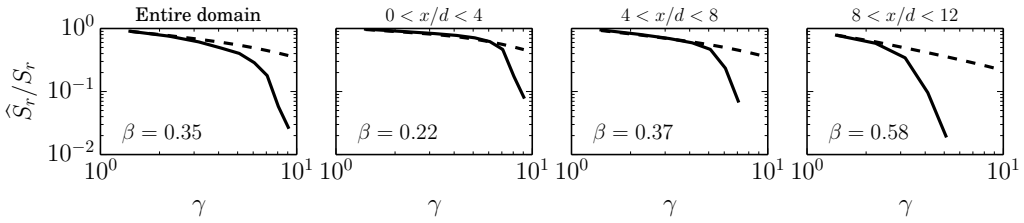

Figure 5.4: *Normalized filtered surface flame as a function of the ratio of test and combustion filter sizes in log-scale. (——) $\widehat{S}_r$ computed using the iso-$\hat{\tilde{c}}$ surface; (- - -) $\widehat{S}_r$ computed using the norm of the filtered progress variable gradient. Results are extracted from the instantaneous resolved field of simulation $L^{1.5\Delta}_{3.0\Delta}$ displayed in Fig. 5.2.*

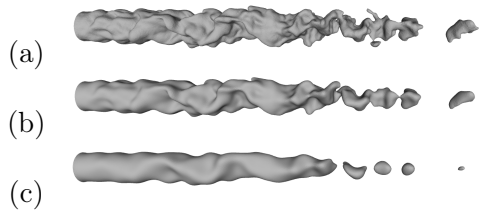

Figure 5.5: *Instantaneous iso-surfaces of the resolved and test-filtered progress variable for the F3 flame. (a) resolved field, (b) $\widehat{\Delta} = 1.5\Delta$, (c) $\widehat{\Delta} = 3\Delta$. Snapshots extracted from simulation $L^{1.5\Delta}_{3.0\Delta}$.*

5.5.3 Mean flow statistics

Mean axial velocity and species mass fractions transverse profiles are compared to experimental data (Chen et al. 1996) in Fig. 5.6 for case $L^{1.5\Delta}_{3.0\Delta}$ (local formulation). Both quasi-Reynolds and Favre averages (see definitions in Section 5.4.1) are extracted from the simulation. Overall quasi-Reynolds statistics are in very good agreement with experimental data that were not mass-weighted. Discrepancies are observed for CO mass fractions, especially for $x/d = 4.5$, but might be due at least in part to experimental uncertainties, estimated to be about 20 to 25% (Chen et al. 1996), and to the simple two-step chemical scheme retained here. However, the unpredicted large values of CO mass fractions observed around $r/d = 1$ for the two first locations ($x/d = 2.5$ and 4.5) come probably from the pilot flame jet, assumed in the simulations to be issued from a complete combustion, without CO.
Note that unweighted $[\widetilde{u}]$ and mass-weighted $\{\widetilde{u}\}$ mean downstream velocity profiles are practically indistinguishable. This finding is in agreement with results presented by Kamal et al. (2015). They compared particle image velocimetry (PIV) and laser Doppler anemometry (LDA) data to discuss differences between Favre-averaged and Reynolds-averaged velocity statistics in a turbulent burner. In the following only unweighted quasi-Reynolds statistics will be displayed.
A mesh convergence was also performed for simulation $L^{1.5\Delta}_{3.0\Delta}$ with a grid containing 110M cells/18.5M nodes approximately with a typical cell size in the reacting zone of $\Delta_x \approx 0.2$ mm. All simulation parameters were kept constant in order to solve exactly the same equations but on a more refined grid to assess that results are controlled by models and not by numerics. In a recent paper, Tirunagari and Pope (2016) referred similar tests as *numerically-accurate solutions*. For instance, the thickening factor was kept $\mathcal{F} = 4$ and the Smagorinsky parameter of the turbulent model was multiplied by two to take into consideration the mesh refinement by a factor 2. For the fine mesh only 3 convective times were simulated to save computational cost. Results are shown in Fig. 5.7 and are very similar and close to experimental data, validating the results obtained with the coarse mesh. A second test would be to divide the thickening factor by two ($\mathcal{F} = 2$) to assess the convergence of the model to DNS. Such a test has not been performed due to a lack of computational resources to get reliable statistics but, by construction, the thickened flame model tends towards DNS when $\mathcal{F}$ goes to unity.

5.5.4 Comparison of global and local formalism

Mean axial velocity, species mass fractions and temperature, as well as corresponding resolved root mean squares (rms), transverse profiles obtained with global ($G^{1.5\Delta}$ case) and local ($L^{1.5\Delta}_{3.0\Delta}$) formulations are compared to experimental data (Chen et al. 1996) in Fig. 5.8 at four different locations $x = 4.5d, 6.5d,$

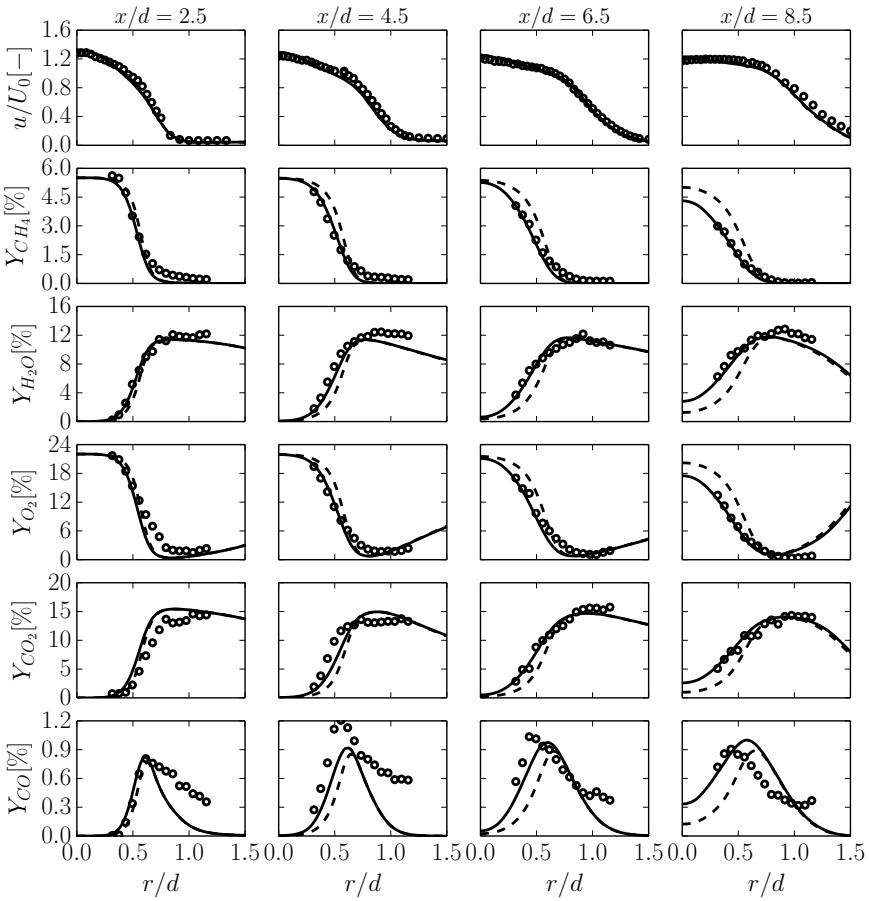

Figure 5.6: *Quasi-Reynolds and Favre average profiles of the axial velocity and species mass fractions for four downstream locations.* (**o**) *Experimental data (Chen et al. 1996); Numerical results from case* $L_{3.0\Delta}^{1.5\Delta}$: (——) $\left[\widetilde{Q}\right]$; (- - -) $\left\{\widetilde{Q}\right\}$.

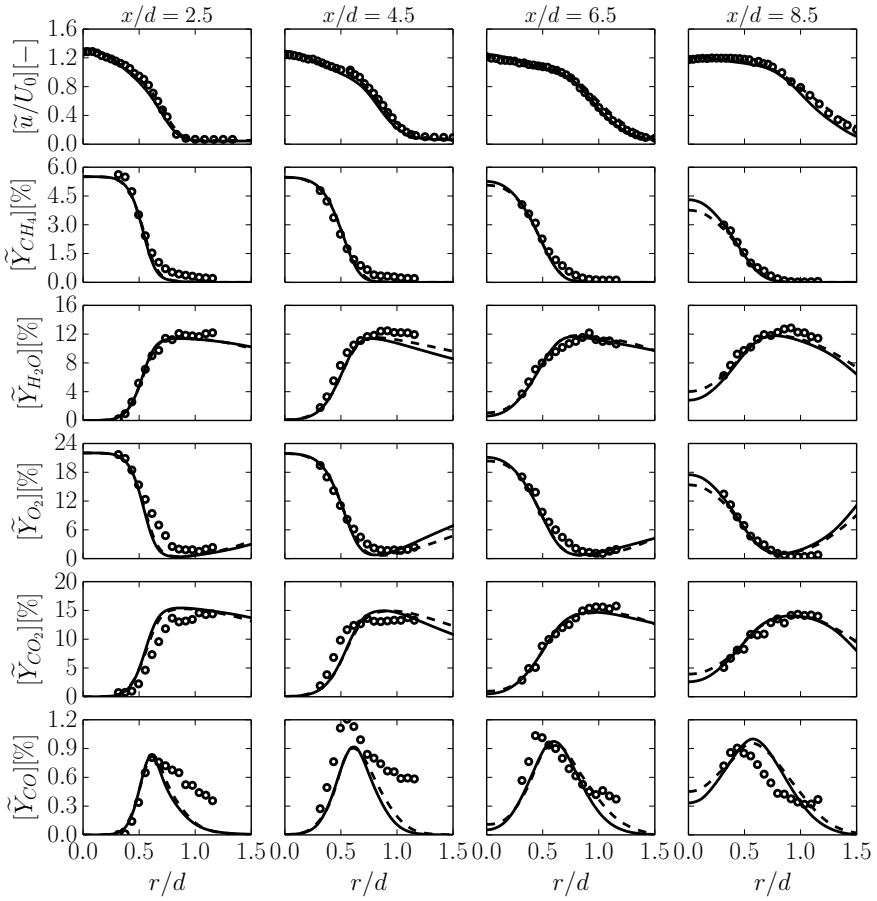

Figure 5.7: *Transverse profiles of mean axial velocity and species mass fractions for four downstream locations obtained with the coarse and fine meshes. (**o**) Experiments (Chen et al. 1996); (——) $L_{3.0\Delta}^{1.5\Delta}$ with coarse mesh; (- - -) $L_{3.0\Delta}^{1.5\Delta}$ with fine mesh.*

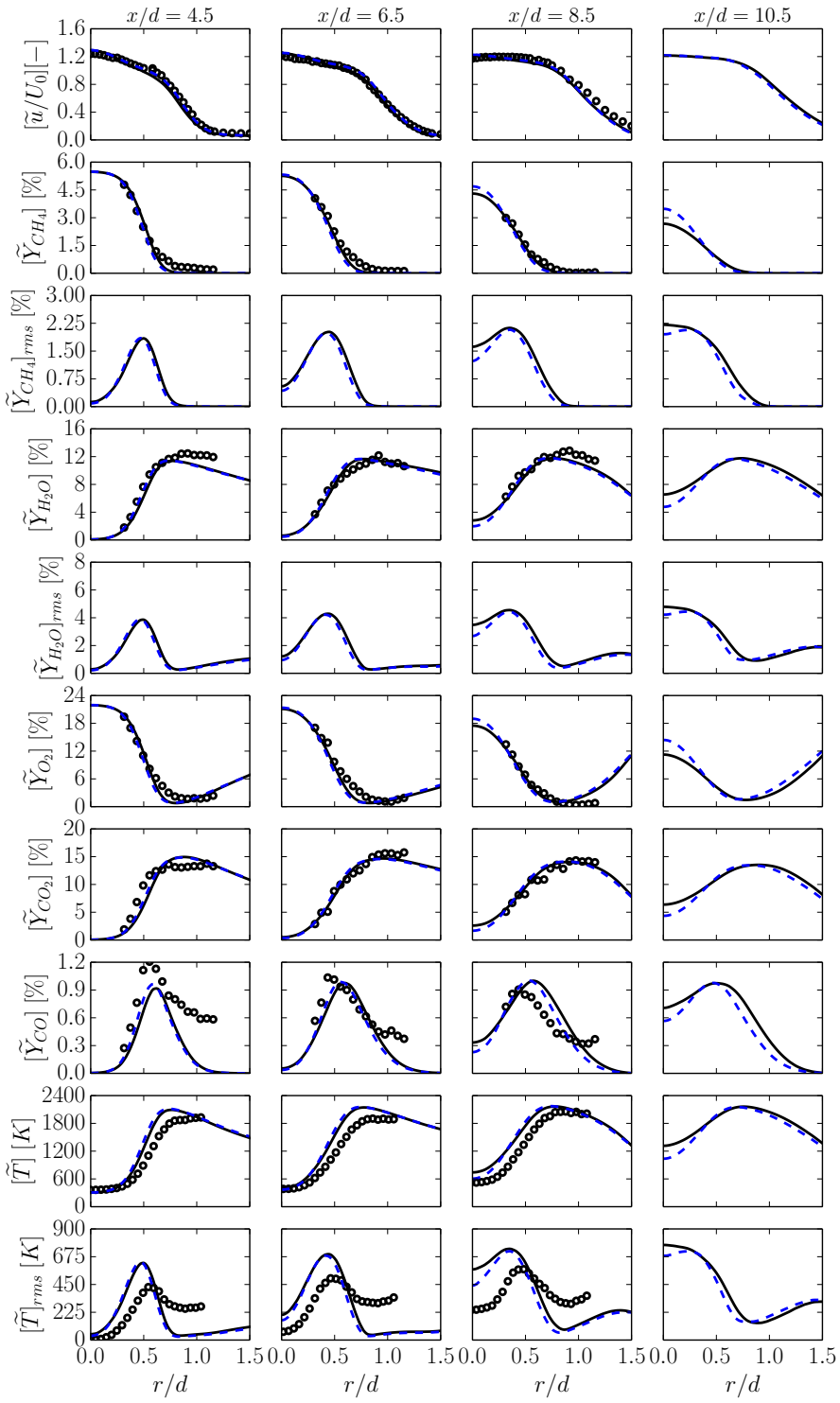

Figure 5.8: *Comparisons between local and global approaches. Transverse profiles of mean axial velocity, species mass fractions and temperature, as well as corresponding resolved rms, are displayed for four downstream locations. (**o**) Experiments (Chen et al. 1996); (——) $L^{1.5\Delta}_{3.0\Delta}$; (- - -) $G^{1.5\Delta}$.*

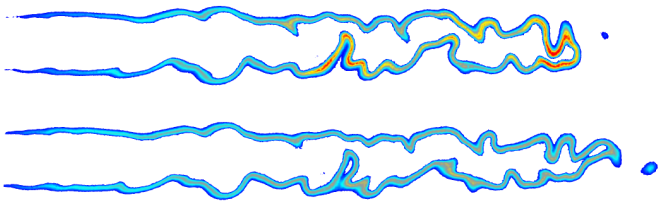

Figure 5.9: *Instantaneous snapshots of the heat release field when using a local ($L^{1.5\Delta}_{3.0\Delta}$, top) and a global ($G^{1.5\Delta}$, bottom) dynamic approach. The red color indicates the maximum heat release observed when using the local model parameter, while blue corresponds to 1% of this maximum value.*

$8.5d$ and $10.5d$. Overall results are in very good agreement with experiments. The influence of the model formulation is observed only at the very end of the flame ($x/d = 10.5$) where, unfortunately, no experimental data are available. These finding are in agreement with previous results using the F-TACLES model (Schmitt et al. 2015). Note that only the contribution due to the resolved motions is included in rms estimations, explaining the reduced influence of the model formulation, while Figs 6.3 and 5.14 below suggest that the local formalism will increase sub-grid scale contributions.
Figure 6.3 compares heat release field snapshots, for both simulations. In the global case, the wrinkling factor Ξ_Δ depends only on time and the heat release has almost the same shape over all the flame. On the other hand, in the local case, the heat release is clearly increased in regions where the flame is more wrinkled. This finding explains the flame length dependence to the model formalism, affecting the mean profiles displayed in Fig. 5.8.

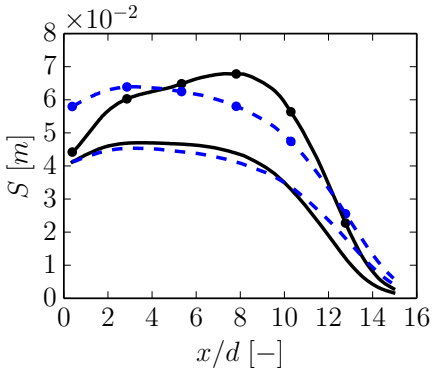

Figure 5.10: *Spatial evolution of resolved ($S_r(x)$, no symbols) and total ($S_t(x)$, symbols) flame surfaces for local (——, case $L^{1.5\Delta}_{3.0\Delta}$) and global (- - -, case $G^{1.5\Delta}$) formalisms.*

The spatial evolutions of mean resolved, $S^s_r(x)$ (Eq. 5.19), and total, $S^s_t(x)$ (Eq. 5.17), flame surfaces per unit of length are displayed in Fig. 5.10 (see also

Table 5.3). As expected, total and resolved flame surfaces are identical near the injection with the local formulation, showing the progressive wrinkling of the flame as convected downstream. The global approach predicts a faster (slower) combustion at the initial (final) part of the flame when compared to the local one. However, even if differences exist between both formulations, mean profiles are modified only at the end of the flame (Fig. 5.8), the local formulation predicting a slightly shorter flame.
Figure 5.11 shows temporal evolutions of resolved and total flame surfaces integrated by slices for different downstream locations. The global flame structures are similar for both local and global approaches. However, fluctuations are amplified when the local model is used. In other words, the frequency of flame surface pulsations does not change while the amplitude does. This finding may have strong implications in the prediction of combustion instabilities.

5.5.5 Influence of the filter sizes

Figure 5.12 compares the conditional downstream evolution of mean, $\beta^s_{avg}(x)$ (Eq. 5.23), and rms, $\beta^s_{rms}(x)$ (Eq. 5.24), model parameters varying test and averaging filter widths. The temporal evolution of the mean ($\overline{\beta}(t)$, Eq. 5.21) and rms ($\beta'(t)$, Eq. 5.22) model parameter over the flame volume is plotted in Fig. 5.13 for the same cases. On the other hand, for the global model, the parameter evolves slightly around $\beta = 0.25$ for case $G^{1.5\Delta}$ and $\beta = 0.30$ for case $G^{3\Delta}$ (not shown). These values, corresponding to the mean values found when using the local model, are in agreement with previous findings (Wang et al. 2011).
As already pointed out, the model parameter is small in the initial flame region and increases downstream as the flame is progressively wrinkled by turbulence. This observation is valid for all three simulations where the local model is used (Fig. 5.12). Figure 5.4 showed that the fractal parameter is independent of the test filter size. This is actually confirmed in the first half of the flame ($x/d < 7$), where the spatial evolution of $\beta^s_{avg}(x)$ is similar for simulations $L^{1.5\Delta}_{3.0\Delta}$ and $L^{3.0\Delta}_{3.0\Delta}$ (Fig. 5.12). This behavior is no longer valid for the second half of the flame. This may be explained by interactions of adjacent flame fronts at the test filter scale and the detachment of fresh gas pockets observed in this last region, leading to overestimation of the model coefficient. However, the change in the mean solution field remains marginal because the overestimation of the flame wrinkling factor affects only a negligible amount of burning reactants. In other situations, for example when the ratio Δ/δ_c is large (see Eq. 5.3), resolved flame front interactions may lead to practical difficulties, requiring the implementation of an adapted correction (Mouriaux et al. 2016). The influence of the averaging filter width is noticed only in the RMS evolution: β_{rms} values are slightly smaller for larger averaging filter sizes, as expected. Thus, the averaging filter size is not a critical parameter, as results of simulations $L^{1.5\Delta}_{3.0\Delta}$ and $L^{1.5\Delta}_{6.0\Delta}$ were found to be practically identical. It is also expected that for

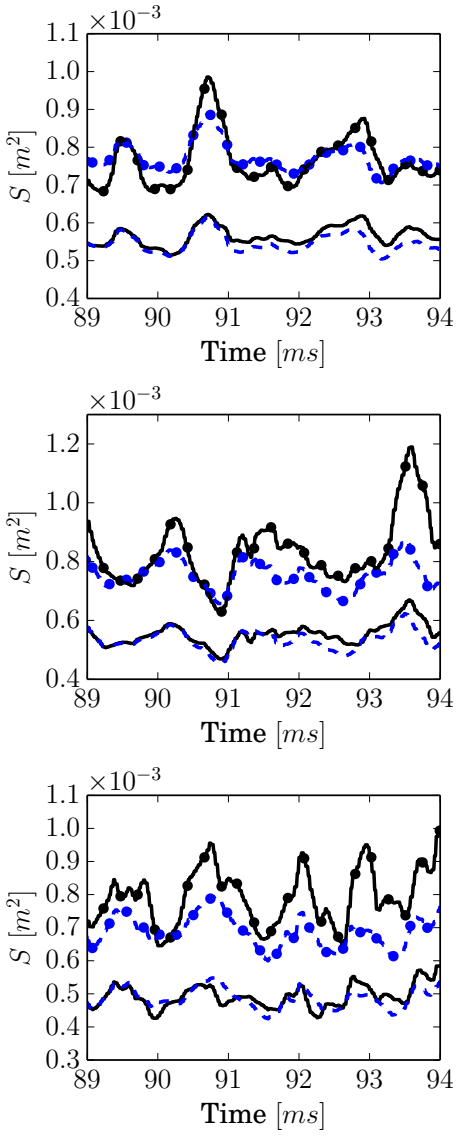

Figure 5.11: *Temporal evolution of the resolved ($S_r(x_0,t)$, no symbols) and total ($S_t(x_0,t)$, symbols) flame surfaces at different locations: $x_0 = 4,5d$ (top); $x_0 = 6,5d$ (middle) and $x_0 = 8,5d$ (bottom). The thickness of the volume slice is 12 mm. (——) $L_{3.0\Delta}^{1.5\Delta}$; (——) $G^{1.5\Delta}$.*

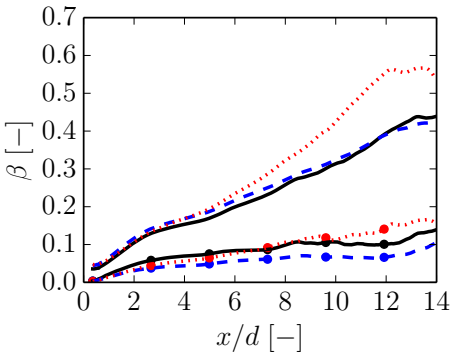

Figure 5.12: *Spatial evolution of $\beta^s_{avg}(x)$ (no symbols) and $\beta^s_{rms}(x)$ (symbols) for simulations varying test and averaging filter widths. (——) $L^{1.5\Delta}_{3.0\Delta}$; (– – –) $L^{1.5\Delta}_{6.0\Delta}$; (···) $L^{3.0\Delta}_{3.0\Delta}$.*

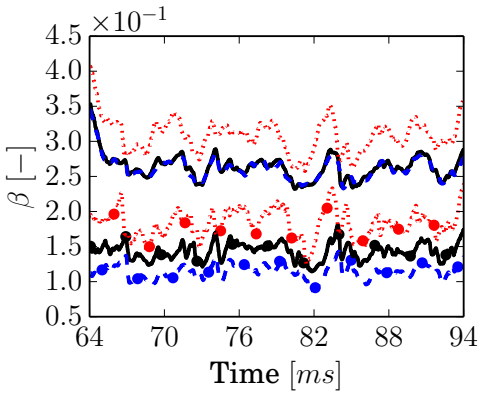

Figure 5.13: *Time evolution of the combustion model parameter integrated over the flame volume $\overline{\beta}(t)$ (no symbols) and $\beta'(t)$ (symbols) for simulations with different filter widths. (——) $L^{1.5\Delta}_{3.0\Delta}$; (– – –) $L^{1.5\Delta}_{6.0\Delta}$; (···) $L^{3.0\Delta}_{3.0\Delta}$.*

$\Delta_{avg} \gg \widehat{\Delta}$, the local formulation behaves like the global one.
The probability density functions of the model parameter β for the three local formulations are displayed in Fig. 5.14 for three different locations. The normalized β-histograms for initial, middle and final flame regions evidence the importance of a local dynamic model. When increasing the test filter width $\widehat{\Delta}$, mean and rms β values become larger specially in the final flame region ($8 < x/d < 12$) where, as already mentioned, gas pockets and flame front interactions are likely to appear. On the other hand, increasing Δ_{avg} decreases the β_{rms}, in agreement with previous observations.
The time evolution of resolved (S_r) and total (S_t) flame surfaces provide information on the flame dynamics and are shown in Fig. 5.15 (see Table 5.3 for definitions). Independently of the model coefficients, the total flame surface is the same, meaning that all the fuel is burnt. Note also that the flame dy-

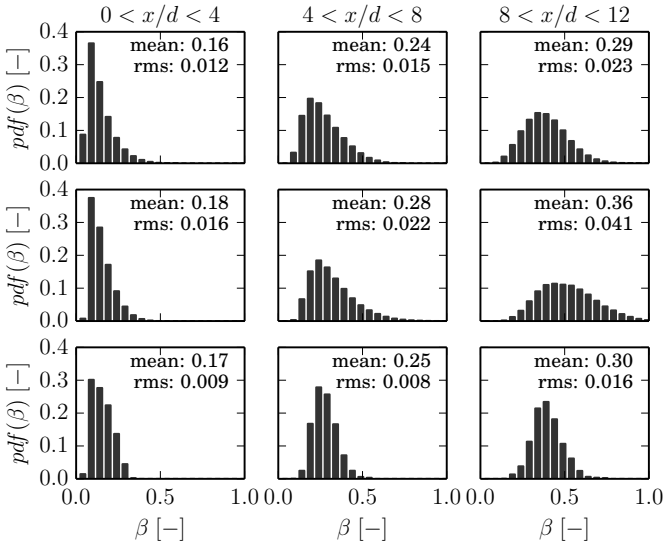

Figure 5.14: *Probability density functions of β parameter extracted from six convective times for cases $L^{1.5\Delta}_{3.0\Delta}$ (top), $L^{3.0\Delta}_{3.0\Delta}$ (middle) and $L^{1.5\Delta}_{6.0\Delta}$ (bottom).*

namics is very similar in all cases. The same conclusion is valid for the global formulation (not shown). As simulation $L^{3.0\Delta}_{3.0\Delta}$ predicts higher local β values, the corresponding resolved flame surface is slightly smaller, but this reduction remains limited (lower than 10%).

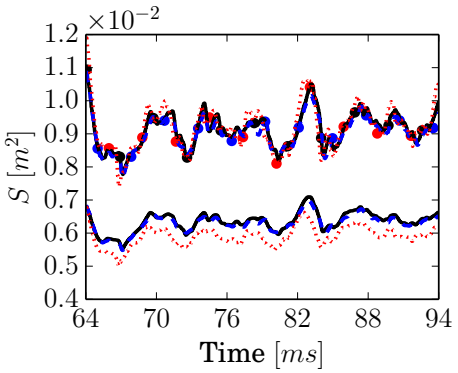

Figure 5.15: *Time evolution of the resolved ($S_r(t)$, no symbols) and total ($S_t(t)$, symbols) flame surfaces over the entire domain for simulations with different filter widths. (——) $L^{1.5\Delta}_{3.0\Delta}$; (- - -) $L^{1.5\Delta}_{6.0\Delta}$; (···) $L^{3.0\Delta}_{3.0\Delta}$.*

5.5.6 Influence of the inner cut-off length scale δ_c

The inner cut-off length scale, δ_c, entering Eq. (5.3) is unknown *a priori*, as being lost during the filtering operation ($\Delta > \delta_c$) and has to be set by the user. There is no unique and well-defined value for δ_c in the literature (see Gülder (1991); Gülder and Smallwood (1995)). For example, Gülder and Smallwood (1995) suggested that the inner cut-off is linked to the Karlovitz number. Note that comparing Eqs (5.2) and (5.3) shows that the Charlette et al. (2002a) model may be viewed, and is derived, as a model for δ_c. Here, the cut-off length scale is assumed constant and its influence on the dynamic procedure is analyzed.

According to Eq. (5.3), to increase δ_c decreases the flame wrinkling factor Ξ_Δ. The sub-grid scale turbulent flame speed $\Xi_\Delta S_L$ is then reduced and the resolved flame becomes more sensitive to resolved turbulence structures. The resolved flame surface is more wrinkled, as confirmed by Fig. 5.16, leading to slightly higher β values, when compared to the reference case $L^{1.5\Delta}_{3.0\Delta}$. However, the increase of resolved flame surface and model parameter does not compensate the decrease in wrinkling factors (Fig. 5.17) and the flame length increases: the simulation $L_{2\delta^0_L}$ burns slower than the reference case (Fig. 5.16). The same observation holds for case $G_{2\delta^0_L}$ (not shown). Despite of the influence of the inner cut-off scale on flame surfaces (Fig. 5.16) and on model parameter (Fig. 5.17), the overall influence on flame statistics remains very limited and visible only at the very end of the flame where experimental data are not available (see supplementary material) proscribing any definitive conclusion. Our experience suggests setting the cut-off scale δ_c between the thermal flame thickness δ^0_L and twice this value, but further works are needed.

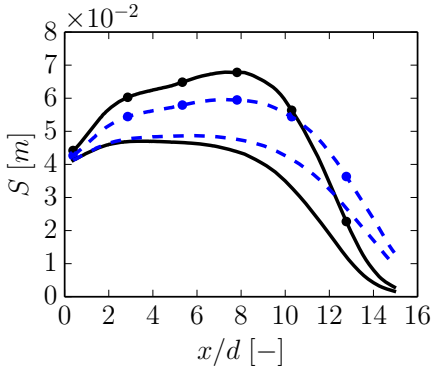

Figure 5.16: *Spatial evolution of resolved ($S_r(x)$, no symbols) and total ($S_t(x)$, symbols) flame surfaces. (——) $L^{1.5\Delta}_{3.0\Delta}$; (- - -) $L_{2\delta^0_L}$.*

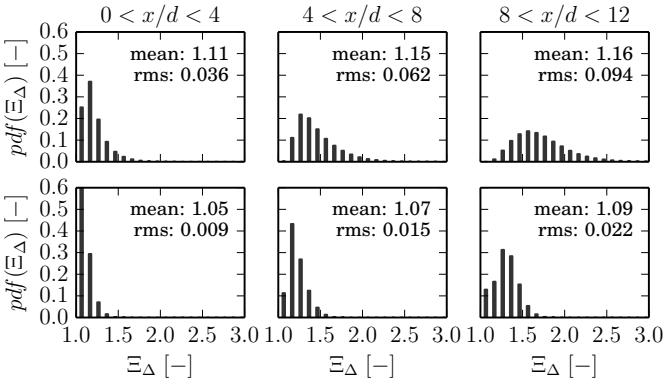

Figure 5.17: *Probability density functions of the sub-grid wrinkling factor* Ξ_Δ *for cases* $L^{1.5\Delta}_{3.0\Delta}$ *(top) and* $L_{2\delta^0_L}$ *(bottom).*

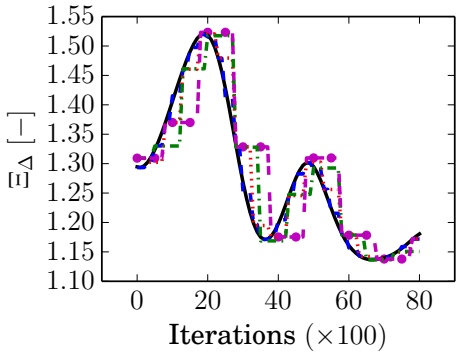

Figure 5.18: *Time evolution of the wrinkling factor* Ξ_Δ *at a point P located in* $(0.102m; 0; 0)$ *(see Fig. 5.2), in terms of the number of iterations for different numbers of time steps n between updates. (——) n = 100; (– – –) n = 250; (···) n = 500; (– · – ·) n = 750; (– ● –) n = 1000.*

5.5.7 Influence of the parameter updating frequency

The dynamic model is obviously computationally more expensive than the regular one, in particular due to the filtering operations. As the code time step is based on the acoustic CFL number and the model parameter is expected to evolve with convection times, the dynamic procedure is not applied every time step. For all computations, the β parameter is updated every $n = 250$ iterations, corresponding to about 30 μs. If $U_0 = 30$ m/s is the characteristic velocity, the distance travelled by a convected fluid particle is lower than 1 mm. The filter sizes being greater than this length, this updating frequency seems acceptable. Actually, a characteristic updating time step based on the ratio of the average filter size and the bulk velocity, a value of $n \approx 1500$ is found. Decreasing the updating time step to $n = 100$ increases the computational time by 17.5%. The determination of the optimum value for this parameter is priceless

to achieve the best CPU performance.
Figure 5.18 displays the time evolution of the wrinkling factor at a given location for different periods between updates and shows that the procedure adapts the value of the local wrinkling factor independently of n. For the cases studied here, the updating frequency does not affect mean flow fields. Additional information can be found as supplementary material.

5.6 Computational costs

Case	Approach	$\widehat{\Delta}$	Δ_{avg}	n	CPU time per iteration [s]	Base 100
Charlette et al. (2002a)	fixed β	–	–	–	1.02	100
$L^{1.5\Delta}_{3.0\Delta}$	local	1.5Δ	3.0Δ	250	1.08	105.9
$L^{1.5\Delta}_{6.0\Delta}$	local	1.5Δ	6.0Δ	250	1.35	132.4
$L^{3.0\Delta}_{3.0\Delta}$	local	3.0Δ	3.0Δ	250	1.18	115.7
$G^{1.5\Delta}$	global	1.5Δ	–	250	1.04	102
$G^{3.0\Delta}$	global	3.0Δ	–	250	1.08	105.9
$L^{1.5\Delta}_{3.0\Delta}$	local	1.5Δ	3.0Δ	100	1.27	124.5

Table 5.5: *Computational costs for each case (see Table 5.4).*

Simulations with the reference mesh were performed on 108 processors on an Altix ICE 8400 LX machine and took about 70 wall clock hours. The simulation with the fine mesh were performed on 8192 cores of an IBM Blue-Gene/Q machine and took about 170 wall clock hours. Computational costs are now compared in Table 5.5. Increasing filter widths increases computational costs by up to 32% compared to the usual non-dynamic model, because of the filtering procedure. For this reason, test and average filter sizes should be kept as small as possible. The only limitation is to ensure that the resolved flame wrinkling at the test filter level is well captured. Obviously, the parameter updating frequency has a significant impact on the CPU cost as well, confirming the importance of this parameter in the code efficiency. The computational cost of the global and local approaches are quite similar (the global version is only 4% faster) but the overall performance of the local procedure justifies its use.
Finally, comparing the reference simulation $L^{1.5\Delta}_{3.0\Delta}$ to the case with the usual

Charlette et al. (2002a)'s model with a fixed parameter, the dynamic formulation is only 5.9% more expensive, a very acceptable value.

5.7 Conclusion

The dynamic determination of the flame wrinkling factor Ξ_Δ for turbulent premixed combustion is investigated in the framework of the thickened flame model (TFLES). Two formulations are compared. In the first one, the model parameter is assumed to be spatially uniform evolving only with time (global formulation) while in the second formulation, the parameter evolves both in space and time (local formulation). In both cases the model parameter is determined by solving a Germano-like equation in terms of the progress variable gradients. Both local and global dynamic models were tested in large eddy simulations of the F3 turbulent premixed Bunsen flame studied experimentally by Chen et al. (1996).

Analyzes using the local dynamic model show that the wrinkling factor has a small value near the injector where the flame is quasi-laminar, and increases downstream where the flame is progressively wrinkled by turbulent motions. Unfortunately, the available experimental mean velocity and mass fraction profiles appear as insufficiently discriminating to assess model performances and all provide very similar mean flow characteristics, even if the flame is slightly shorter when computed with a local model parameter. Refined experimental data characterizing flame dynamics are mandatory to go further in the model validation.

An effort was also made to characterize the influence of physical and numerical inputs of the model. Results were discussed in terms of mean flow fields as well as dynamical behavior. Test filter widths, for instance, should be large enough to capture the resolved flame front wrinkles and small enough to avoid interactions of adjacent flame fronts at the test filter scale and save computational cost. Therefore, we recommend setting test and averaging filter sizes widths about $1.5 - 2\Delta$ in our configuration. An input that may influence the mean field is the inner cut-off length scale δ_c. Some authors suppose δ_c proportional to the laminar flame thickness, but this assumption is probably too rough. On the other hand, a refined model for this physical parameter would introduce other characteristics, such as the sub-grid scale turbulence intensity, requiring additional modeling.

The local dynamic model appears as very robust and no specific difficulties were encountered either in terms of implementation nor use. Future works intend to assess dynamic model performances in more complex configurations representative of industrial and practical systems. To compare the dynamic estimation of the wrinkling factor Ξ_Δ to solving a balance equation for the flame surface density (Hawkes and Cant 2000; Richard et al. 2007) or the wrinkling factor (Weller et al. 1998), both able to handle off-equilibrium situations, would

be of interest. A first attempt (Mouriaux et al. 2016) gives an advantage to the dynamic procedure (closures of balance equations introduce additional parameters) but this procedure will require an adapted sub-model for the initial flame kernel, to be developed, when investigating internal combustion engines.

5.8 Supplementary material

The goal of this section is to show how the input parameters of the local dynamic model influence the mean flow variable fields. Figures 5.19, 5.20 and 5.21 analyze the influence of filter widths, inner cut-off length scale and filtering frequency, respectively.

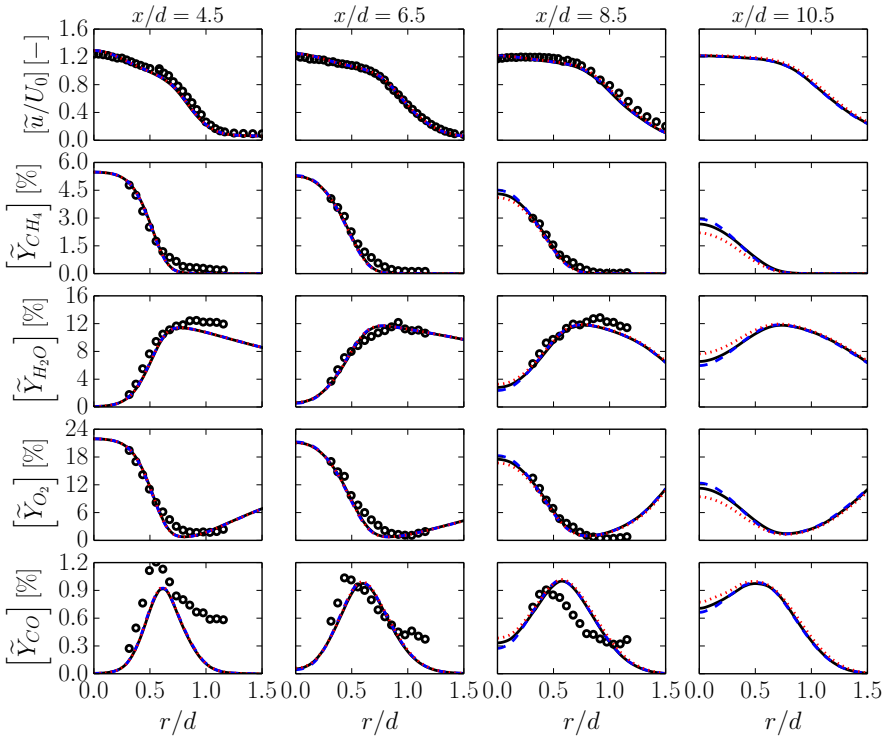

Figure 5.19: *Influence of the filter widths on mean filtered variable transverse profiles for different downstream locations.(**o**) Experiments (Chen et al. 1996); (——) $L_{3.0\Delta}^{1.5\Delta}$; (– – –) $L_{6.0\Delta}^{1.5\Delta}$; (···) $L_{3.0\Delta}^{3.0\Delta}$.*

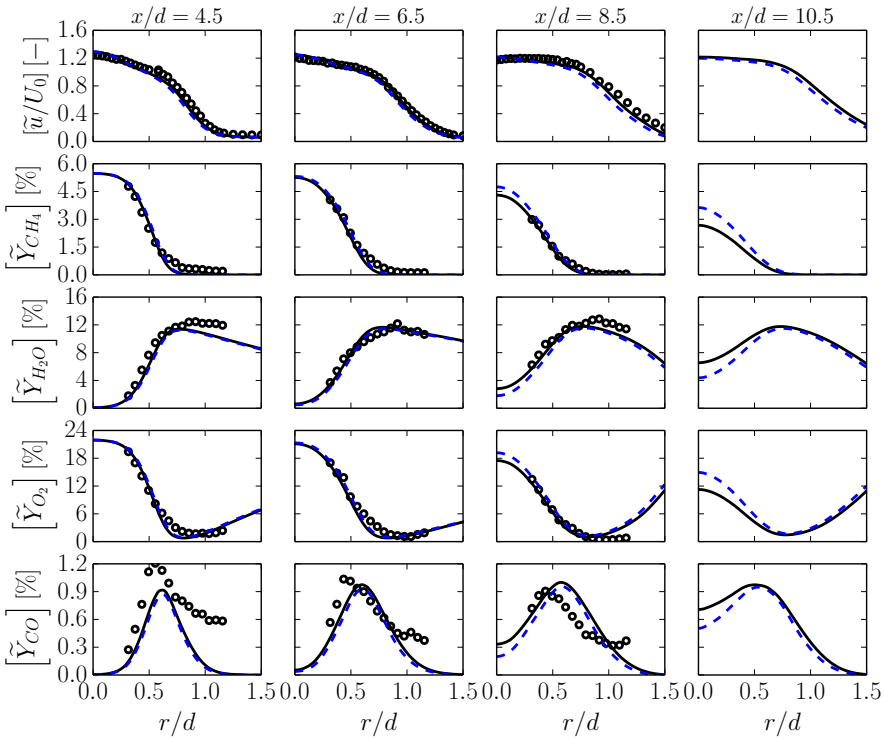

Figure 5.20: *Transverse profiles of the mean filtered variables for different downstream locations. Influence of the inner cut-off length scale.* ***(o)*** *Experiments (Chen et al. 1996);* (———) $L_{3.0\Delta}^{1.5\Delta}$; (- - -) $L_{2\delta_L^0}$.

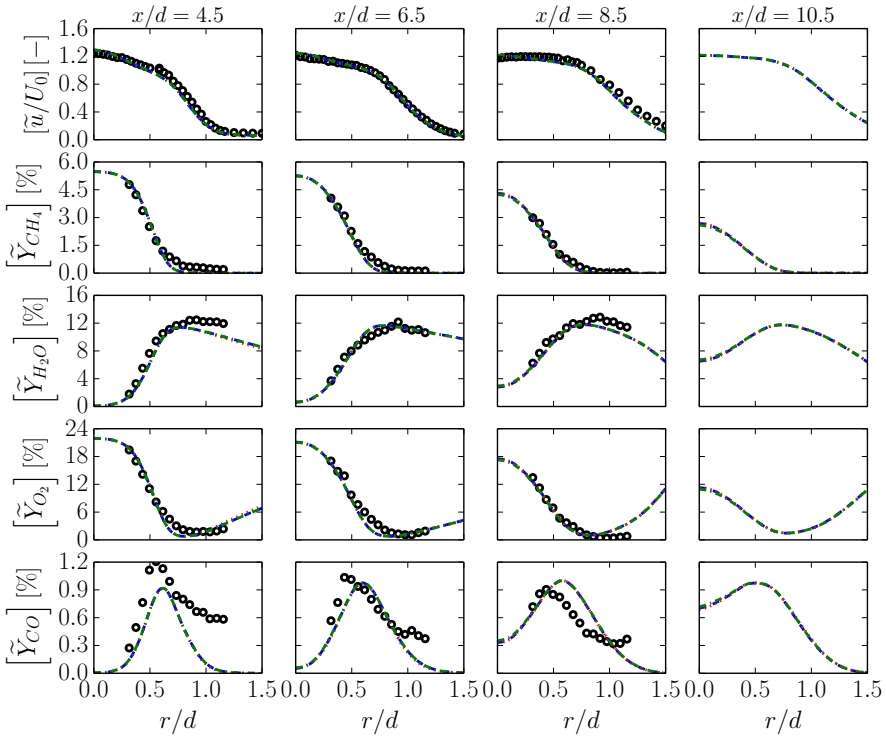

Figure 5.21: *Transverse profiles of the mean filtered variables for different downstream locations. Influence of the parameter updating frequency.* ***(o)*** *Experiments (Chen et al. 1996);* (- - -) $n = 250$; (···) $n = 500$; (-·-) $n = 750$.

Chapter 6

Large eddy simulation of a turbulent swirling premixed flame coupling the TFLES model with a dynamic wrinkling formulation

Dynamic models that take advantage of the known resolved scales to automatically adjust the model parameters have proved to be very effective in large eddy simulations (LES). Global (uniform parameter evolving only with time) and local (parameter evolving both in space and time) dynamic formulations for the flame wrinkling factor are combined with the Thickened Flame (TFLES) model and simulations of the semi-industrial PRECCINSTA burner studied experimentally by Meier et al. (2007) are performed for the stable and unstable configurations. The global formulation predicts a time-dependent model exponent that remains close to 0.5 for the stable flame and oscillates strongly around 0.8 for the pulsating flame. The local formulation adapts the model parameter locally and automatically damps the wrinkling factor in the vicinity of walls, contrary to the global formulation requiring a wall law. The usual non-dynamic approach with an appropriate parameter is found to capture flow statistics of the stable flame with good accuracy, both in terms of Favre and quasi-Reynolds averages. However, the self-excited mode of the pulsating flame is predicted only with the dynamic formalism. The fractal dimension of the unstable flame is found to vary locally and depends on the phase within the period of oscillation. Dynamic models may then play an important role in the prediction of combustion instabilities.

6.1 Introduction

Dynamic models have proved to be a powerful tool in Large Eddy Simulations (LES). The basic idea of such models, developed to describe sub-grid scale momentum transport (Germano et al. 1991), is to take advantage of the known instantaneous resolved large scales to automatically adjust model parameters. The instantaneous resolved field is filtered at a test filter scale larger than the original LES filter. The model is then assumed to hold at both scales and model parameters are solutions of a Germano-like equation.

While dynamic models are now routinely used for momentum transport, their application to reaction rate modeling in combusting flows remains rather scarce and often restricted to simple flow configurations (flame embedded in a homogeneous isotropic turbulent flow (Im et al. 1997; Charlette et al. 2002b; Wang et al. 2012), jet flames (Knudsen and Pitsch 2008; Wang et al. 2011; Schmitt et al. 2015; Volpiani et al. 2016). Few studies treat relatively more complex geometries and realistic burners (Schmitt et al. 2013; Mercier et al. 2015; Ibrahim et al. 2009; Gubba et al. 2011). One main reason explains this situation. Combustion and turbulence behave very differently: most of the turbulence energy is resolved in LES, a way to check simulation quality (Pope 2004), while combustion is mainly a sub-grid scale phenomenon, possibly leading to an ill-posed problem when looking for a linear parameter in a dynamic procedure (Charlette et al. 2002b).

Flame front wrinkling factors, quantifying flame/turbulence interactions in terms of ratio of total to resolved flame surfaces in the filter volume enter directly flame surface density (FSD) (Boger et al. 1998), thickened flame (TFLES) (Colin et al. 2000; Charlette et al. 2002a) and F-TACLES (Fiorina et al. 2010) models. They also may be used to model the sub-grid scale turbulence flame speed in level-set formalism (Pitsch 2006; Knudsen and Pitsch 2008). Charlette et al. (2002b) proposed a global dynamic formulation where the spatially-uniform time-dependent exponent parameter of a fractal wrinkling factor expression is determined automatically.

Wang et al. (2011); Wang et al. (2012) have shown the ability of such a dynamic model to reproduce a statistically steady jet flame (Chen et al. 1996) and the transient ignition of a flame kernel (Renou 1999) under several operating conditions. The TFLES model was used in the first case while the second retained the Boger et al. (1998) algebraic FSD model.

Knikker et al. (2002); Knikker et al. (2004) proposed a Dynamic Flame Surface Density (DFSD) model based on a fractal analysis (Gouldin 1987; Gülder 1991) and on a similarity assumption (Bardina et al. 1980). This model was validated a priori from experimental data and, more recently, tested a posteriori by Ibrahim et al. (2009) and Gubba et al. (2011) to simulate the propagation of a turbulent premixed flame through obstacles in a laboratory scale combustion chamber.

Using the level-set formalism, Knudsen and Pitsch (2008) performed simula-

tions where the parameter of a model expression for the sub-grid scale turbulent flame speed depends on both space coordinates and time. Schmitt et al. (2013); Schmitt et al. (2015) adopted a similar strategy coupling a dynamic fractal wrinkling factor expression with the tabulated chemistry F-TACLES method. They simulated the Tecflam turbulent swirl burner (Schneider et al. 2005; Gregor et al. 2009) and, later, turbulent Bunsen flames Chen, Peters, Schneemann, Wruck, Renz, and Mansour (1996) over three different operating conditions. Volpiani et al. (2016) simulated the F3 jet flame studied by Chen et al. (1996) and investigated the influence of physical and numerical characteristics of a flame wrinkling factor dynamic model for both, global (i.e. spatially-uniform time-dependent) and local (space and time dependent), model parameters. A similar local flame wrinkling factor dynamic formalism, combined with the Boger et al. (1998) model, gives very promising results to predict the development of a flame kernel in an internal combustion engine (Mouriaux et al. 2016), even if an adapted ignition model remains to be developed.
Other authors applied the dynamic formalism to compute variances and scalar dissipation rates of a mixture fraction, that enter non-premixed combustion models (Réveillon and Vervisch 1998; Pierce and Moin 1998; Pierce and Moin 2004; Balarac et al. 2008; Kaul et al. 2013). These procedures can be denoted “indirect approaches", to differ from the previous one that involve directly reaction rate terms.
The goal of this paper is to apply the TFLES combustion model coupled with global and local dynamic procedures in simulations of a realistic burner configuration and to assess the influence of the dynamic model in the prediction of combustion instabilities. The chosen configuration is the PRECCINSTA swirl burner derived from a gas turbine designed by Turbomeca. This configuration has been the subject of many experimental (Meier et al. 2007; Dem et al. 2015) and numerical (Roux et al. 2005; Galpin et al. 2008; Moureau et al. 2007; Moureau et al. 2011; Wang et al. 2014; Wang et al. 2016) studies. Experimental studies using the PRECCINSTA burner evidenced two combustion regimes (Meier et al. 2007): a quiet flame at equivalence ratio $\phi = 0.83$ and a pulsating flame at $\phi = 0.70$. Numerical simulations commonly assume perfect mixing between fuel and air at the combustion chamber inlet because in the experiment methane is injected in the swirler, far upstream of the combustor. However, in the configuration where self-excited combustion oscillations are found, simulations assuming perfect mixing fail to predict the combustion instability (Franzelli et al. 2012).
The paper is organized as follows: basic concepts of the TFLES combustion model are first reviewed. The dynamic procedure is then briefly discussed. Experimental and numerical set-ups are presented. Numerical results are then compared to experiments and discussed for both stable and unstable cases. Conclusions are drawn.

6.2 Modeling

6.2.1 The thickened flame model (TFLES)

Flames are artificially thickened to be resolved on the numerical grid by multiplying diffusion and dividing reaction rates by a thickening factor $\mathcal{F}$ but conserving the laminar flame speed S_L (Butler and O'Rourke 1977; O'Rourke and Bracco 1979). An efficiency function is added to correct the reduction of flame surface induced by the thickening operation (Colin et al. 2000; Charlette et al. 2002a). Charlette et al. (2002a) express this term as a sub-grid scale wrinkling factor, Ξ_Δ that measures the ratio between the total and the resolved flame surface. Thus, the balance equations for filtered species mass fractions $\widetilde{Y}_k$ are written as:

$$\frac{\partial \overline{\rho}\widetilde{Y}_k}{\partial t} + \nabla \cdot (\overline{\rho}\widetilde{\mathbf{u}}\widetilde{Y}_k) = -\nabla \cdot (\Xi_\Delta \mathcal{F} \overline{\rho \mathbf{V}_k} \widetilde{Y}_k) + \frac{\Xi_\Delta}{\mathcal{F}} \dot{\omega}_k(\widetilde{Q}) \tag{6.1}$$

where ρ is the density, $\mathbf{u}$ the velocity vector, $\mathbf{V_k}$ the diffusion velocity of species k, expressed here using the Hirschfelder and Curtiss approximation (Poinsot and Veynante 2011; Hirschfelder et al. 1954) and $\dot{\omega}_k$ the reaction rate of species k, estimated from Arrhenius law. Any quantity $\overline{Q}$ corresponds to the filtering of the Q-field, while $\widetilde{Q} = \overline{\rho Q}/\overline{\rho}$ denotes mass-weighted filtering. Similarly, the balance equation for the filtered total energy $\widetilde{E}$ is written:

$$\begin{aligned} \frac{\partial \overline{\rho}\widetilde{E}}{\partial t} + \nabla \cdot (\overline{\rho}\widetilde{\mathbf{u}}\widetilde{E}) = & - \nabla \cdot \left[\widetilde{\mathbf{u}}\overline{P} - \widetilde{\mathbf{u}}\,\overline{\boldsymbol{\tau}} + \Xi_\Delta \mathcal{F} \left(\overline{\mathbf{q}}_T - \sum_{k=1}^{N} \overline{\rho \mathbf{V}_k} \widetilde{Y}_k \widetilde{h}_{s,k} \right) \right] \\ & + \frac{\Xi_\Delta}{\mathcal{F}} \dot{\omega}_T(\widetilde{Q}) \end{aligned} \tag{6.2}$$

where $\overline{P}$ is the filtered pressure, $\widetilde{h}_{s,k}$ the sensible enthalpy of species k, $\overline{\tau}$ the viscous tensor, $\overline{q}_T$ the thermal flux due to temperature gradients and modeled using a Fourier law and $\dot{\omega}_T$ the heat release rate. Equations (6.1 - 6.2) propagate a flame front of thickness $\mathcal{F}\delta_L^0$ at the sub-grid scale turbulent velocity $S_T = \Xi_\Delta S_L$, where δ_L^0 is the laminar flame thickness.

6.2.2 Dynamic wrinkling model

Charlette et al. (2002a) modeled the wrinkling factor Ξ_Δ by an algebraic expression derived assuming an equilibrium between turbulence motions and flame front wrinkling:

$$\Xi_\Delta = \left(1 + \min \left[\max \left(\frac{\Delta}{\delta_L^0} - 1, 0 \right), \Gamma_\Delta \left(\frac{\Delta}{\delta_L^0}, \frac{u'_\Delta}{S_L}, Re_\Delta \right) \frac{u'_\Delta}{S_L} \right] \right)^\beta \tag{6.3}$$

where the efficiency function Γ_Δ measures the ability of vortices to effectively wrinkle the flame front, u'_Δ and $Re_\Delta = u'_\Delta \Delta/\nu$ are the sub-grid scale turbulence

intensity and Reynolds number, respectively, ν being the fresh gas kinematic viscosity. β is the model parameter to be specified. Note that the (-1) contribution in Eq. (6.3) was introduced later (Wang et al. 2011) to recover Eq. (6.4) below in the limit of large turbulence intensities.
In practice, Eq. (6.3) is often saturated and dominated by Δ/δ_L^0, reducing to (Veynante et al. 2012):

$$\Xi_\Delta = \left(\frac{\Delta}{\delta_L^0}\right)^\beta \tag{6.4}$$

corresponding to a fractal model with a flame surface of fractal dimension $D = \beta + 2$ and an inner cut-off scale sets to the laminar flame thickness δ_L^0 (Gouldin 1987; Gouldin et al. 1989; Gülder and Smallwood 1995). The exponent β is now determined dynamically equating flame surfaces when computed at filtered and test-filtered level (Germano-like identity) (Wang et al. 2012; Veynante et al. 2012; Schmitt et al. 2015; Veynante and Moureau 2015):

$$\left\langle \widehat{\Xi_\Delta \left|\nabla \widetilde{c}\right|} \right\rangle = \left\langle \Xi_{\gamma\Delta} \left|\nabla \widehat{\widetilde{c}}\right| \right\rangle \tag{6.5}$$

where the hat symbol denotes a test-filtering operation. The effective filter size when combining two Gaussian filters of size Δ and $\widehat{\Delta}$, is $\gamma\Delta$, with

$$\gamma = \sqrt{1 + \left(\frac{\widehat{\Delta}}{\Delta}\right)^2} \tag{6.6}$$

Symbol $\langle\cdot\rangle$ denotes an averaging operator (Charlette et al. 2002b) that may be the overall computational volume (*global formulation*) or a small local volume (*local formulation*). For the latter case and following (Veynante et al. 2012; Veynante and Moureau 2015), the averaging operation is here replaced by a Gaussian filter Δ_{avg}, easier to implement on massively parallel solvers with unstructured meshes (Moureau et al. 2011). Combining Eqs (6.4) and (6.5) and assuming that β is constant over the averaging domain $\langle\cdot\rangle$ give:

$$\beta = \frac{\log\left(\left\langle \widehat{\left|\nabla \widetilde{c}\right|} \right\rangle / \left\langle \left|\nabla \widehat{\widetilde{c}}\right| \right\rangle\right)}{\log(\gamma)} \tag{6.7}$$

However, strictly speaking, a thickened flame is not a filtered flame following the standard LES definitions and an equivalent filter size Δ should be specified to enter relations (6.4) and (6.6). As the inner cut-off scale is estimated to

be the laminar flame thickness δ_L^0 in Eq. (6.4), we relate here the outer cut-off scale, Δ, to the resolved flame thickness, i.e. $\Delta = \mathcal{F}\delta_L^0$. Equation (6.4) becomes:

$$\Xi_\Delta = \mathcal{F}^\beta \tag{6.8}$$

Note that Wang et al. (2011), deriving their dynamic model by comparing reaction rates, wrote $\Delta = \alpha\mathcal{F}\delta_L^0$, introducing a calibration factor $\alpha = 2.2$ to recover $\beta = 0$ and $\Xi_\Delta = 1$ for planar laminar flames. Here, the model is derived from flame surfaces and this condition is automatically enforced by Eq. (6.7). In the following, test and averaging filter sizes are constant and equal to 2.0Δ and 2.7Δ respectively. Figures 6.10 and 6.17 discussed later will confirm that results are not sensitive the test filter width. The influence of the averaging filter was not investigated here but its characteristics were chosen according to a previous study Volpiani et al. (2016). Increasing its width mainly reduces model parameter and wrinkling factor variances without affecting the overall results, at least when not too large.

6.2.3 Wall correction for the global formulation

The interaction of turbulence, flame and wall is a complex phenomenon, which is present in the majority of practical industrial systems. The objective of this work is not to develop a model for turbulent flame/wall interactions and a simple wall correction is introduced as a first step in the global saturated dynamic formulation. Walls limit flame wrinkling and act as a sink term for the flame surface density Σ or the wrinkling factor Ξ_Δ (Poinsot and Veynante 2011; Poinsot et al. 1993; Bruneaux et al. 1997). Thus, while the local formulation automatically predicts low wrinkling factors Ξ_Δ near walls because of reduced resolved flame wrinkling, the global formulation, assuming uniform model parameter β and wrinkling factor Ξ_Δ over the computational domain, needs correction. In this latter case, a simple ad hoc damping function is implemented:

$$\Xi_\Delta = \left[1 - \exp\left(\frac{-d_w}{0.5\Delta}\right)\right]\left[\left(\frac{\Delta}{\delta_L^0}\right)^\beta - 1\right] + 1 \tag{6.9}$$

where Δ is the combustion filter size and d_w is the distance to the closest wall. Such an expression affects the wrinkling factor for $d_w < 2\Delta$, but because of the exponential, the influence is initially small: the wrinkling factor is equal to 87% of its initial value for $d_w = \Delta$, then goes to unity at wall. This model is rough and is designed to reduce sub-grid scale flame wrinkles because of mechanical constraints without taking into account explicitly heat losses. Anyway, the importance of this correction is more conceptual (wrinkling factors are not

expected to be large in the vicinity of walls) than practical: its influence on statistics is negligible (not shown for brevity). A refined law-of-the-walls model for combustion compatible with the proposed modeling approach is left for future works.

6.3 The Preccinsta burner

6.3.1 Experimental configuration

The burner configuration investigated by Meier et al. (2007) derives from an industrial gas turbine designed by Turbomeca. This configuration, representative of a realistic combustor, has been widely studied to validate combustion models, reduced chemical mechanisms or numerical methods (Roux et al. 2005; Galpin et al. 2008; Moureau et al. 2007; Moureau et al. 2011; Franzelli et al. 2012; Wang et al. 2014; Wang et al. 2016). The combustor, displayed in Fig. 6.1, comprises four main parts: 1) the plenum, where ambient air is injected through one large hole; 2) the injector, where the air flow is swirled by twelve radial veins and mixed with pure methane injected through the swirler blades; 3) the combustion chamber of dimensions 114 mm × 85 mm × 85 mm equipped with 1.5 mm thick quartz walls to enable optical measurements; 4) the converging tube that connects the combustion chamber to the atmosphere. Three different regimes, summarized in Table 6.1, were studied experimentally. Only cases at equivalence ratio $\phi = 0.70$ (case 1) and $\phi = 0.83$ (case 2a) are addressed herein.

Experimental case	1	2a	2b
Air flow rate (g/min)	734.2	734.2	734.2
CH_4 flow rate (g/min)	30.0	35.9	32.3
Thermal power (kW)	25.1	30.0	27.0
Equivalence ratio (-)	0.70	0.83	0.75
Experimental behavior	Unstable	Stable	Stable
Measurements	LDV+Raman	Raman	LDV

Table 6.1: *Details of the experimental cases.*

Laser Raman scattering measurements are available for concentration of the

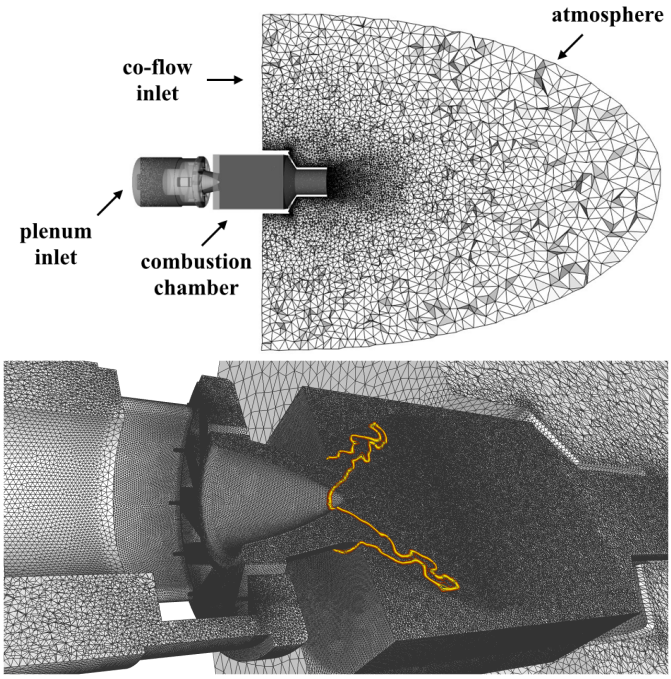

Figure 6.1: *Sketch of the Preccinsta burner and the corresponding computational domain and mesh (top). Bottom: zoom on the combustion chamber.*

major species (CH_4, H_2O, O_2, CO_2, CO, N_2, H_2) and temperature in vertical planes at eight different sections downstream of the injector (h = 6, 10, 15, 20, 30, 40, 60, 80 mm, where h = 0 mm corresponds to the exit plane of the nozzle). The systematic and statistical uncertainties are less than 4% and 2.5% respectively for temperature and less than 5% and 7% respectively for all species except for CO and H_2 for which statistical uncertainty is between 20% and 50%.
Laser Doppler Velocimetry (LDV) measurements of the velocity field were also performed in sections located at five different axial positions (h = 1.5, 5, 15, 25, 35 mm). However, these measurements were carried out at a global equivalence ratio of ϕ = 0.75 (case 2b) and not ϕ = 0.83 (case 2a) unfortunately. Thereby, comparisons between numerical results and experimental data must be accomplished with care.

6.3.2 Numerical setup

Instead of injecting fuel and oxidizer separately, a perfectly methane/air mixture is directly injected in the plenum inlet. This perfect mixing assumption was made because works in the literature showed good agreement at least for the stable regime (Roux et al. 2005; Galpin et al. 2008; Moureau et al. 2007; Moureau et al. 2011; Franzelli et al. 2012).

The AVBP compressible solver developed at CERFACS and IFPEN is employed to run the simulations (Schonfeld and Rudgyard 1999). An overview of the computational domain is illustrated in Fig. 6.1. The plenum and atmospheric inlets were prescribed using the Navier-Stokes Characteristic Boundary conditions (NSCBC) (Poinsot and Lele 1992) to ensure a physical representation of the acoustic wave propagation and reflection. The burner is fed steadily with a mixture of methane and air at an equivalence ratio of 0.83/0.70, and the total mass flow rate is 12.9 g/s at a temperature of 320 K. For the inlet of the atmosphere, a co-flow of N_2 is injected with low velocity (0.5 m/s) at the temperature of the burnt gases to mimic entrainment and avoid any unphysical recombination between burnt and fresh air at the chamber exit. The outer atmosphere boundary is also specified using NSCBC. Adiabatic and no-slip conditions are imposed at walls. These choices were based on the work by Franzelli et al. (2012).
The third-order finite element TTGC scheme (Colin and Rudgyard 2000) is used. Sub-grid stresses are described by the WALE model (Nicoud and Ducros 1999). A two-step reduced chemical mechanism for the methane oxidation is considered (Selle et al. 2004):

$$CH_4 + 1.5O_2 \longrightarrow CO + 2H_2O \tag{6.10}$$
$$CO + 0.5O_2 \longleftrightarrow CO2 \tag{6.11}$$

The corresponding reaction rates are modeled using Arrhenius laws:

$$q_1 = A_1 \exp\left(\frac{-E_{a1}}{RT}\right)\left(\frac{\rho Y_{CH_4}}{W_{CH_4}}\right)^{n^1_{CH_4}}\left(\frac{\rho Y_{O_2}}{W_{O_2}}\right)^{n^1_{O2}} \tag{6.12}$$
$$q_2 = A_2 \exp\left(\frac{-E_{a2}}{RT}\right)\left[\left(\frac{\rho Y_{CO}}{W_{CO}}\right)^{n^2_{CO}}\left(\frac{\rho Y_{O_2}}{W_{O_2}}\right)^{n^2_{O2}} - \frac{1}{K_e}\left(\frac{\rho Y_{CO_2}}{W_{CO_2}}\right)^{n^2_{CO_2}}\right] \tag{6.13}$$

where pre-exponential factors, activation energies and model exponents are summarized on Table 6.2. K_e is the equilibrium constant for the second reaction. The corresponding laminar flame properties are listed in Table 6.3.
The full geometry is meshed as shown in Fig. 6.1. The mesh is unstructured and contains about 21M cells and 3.7M nodes. The typical cell size in the reaction zone is $\Delta_x \approx 0.5$ mm. The thickening factor $\mathcal{F}$ is chosen to resolve the flame front with at least n cells in the simulation, i.e. such as $\mathcal{F}\delta_L^0 \geq n\Delta_x$. Here, according to Table 6.3, Δ_x/δ_L^0 goes from 0.9 ($\phi = 0.70$) to 1.25 ($\phi = 0.83$) while usually $n = 4-5$ with AVBP. The thickening factor is then set to $\mathcal{F} = 5$.

Reaction	Coefficients	A_n	E_{an}
1	$n^1_{CH_4} = 0.9\ n^1_{O_2} = 1.1$	2.0×10^{15}	3.5×10^4
2	$n^2_{CO} = 1.0\ n^2_{O_2} = 0.5\ n^2_{CO_2} = 1.0$	2.0×10^9	1.2×10^4

Table 6.2: *Two-step reduced chemical mechanism for $CH_4 - Air$. Coefficients for reaction rates (Selle et al. 2004). Activation energies are in cal/mol and pre-exponential constants in cgs units.*

ϕ	S_L [m/s]	δ^0_L [mm]	T_b [K]
0.83	0.30	0.40	2058
0.70	0.20	0.55	1846

Table 6.3: *Laminar flame properties for different mixtures at P_{atm} and T_{atm}. S_L, δ^0_L and T_b stand for the laminar flame speed, the laminar flame thickness based on the temperature gradient and the burnt gas temperature, respectively.*

6.4 Data processing

6.4.1 Flow field statistics

LES of compressible reactive flows computes Favre (mass-weighted) filtered quantities $\widetilde{Q}$. "Quasi-Reynolds" average over a time period τ and the corresponding resolved variance are defined as:

$$\left[\widetilde{Q}\right] = \frac{1}{\tau}\int_0^\tau \widetilde{Q}(\mathbf{x},t)\,dt \tag{6.14}$$

$$\left[\widetilde{Q}\right]_{rms} = \sqrt{\left[\widetilde{Q}^2\right] - \left[\widetilde{Q}\right]^2} \tag{6.15}$$

Favre average and resolved variance can be estimated as (Veynante and Knikker 2006):

$$\left\{\widetilde{Q}\right\} = \frac{\left[\overline{\rho}\widetilde{Q}\right]}{[\overline{\rho}]} \tag{6.16}$$

$$\left\{\widetilde{Q}\right\}_{rms} = \sqrt{\frac{1}{[\overline{\rho}]}\left(\left[\overline{\rho}(\widetilde{Q})^2\right] - \frac{\left[\overline{\rho}\widetilde{Q}\right]^2}{[\overline{\rho}]}\right)} \tag{6.17}$$

"Quasi-Reynolds" averages are widely retained because most diagnostic techniques provide unweighted filtered quantities and $[\widetilde{Y}_k]$ is closer to experimental results than $\{\widetilde{Y}_k\}$ (Veynante and Knikker 2006). Fortunately, for the PRECCINSTA burner both Reynolds and Favre statistics are available.
Statistics are collected over 20 ms. This duration may be compared to the turn-over time of the swirl motion, which is about 2.0 ms. The total wall clock time for both convergence and statistics are around of 50h on 2048 cores of an IBM BlueGene/P machine for the stable case and twice as long for the unstable one.

6.4.2 Model parameter statistics

For the local formulation, the mean combustion model parameter, $\overline{\beta}(t)$ and its fluctuation, $\beta'(t)$ are computed using the following definitions:

$$\overline{\beta}(t) = \frac{\int_{\mathcal{V}_f}\beta(x,y,z,t)d\mathcal{V}}{\int_{\mathcal{V}_f}d\mathcal{V}} \tag{6.18}$$

$$\beta'(t) = \sqrt{\overline{\beta^2}(t) - (\overline{\beta}(t))^2} \tag{6.19}$$

where $\mathcal{V}_f$ denotes the instantaneous resolved flame volume defined as $\varepsilon \leq \widetilde{c} \leq 1-\varepsilon$, for $\varepsilon = 0.05$.

6.4.3 Flame surfaces statistics

Resolved flame surfaces at the filter (Δ) and test-filtered ($\widehat{\Delta}$) scales can be estimated as:

$$S_r = \int_{\mathcal{V}} |\nabla \widetilde{c}| \, d\mathcal{V} \tag{6.20}$$

$$\widehat{S}_r = \int_{\mathcal{V}} \left|\nabla \widehat{\widetilde{c}}\right| d\mathcal{V} \tag{6.21}$$

where $\mathcal{V}$ is the computational volume.

6.5 Simulations results and discussions

Results are now discussed for the quiet and pulsating flames. Table 6.4 resumes the simulated cases.

Simulation	Model parameter	ϕ	Numerical behavior
$C_{0.83}$	$\beta = 0.5$	0.83	Stable
$G_{0.83}$	Global: $\beta(t)$	0.83	Stable
$L_{0.83}$	Local: $\beta(\mathbf{x}, t)$	0.83	Stable
$C_{0.70}$	$\beta = 0.5$	0.70	Stable
$G_{0.70}$	Global: $\beta(t)$	0.70	Unstable
$L_{0.70}$	Local: $\beta(\mathbf{x}, t)$	0.70	Unstable

Table 6.4: *Summary of simulated cases. C, G and L stand for constant, global and local formulations, respectively. The subscript of X_α denotes the equivalence ratio. Simulations using the constant model assumed $\beta = 0.5$, according to Charlette et al. (2002a). Filter, test-filter and averaging filter widths are set to $\Delta = \mathcal{F}\delta_L^0$, $\widehat{\Delta} = 2.0\Delta$ and $\Delta_{avg} = 2.7\Delta$, respectively, following Volpiani et al. (2016), where $\mathcal{F}$ is the flame thickening factor and δ_L^0 the laminar flame thickness.*

6.5.1 The quiet flame - $\phi = 0.83$

All simulations of Case 2a ($\phi = 0.83$) reproduce a stable flame stabilized at the nozzle exit in agreement with experiments. When using the local approach, the model parameter is low near the nozzle and increases downstream as the flame is progressively wrinkled by turbulence (see Fig. 6.2). Therefore, a constant/global model parameter may overestimate the front wrinkling factor during the early flame development and underestimate it when flame/turbulence equilibrium is reached. These observations emphasize the advantages of the local formulation.

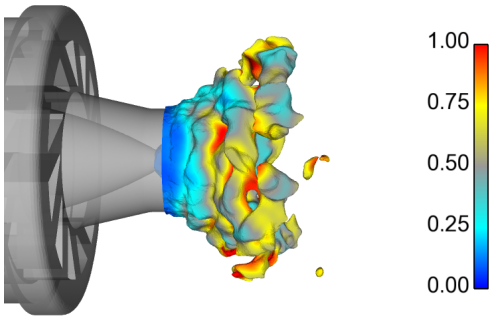

Figure 6.2: *Instantaneous field of the filtered progress variable $\widetilde{c} = 0.5$ iso-surface colored by the β parameter (local approach, $L_{0.83}$).*

Figure 6.3 compares snapshots of the heat release field for simulations using global and local approaches. Note that in the global case, the heat release is uniform all over the flame. On the other hand, in the local case, the heat release increases in regions where the flame is more wrinkled. The constant model parameter (not shown) gives the same distribution than the global dynamic model.

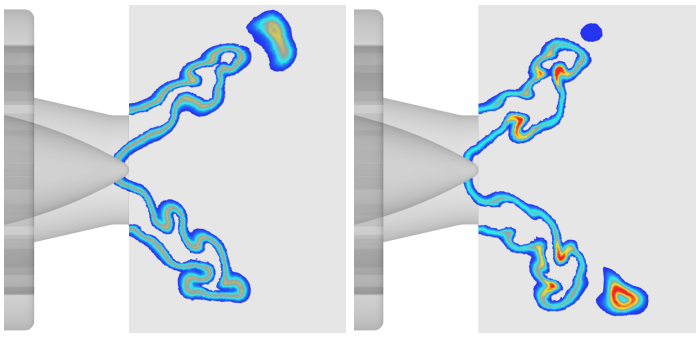

Figure 6.3: *Instantaneous snapshots of the heat release field when using global ($G_{0.83}$, left) and local ($L_{0.83}$, right) dynamic approaches. The red color indicates the maximum heat release observed when using the local model parameter (2000 MW/m^3), while blue corresponds to 1% of this maximum value.*

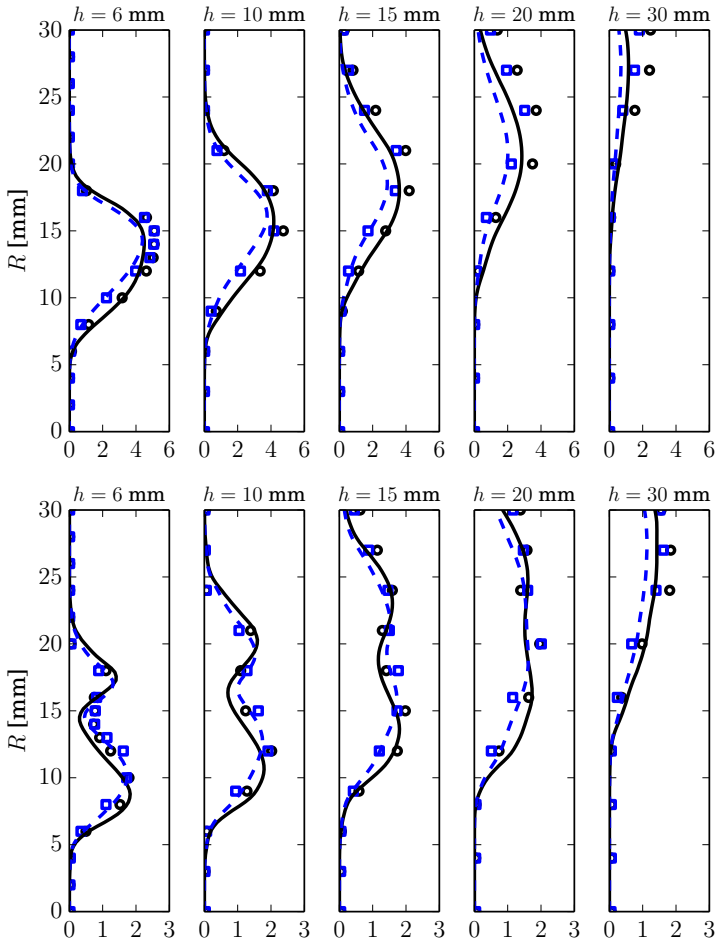

Figure 6.4: *Mean (top) and resolved RMS (bottom) CH_4 [%] transverse mass fraction profiles at five downstream locations for simulation $L_{0.83}$. Symbols: experimental data from (Meier et al. 2007) (**o**): Favre measurements; (□): Reynolds measurements; (- -) Quasi-Reynolds filtered quantity (Eqs. 6.14-6.15); (——) Favre filtered quantity (Eqs. 6.16-6.17).*

Figure 6.4 compares Reynolds (Eqs 6.14 - 6.15) and Favre (Eqs 6.16 - 6.17) mean and RMS methane profiles at five different sections in the chamber for the local approach ($L_{0.83}$). Favre filtered quantities agree with Favre measurements (Veynante and Knikker 2006). Interestingly, quasi-Reynolds filtered quantities compare to Reynolds measurements as well. Even though Veynante and Knikker (2006) showed that $[\widetilde{Y}_k]$ is not a good approximation of $[Y_k]$, at least for infinitely thin flame fronts, most works retain this approximation that seems acceptable for both mean and RMS quantities. In the following, only Favre averages and variances will be displayed.
Figure 6.5 compares Favre mean and resolved RMS carbon dioxide mass fraction profiles at five different sections in the combustion chamber. Local and

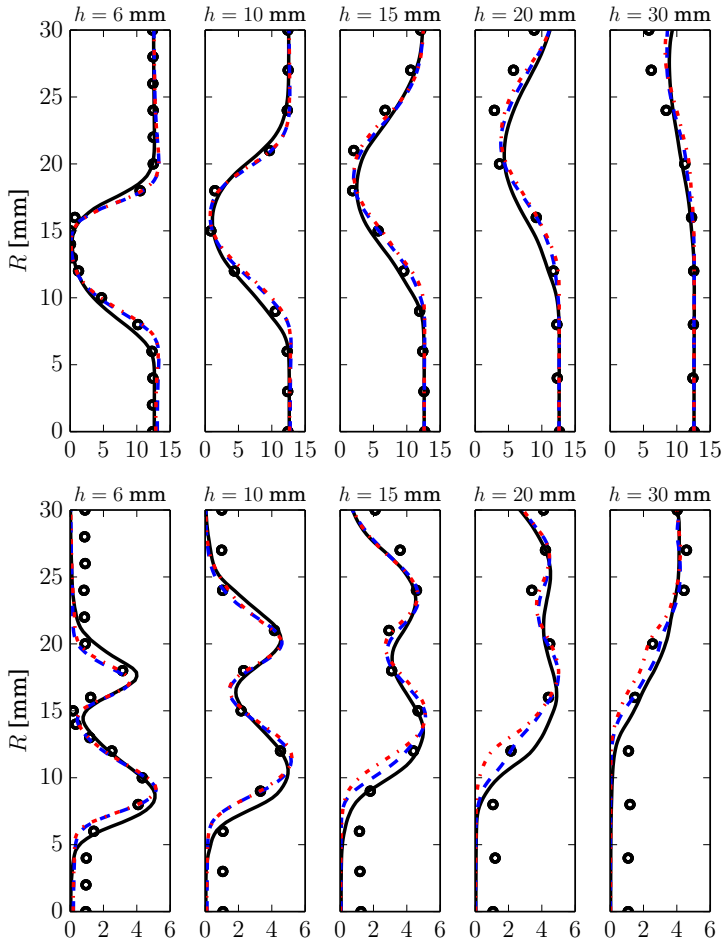

Figure 6.5: *Favre mean (top) and resolved RMS (bottom) CO_2 [%] transverse mass fraction profiles at five downstream locations. (○): Favre measurements; (——) $L_{0.83}$; (– – –) $G_{0.83}$; (–·–·–) $C_{0.83}$.*

global formulations of the TFLES dynamic model give very close statistics in agreement with experimental data, validating the present combustion model. The description of species fluctuations is similar with both formulations. The discrepancies observed on $h = 20$ mm profiles might be due to insufficiently converged statistics, missing low frequency motions of the inner recirculation zone and/or the flame tip.ÊUsing a constant model parameter $\beta = 0.5$ (as recommended by Charlette et al. (2002a)) gives similar results as the global approach for which the model parameter is found to slightly oscillate around this value. Anyway, mean and RMS profiles are probably not sufficient to fully assess model formulations and additional experimental data characterizing the flame dynamics are mandatory.

Mean and resolved RMS temperature profiles are displayed in Fig. 6.6. Once

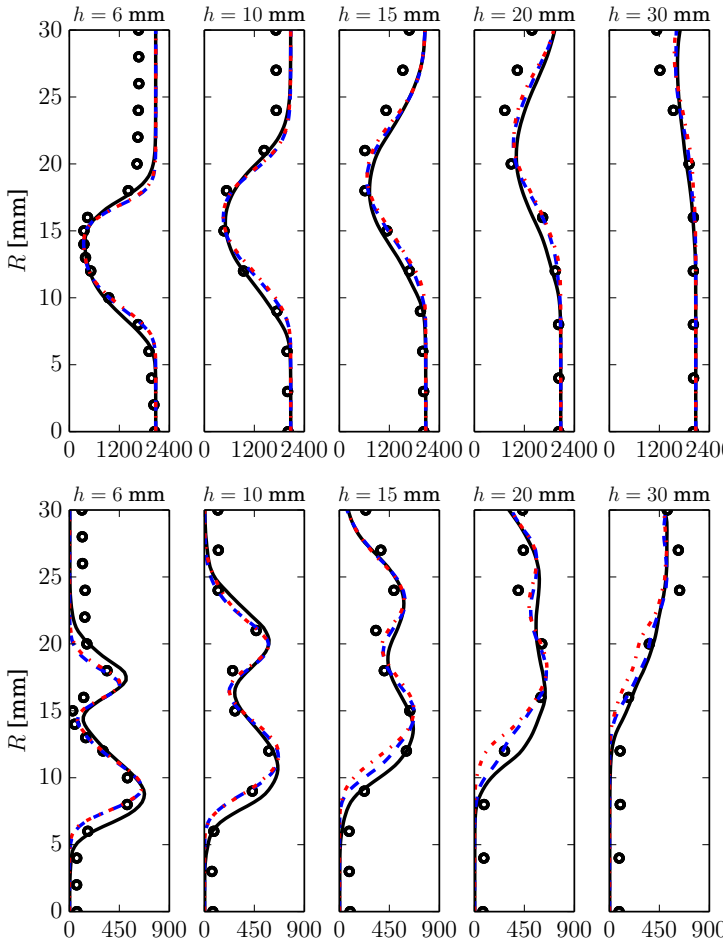

Figure 6.6: *Favre mean (top) and resolved RMS (bottom) temperature T $[K]$ transverse profiles at five downstream locations. (○): Favre measurements; (——) $L_{0.83}$; (- - -) $G_{0.83}$; (-·-·-) $C_{0.83}$.*

again, the experiment is well reproduced by simulations. The overestimation of temperature near walls at $h = 6$ and 10 mm, at the outer recirculation zone, are due to the adiabaticity hypothesis: heat losses and radiation effects are neglected in the present simulations. Similar temperature overestimation is observed in other studies conducted under the same assumption Moureau et al. (2011).

Mean CO mass fraction profiles are compared to experimental points in Fig. 6.7. For this species, the statistical uncertainty reaches 50% and is also plotted. Even if some differences appear close to the injector at the outer recirculation zone, the results are very satisfactory for a reduced mechanism that takes into consideration only 2 reactions and 6 species. The overestimation of mean CO mass fraction profiles close to the injector at $R = 20$ mm are probably due to

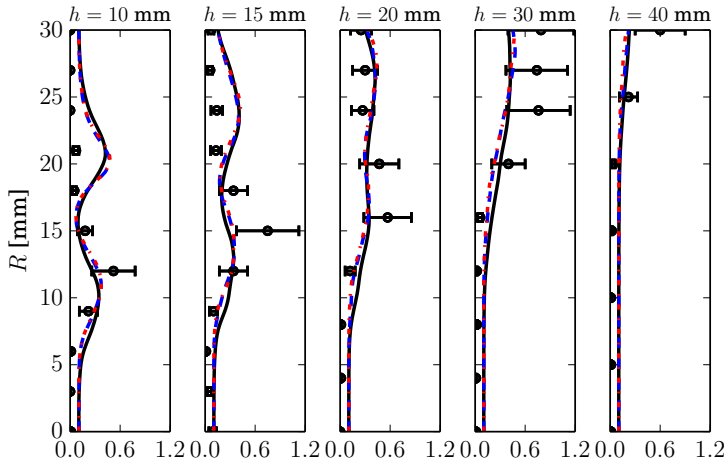

Figure 6.7: *Favre mean CO* [%] *transverse mass fraction profiles at five downstream locations. (○): Favre measurements; (——) $L_{0.83}$; (- - -) $G_{0.83}$; (-·-·-) $C_{0.83}$.*

the overestimation of temperature in the same region.
Overall, even for simulation using a constant model parameter, LES statistical properties are in line with measurements. However, note that for case $C_{0.83}$, the model parameter was known *a priori* from simulation $G_{0.83}$ (Fig. 6.8). Still, the global formulation has the advantage to adapt automatically the model parameter without the need to adjust it by hand case-by-case, giving a decisive advantage to the dynamic formalism. Figure 6.8 displays the temporal evolution of the global parameter that oscillates around 0.5. The mean and RMS model parameter from simulation $L_{0.83}$ are also plotted. One may note that the mean parameter value predicted by the local formalism, about $\beta = 0.60$, is slightly larger than the one found with the global model ($\beta \approx 0.52$) while statistics are very similar (Figs 6.5 - 6.7). This finding might be due to the thresholding introduced in definition (6.18) that removes the low values of the resolved progress variable gradients at fresh ($\widetilde{c} < \varepsilon$) and burnt ($\widetilde{c} > 1 - \varepsilon$) gas limits, while these values enter the computation of the global parameter.
Assuming a fractal behavior of the flame surface (Eq. 6.4) gives:

$$\frac{\Xi_\Delta}{\Xi_{\gamma\Delta}} = \frac{\widehat{S}_r}{S_r} = \left(\frac{\gamma\Delta}{\Delta}\right)^{-\beta} \tag{6.22}$$

Figure 6.9 shows how the flame surface changes when a test-filter is applied. According to Eq. (6.22), the normalized filtered flame surface is then expected to be a straight line of slope $-\beta$ when plotted as a function of the filter width ratio in log-log scales, as confirmed by Fig. 6.10, where the test filter width is varied from Δ to 4.0Δ taking into consideration the entire domain, upstream ($h < 15$ mm) and downstream ($h > 15$ mm) half of the flame where h is the downstream location. This figure also evidences the relevance and the

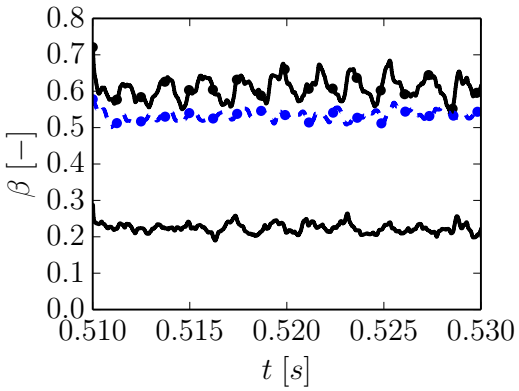

Figure 6.8: *Temporal evolution of the global parameter $\beta(t)$ (– • –), local average model parameter $\overline{\beta}(t)$, Eq. 6.18 (—•—) and its fluctuation $\beta'(t)$, Eq. 6.19 (——).*

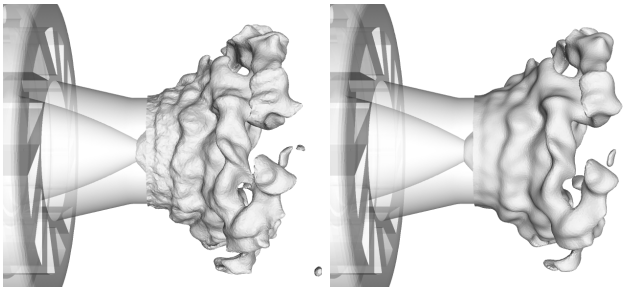

Figure 6.9: *Instantaneous LES resolved fields and corresponding test-filtered quantities. (left) Iso-$\widetilde{c}$ surface, (right) Iso-$\widehat{\widetilde{c}}$ surface when $\gamma = 1.5$.*

robustness of the dynamic formulation as the model parameter β is only very marginally dependent on $\widehat{\Delta}$, at least when not too large. In fact, plots display a slight curvature but its impact on β values is negligible. The mean slope of the curve for the overall domain gives $\beta = 0.58$. Concerning the local analysis, we found $\beta = 0.42$ for the first half and 0.68 for the second half of the flame. These results are in agreement with Fig. 6.11 that displays the distribution of β for the same zones and timestep.

Figure 6.11 shows that the local parameter exceeds unity is some limited regions. Two explanations may be suggested to explain this a priori surprising finding: *(i)* the model is written here in terms of "generalized" surfaces (i.e. $|\nabla\widetilde{c}|$) and not surfaces corresponding to a given value c^* of the filtered progress variable (i.e. $\widetilde{c} = c^*$); *(ii)* in highly wrinkled resolved flame regions or when flame fronts interact, $|\nabla\widehat{\widetilde{c}}|$ may takes low values, increasing the model parameter β (Eq. 6.7). This point needs further analysis but these locally large β values do not induce numerical problems nor affect overall results here. Note, however, that Mouriaux et al. (2016) faced recently practical difficulties for internal combustion engines where ratios Δ/δ_L^0 are large, leading to large wrin-

kling factor values, and introduced model corrections.

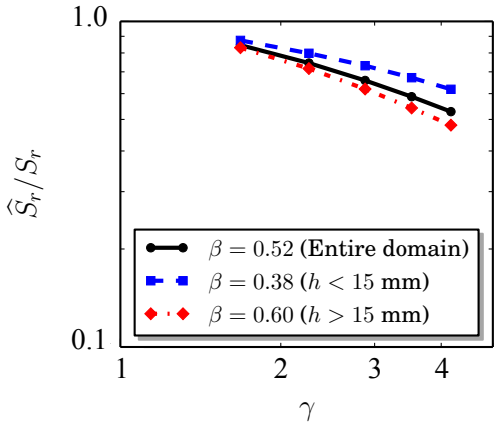

Figure 6.10: *Normalized filtered flame surface, $\widehat{S}_r/S_r$, as a function of γ (Eq. 6.6) comparing test and combustion filter widths in log-log scales. Surfaces are computed from a single instantaneous field using Eqs (6.20) and (6.21) where the volume $\mathcal{V}$ is either the entire domain, the upstream ($h < 15$ mm) or the downstream ($h > 15$ mm) half of the flame. The β values corresponds to the mean curve slopes.*

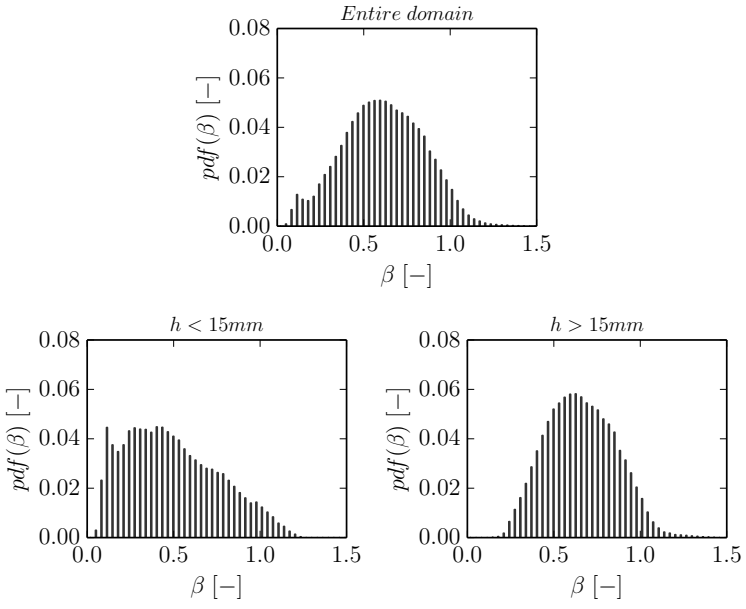

Figure 6.11: *Probability density function of the model parameter β for the entire domain (top), $h < 15$ mm (bottom left) and $h > 15$ mm (bottom right), where h is the downstream location, for the quiet flame corresponding to Fig. 6.2 (case $L_{0.83}$). Data are extracted from the same timestep than Fig. 6.10.*

6.5.2 The pulsating flame - $\phi = 0.70$

Figure 6.12 displays the temporal evolution of the total heat release per unit volume for the three numerical simulations performed at this operating point (Table 6.4). While the total heat release oscillates due to strong flame movements when using the dynamic approach, a stable regime is observed with a constant model parameter. Assuming perfect reactant mixing, Franzelli et al. (2012) also found a quiet flame with a non-dynamic model. In Fig. 6.13, a zoom on the heat release signal is plotted with the temporal evolution of the pressure fluctuation in the combustion chamber, P_c, and in the plenum, P_p. Heat release and pressure P_c oscillate at the same frequency, suggesting that the instability is fed by a flame/acoustic coupling. Moreover, chamber and plenum pressure fluctuations oscillates practically in phase opposition, in agreement with mechanisms identified in others studies (Franzelli et al. 2012).

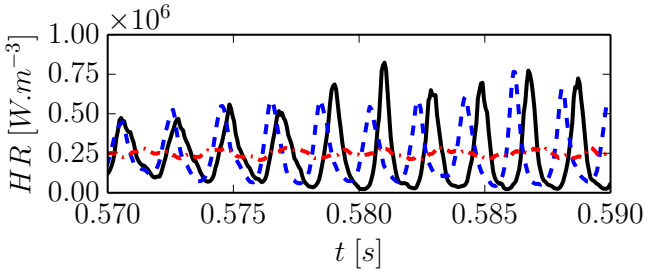

Figure 6.12: *Temporal evolution of the total heat release per unit volume for simulations using local ($L_{0.70}$, ———), global ($G_{0.70}$, - - -) dynamic and non-dynamic ($C_{0.70}$, -·- -) models.*

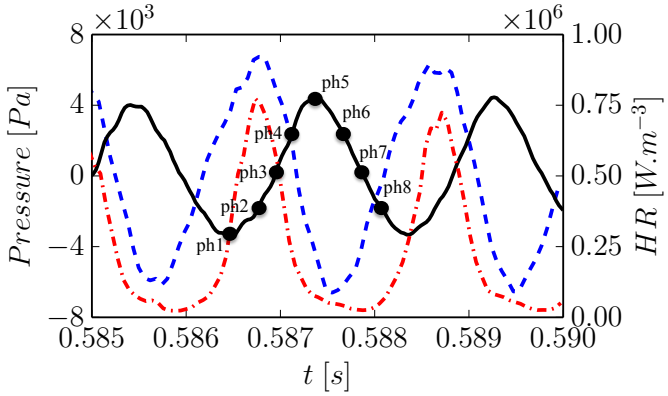

Figure 6.13: *Temporal evolution of the plenum pressure fluctuation P_p (———); the chamber pressure fluctuation P_c (- - -) and the total heat release (-·- -) for simulation $L_{0.70}$ using the local dynamic model. Phases $ph1 - ph8$ of the oscillation (see Fig. 6.14) are also indicated.*

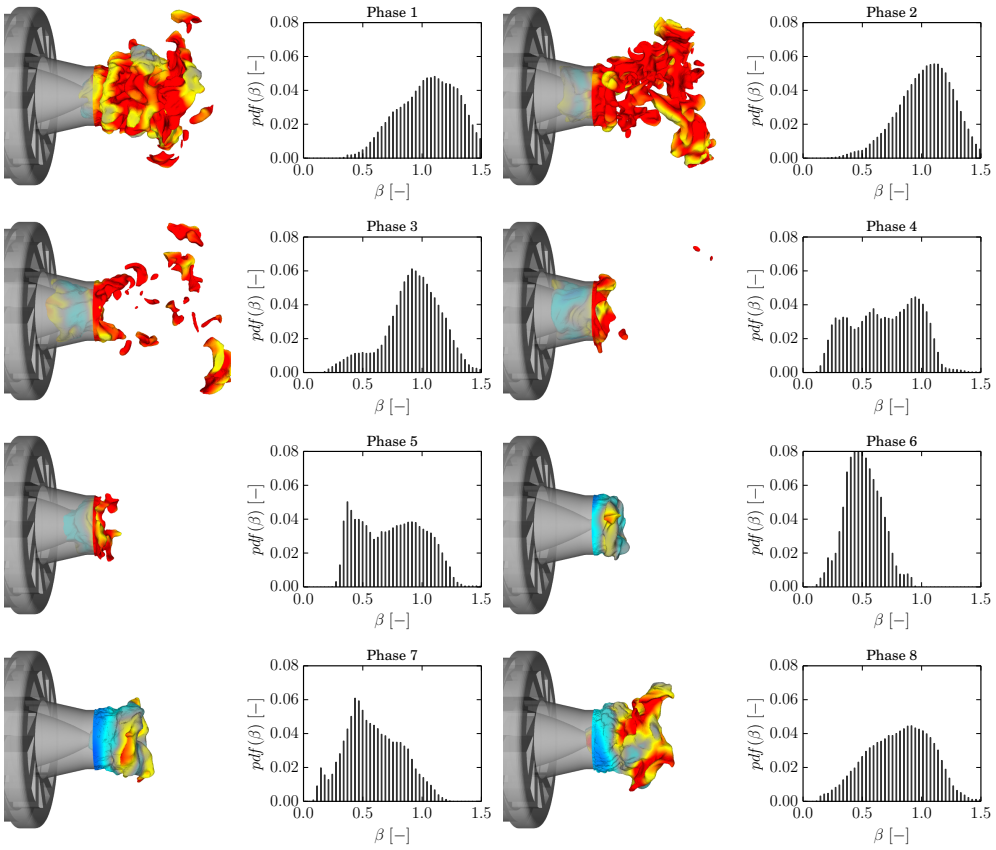

Figure 6.14: *Instantaneous field of* $\widetilde{c} = 0.5$ *iso-surface colored by the* β *parameter (local approach, case* $L_{0.70}$*) for eight different phases: (a)* $ph1$*, (b)* $ph2$*, (c)* $ph3$*, (d)* $ph4$*, (e)* $ph5$*, (f)* $ph6$*, (g)* $ph7$ *and (h)* $ph8$ *for the pulsating flame (see Fig. 6.13). Probability density function of the fractal model parameter* β *is also plotted for each phase. The blue color corresponds to* $\beta = 0$ *and the red color to* $\beta = 1$*.*

The predicted frequency is about 500 Hz while 300 Hz is observed in the experiment. Franzelli et al. (2012) found 400 Hz, when injecting the reactants separately. These discrepancies are probably linked to the injection impedance, which was not characterized in the experiment and arbitrarily imposed in LES. Note also that a simple turbulent velocity profile is imposed at the plenum inlet and walls are assumed adiabatic in simulations, which may differ from the actual experimental conditions. Further investigations are required to confirm these findings but our goal is also to point out that a relatively minor change in the model may induce large variation in the unsteady flow behavior. To our feeling, the description of mixing in Franzelli et al. (2012) or the dynamic formalism in the present results introduces a degree of freedom in reaction rate expressions, making them more sensitive to external perturbations, possibly promoting the development of an unstable mode. These modes are also observed for the stable

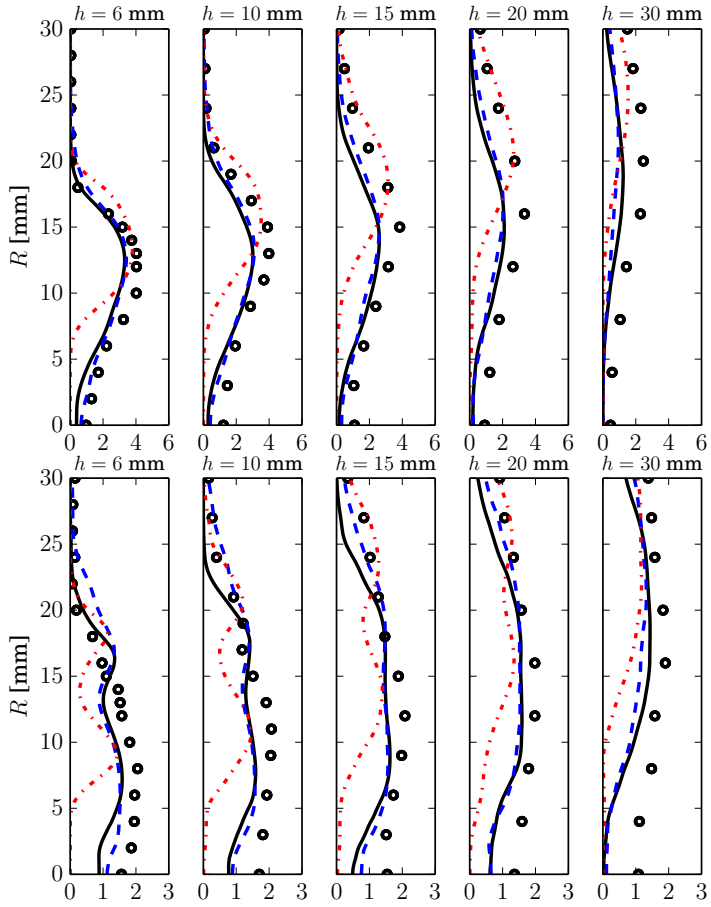

Figure 6.15: *Favre mean (top) and resolved RMS (bottom) CH_4 [%] transverse mass fraction profiles. (○): Favre measurements; (——) $L_{0.70}$; (– – –) $G_{0.70}$; (– · – · –) $C_{0.70}$.*

case but with reduced amplitudes.

The cycle of the self-sustained oscillation is visualized in Fig. 6.14 displaying the instantaneous $\widetilde{c} = 0.5$ isosurface colored by β and the β probability density function for eight phases of the plenum pressure P_p fluctuation, referred as $ph1$ to $ph8$ in (Meier et al. 2007) and Fig. 6.13. During $ph1$, the plenum pressure is minimal. The flame is fully developed at $ph2$. At this point, the combustion intensity is maximal. The high pressure inside the combustion chamber forces the flame to move upstream. In $ph3$, the flame starts to disintegrate and is pushed back inside the injector. The flame is located practically inside the nozzle during $ph4$ and $ph5$, when the plenum pressure is maximal. During $ph6$, the flame starts its expansion and re-enters the combustion chamber, where pressure is minimal. In $ph7$ and $ph8$, the flame moves downstream reinitiating the cycle. For the global approach the model parameter is minimal (maximal) when the flame is shorter (longer).

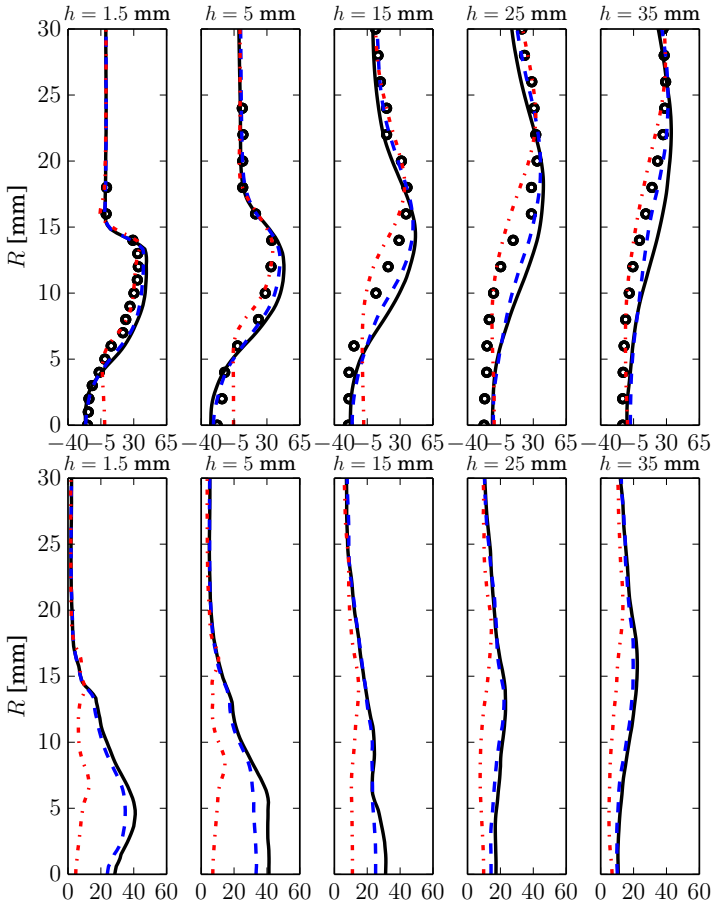

Figure 6.16: *Favre mean (top) and resolved RMS (bottom) transverse axial velocity [m/s] profiles. (○): Favre measurements; (——) $L_{0.70}$; (– – –) $G_{0.70}$; (–·–·–) $C_{0.70}$.*

Favre mean and resolved RMS mass fraction profiles for the three simulations studied are compared to experimental results in Fig. 6.15. When using the dynamic (local or global) model, mean and RMS profiles of CH_4 provide similar levels of agreement with experiments. On the other hand, numerical results are deteriorated when the model parameter is fixed. This finding is not surprising, because as already mentioned in (Franzelli et al. 2012) and confirmed by Fig. 6.12, the unstable mode is not recovered when imposing a constant model parameter. Figure 6.16 displays the mean and RMS axial velocity at five sections downstream of the injector. The negative velocity characterizing the inner recirculation zone reaches approximately 20 m/s at $h = 1.5$ mm and is recovered numerically. The RMS of the axial velocity was not measured experimentally but is almost of the same order of the mean value, indicating a strong activity inside the combustion chamber.

One of the most interesting points is that the fractal dimension ($D = \beta + 2$) is actually not constant and depends on time within a period of the instability.

This is evidenced plotting the normalized filtered flame surfaces as a function of the ratio of filters, γ, in log-log scales, considering the entire domain as done in the previous section. The slope and accordingly β values depend on the phase within the oscillation, as shown in Fig. 6.17. The straight lines in this figure confirms the robustness of the dynamic formulation as, once again, the model parameter is not sensitive to the test filter width.

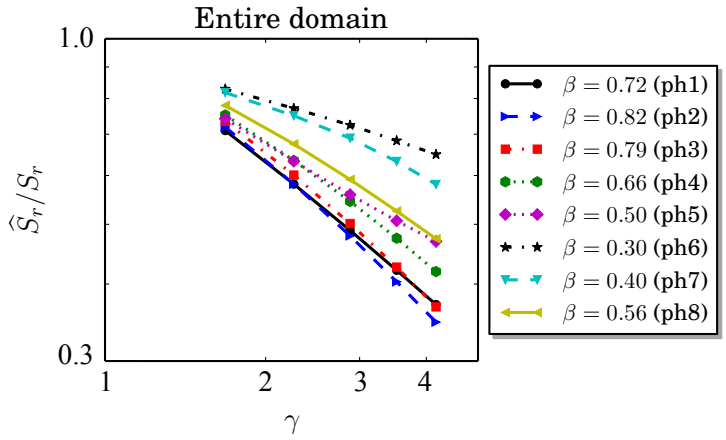

Figure 6.17: *Normalized filtered surface flame as a function of the ratio of test and combustion filter sizes in log-log scales for eight different phases:*$ph1 - ph8$ *corresponding to Fig. 6.14 (case* $L_{0.70}$*).*

These results are also confirmed by Fig. 6.18 that displays the temporal evolution of the mean model parameter, $\overline{\beta}$ (Eq. 6.18), and the total heat release for simulation using the local dynamic model ($L_{0.70}$). In contrast to the stable flame, the $\overline{\beta}$ oscillates strongly between 0.4 and 1.1. Moreover, the model parameter oscillates in phase with the heat release, meaning that β is maximum (minimum) when the flame is expanded (compressed). Similar results can be found for the global case ($G_{0.70}$), as confirmed in Fig. 6.19. Note that differences between Figs. 6.17 and 6.18 are due to the fact that the slope computation is based on one single snapshot, while Fig. 6.18 shows five consecutive periods. Yet, the agreement is very good.

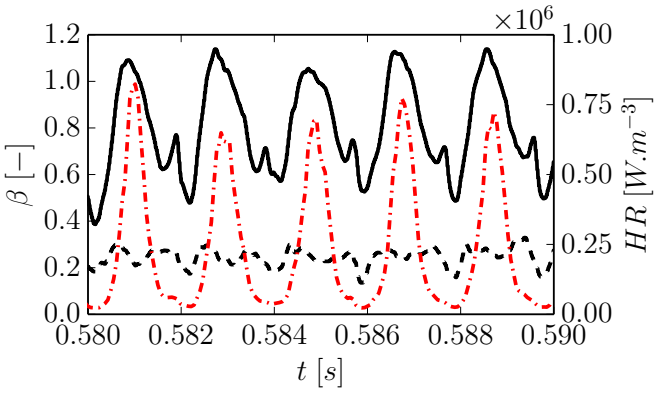

Figure 6.18: *Temporal evolution of the mean model parameter $\overline{\beta}$ (Eq. 6.18, ———), its fluctuation β' (Eq. 6.19, - - -), and the total heat release (-·-·-) for simulation using the local dynamic model (case $L_{0.70}$).*

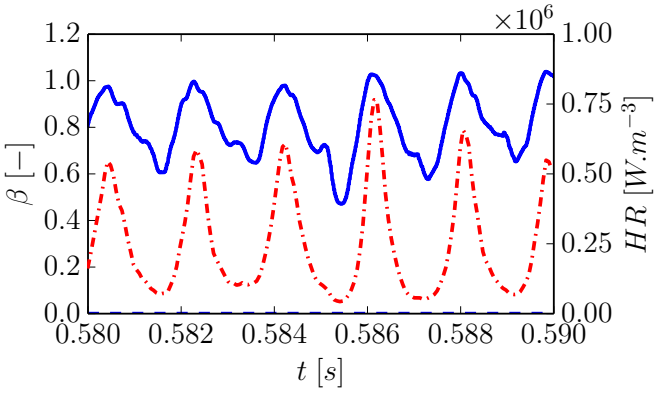

Figure 6.19: *Temporal evolution of the global parameter β (———) and the total heat release (-·-·-) for simulation using the global dynamic model (case $G_{0.70}$).*

6.5.3 Mesh convergence for the pulsating flame

Even though recent experimental works (Caux-Brisebois et al. 2014; Steinberg et al. 2013) treated the same combustor burning perfectly premixed methane-air flames and investigated the thermo-acoustic coupling, data are not yet available for comparison to the unstable case simulated herein. Any change in the configuration (geometry, boundary conditions, etc) may damp or promote self-excited oscillations of the burner (Lartigue et al. 2004). Therefore, the model validation requires to check whether the oscillations reproduce the physics or are artificially introduced by the dynamic formalism. The local dynamic model was tested using a finer mesh with 65M cells/11M nodes and a thickening factor $\mathcal{F} = 3$ reducing the impact of the LES model.

The CPU time for computation using the fine mesh is approximately 4 times longer than the standard mesh (21M cells/3.7M nodes). In order to have the

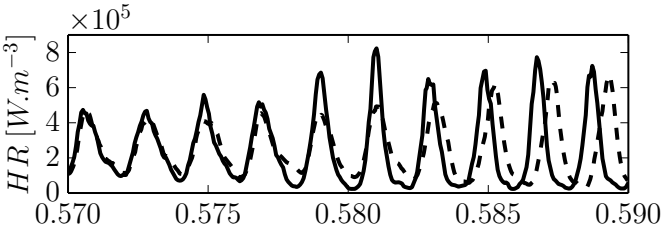

Figure 6.20: *Temporal evolution of the total heat release per unit volume for the pulsating flame using the local dynamic model. (——) standard mesh; (- - -) fine mesh.*

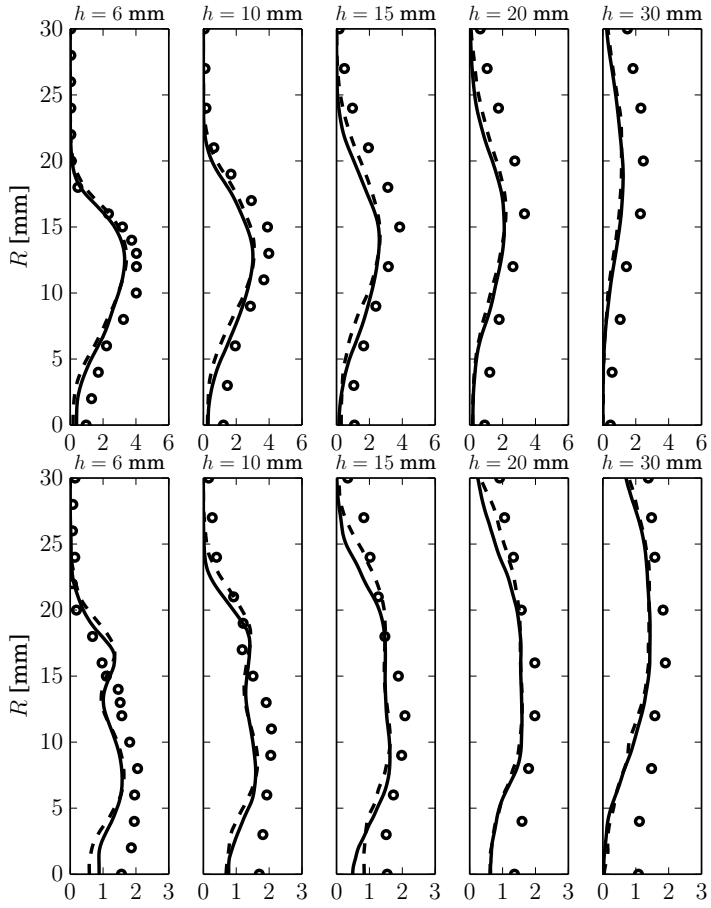

Figure 6.21: *Favre mean (top) and resolved RMS (bottom) CH_4 [%] transverse mass fraction profiles at five downstream locations. (○): Favre measurements; (——) standard mesh; (- - -) fine mesh*

same physical time, 8192 cores were used to run the simulation (instead of 2024) on the same IBM BlueGene/P machine. Figure 6.20 displays the temporal evolution of the total heat release using the local dynamic model for both meshes.

The strong oscillation is also present in the simulation using the fine grid. A slight phase shift between coarse and fine grid simulations is observed during the instability development but instantaneous LES signals cannot be directly compared: only the comparison of statistics, such as phase averages during the well-established instability cycle, is relevant (Pope 2004). Time-shifting signals to superimpose the last periods (not displayed here) shows that pulsation frequencies are identical, validating previous results. This conclusion is also confirmed by mean and RMS profiles, as shown in Fig. 6.21. Instantaneous field of $\widetilde{c} = 0.5$ iso-surface colored by the β parameter for simulation using the fine mesh for 8 different phases can be found as supplementary material.

6.6 Conclusion

In this work, the global and local dynamic formulations for the flame wrinkling factor were combined with the Thickened Flame (TFLES) model and simulations of the semi-industrial PRECCINSTA burner studied experimentally by Meier et al. (2007) were performed for the stable and unstable cases. The global formulation predicts a time-dependent model exponent that remains at a level close to 0.5 for the stable flame and oscillates strongly around 0.8 for the pulsating flame. Moreover, the global saturated model was corrected by applying a wrinkling factor damping near the walls to take into account flame/wall interactions. The local formulation adapts the parameter locally based on the gradients of the resolved progress variable all over the domain and does not need this modification. The usual non-dynamic formulation with an appropriate constant, to be set by trial and error, is sufficient to capture flow and combustion time averaged and RMS fields with good accuracy (both in terms of Favre and quasi-Reynolds quantities) in the stable case. However, the self-excited modes of the pulsating flame are captured only with the dynamic model. The fractal dimension of the unstable flame is found to vary locally and depends on the phase within the period of oscillation. While Franzelli et al. (2012) suggested that methane/air mixing could be linked to the flame pulsation, the details of the exact mechanism controlling the instability itself has not been identified yet. We conclude that dynamic models may have an effect on the prediction of combustion instabilities. A simulation combining the description of the fuel / air mixing with the dynamic formalism would be an interesting complementary test. Unfortunately, it cannot be conducted in a near future because the dynamic model has been developed and validated only for premixed combustion and must be first extended to partially premixed and non-premixed regimes. Also, such a simulation needs large computational resources: the fuel is injected through small holes in the swirler vanes requiring a very refined mesh in this region. Anyway, the unsteady behavior of the dynamic model will be analyzed in details in a near future to fully understand our findings.

Acknowledgments

This work was performed using HPC resources of IDRIS under the allocation 2015-90164 made by GENCI (Grand Equipement National de Calcul Intensif). The authors would like to thank Prof. W. Meier and Dr. B. Franzelli for fruitful discussions.

6.7 Supplementary material

Figure 6.22 shows snapshots of $\widetilde{c} = 0.5$ iso-surface colored by β for the local approach using the fine mesh with 65M cells/11M nodes and a thickening factor $\mathcal{F} = 3$. The flame oscillation is very intense, going back and forth from the combustion chamber to the injector, in agreement with results displayed in (Meier et al. 2007).

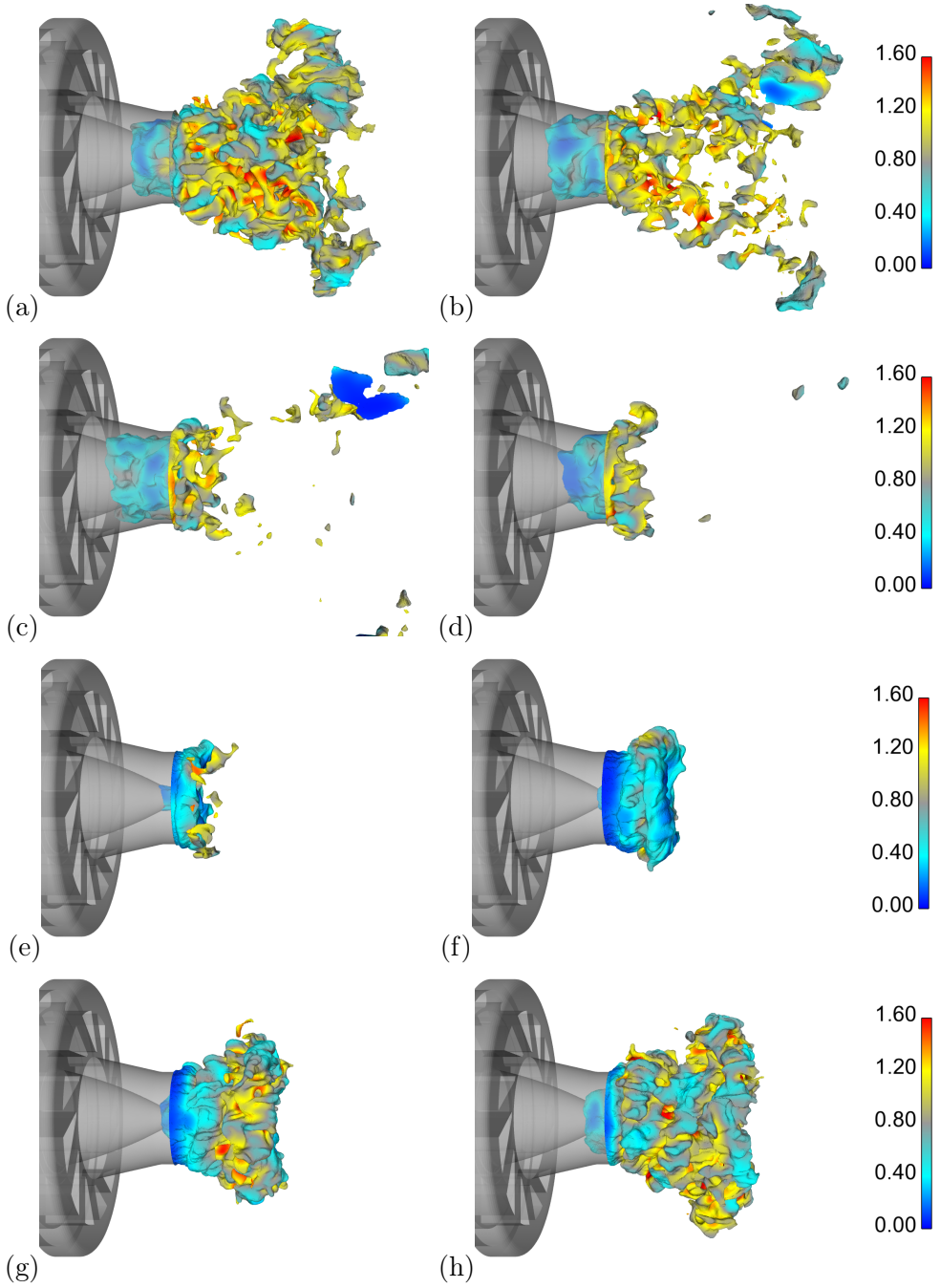

Figure 6.22: *Instantaneous field of* $\widetilde{c} = 0.5$ *iso-surface colored by the* β *parameter (local approach) for 8 different phases: (a) ph1, (b) ph2, (c) ph3, (d) ph4, (e) ph5, (f) ph6, (g) ph7 and (h) ph8 for the pulsating flame. Simulation using the fine mesh.*

Chapter 7

Large eddy simulation of explosion deflagrating flames using a dynamic wrinkling formulation

Reliable predictions of flames propagating in a semi-confined environment are vital for safety reasons, once they are representative of accidental explosion configurations. Large eddy simulations of deflagrating flames are carried out using a dynamic flame wrinkling factor model. This model, validated from a posteriori analysis, is able to capture both laminar and turbulent flame regimes. At early stages of the flame development, a laminar flame propagates in a flow essentially at rest and the model parameter is close to zero, corresponding to a unity-wrinkling factor. Transition to turbulence occurs when the flame interacts with the flow motions generated by thermal expansion and obstacles. The model parameter and wrinkling factor take higher values at these stages. Three configurations investigated experimentally by Masri et al. (2012) corresponding to different scenarios of flame acceleration are simulated. The first case (OOBS) is characterized by a long laminar phase. In the second one (BBBS) the flame is the most turbulent and the highest overpressure is observed in the vessel. For the last case (BOOS), the flame front is relaminarized after crossing the first row of obstacles. In all configurations, large eddy simulations (LES) predict the flow dynamics and maximum overpressure with good accuracy.

7.1 Introduction

Accidental explosions of flammable gases are a current issue in process industries. Selecting the optimal conditions and parameters in the design and operation of chemical, petrochemical, mining, nuclear and others industrial plants is not only a matter of safety but also economical and environmental issues. In gas explosions of a premixed gas cloud, the pressure increase is governed by a complex unsteady interaction between flame propagation, turbulence and geometry. This overpressure is often considered as the key parameter, since it controls the severity of the explosion and corresponding damages. This complex phenomenon is very challenging for computational fluid dynamics (CFD) problems since it involves a large spectrum of spatial and time scales and encompasses a large range of flow and combustion regimes.

The typical research configuration used to study explosions in buildings consist in vessels with obstacles filled with a premixed flammable mixture. After the ignition, a laminar flame propagates in a flow essentially at rest. Transition to turbulence takes place when the flame starts to interact with obstacles and their wakes. This interaction strongly influences the shape of the flame front, the burning rate and, as a consequence, the overpressure. This flame induced flow field increases turbulence and combustion intensity, leading to flames, which can propagate at 100 to 200 m/s. In the worst scenario, the initial flame can transition to detonation and cause the destruction of the whole building.

A large number of experiments have been carried out in order to understand flame/turbulence interactions in vented explosion chambers with solid obstacles (Fairweather et al. 1999; Kent et al. 2005; Hall et al. 2009; Masri et al. 2012; Masri et al. 2000; Oran and Gamezo 2007; Ciccarelli and Dorofeev 2008; Dorofeev 2011). Effects of geometry (Fairweather et al. 1999; Kent et al. 2005; Hall et al. 2009; Masri et al. 2012) and fuel type (Kent et al. 2005; Hall et al. 2009; Masri et al. 2012) have been analyzed in order to point out mechanisms involved in the overpressure generation. Flame acceleration and deflagration to detonation transition are also subjects of several reviews (Oran and Gamezo 2007; Ciccarelli and Dorofeev 2008; Dorofeev 2011). This work focuses on the configurations studied experimentally by Masri and co-workers (Kent et al. 2005; Masri et al. 2012). Different geometries, fuel types and scales were reported. The experiments have access to the pressure evolution inside the chamber, the flame speed and flame front position along the middle section of the chamber. Additionally, they have well prescribed initial and boundary conditions and for this reason are very appropriate for model validation.

On the numerical side, thanks to the growing computational power and the availability of parallel computing algorithms, large eddy simulation (LES) is becoming a routinely used tool to predict and reproduce turbulent reactive flows (Janicka and Sadiki 2005; Pitsch 2006; Poinsot and Veynante 2011; Gicquel et al. 2012). In LES, the large turbulent structures of the flow are resolved and the effect of small structures that exhibit a more universal behavior are

modeled. Unfortunately, chemical reactions in combustion processes occur at characteristic scales that are smaller than the mesh resolution and a good combustion model is vital to capture the physics of the flow. Several numerical studies dealing with deflagrations in semi-confined chambers are reported in the literature (Kirkpatrick et al. 2003; Di Sarli et al. 2009; Di Sarli et al. 2009; Di Sarli et al. 2010; Gubba et al. 2008; Gubba et al. 2009; Gubba et al. 2011; Ibrahim et al. 2009; Johansen and Ciccarelli 2013; Quillatre et al. 2013).
The majority of LES of premixed flame deflagration in the presence of obstacles relies on the Flame Surface Density (FSD) approach. In this case, the species transport equations are simplified in the form of a transport equation for the reaction progress variable, which is zero within fresh reactants and unity within burned products (Kirkpatrick et al. 2003; Di Sarli et al. 2009; Di Sarli et al. 2009; Di Sarli et al. 2010; Gubba et al. 2008; Gubba et al. 2009; Gubba et al. 2011; Ibrahim et al. 2009; Johansen and Ciccarelli 2013). The only exception is Quillatre et al. (2013) that use the Thickening Flame model for LES (TFLES) together with reduced kinetic schemes for CH_4 - C_3H_8 and H_2/air combustion. While the former method has the advantage of being computationally cheaper, the latter one takes into account molecular and thermal transports, which turn out to have a significant impact on the results (Quillatre et al. 2013).
Di Sarli et al. (2010) highlighted the importance of the sub-grid closure in the reproduction of the experiment, studied by Patel et al. (2002), in terms of flame acceleration and deceleration around each obstacle, flame shape and speed as well as pressure peak. Actually, most of the models employed in their study needed parameter adjustments to obtain more realistic trends. As a matter of fact, non-dynamic LES combustion models, such as those based on algebraic expressions for the turbulent flame speed (Peters 1999; Pitsch and De Lageneste 2002), the flame surface density (Boger et al. 1998) or the flame surface wrinkling factor (Colin et al. 2000; Charlette et al. 2002a), may suffer to reproduce this kind of situation. Actually, every computation may need its own set of constants: any small change in the operating conditions or in the geometry requires an adjustment of the model parameters (Vermorel et al. 2017).
Possible solutions are then to use more refined models, for instance by solving an additional balance equation for the flame surface density (Hawkes and Cant 2000; Richard et al. 2007; Vermorel et al. 2009) or the wrinkling factor measuring the ratio of total and resolved flame surfaces (Weller et al. 1998). Unfortunately, this methodology originates new unclosed terms that also need modeling. Besides, adjusting model coefficients is a common practice when dealing with engines at different speeds (Mouriaux 2016).
As a matter of fact, dynamic models, which take advantage of the known resolved large scales to automatically adjust model parameters, seem much more appropriate for these situations. The model is written at LES and test-filtered scales and the parameter is the solution of a Germano-like equation (Germano et al. 1991). Validated in simple flow configurations (flame embedded in a

homogeneous isotropic turbulence) (Charlette et al. 2002b; Wang et al. 2012; Im et al. 1997), dynamic models have proven to be very effective in reproducing steady stable (Knudsen and Pitsch 2008; Wang et al. 2011; Schmitt et al. 2013; Schmitt et al. 2015; Volpiani et al. 2016) and unstable (Volpiani et al. 2017) flames. They were successfully employed to simulate transient phenomena as well. Mouriaux et al. (2016) obtained very good results, when dealing with internal combustion engines at distinct speeds. Ibrahim et al. (2009); Gubba et al. (2011) obtained accurate predictions using the dynamic FSD similarity formulation developed by Knikker et al. (2004) for distinct explosion configurations studied experimentally by Masri et al. (2012).
This work aims to validate the local dynamic wrinkling factor approach coupled with the Thickened Flame (TFLES) combustion model in the explosion test-cases studied experimentally by Masri et al. (2012). This combination has already been employed in other studies (Charlette et al. 2002b; Wang et al. 2011; Volpiani et al. 2016; Volpiani et al. 2017). The present manuscript is organized as follows: basic concepts of TFLES and the dynamic approach are discussed in Section 7.2. In Section 7.3, the experimental test cases are presented. Then, the chemical scheme employed in our computations is presented (Section 7.4). In Section 7.5, a sensitivity analysis, regarding mesh sizes, transport models, boundary conditions and other features of numerical simulations, is carried out on 2D-DNS and 2D-LES configurations and serves as basis for the three-dimensional study. The numerical set-up for the three-dimensional configurations is introduced in Section 7.6. Finally, a posteriori results for different geometries, corresponding to three scenarios of flame acceleration, are discussed (Section 7.7). Conclusions are drawn.

7.2 Modeling

7.2.1 The thickened flame model (TFLES)

One of the challenges in large eddy simulations of premixed combusting flows is the fact that the flame front cannot be resolved on the computational mesh. A common procedure to overcome this problem is to artificially thicken the flame by multiplying diffusion and dividing reaction rates by a thickening factor $\mathcal{F}$ (Butler and O'Rourke 1977). The modified flame front of thickness $\mathcal{F}\delta_L^0$ propagates at the same laminar flame speed S_L as the original flame of thickness δ_L^0. However, the Damköhler number is modified and the flame becomes less sensitive to turbulence (Colin et al. 2000). A wrinkling factor Ξ_Δ is then introduced to counterbalance the reduction of flame surface induced by the thickening operation (Colin et al. 2000; Charlette et al. 2002a). The balance equations for filtered species mass fractions $\widetilde{Y}_k$ are written as:

$$\frac{\partial \overline{\rho}\widetilde{Y}_k}{\partial t} + \nabla \cdot (\overline{\rho}\widetilde{\mathbf{u}}\widetilde{Y}_k) = -\nabla \cdot (\Xi_\Delta \mathcal{F}\overline{\rho \mathbf{V}_k}\widetilde{Y}_k) + \frac{\Xi_\Delta}{\mathcal{F}}\dot{\omega}_k(\widetilde{Q}) \tag{7.1}$$

where ρ is the density, $\mathbf{u}$ the velocity vector, $\mathbf{V_k}$ the diffusion velocity of species k, expressed here using the Hirschfelder and Curtiss approximation (Poinsot and Veynante 2011) and $\dot{\omega}_k$ the reaction rate of species k. Any quantity $\overline{Q}$ corresponds to the filtered Q-field, while $\widetilde{Q} = \overline{\rho Q}/\overline{\rho}$ denotes mass-weighted filtering. Equation (7.1) propagates a flame front of thickness $\mathcal{F}\delta_L^0$ at the sub-grid scale turbulent velocity $S_T = \Xi_\Delta S_L$. The balance equation for the filtered total energy is modified in the same manner.

7.2.2 Dynamic wrinkling model

The wrinkling factor Ξ_Δ models the ability of sub-grid scale vortices to wrinkle the flame front. This term is usually modeled in the literature by complex algebraic expressions. Generally, these expressions involve other unresolved terms (for instance, the sub-grid scale turbulent velocity, u'_Δ), which also need modeling. Assuming that the flame surface is fractal (Gouldin 1987; Gouldin et al. 1989; Gülder and Smallwood 1995), Ξ_Δ can be written in a very simple form:

$$\Xi_\Delta = \left(\frac{\Delta}{\delta_c}\right)^\beta \tag{7.2}$$

where $D = \beta + 2$ is the fractal dimension of the flame surface and δ_c the inner cut-off length scale (i. e. the smallest scale for the interaction of turbulent eddies with the premixed flame front). In the present work, the inner cut-off is identified to the laminar flame thickness. This assumption is validated using two-dimensional simulations (see Subsection 7.5.6) and is in agreement with other studies (Charlette et al. 2002b; Veynante and Moureau 2015). It is worth noting that, in the following, the β parameter is determined dynamically during the computation and may vary both with time and location in the flow. In that sense, Eq. (7.2) is more general than a fractal model prescribing a given fractal dimension D. The model parameter β is determined equating flame surfaces computed at the test-filtered level and using test-filtered variables (Wang et al. 2012; Schmitt et al. 2015; Veynante and Moureau 2015):

$$\widehat{\langle \Xi_\Delta |\nabla \widetilde{c}| \rangle} = \langle \Xi_{\gamma\Delta} |\nabla \widehat{\widetilde{c}}| \rangle \tag{7.3}$$

c stands for the progress variable, increasing from 0 in fresh to 1 in burnt gases and is computed here from temperature. The hat symbol denotes a test-filtering operator. The effective filter size is $\gamma\Delta$, with $\gamma = [1 + (\widehat{\Delta}/\Delta)^2]^{1/2}$ when combining two Gaussian filters of width Δ and $\widehat{\Delta}$. Symbol $\langle\cdot\rangle$ denotes an averaging operator over a given volume. In the current work, this operation is replaced by a Gaussian filter Δ_{avg}, easier to implement as unsteady diffusion operators (Moureau et al. 2011) when using unstructured meshes and a parallel solver (Veynante and Moureau 2015).

Combining Eqs (7.2) and (7.3) and assuming that β is constant over the averaging domain $\langle . \rangle$ give:

$$\beta = \frac{\log\left(\langle|\widehat{\nabla \widetilde{c}}|\rangle / \langle|\nabla \widehat{\widetilde{c}}|\rangle\right)}{\log(\gamma)} \tag{7.4}$$

A thickened flame is not strictly equivalent to a filtered flame. Here, an equivalent filter size, Δ, is estimated as a function of the thickening factor and the laminar flame thickness as $\Delta \approx \mathcal{F}\delta_L^0$ (Charlette et al. 2002a). Test and averaging filter sizes are constant and set to 2Δ and 2.7Δ respectively. This choice results from extensive test validations (Volpiani et al. 2016).
As the code time step is based on the acoustic CFL number and the model parameter is expected to evolve with convective times, the dynamic procedure is not applied every time step. This technique saves computational cost linked to the filtering operation. A simple analysis that compute the flame convective characteristic time based on the ratio of test filter size and maximum velocity shows that updating the model parameter every 100 iterations is sufficient[1]. Note that this artifice used to save computational time is no longer valid when using the dynamic flame surface density (DFSD) formulation (Ibrahim et al. 2009; Gubba et al. 2011) developed by Knikker et al. (2004). As a matter of fact, the DFSD model is based on a similarity assumption and needs a filtering operation every time step, not only to compute β, but also the flame surface Σ:

$$\Sigma = \Xi_\Delta |\nabla \bar{c}| = |\nabla \bar{c}| + \frac{1}{1-\gamma^{-\beta}} \left[\left(\frac{\Delta}{\delta_c}\right)^\beta - 1\right] \left[|\widehat{\nabla \bar{c}}| - |\nabla \widehat{\bar{c}}|\right] \tag{7.5}$$

In Eq. (7.5), the term $|\widehat{\nabla \bar{c}}| - |\nabla \widehat{\bar{c}}|$ needs to be test-filtered every iteration. For this reason, using Knikker et al. (2004) model in a compressible CFD solver, as done by Gubba et al. (2011); Ibrahim et al. (2009) for the same configuration, may be extremely expensive[2] and the present methodology is preferred.

7.3 Experimental set-up

Different geometries of a small scale combustion chamber studied experimentally by Masri and co-workers (Masri et al. 2012) are investigated in this work. The experiment is composed of a square cross section combustion chamber (5 cm $\times$ 5 cm $\times$ 25 cm) with solid obstacles. The geometry is detailed in Fig. 7.1

[1] Assuming a characteristic length scale equal to the test filter size $\widehat{\Delta} = 3.4$ mm, a maximum velocity about 150 m/s and a time step of 0.5×10^{-7} s, a value of 400 iterations is found.

[2] A simple computation indicates that the CPU time is multiplied by a factor ≈ 20.

with dimensions in millimeters. The left side of the chamber is closed, while the right side is opened out to the atmosphere. Removable baffle plates can be placed at various distances from the ignition source. Each one consists of five strips, 4 mm wide, equally separated by six gaps, 5 mm wide and they are placed 20, 50 and 80 mm from the closed end. Downstream of the baffle plates, an obstacle of cross section 12×12 mm^2 is placed at 94 mm from the ignition point.

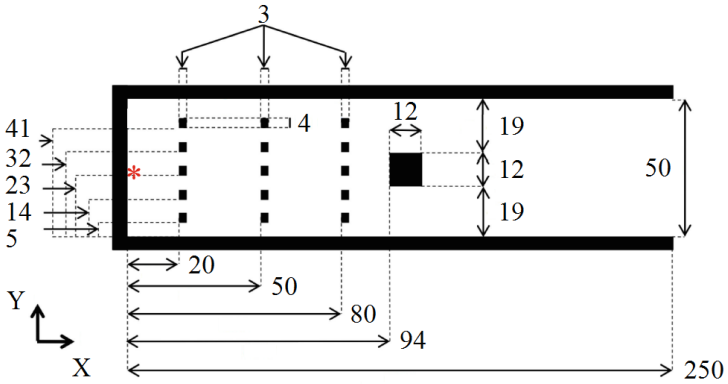

Figure 7.1: *Top view of the studied combustion chamber (Masri et al. 2012). Dimensions are in millimeters. Symbol $*$ corresponds to the pressure transducer location.*

The fuel-air mixture is initially at rest and is ignited by focusing a laser at the closed end of the chamber. Even though, different fuels are available, a focus is made to the liquefied petroleum gas LPG (95% C_3H_8) at equivalence ratio $\phi = 1$. The experimental database includes pressure-time measurements and flame front visualizations based on high-speed laser induced fluorescence OH (LIF-OH) imaging.
Figure 7.2 illustrates the three cases studied: BBBS, OOBS and BOOS. The nomenclature from (Masri et al. 2012) is kept, where 'B' indicates the presence of a baffle plate, 'O' indicates its absence and 'S' stands for the small central obstacle located after the grids. The three configurations correspond to distinct scenarios of flame acceleration. In configuration BBBS, the transition takes place in the early stages of the flame development, resulting in a strong overpressure. Case OOBS is characterized by a long laminar phase, once obstacles are placed far away of the ignition point. In case BOOS, after passing the first baffle, the flame is relaminarized before reaching the central obstacle. This set of configurations seems appropriate to validate the dynamic combustion model, once the flame characteristics strongly differ from case to case.

7.4 Chemical scheme

The fuel will be identified to pure propane in the following. Detailed chemistry mechanisms for propane/air combustion such as GRI-MECH 3.0 (Smith et al.

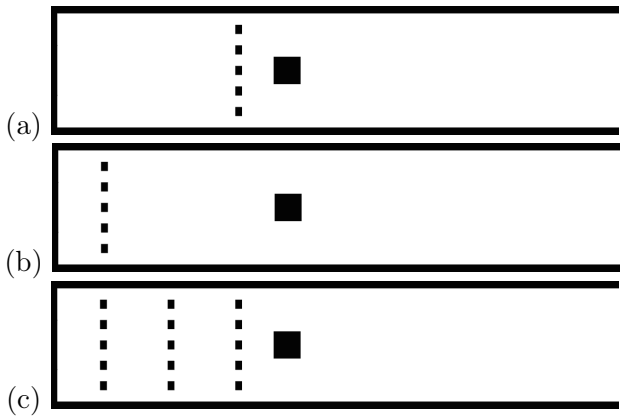

Figure 7.2: *Studied configurations (a) OOBS, (b) BOOS and (c) BBBS.*

1999) involve more than 50 species and 350 reactions and, as a result, their implementation in turbulent flame simulations turn out to be prohibitive. A solution is to use reduced chemical schemes that reproduce the same laminar flame speed and burnt gas temperature as the detailed one. The two-step reduced chemical mechanism developed by Quillatre et al. (2013) is retained here:

$$C_3H_8 + 3.5O_2 \longrightarrow 3CO + 4H_2O \tag{7.6}$$

$$CO + 0.5O_2 \longleftrightarrow CO2 \tag{7.7}$$

The corresponding reaction rate expressions are given by:

$$q_1 = A_1 \exp\left(\frac{-E_{a1}}{RT}\right)\left(\frac{\rho Y_{C_3H_8}}{W_{C_3H_8}}\right)^{n^1_{C_3H_8}}\left(\frac{\rho Y_{O_2}}{W_{O_2}}\right)^{n^1_{O2}} \tag{7.8}$$

$$q_2 = A_2 \exp\left(\frac{-E_{a2}}{RT}\right)\left[\left(\frac{\rho Y_{CO}}{W_{CO}}\right)^{n^2_{CO}}\left(\frac{\rho Y_{O_2}}{W_{O_2}}\right)^{n^2_{O2}} - \frac{1}{K_e}\left(\frac{\rho Y_{CO_2}}{W_{CO_2}}\right)^{n^2_{CO_2}}\right] \tag{7.9}$$

where the pre-exponential factor, the activation energy and the model exponents are summarized on Table 7.1 for each equation. K_e is the equilibrium constant for the second reaction. The corresponding laminar flame properties are listed in Table 7.2.

The Lewis number Le_k of species k measures the competition between thermal and mass diffusion effects: $Le_k = D_T/D_k$, where D_T and D_k denote respectively the thermal and mass diffusivities. Assuming unity Lewis numbers is common in reactive CFD codes, but this simplification not only imposes the same thermal and mass diffusivities for all species but also strongly modifies

n	Coefficients	A [cgs units]	E_a [cal/mole]
1	$n^1_{C_3H_8} = 0.55$ $n^1_{O_2} = 0.9$	1.33×10^{12}	4.15×10^4
2	$n^2_{CO} = 1.0$ $n^2_{O_2} = 0.5$ $n^2_{CO_2} = 1.0$	4.5×10^{10}	2.0×10^4

Table 7.1: *Two-step reduced chemical mechanism for $C_3H_8 - Air$. Coefficients for the Arrhenius formulation (Quillatre et al. 2013).*

S_L [m/s]	δ^0_L [mm]	T_b [K]
0.383	0.341	2300

Table 7.2: *Laminar flame properties for the given mixture at equivalence ratio $\phi = 1.0$, $P_{atm} = 101325\,Pa$ and $T_{atm} = 300\,K$. S_L, δ^0_L and T_b stand for the laminar flame speed, the laminar flame thickness based on the temperature gradient and the burnt gas temperature, respectively.*

the flame response to stretch. Actually, in the limit of small stretches, the consumption speed S_C (defined as the integral of the fuel burning rate across the flame front) is given by (Bush and Fendell 1970; Clavin 1985):

$$\frac{S_C}{S_L} = 1 - \mathcal{L}^c_a \frac{\kappa}{S_L} \tag{7.10}$$

where $\kappa = (1/S)dS/dt$ is the flame stretch, S being the flame surface area. $\mathcal{L}^c_a$ is the Markstein length and is linked to the Lewis number through the following expression (Clavin and Joulin 1983):

$$\mathcal{L}^c_a = \frac{1}{2}\zeta\delta^0_L(Le_F - 1)\frac{T_f}{T_b - T_f}\int_0^{(T_b-T_f)/T_f}\frac{\ln(1+x)}{x}dx \tag{7.11}$$

where T_b and T_f are the burnt and fresh gas temperatures, respectively, and δ^0_L is the unstretched flame thickness. The parameter $\zeta = (T_b - T_f)T_a/T_b^2$ measures the activation energy, T_a being the activation temperature ($T_a = E_a/R$, R being the perfect gas constant).
Equations (7.10) and (7.11) show that the Lewis number has a direct influence on the consumption speed when the flame is stretched. The consumption speed of a fuel with $Le > 1$ (C_3H_8 for instance) will be significantly reduced for

high curvatures, as typically encountered in the early times following ignition (Quillatre et al. 2013).
The assumption of a unity Lewis number is too restrictive for the present configuration as shown in (Quillatre et al. 2011). Moreover, the thickening operation introduced by the TFLES model affects the flame response to stretch through the flame thickness entering Eq. (7.11), reducing the consumption speed and the burnt gas temperature. This issue is discussed in details by Quillatre (2014). To overcome this problem, the author proposed to keep the quantity $\delta_L^0(Le_k - 1)$ constant. Therefore, when using the TFLES model, the Lewis number is modified (Le_K^*) to preserve the flame response to stretch:

$$\mathcal{F}\delta_L^0(Le_k^* - 1) = \delta_L^0(Le_k - 1) \tag{7.12}$$

giving:

$$Le_k^* = 1 + \frac{Le_k - 1}{\mathcal{F}} \tag{7.13}$$

In our simulations, a constant Prandtl number is specified ($Pr = 0.68$ herein), meaning that Schmidt numbers become:

$$Sc_k^* = Pr + \frac{Sc_k - Pr}{\mathcal{F}} \tag{7.14}$$

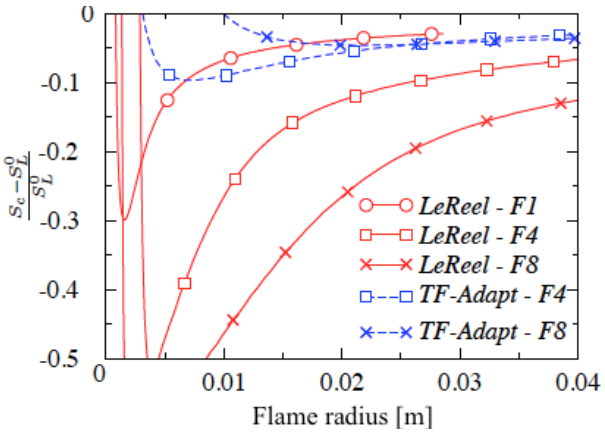

Figure 7.3: *Normalized consumption speed as a function of the flame radius for different thickening factor with and without correction. Real transport coefficients* $\mathcal{F} = 1$ *(—◯—), Transport coefficients without correction for* $\mathcal{F} = 4$ *(—×—) and* $\mathcal{F} = 8$ *(—□—), and with correction for* $\mathcal{F} = 4$ *(– □ –) and* $\mathcal{F} = 8$ *(– ◯ –). From Quillatre (2014).*

The proposed procedure is verified and validated by simulating a cylindrical laminar flame, which is representative of the first moments after ignition. Figure

7.3 shows the normalized consumption speed as a function of the flame radius for different thickening factors with and without correction. When the flame is thickened, the effect of stretching on the flame is amplified and its consumption speed is drastically reduced. However, when Lewis (Eq. 7.13) and Schmidt (Eq. 7.14) numbers are corrected, this discrepancy is remarkably reduced.
Table 7.3 gives real ($\mathcal{F} = 1$) and modified ($\mathcal{F} = 5$, Eq. 7.13) Lewis numbers. Corresponding Schmidt numbers, computed from Eq. (7.14), can be found in Table 7.4.

Lewis number/species	CH_4	H_2O	CO_2	CO	O_2	N_2
Real (Giovangigli 1999)	1.825	0.8	1.39	1.103	1.087	1.068
Adapted ($\mathcal{F} = 5$)	1.165	0.96	1.08	1.020	1.017	1.014

Table 7.3: *Table of real ($\mathcal{F} = 1$) and modified ($\mathcal{F} = 5$, Eq. 7.13) Lewis numbers.*

Schmidt number/species	CH_4	H_2O	CO_2	CO	O_2	N_2
Real (Giovangigli 1999)	1.241	0.544	0.945	0.750	0.739	0.726
Adapted ($\mathcal{F} = 5$)	0.792	0.653	0.733	0.694	0.692	0.689

Table 7.4: *Table of real ($\mathcal{F} = 1$) and modified ($\mathcal{F} = 5$, Eq. 7.14) Schmidt numbers.*

7.5 Preliminary results on a two-dimensional configuration

In this work, the massively parallel AVBP solver (Schonfeld and Rudgyard 1999) is employed to solve the unsteady compressible and reactive multi-species Navier-Stokes equations on unstructured grids. The main advantage of 2D simulations is that they do not demand huge computational resources and a sensitivity analysis is easily performed. The authors are aware of the limitations introduced by two-dimensional simulations, which does not allow direct comparison with experiments. The only objective of this simple test case is to clarify important points and numerical constraints. The influence of the following parameters are investigated:

- boundary conditions
- mesh resolution
- numerical scheme
- inner cut-off length scale δ_c
- transport modeling

7.5.1 Numerical set-up for the 2D configuration

The computational domain is 250 mm long and 50 mm wide. Only the most turbulent geometry, BBBS (three ranges of baffle plates and a square section obstacle), is discussed.
Table 7.5 indicates all bi-dimensional test-cases studied with their respective numerical conditions, while Table 7.6 summarizes the five grids employed to run the simulations. First of all, the 2D-DNS are analyzed. The influence of wall conditions is investigated. For the atmosphere outlet, Navier-Stokes Characteristic Boundary conditions (NSCBC) (Poinsot and Lele 1992) are prescribed. The initial flame kernel radius is set to $r_i = 10$ mm. This technique has been employed in other studies (Quillatre et al. 2013; Vermorel et al. 2017) and presents the advantage of initializing the combustion process without any complex transient phase. For example, the distribution of temperature at a radius, r, from the ignition point is defined as:

$$\widetilde{T}(r) = T_{ad}\left\{1 - \left[0.5 + 0.5\tanh\left(\frac{r - r_i}{\delta_r}\right)\right]\right\} \tag{7.15}$$

The temperature within the ignition radius is set to the adiabatic flame temperature $T_{ad} = 2275$ K. The initial numerical flame thickness $\delta_r = \mathcal{F}\delta_L^0$. The thickening factor is set to $\mathcal{F} = n\Delta_x/\delta_L^0$, n being the number of cells used to resolve the flame front ($n = 5$ in the present calculations).

Simulation	Mesh	$\mathcal{F}$	Numerical scheme	Boundary conditions	δ_r [mm]	δ_c	Transport coefficients	ΔP_{num} [mbar]	Deviation [%]
2D-DNS1	Very fine	1	TTGC	Adiab/no-slip	0.34	–	Real	495	–
2D-DNS2	Very fine	1	TTGC	Isot/no-slip	0.34	–	Real	405	−18
2D-LES1	Fine	2	TTGC	Adiab/no-slip	0.68	δ_L^0	Adapted	479	−3
2D-LES2	Normal	4	TTGC	Adiab/no-slip	1.36	δ_L^0	Adapted	495	0
2D-LES3	Coarse	5	TTGC	Adiab/no-slip	1.70	δ_L^0	Adapted	497	+0.4
2D-LES4	Very coarse	7	TTGC	Adiab/no-slip	2.38	δ_L^0	Adapted	366	−26
2D-LES5	Normal	4	TTGC	Adiab/no-slip	1.36	$2\delta_L^0$	Adapted	342	−31
2D-LES6	Normal	4	TTGC	Adiab/no-slip	1.36	δ_L^0	Not-Adapted	373	−25
2D-LES7	Normal	4	LW	Adiab/no-slip	1.36	δ_L^0	Adapted	410	−17

Table 7.5: *Details of two-dimensional simulations and numerical parameters. $\mathcal{F}$ stands for the thickening factor, δ_c for the inner cut-off and ΔP_{num} for the maximum overpressure found numerically. TTGC: two-step Taylor-Galerkin scheme (Colin and Rudgyard 2000), LW: Lax-Wendroff scheme (Lax and Wendroff 1964).*

2D meshes	N_{Cells} [M]	N_{Nodes} [M]	Δ_x [mm]	$\mathcal{F}$
Very fine	5.47	2.74	0.07	1
Fine	1.46	0.73	0.14	2
Normal	0.35	0.18	0.28	4
Coarse	0.24	0.12	0.34	5
Very coarse	0.11	0.06	0.5	7

Table 7.6: *Details of numerical meshes. N_{Cells} stands for the number of cells and N_{nodes} for the number of nodes. Δ_x denotes the grid spacing and $\mathcal{F}$ the thickening factor.*

Then, numerical aspects of the 2D-LES are investigated. The influence of mesh size, inner cut-off, transport coefficients and numerical schemes are considered. For the 2D-LES, the dynamic Smagorinsky model (Germano et al. 1991) closes the sub-grid stress tensors. This choice was made because the WALE (Nicoud and Ducros 1999) model, used in our 3D LES, is not conceived for 2D simulations.

7.5.2 Analysis of the 2D-DNS1

The flame propagation and the vorticity field are shown in Fig. 7.4 for different moments of the simulation 2D-DNS1 ($t = 4, 4.5, 5, 5.5, 6, 6.5$ ms). At early stages, the flame is laminar. The kernel moves gradually through the first range of obstacles and the flame, perfectly symmetrical and still laminar, starts to roll up. The expanding gases generate vortex cores behind the baffle plates that interact with the flame front subsequently. After $t = 5$ ms, the flow symmetry is broken. This flame induced flow field increases turbulence, which in turn feeds the combustion, increasing the flame speed and the pressure inside the domain. Vortices interact strongly with the flame front and are essential to capture the correct flame behavior. Note that, even at the initial moments, when the flame is still at the first grid, turbulent structures are generated in the wake of the other obstructions (Fig. 7.4a). This limits the interest of mesh adaptation techniques, i.e. refine only in the flame region and degenerate the mesh elsewhere. Therefore, to perform an accurate LES, the mesh should be sufficiently fine and homogeneous, in order to capture these phenomena that are inter-correlated.

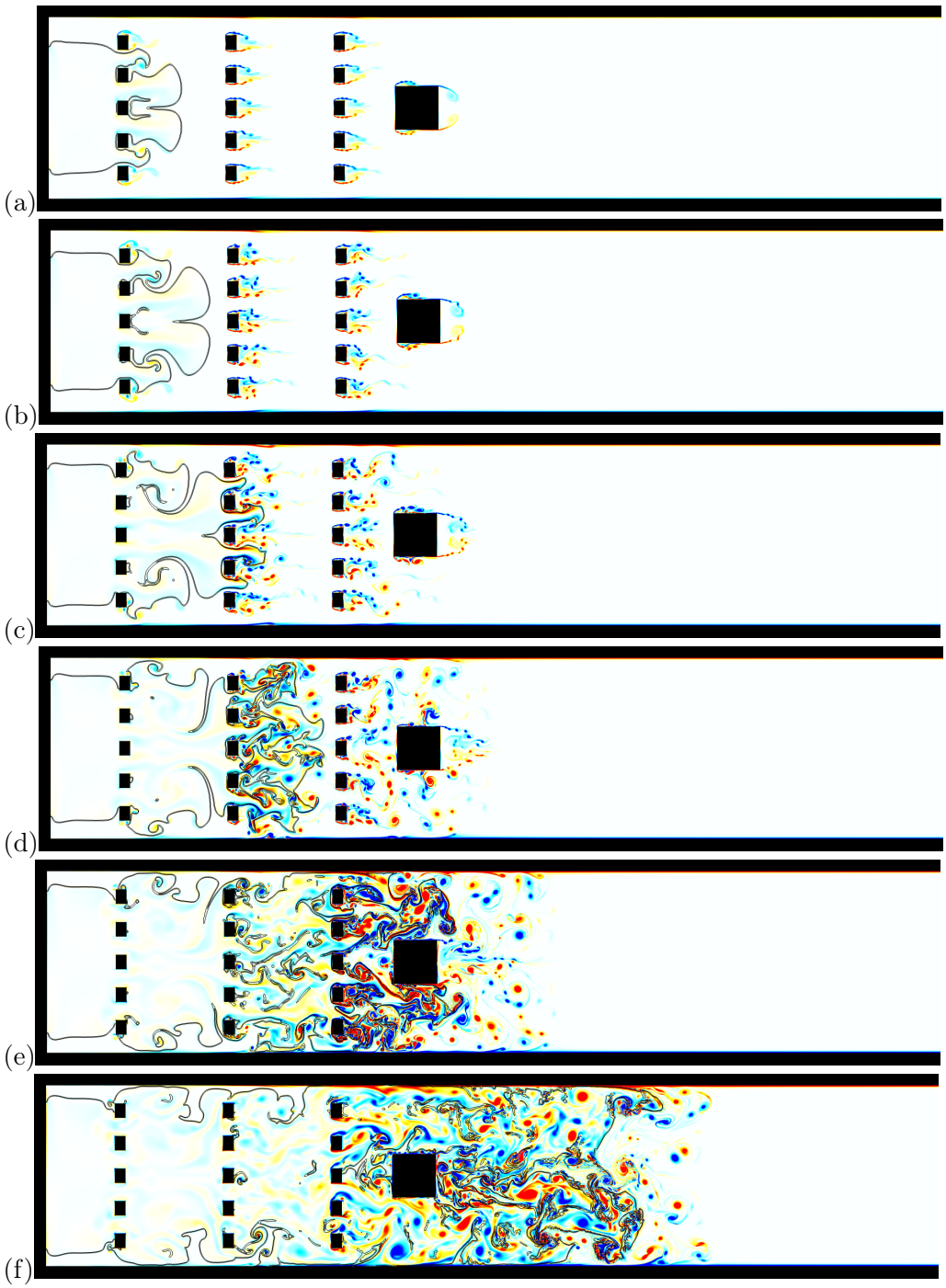

Figure 7.4: *Snapshots of the vorticity field with iso-contours of the progress variable ($c = 0.2$ and $c = 0.8$) that indicates the flame front for: (a) $t = 4$ ms, (b) $t = 4.5$ ms, (c) $t = 5$ ms, (d) $t = 5.5$ ms, (e) $t = 6$ ms and , (f) $t = 6.5$ ms. The red color corresponds to $\Omega_z = 5 \times 10^4$ s^{-1}, while blue corresponds to $\Omega_z = -5 \times 10^4$ s^{-1}. Simulation 2D-DNS1.*

7.5.3 Influence of the boundary conditions

The reference case assumes no-slip and adiabatic walls, once the deflagration takes place in a very short period of time (7 ms for the 2D case). Another test was made with isothermal walls at temperature 300 K. A reduction of 18 % of the maximum overpressure is reported (Fig. 7.5 and Table 7.7) and is linked to the fact that burnt gases are cooled by the lower wall temperature, influencing the expanding rate and, consequently, the pressure inside the combustion chamber. This effect should be amplified when dealing with three-dimensional configurations, due to a more significant surface to volume ratio. Therefore, simulations assuming adiabatic walls should predict higher pressures than simulations considering isothermal walls. We conclude that to predict the maximum overpressure inside an explosion chamber, boundary conditions must be specified with care.

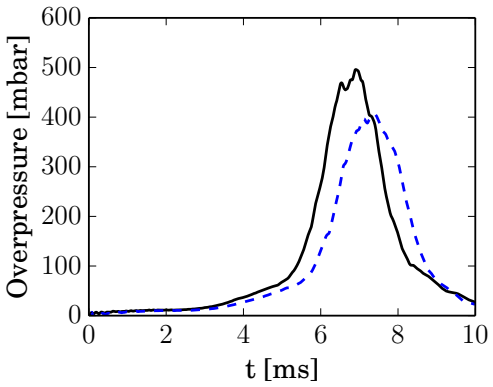

Figure 7.5: *Comparison of overpressure signals for different 2D-DNS: (——) 2D-DNS1 (adiabatic/no-slip walls); (– – –) 2D-DNS2 (isothermal/no-slip walls).*

7.5.4 Influence of the mesh resolution

The influence of the mesh resolution and, consequently, the thickening factor $\mathcal{F}$ is now analyzed ($\mathcal{F} = n\Delta_x/\delta_L^0$, with $n = 5$). Figure 7.6 shows the overpressure evolution inside the combustion chamber for different values of $\mathcal{F}$. For $\mathcal{F} \leq 5$, the reference overpressure obtained from DNS is well predicted by the LES, whereas for $\mathcal{F} = 7$, the mesh is too coarse to capture properly the dynamics of the flow. As a matter of fact, two key points must be highlighted: *(i)* the mesh has to be reasonably fine so that two flame fronts can pass between the obstacles (see Fig. 7.7) and *(ii)* it needs to reproduce the essential vortex structures of the wakes. Considering the first point, if the flame front must be resolved within 5 grid points, a mesh size of $\Delta_x = 0.5$ mm, resulting in 10 points between the strips, is clearly not sufficient to carry out an accurate LES. The 2D-LES indicates that at least 15 points is needed between each grid. For

the second point, Fig. 7.7 shows that the vorticity intensity is decreased, when using the coarsest mesh ($\mathcal{F} = 7$). As discussed in subsection 7.5.2, one cannot simulate correctly this type of flow if the vortices are mispredicted. The mesh corresponding to $\mathcal{F} = 5$ is still able to capture the vortices behind the obstacles and is kept to run the 3D simulations.
Note that the pressure peak instant do not match and depends on the simulation. This point is linked to the fact that the response time of the flame is not the same for different thickening factors. There is also the response of the dynamic model, which by construction forces the unresolved scales to respond as the resolved ones. The unsteady response of the dynamic model will be studied in a near future and is not treated in this work. For these reasons, LES results are only based on the magnitude of the overpressure signal.

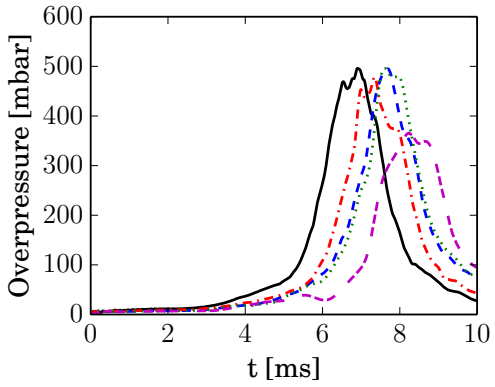

Figure 7.6: *Comparison of overpressure signals for several 2D-LES using different mesh resolutions: (——) 2D-DNS1 ($\mathcal{F} = 1$); (—·—) 2D-LES1 ($\mathcal{F} = 2$), (– – –) 2D-LES2 ($\mathcal{F} = 4$), (···) 2D-LES3 ($\mathcal{F} = 5$), (– – –) 2D-LES4 ($\mathcal{F} = 7$).*

7.5.5 Influence of the numerical scheme

The third order TTGC scheme (2D-LES2) is compared with the second order Lax-Wendroff (2D-LES7) convective scheme in Fig. 7.8. The importance of a high order numerical scheme is clear when dealing with large eddy simulations, especially in this transient configuration, where the propagation of the information is crucial and dissipative and dispersive errors may affect negatively the results. As shown in Fig. 7.8, using a less precise numerical scheme may lead to an under-estimation of 17% of the maximum overpressure. We conclude that high order schemes are essential to predict the maximum overpressure in this type of flow (at least for the present mesh).

7.5.6 Influence of the inner cut-off length scale δ_c

The inner cut-off length scale δ_c plays an important role in the prediction of the maximum overpressure, as shown in Fig. 7.8. Setting $\delta_c = \delta_L^0$, the 2D-LES2

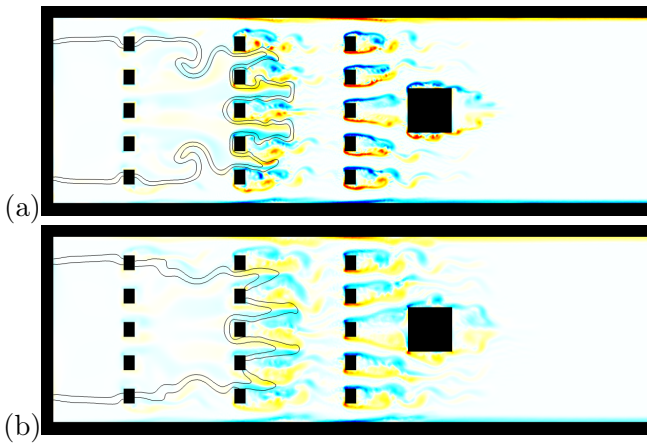

Figure 7.7: *Snapshots of the vorticity field with iso-contours of the progress variable ($c = 0.2$ and $c = 0.8$) that indicates the flame front for simulations: (a) 2D-LES3 ($\mathcal{F} = 5$, $t = 6$ ms), (b) 2D-LES4 ($\mathcal{F} = 7$, $t = 6.5$ ms). The red color corresponds to $\Omega_z = 5 \times 10^4$ s^{-1}, while blue corresponds to $\Omega_z = -5 \times 10^4$ s^{-1}.*

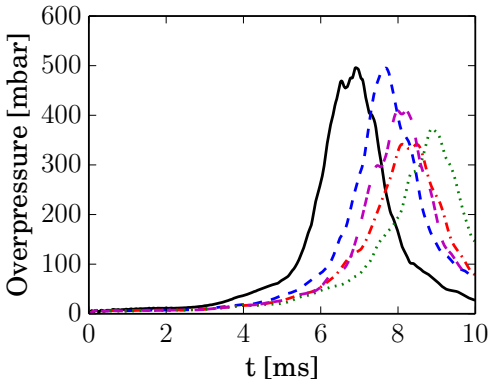

Figure 7.8: *Comparison of overpressure signals for different simulations: ( ) 2D-DNS1; ( ) 2D-LES2 (TTGC, $\delta_c = \delta_L^0$, adapted transport coefficients), ( ) 2D-LES5 ($\delta_c = 2\delta_L^0$); ( ) 2D-LES6 (non-adapted transport coefficients), ( ) 2D-LES7 (LW).*

give good results, if compared to the 2D-DNS1. On the other hand, changing $\delta_c = 2\delta_L^0$ (2D-LES5) highly impacts the results and the maximum pressure value is underestimated by about 30 % (Table 7.5).

Note that δ_c, which is the minimum curvature radius of the flame front, cannot be determined from a dynamic procedure, once it corresponds to scales lost in the filtering process ($\Delta > \delta_c$). Volpiani et al. (2016) showed the influence of this parameter by simulating a turbulent jet flame. Veynante and Moureau (2015) carried out a priori analysis and showed that the inner cut-off length scale is close to the laminar flame thickness, in agreement with the present study. Gülder and Smallwood (1995) suggested that the inner cut-off length

scale may depend on the Karlovitz number. A more refined model for this physical parameter requires modeling of additional terms, such as the sub-grid scale turbulence intensity, and a simpler formulation is preferred here.

7.5.7 Influence of the transport modeling

Figure 7.8 shows the overpressure evolution inside the combustion chamber for simulations 2D-DNS1 (reference), 2D-LES2 ($\mathcal{F} = 4$ with modified transport coefficients) and 2D-LES6 ($\mathcal{F} = 4$ without modified transport coefficients). In accordance with (Quillatre et al. 2011) and Fig. 7.3, results indicate that an adapted transport model reproducing the response of the thickened flame to stretch is essential to capture the correct overpressure. All 3D simulations have been carried out using the adapted transport model.

7.6 Numerical set-up for the 3D LES

The three-dimensional computational domain comprises the combustion chamber and a plenum attached to its open end. This plenum, which mimics the atmosphere, allows a better handling of acoustic waves, especially after the peak pressure and avoids imposing a boundary condition at the exit plane of the chamber. Simulations are performed with the two-step Taylor-Galerkin weighted residual central distribution scheme, third order in time and space (TTGC) (Colin and Rudgyard 2000) that complies with the necessity of low-dissipation for LES. The walls of the chamber and obstacles are modeled using isothermal law of the wall (Kader 1981). This type of boundary condition have also been employed in other studies by Masri and co-workers (Gubba et al. 2008; Gubba et al. 2009; Gubba et al. 2011). Nevertheless, a comparison with adiabatic no-slip walls classically used in this kind of configuration (Di Sarli et al. 2009; Di Sarli et al. 2009; Di Sarli et al. 2010) is also performed. For the atmosphere outlet, Navier-Stokes Characteristic Boundary conditions (NSCBC) (Poinsot and Lele 1992) are prescribed. The Wall Adapting Local Eddy (WALE) model (Nicoud and Ducros 1999) describes sub-grid stress tensors. Abdel-Raheem et al. (2015) investigated the influence of initial conditions in the same combustion chamber (BBBS) for a premixed hydrogen/air mixture. The shape of the ignition kernel was varied from hemispherical to spherical and the ignition energy was varied by increasing the radius from 2 to 5 mm. They concluded that the predicted overpressure is independent of the ignition radius and that the only change is in the timing of the occurrence of the pressure peak. Thus, results are not affected at least for $r_i \leq 5$ mm. In our 3D cases, calculations are initialized by a small sphere of burnt gases (radius 5 mm) at the ignition point (Fig. 7.9).

The LES mesh contains about 60M cells/11M nodes and the typical cell size inside the chamber is $\Delta_x \approx 0.35$ mm, corresponding to a thickening factor $\mathcal{F} \approx 5$. The choice of the grid spacing takes into consideration the extensive study concerning the bi-dimensional test case.

The total wall clock simulation time is about 60 h on 4096 cores of an IBM BlueGene/Q machine for the 3D LES cases.

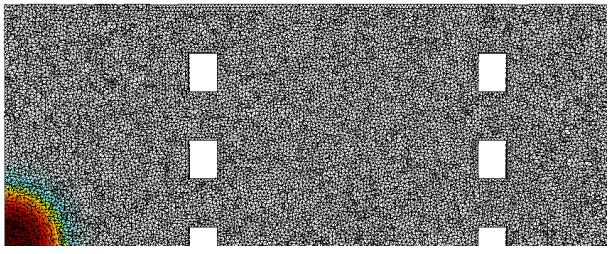

Figure 7.9: *Zoom on the mesh and detail of the initial condition. The semi sphere in red indicates the region where temperature is higher than 1000 K. For sake of clarity, only half of the $y = 0$ plane is shown.*

7.7 A posteriori tests on the 3D LES of the small-scale experiment

Numerical results are now compared to experimental data for three different geometries. They are discussed in terms of flow field visualization, over-pressure, flame surface and model parameter evolutions.
The overpressure signal is extracted from a probe located at the closed end of the chamber, as in experiments (indicated in Fig. 7.1). Note that LES results are not discussed in terms of timing criteria but only on the magnitude and trend of the overpressure signal. Firstly, because numerical parameters such as the initial flame kernel radius influences the timing of the peak location. Secondly, because of the variability of the experimental results. Different experimental realizations provided similar results for the maximum pressure and its rate of change but larger variations were observed for the time to reach the pressure peak. Therefore, in order to overcome experimental and numerical uncertainties, experimental signals have been shifted in time to match the LES peak. The same procedure is used experimentally.
Some definitions are now introduced. Resolved (S_r) and total (S_t) flame surfaces are estimated here as (Volpiani et al. 2016):

$$S_r(t) = \int_{\mathcal{V}} |\nabla \widetilde{c}| \, d\mathcal{V} \tag{7.16}$$

$$S_t(t) = \int_{\mathcal{V}} \Xi_\Delta \, |\nabla \widetilde{c}| \, d\mathcal{V} \tag{7.17}$$

The temporal evolution of these quantities provides information on the flame dynamics. The spatially averaged $\overline{\beta}$ parameter is defined as:

$$\overline{\beta}(t) = \frac{\int_{\mathcal{V}_f} \beta(x,y,z,t) d\mathcal{V}}{\int_{\mathcal{V}_f} d\mathcal{V}} \tag{7.18}$$

where $\mathcal{V}_f$ denotes the flame volume defined as $0.05 \leq \widetilde{c} \leq 0.95$.

7.7.1 Configuration OOBS

Figure 7.10 presents snapshots of the flame front corresponding to $\widetilde{c} = 0.5$ colored by the model parameter for case OOBS. In the early stages of the flame development, when the flame is still laminar, the model parameter is close to zero as expected. When the flame starts to interact with the turbulence generated by the obstacles, the model exponent takes larger values depending on the local flame wrinkling. Differently from classical non-dynamic models which, most of the time, need some kind of tuning (Di Sarli et al. 2010), the

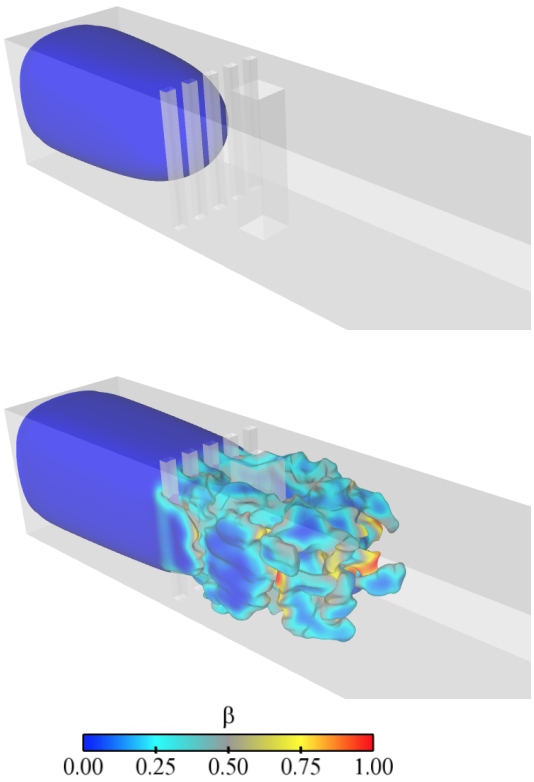

Figure 7.10: *Instantaneous snapshots of the flame front corresponding to* $\widetilde{c} = 0.5$*, obtained from simulation LES-OOBS, colored by the model parameter* β*. Instants correspond to* $t = 13.5$ *ms (top) and* $t = 15.5$ *ms (bottom).*

proposed local dynamic formulation adjusts the model parameter automatically on the fly as evidenced in Fig 7.10.

Figure 7.11 displays a sequence of images of the flame development in the middle plane $y = 0$. At the early stages, the flame is laminar and propagates with a semi-spherical shape. The expanding gases generate vortex cores behind the baffle plates that interact with the flame front subsequently (as discussed in the previous section). Finger-like structures are generated when the flame crosses the first grid. Finally, this flame induced flow field increases turbulence and combustion intensity.

Figure 7.12 shows the temporal evolution of the overpressure together with the experimental envelope for case OOBS. The LES reproduces the over-pressure peak and oscillations very well.

At early stages of the flame development, when the flame is not yet wrinkled by turbulence motions, resolved and total flame surfaces are equal and the model parameter is expected to be zero. As turbulence is generated, the sub-grid wrinkling factor increases to take into account the non-resolved flame surface.

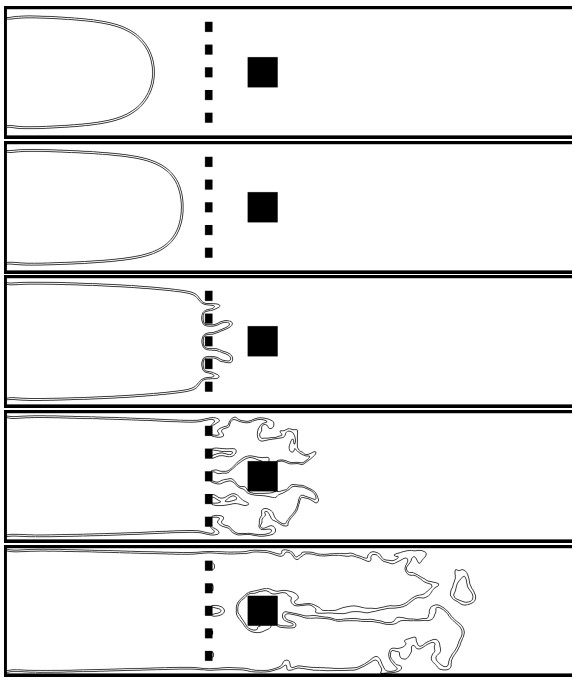

Figure 7.11: *Instantaneous snapshots of the flame front represented by iso-contours* $\widetilde{c} = 0.2$ *and* $\widetilde{c} = 0.8$ *for configuration OOBS. Instants correspond to t = 12, 13, 14, 15 and 16 ms (from top to bottom).*

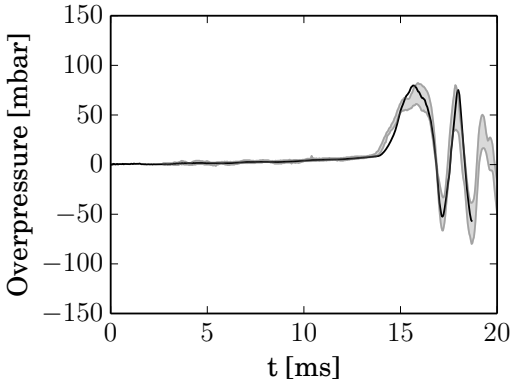

Figure 7.12: *Comparison of overpressure signals between LES (solid line) and experiments (Masri et al. 2012) (grey envelope) for configuration OOBS. Note that the experimental envelope has been shifted in time to match the LES peak.*

These observations are confirmed in Figs. 7.13 and 7.14 that display, respectively, the evolution of flame surfaces and mean model parameter as a function of the flame position defined as the maximum downstream $x-$location where the flame front is present. Passing the square obstacle, the flame accelerates and sub-grid wrinkling is detected automatically by the dynamic wrinkling factor

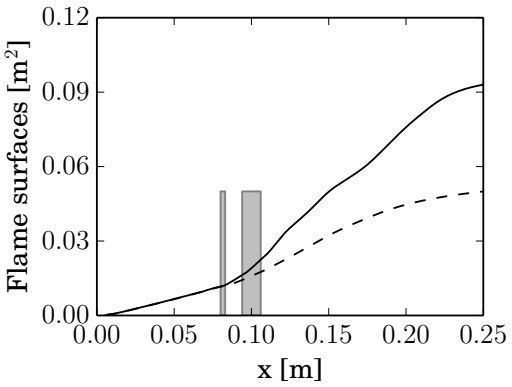

Figure 7.13: *Evolution of resolved (Eq. 7.16, dashed line) and total (Eq. 7.17, solid line) flame surfaces as a function of the flame position for configuration OOBS.*

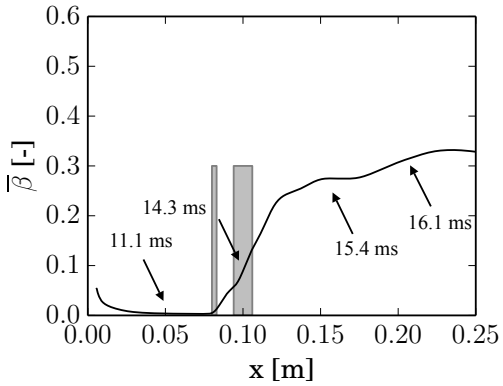

Figure 7.14: *Evolution of the spatially averaged $\overline{\beta}$ parameter (Eq. 7.18) as a function of the flame position for configuration OOBS. The instants of the simulation are also indicated in the figure.*

model.
The mean parameter $\overline{\beta}$ remains close to zero until the moment the flame reaches the grid. The slight decrease of $\overline{\beta}$ at the beginning of the simulation is linked to the initial conditions and because the model predicts some wrinkling for small spherical laminar flame kernels (Mouriaux et al. 2016). Thereafter, it takes higher values and stabilizes around $\overline{\beta} \approx 0.3$. Note the strong flame acceleration. The flame takes 14.3 ms to move 0.10 m and achieve the central obstacle. On the other hand, after turbulent transition, it takes less than 2 ms to travel the same distance (from $x = 0.10$ to $x = 0.20$ m).

7.7.2 Configuration BBBS

The flame front corresponding to $\widetilde{c} = 0.5$ colored by the model parameter for configuration BBBS in shown in Fig. 7.15. Compared to the other geometries,

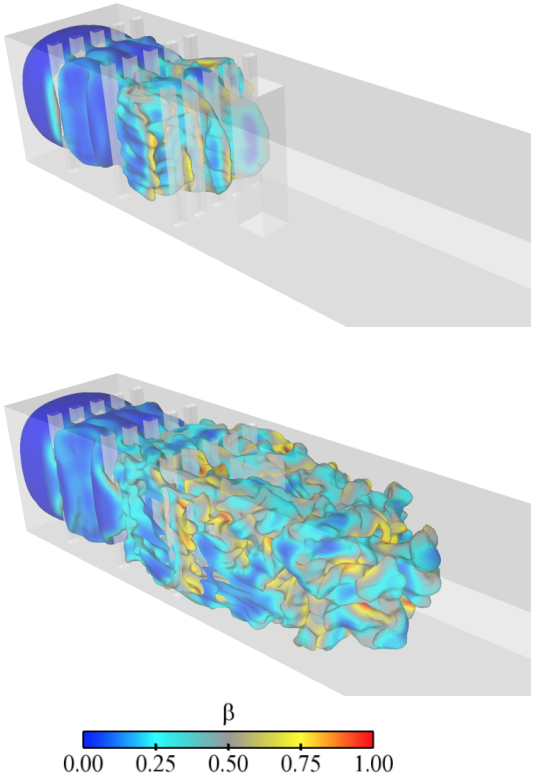

Figure 7.15: *Instantaneous snapshots of the flame front corresponding to* $\widetilde{c} = 0.5$*, obtained from simulation LES-BBBS, colored by the model parameter* β*. Instants correspond to* $t = 11.5$ *ms (top) and* $t = 12.5$ *ms (bottom).*

case BBBS combines three baffle plates and the square obstacle, leading to the largest turbulent intensity. The turbulent transition takes place when the flame reaches the second baffle plate. At this moment, the model parameter takes higher values. The flame is then strongly accelerated, resulting in a huge overpressure.

Figure 7.16 shows instantaneous snapshots of iso-contours of $\widetilde{c} = 0.2$ and $\widetilde{c} = 0.8$ for configuration BBBS. When the flame reaches the first baffle plate, it passes first through the two central passages and then through the lateral passages. At this point, the flame is practically laminar, as the turbulence generated in the wake of the first obstacle is very low (as already shown by the 2D-DNS). Then, the flame develops four finger-like structures, which are wrinkled by turbulence motions after crossing the second grid. The flame is strongly accelerated after passing the last baffle plate and square obstacle.

The temporal evolution of the overpressure signal is plotted against experimental measurements in Fig. 7.17. The LES is able to reproduce the overpressure magnitude with good accuracy. Similarly to the previous case, post-maximum

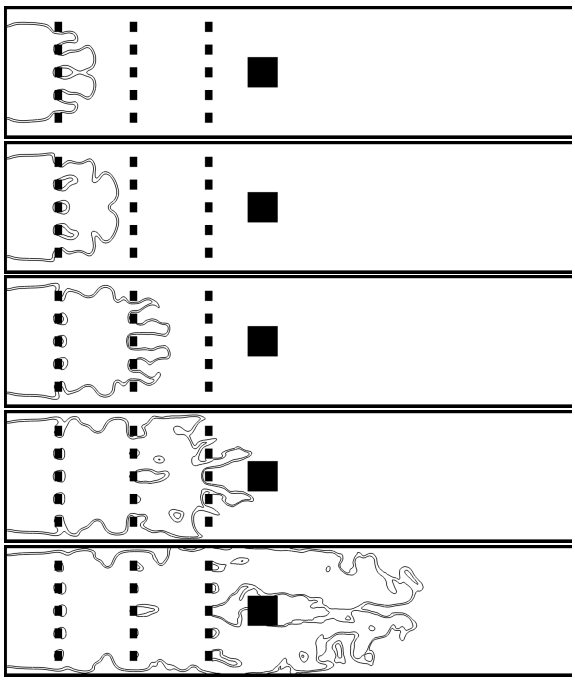

Figure 7.16: *Instantaneous snapshots of the flame front represented by iso-contours* $\widetilde{c} = 0.2$ *and* $\widetilde{c} = 0.8$ *for configuration BBBS. Instants correspond to* $t = 8.5$*, 9.5, 10.5, 11.5 and 12.5 ms (from top to bottom).*

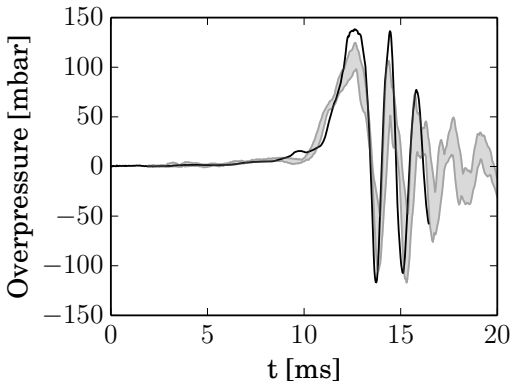

Figure 7.17: *Comparison of overpressure signals between LES (solid line) and experiments (Masri et al. 2012) (grey envelope) for configuration BBBS.*

overpressure oscillations are correctly captured as well. As expected, this configuration present the strongest overpressure among the three studied cases. This is due to the high level of turbulence in the chamber, as already mentioned by Masri et al. (2012).

Figure 7.18 shows the evolution of resolved and total flame surfaces as a function of the flame position. Resolved and total flame surfaces are similar until the

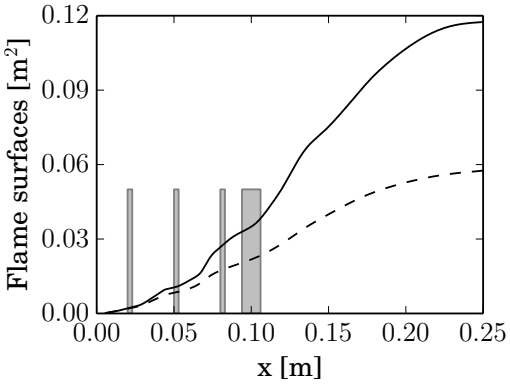

Figure 7.18: *Evolution of resolved (Eq. 7.16, dashed line) and total (Eq. 7.17, solid line) flame surfaces as a function of the flame position for configuration BBBS.*

flame reaches the second grid approximately. Then, turbulence is increased, and the dynamic wrinkling factor model captures the sub-grid flame surface. When the flame exits the chamber, the total surface is about twice the resolved flame surface.

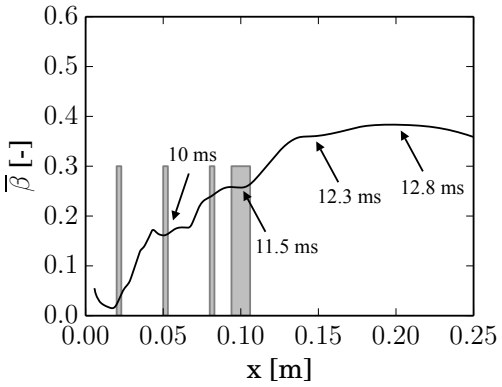

Figure 7.19: *Evolution of the spatially averaged $\overline{\beta}$ parameter (Eq. 7.18) as a function of the flame position for configuration BBBS. The instants of the simulation are also indicated in the figure.*

In Fig. 7.19, the spatially averaged parameter, $\overline{\beta}$, is plotted as a function of the flame position. For case BBBS, the model parameter is progressively increased and it takes a constant value when flame/turbulence equilibrium is reached after the obstacles. At this point, the average parameter is close to $\overline{\beta} \approx 0.4$. This value is larger than the one found in the previous configuration ($\overline{\beta} \approx 0.3$), highlighting the advantage of using a dynamic combustion model for this type of flow. Note that the flame takes about the same time as in configuration OOBS to reach $x = 0.05$ m, then it accelerates brutally: 11.5 ms (against 14.3) for $x = 0.10$ m and 12.8 (against 16.1) for $x = 0.20$ m.

7.7.3 Configuration BOOS

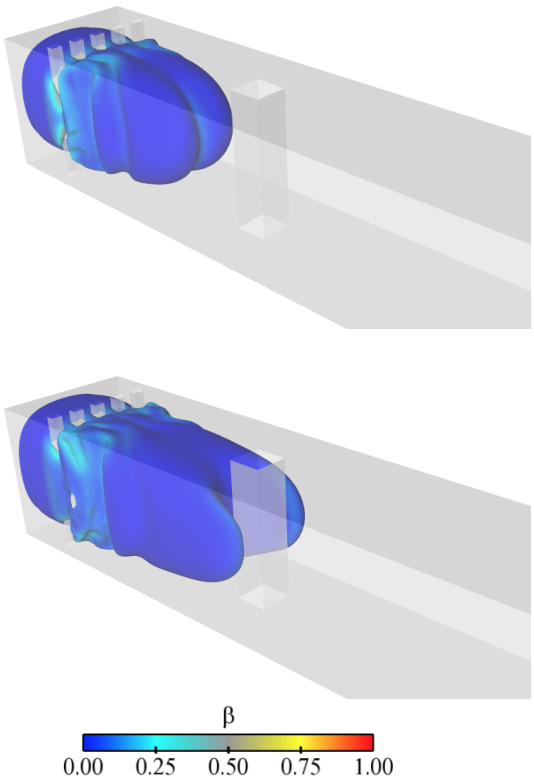

Figure 7.20: *Instantaneous snapshots of the flame front corresponding to* $\widetilde{c} = 0.5$*, obtained from simulation LES-BOOS, colored by the model parameter* β*. Instants correspond to* $t = 12$ *ms (top) and* $t = 13.5$ *ms (bottom).*

Figure 7.20 presents snapshots of the flame front corresponding to $\widetilde{c} = 0.5$ colored by the model parameter for case BOOS. In this case, the flame re-laminarizes after crossing the baffle plates placed near the ignition point. The model parameter remains close to zero even after the flame passes the central obstacle, indicating a laminar behavior.
Figure 7.21 shows LES images of the flame propagation for case BOOS. After passing the first baffle plate, the finger-like structures are generated as in case BBBS. However, the flame relaminarizes before the square obstacle, meaning that the turbulence intensity generated by the first baffle is not sufficient to accelerate the flame front. Even after passing the square obstacle, the flame front remains less wrinkled than cases OOBS and BBBS.
The time history of overpressure for the LES and experimental results is plotted in Fig. 7.22. The overpressure trend and its maximum value are in good agreement with experiments, although pressure is slightly over-predicted after crossing the baffle plate. As expected, configuration BOOS presents the lower

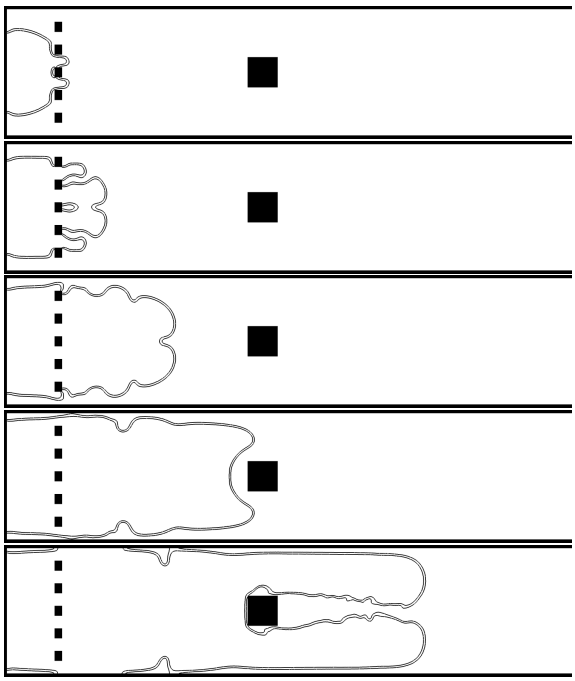

Figure 7.21: *Instantaneous snapshots of the flame front represented by iso-contours* $\widetilde{c} = 0.2$ *and* $\widetilde{c} = 0.8$ *for configuration BOOS. Instants correspond to* t *= 7, 9, 11, 13 and 15 ms (from top to bottom).*

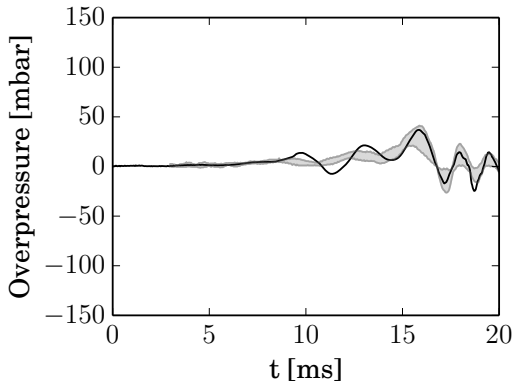

Figure 7.22: *Comparison of overpressure signals between LES (solid line) and experiments (Masri et al. 2012) (grey envelope) for configuration BOOS.*

overpressure among the three configurations. The present model predicts the maximum pressure value within the experimental envelope. Gubba et al. (2011) obtained a value 41 % greater than experiments (see Table 7.7), showing the challenge to correctly reproduce this configuration. For all other cases, they obtained good agreement with experimental data.
Figures 7.23 and 7.24 display the evolution of flame surfaces and mean model

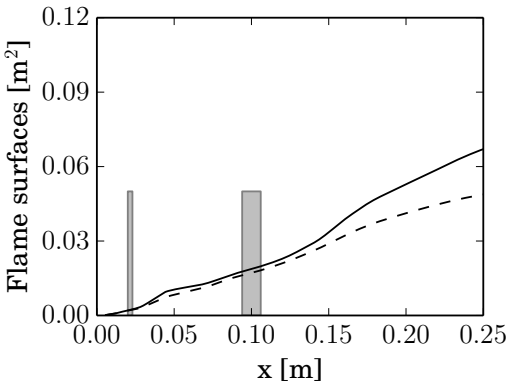

Figure 7.23: *Evolution of resolved (Eq. 7.16, dashed line) and total (Eq. 7.17, solid line) flame surfaces as a function of the flame position for configuration BOOS.*

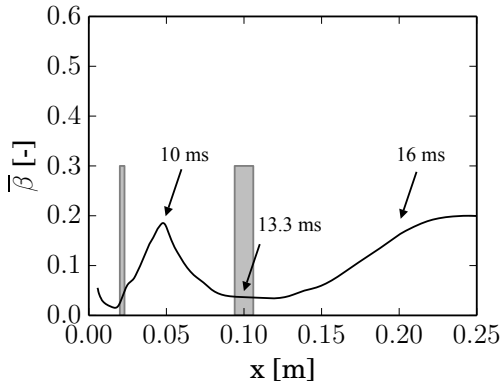

Figure 7.24: *Evolution of the spatially averaged $\overline{\beta}$ parameter (Eq. 7.18) as a function of the flame position for configuration BOOS. The instants of the simulation are also indicated in the figure.*

parameter as a function of the flame position, respectively. For case BOOS, the flame is well resolved and remains laminar even after crossing the first grid. Note that the model parameter increases after the first grid, but then it decreases close to zero, indicating the relaminarization of the flame (Fig. 7.24). Only at the end of the chamber, the flame accelerates and the present model detects some sub-grid wrinkling (Fig. 7.23). Note that, at the beginning, the flame goes barely faster than case OOBS, but at the end they leave the chamber exit practically at the same instant.

7.7.4 Adiabatic vs Isothermal boundary conditions

A secondary goal of this study is to point out that numerical results are very sensitive to boundary conditions and they have to be chosen with care. Adiabatic no-slip walls are easy to implement in a numerical code and are therefore

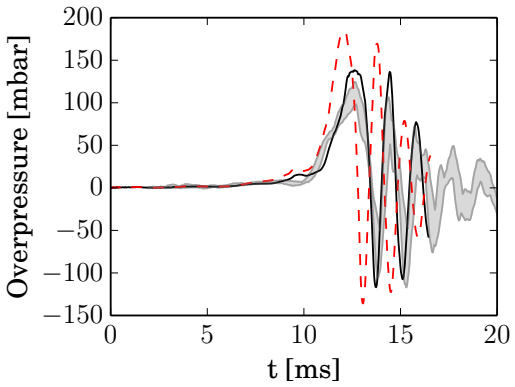

Figure 7.25: *Comparison of overpressure signals between LES using isothermal wall-law (solid line), LES using no-slip adiabatic walls (dashed line) and experiments (grey envelope) for configuration BBBS.*

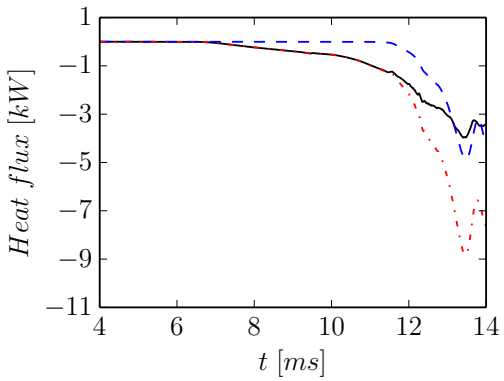

Figure 7.26: *Heat fluxes as a function of simulation time: (——) heat flux through obstruction walls; (– – –) heat flux through chamber walls and (–·–) sum of heat fluxes.*

largely employed to simulate deflagrating flames (Di Sarli et al. 2009; Di Sarli et al. 2009; Di Sarli et al. 2010; Quillatre et al. 2013). Hence, computations assuming adiabatic no-slip walls are also performed and compared to isothermal walls using a wall-law (Kader 1981). As a matter of fact, heat transfer may play an important role in this type of configuration, especially in the most turbulent geometry (BBBS) as confirmed by the two-dimensional DNS. Figure 7.25 shows that the correct overpressure is predicted only when using isothermal walls. When heat transfer is neglected, the thermal expansion of hot gases are much more intense, inducing a higher flame acceleration and overpressure. Figure 7.26 shows the heat loss distribution as a function of the simulation time. Initially, from $t = 7$ to $t = 11.5$ ms (see Fig. 7.16), heat transfer happens essentially through the obstruction walls. Heat losses through the chamber walls become important and of the same order of magnitude as the losses due

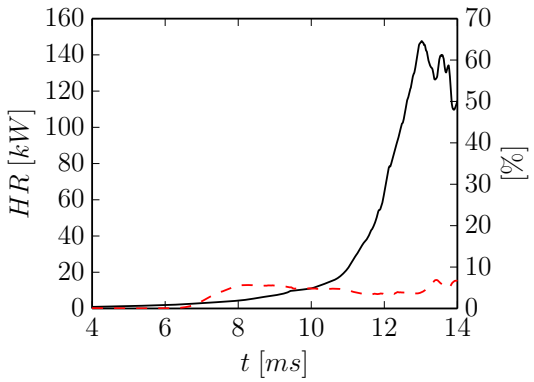

Figure 7.27: *Heat released by the flame as a function of time (——) and percentage lost by the cold walls (- - -).*

to the baffle plates only when the flame is fully turbulent and passes the square obstacle. Around $t = 13.1$ ms, the flame exits the combustion chamber. The heat released by the flame is plotted as a function of time in Fig. 7.27. It can be seen that the percentage of heat losses due to the cold walls is around 5% of the total heat released.

7.7.5 Summary

Simulation	ΔP_{exp}	ΔP_{num}	Gubba et al. (2011)
LES-OOBS	61 - 82	80	71
LES-BOOS	21 - 41	37	58
LES-BBBS	98 - 125	138	125

Table 7.7: *Summary of simulations and geometries studied. ΔP_{exp} [mbar] and ΔP_{num} [mbar] stand for the maximum overpressure found experimentally and numerically, respectively. Values obtained by Gubba et al. (2011) are also shown for comparison.*

Table 7.7 summarizes the different cases studied. It also compares measurements (Masri et al. 2012) and numerical predictions given by the present study and the ones found in the literature (Gubba et al. 2011). The present dynamic model gives excellent results for all three simulated cases. In addition, with a formulation a priori simpler and cheaper than the dynamic FSD model (Knikker et al. 2004), over-pressure predictions are as good as, or even better

than the ones found by Gubba et al. (2011).

7.8 Conclusion

Simulations of turbulent premixed flames propagating past repeated obstacles are performed and the dynamic wrinkling factor model is validated using a posteriori analysis. Three distinct configurations studied experimentally by Masri et al. (2012) are treated in this article. Configuration BBBS presents the larger number of obstacles, three grids followed by a small square obstruction, displaying the stronger overpressure. Case OOBS presents the second highest pressure and is characterized by a long laminar phase, once obstacles are placed far away of the ignition point. In case BOOS, after crossing the first baffle, the flame front is relaminarized before reaching the central obstacle leading to the lowest observed overpressure. Large eddy simulations reproduce all phases of the flame propagation extremely well and are in agreement with discussions presented in (Masri et al. 2012).
An extensive sensitivity analysis has also been carried out based on a two-dimensional geometry. Important points of numerical simulations have been discussed: initial and boundary conditions, numerical schemes, grid refinements, transport coefficients and inner cut-offs. Using consistent information is vital to obtain accurate results.
The dynamic fractal-like model is able to capture both laminar and turbulent flame regimes. At early stages of the flame development, a laminar flame propagates in a flow essentially at rest and the model parameter is close to zero. Then, the flame front interacts with the obstacles, increasing turbulence and combustion intensity and the model parameter takes higher values at these stages. Hence, when using the dynamic formulation, the model parameter is computed on the fly and varies in time and location. Therefore, it presents a huge advantage if compared to classical non-dynamic models, as *ad hoc* tuning is no longer necessary. We conclude that LES is able to correctly estimate critical parameters of the explosion such as the overpressure and to improve understanding of this type of flows.

Acknowledgments

This work was performed using HPC resources of IDRIS under the allocation 2016-020164 made by GENCI (Grand Equipement National de Calcul Intensif). The authors would like to thank Prof. A. R. Masri for providing the experimental data.

General conclusions

The dynamic modeling adopted in this thesis relies on the generic flamelet formulation that identifies the turbulent flame as a collection of laminar flame elements. Two formulations are considered: global and local. In both cases the model parameter is computed by solving a Germano-like equation in terms of the progress variable gradients. In the first approach, the global parameter evolves only with time, while in the second one it depends on time and space coordinates.
The turbulent jet flame Chen et al. (1996), already used as a reference by Wang et al. (2011) and Schmitt et al. (2015) for the first tests using the dynamic model, was selected to perform the parametric study of the model. Analyzes using the local dynamic model show that the model parameter takes small values near the injector where the flame is quasi-laminar, and increases downstream where the flame is progressively wrinkled by turbulent motions. In terms of statistical quantities, both LES results are in good agreement with experimental data, showing that more refined experiments are indispensable to assess model performances. The influence of physical (flame wrinkling inner cut-off length scale) and numerical (test filter width, averaging procedure, filtering frequency) characteristics of the model have also been investigated in this simple configuration. The dynamic model is found to be relatively insensitive to numerical input coefficients to be provided beforehand in the code as long as the test filter size remains relatively low to avoid flame front interactions. On the other hand, the inner cut-off length scale is a parameter that may influence numerical results and a good estimate of δ_c is required.
After characterizing the model in a simple geometry, a semi-industrial configuration was studied. Experimental investigations using the PRECCINSTA burner evidenced two combustion regimes (Meier et al. 2007): a quiet flame at equivalence ratio $\phi = 0.83$ and a pulsating flame at $\phi = 0.70$. Both cases have been simulated. For the stable flame, dynamic and non-dynamic approaches capture flow and combustion statistics with good accuracy. Interestingly, the self-excited mode is reproduced only when dynamic formulations are employed. A mesh convergence proves that the observed instability is not the result of a numerical artifact and a different mechanism other than the hypothesis of imperfect mixing, as suggested by Franzelli et al. (2012), can influence the flame pulsation. Probably, leaving the model parameter free introduces a degree of

freedom in reaction rate expressions, in the same manner as the description of the mixture in the Franzelli et al. (2012) calculations, which contributes to the development of this instability. One of the observations of these simulations is that the fractal dimension of the flame surface depends on the phase pulsation. Flames propagating in a semi-confined environment are representative of an accidental explosion configuration and reliable predictions of such situations are vital for safety reasons. During an explosion, different phases may be distinguished. The flame is first ignited and propagates in a flow initially at rest. Then, a turbulent propagation takes place due to the interaction of the flame with obstacles and the turbulent motions generated by the flame itself. Non-dynamic combustion models may suffer to reproduce this kind of situation, as the model parameter may be case dependent. On the other hand, the dynamic model is perfectly suitable for this kind of situation. The local dynamic model is able to capture both laminar and turbulent flame regions. Three different scenarios of flame acceleration are investigated. The first case is characterized by a long laminar phase. In the second one the flame is the most turbulent and the highest overpressure in the vessel is observed. For the last case, the flame front is relaminarized after crossing the first row of obstacles. In all configurations, large eddy simulations (LES) predict the flow dynamics and maximum overpressure with good accuracy.
We conclude that dynamic models are a very powerful tool, once it can handle academic and industrial configurations, stationary and unsteady flames, steady state and transient regimes very precisely as discussed in this manuscript.

Perspectives

The different points developed in this thesis open the way to further developments:

- The dynamic model studied in this manuscript was used in several perfectly premixed configurations. Its extension to diffusion flames is an essential step for use in realistic industrial configurations, where mixed regimes are found. For diffusion flames, the parameter determination will probably be linked to the mixture fraction and no longer to the progress variable field, and further analyses are compulsory. Moreover, an additional challenge appears: while in the perfectly premixed regime the inner cut-off scale δ_c can be approximated by the laminar flame thickness, in the non-premixed regime, estimating this physical parameter is more critical and it may vary locally with species composition.

- A need for finer experimental data, other than statistical quantities, is observed to assess model performances. Experiments characterizing flame dynamics (for example, the temporal evolution of the flame surface) are mandatory to go further in the model validation.

- A theoretical analysis concerning the unsteady response of the dynamic model is also desired.

- Additional investigations concerning the inner cut-off length scale are also needed. It is shown that this physical parameter can influence numerical results, especially when dealing with transient configurations. The problem with a more refined model for δ_c (such the one proposed by Gülder and Smallwood (1995)) is that new unknown terms appear, such as the sub-grid scale turbulence intensity, requiring additional modeling. However, the current choice for the cut-off length scale makes possible to retain a simple and efficient formulation of the dynamic model. New experiments and direct numerical simulations have to be performed in order to determine this physical parameter.

- Finally, the study carried out for the small-scale combustion chamber (0.25 m length) using the database accomplished at University of Sydney confirmed that LES reproduces faithfully transient phenomena such as explosions. However, it is desired to extend the study to larger scales typical of buildings where an accident may unfortunately happen. To this end, simulations using the medium- (1.5 m length) and large-scale (6.1 m length) combustion chamber should also be carried out.

Appendix A

Résumé en français

Avec l'accroissement considérable de la puissance de calcul, les simulations aux grandes échelles (SGE) sont maintenant utilisées de façon routinière dans de nombreuses applications d'ingénierie. La conception de moteurs moins polluants, la réduction des coûts et temps de développement d'une chaudière industrielle, ou la prédiction des instabilités thermo-acoustiques dans une turbine à gaz, ne sont plus possibles sans l'utilisation des SGE. Cette méthode numérique est basée sur le filtrage des équations de Navier-Stokes, où seules les structures les plus énergétiques de l'écoulement sont résolues par la grille de calcul. Les effets des petites échelles, responsables de la dissipation d'énergie turbulente, sont modélisés.

Bien entendu, la capacité de prédire correctement le comportement de systèmes complexes dépend de la précision des modèles de sous-maille. Les modèles de combustion usuels sont le plus souvent basés sur une hypothèse d'équilibre entre le mouvement des structures turbulentes et le plissement de la surface de la flamme. Ils s'écrivent alors sous forme d'expressions algébriques fonctions de grandeurs connues aux échelles résolues ainsi que de paramètres dont l'ajustement est à la charge de l'utilisateur selon la configuration étudiée et les conditions opératoires. L'hypothèse d'équilibre est elle-même parfois mise en défaut : une flamme est en général initialement laminaire puis progressivement plissée par les structures turbulentes au fur et à mesure de son développement. Renoncer à cette simplification suppose la plupart du temps la résolution d'une équation additionnelle, par exemple pour la densité de surface de flamme.

Une alternative efficace est de conserver une formulation algébrique et d'ajuster automatiquement au cours du calcul, en tirant parti de la connaissance des échelles résolues, les paramètres de modélisation qui peuvent alors dépendre du temps et de l'espace. Très utilisée pour décrire le transport turbulent non-résolu, cette approche dynamique reste très peu explorée pour la combustion malgré un potentiel très intéressant.

Cette thèse présente une étude détaillée d'un modèle dynamique pour la simulation aux grandes échelles de la combustion turbulente prémélangée. L'objectif

est de caractériser, explorer les avantages et les inconvénients, appliquer et valider le modèle dynamique global (paramètre du modèle dépendant du temps) et local (paramètre du modèle dépendant du temps et de l'espace) dans plusieurs configurations. Le code massivement parallèle AVBP est utilisé pour résoudre les équations multi-espèces, compressibles et réactives de la mécanique des fluides sur des maillages non structurés. Tout d'abord, une flamme jet turbulente est simulée afin de réaliser une étude systématique de l'influence des paramètres physiques et numériques du modèle. Nous montrons ainsi que le modèle dynamique est robuste et peu sensible aux paramètres numériques qui doivent être fixés au préalable par l'utilisateur. D'autre part, le modèle est validé dans une géométrie de brûleur aéronautique où il s'avère que la formulation dynamique peut jouer un rôle important dans la prédiction des instabilités de combustion. Enfin, un noyau de flamme se propageant dans une chambre de combustion semi-confiné est simulé. Cette situation correspond au développement d'un front de flamme dans un milieu initialement au repos, puis à son accélération par la turbulence générée par l'expansion thermique des gaz. Le modèle dynamique local est capable de prédire les phases laminaire et turbulente de la flamme. En outre, le surcoût numérique introduit par la procédure dynamique reste limité, de l'ordre de 5 à 10 % du coût total de calcul, et est donc parfaitement acceptable. Ainsi, le modèle dynamique se révèle très puissant, car il est adapté à la fois à des géométries académiques et industrielles, des flammes stables et instables, des régimes permanents et transitoires comme décrit dans ce manuscrit.

Mots clés Modèle dynamique, Combustion turbulente prémélangée, Simulations aux grandes échelles, Modèle de flamme épaissie, Flamme jet turbulente, Brûleur swirlé , Instabilité de combustion, PRECCINSTA, Explosion

Appendix B

Conclusion en français

La modélisation dynamique adoptée dans cette thèse est conduite dans le cadre des modèles de flammelettes qui identifient la flamme à une collection d'éléments de flammes laminaires. La flamme jet turbulente de Chen et al. (1996), déjà utilisée comme référence par Wang et al. (2011) et Schmitt et al. (2015) pour les premiers tests de modélisation dynamique, a été retenue pour réaliser l'étude systématique du comportement du modèle. Deux formulations, globale et locale, sont considérées. Dans la première approche, le paramètre global évolue seulement avec le temps, alors que dans le second, il varie aussi en espace. Des analyses avec la formulation dynamique locale montrent que le paramètre du modèle prend de petites valeurs près de l'injecteur où la flamme est quasi-laminaire, et augmente en aval, où la flamme est progressivement plissée par des structures turbulentes. En termes de quantités statistiques, les deux résultats des SGE sont en bon accord avec les données expérimentales, montrant que des expériences plus raffinées sont indispensables pour évaluer les performances des modèles.
L'influence de paramètres physique (échelle de coupure) et numériques (largeur du filtre test, procédure de moyenne, fréquence de filtrage) caractéristiques du modèle a également été étudiée dans cette configuration simple. On montre que le modèle dynamique est relativement peu sensible aux paramètres numériques qui doivent être définis au préalable, sous condition que la taille du filtre test reste relativement faible pour éviter des interactions de front de flamme. D'autre part, l'échelle de coupure, paramètre physique, peut affecter modérément la longueur de la flamme et nécessite une modélisation soignée. Le modèle s'avère aussi robuste et n'a induit aucune difficulté numérique que ce soit dans ses formulations globale et locale. Le surcoût numérique du modèle dynamique reste limité, de l'ordre de 5 à 10 % du coût calcul total, et donc parfaitement acceptable.
Schmitt et al. (2015) avaient montré en pulsant numériquement la flamme jet turbulente de Chen et al. (1996) que le modèle dynamique et sa formulation, locale ou globale, pouvaient avoir une influence sur le comportement instation-

naire de la flamme, et donc sur la prédiction d'éventuelles instabilités. Ce point a été étudié ici par simulation du brûleur PRECCINSTA, injecteur de turbine à gaz Turboméca implanté dans une chambre de combustion de laboratoire et étudiée au DLR en Allemagne Meier et al. (2007). Deux régimes sont considérés, l'un stable (richesse 0.83), l'autre instable (richesse 0.70). Le modèle dynamique semble plus sensible aux instabilités que le modèle "classique" avec un paramètre constant. Ainsi, le mode instable observé expérimentalement sur le foyer PRECCINSTA n'est pas reproduit avec un paramètre constant, ce qui a conduit Franzelli et al. (2012) à l'attribuer à des imperfections du mélange réactif. Avec le modèle dynamique, ce mode instable est retrouvé avec des réactifs parfaitement mélangés. Il est probable que le modèle dynamique, laissant "libre" le paramètre de modélisation, introduit un degré de liberté suffisant, comme la description du mélange dans les calculs de Franzelli et al. (2012), pour favoriser le développement de cette instabilité. Une convergence en maillage montre que l'instabilité observée ne résulte pas d'un artefact numérique, indiquant que d'autres mécanismes peuvent déclencher la pulsation de la flamme. L'un des enseignements de ces simulations est que la dimension fractale de la surface de flamme dépend de la phase de la pulsation.
Le modèle dynamique a aussi été appliqué aux simulations de type explosion dont des prédictions fiables sont un atout pour la sécurité. Lors d'une explosion, différentes phases peuvent être distinguées. Le mélange est d'abord allumé et la flamme se propage dans un écoulement initialement au repos. Ensuite, une propagation turbulente se produit en raison de l'interaction de la flamme avec les obstacles et les mouvements turbulents générés par la flamme elle-même. Les modèles classiques à coefficients constants peuvent éprouver des difficultés à reproduire ce type de configuration, étant donné que le paramètre du modèle peut varier selon la géométrie. En revanche, le modèle dynamique est parfaitement adapté dans ce cas. Le modèle dynamique local est capable de capturer à la fois le régime laminaire et turbulent de la flamme. Trois scénarios différents d'accélération de la flamme sont étudiés. Le premier cas est caractérisé par une longue phase laminaire. Le second présente une forte surpression et une intensité de turbulence élevée. Pour le dernier cas, le front de flamme redevient laminaire après avoir franchi la première rangée d'obstacles. Dans toutes les configurations, les simulations aux grandes échelles (LES) prédisent la dynamique d'écoulement et la surpression maximale avec une bonne précision.

Perspectives

Les différents points étudiés dans cette thèse ouvrent la voie à de nouveaux développements:

- Le modèle dynamique discuté dans ce manuscrit a été utilisé pour simuler des flammes parfaitement prémélangées. Son extension aux flammes de diffusion est une étape essentielle pour pouvoir l'utiliser

dans des configurations industrielles plus réalistes où des régimes de combustion mixtes sont présents. Pour les flammes de diffusion, la détermination des paramètres sera probablement liée à la fraction de mélange et non plus à la variable de progrès, et des analyses complémentaires sont obligatoires. De plus, un défi supplémentaire appara"t: alors que dans le régime parfaitement prémélangé l'échelle de coupure introduite dans le modèle fractal peut être approchée par l'épaisseur de la flamme laminaire, dans le régime non prémélangé, l'estimation de ce paramètre physique est plus délicate et peut varier localement avec la composition des espèces.

- Des données expérimentales plus fines, autres que des quantités statistiques, sont obligatoires pour évaluer les performances des modèles. Des expériences caractérisant la dynamique des flammes (par exemple, l'évolution temporelle de la surface de la flamme) sont essentielles pour aller plus loin dans la validation du modèle.

- Une analyse théorique concernant la réponse instationnaire du modèle dynamique est également envisagée.

- Des études supplémentaires concernant l'échelle de coupure δ_c sont également nécessaires. On a montré que ce paramètre physique peut influencer les résultats numériques, en particulier lorsqu'il s'agit de configurations transitoires. Le problème avec un modèle plus raffiné pour δ_c (tel que celui proposé par Gülder and Smallwood (1995)) est que de nouveaux termes inconnus apparaissent, comme l'intensité turbulente de sous-maille, nécessitant une modélisation supplémentaire. Cependant, le choix actuel de l'échelle de coupure permet de conserver une formulation simple et efficace du modèle dynamique. De nouvelles expériences et des simulations numériques directes doivent être effectuées afin de déterminer ce paramètre physique.

- Enfin, l'étude réalisée pour la chambre de combustion à petite échelle (0.25 m de longueur) de l'Université de Sydney a confirmé que les SGE reproduisent fidèlement des phénomènes transitoires tels que les explosions. Cependant, il est souhaitable d'étendre l'étude à des échelles plus grandes, typiques des b‰timents où une telle situation d'explosion peut arriver. à cette fin, des simulations utilisant la chambre de combustion à moyenne (1.5 m de longueur) et à grande échelles (6.1 m de longueur) devraient également être effectuées.

References

Abdel-Raheem, M. A., S. S. Ibrahim, W. Malalasekera, and A. R. Masri (2015). Large eddy simulation of hydrogen–air premixed flames in a small scale combustion chamber. *International Journal of Hydrogen Energy 40*(7), 3098–3109. *(p. 164)*

Angelberger, C., D. Veynante, F. Egolfopoulos, and T. Poinsot (1998). Large eddy simulations of combustion instabilities in premixed flames. In *Proc. of the Summer Program*, pp. 61–82. Citeseer. *(p. 44)*

Balarac, G., H. Pitsch, and V. Raman (2008). Development of a dynamic model for the subfilter scalar variance using the concept of optimal estimators. *Physics of Fluids 20*(3), 035114. *(p. 75, 85, 117)*

Bardina, J., J. Ferziger, and W. Reynolds (1980). Improved subgrid scale models for large eddy simulation. *AIAA Paper No. 80 1357*. *(p. 69, 72, 85, 116)*

Battista, F., G. Troiani, and F. Picano (2015). Fractal scaling of turbulent premixed flame fronts: Application to LES. *International Journal of Heat and Fluid Flow 51*, 78–87. *(p. 48, 49, 77, 78)*

Bird, R. B., W. E. Stewart, and E. N. Lightfoot (1960). *Transport phenomena*. John Wiley & Sons. *(p. 15)*

Boger, M. and D. Veynante (2000). Large eddy simulation of a turbulent premixed v-shaped flame. *Advances in Turbulence VIII*, 449–452. *(p. 42)*

Boger, M., D. Veynante, H. Boughanem, and A. Trouvé (1998). Direct numerical simulation analysis of flame surface density concept for large eddy simulation of turbulent premixed combustion. In *Symposium (International) on Combustion*, Volume 27, pp. 917–925. Elsevier. *(p. 41, 42, 46, 60, 61, 84, 85, 87, 116, 117, 147)*

Borghi, R. (1985). On the structure and morphology of turbulent premixed flames. In *Recent advances in the Aerospace Sciences*, pp. 117–138. Springer. *(p. 23)*

Borghi, R. and M. Destriau (1998). *Combustion and flame: chemical and physical principles*. Editions Technip. *(p. 23, 24)*

Boughanem, H. and A. Trouvé (1998). The domain of influence of flame instabilities in turbulent premixed combustion. In *Symposium (International) on Combustion*, Volume 27, pp. 971–978. Elsevier. *(p. 42)*

Boussinesq, J. (1877). Essai sur la théorie des eaux courantes du mouvement

nonpermanent des eaux souterraines. *Acad. Sci. Inst. Fr. 23*, 252–260. *(p. 35)*

Bruneaux, G., T. Poinsot, and J. Ferziger (1997). Premixed flame–wall interaction in a turbulent channel flow: budget for the flame surface density evolution equation and modelling. *Journal of Fluid Mechanics 349*, 191–219. *(p. 120)*

Bush, W. B. and F. E. Fendell (1970). Asymptotic analysis of laminar flame propagation for general lewis numbers. *Combustion Science and Technology 1*(6), 421–428. *(p. 21, 153)*

Butler, T. and P. O'Rourke (1977). A numerical method for two dimensional unsteady reacting flows. In *Symposium (International) on Combustion*, Volume 16, pp. 1503–1515. Elsevier. *(p. 44, 84, 86, 118, 148)*

Bykov, V. and U. Maas (2007). The extension of the ildm concept to reaction–diffusion manifolds. *Combustion Theory and Modelling 11*(6), 839–862. *(p. 40)*

Cailler, M., N. Darabiha, D. Veynante, and B. Fiorina (2016). Building-up virtual optimized mechanism for flame modeling. *Proceedings of the Combustion Institute*. *(p. 40)*

Candel, S. M. and T. J. Poinsot (1990). Flame stretch and the balance equation for the flame area. *Combustion Science and Technology 70*(1-3), 1–15. *(p. 21)*

Caux-Brisebois, V., A. M. Steinberg, C. M. Arndt, and W. Meier (2014). Thermo-acoustic velocity coupling in a swirl stabilized gas turbine model combustor. *Combustion and Flame 161*(12), 3166–3180. *(p. 139)*

Charlette, F., C. Meneveau, and D. Veynante (2002a). A power-law flame wrinkling model for LES of premixed turbulent combustion part i: non-dynamic formulation and initial tests. *Combustion and Flame 131*(1), 159–180. *(p. 44, 47, 53, 58, 61, 63, 64, 65, 84, 86, 107, 109, 110, 116, 118, 126, 129, 147, 148, 150)*

Charlette, F., C. Meneveau, and D. Veynante (2002b). A power-law flame wrinkling model for LES of premixed turbulent combustion part ii: Dynamic formulation. *Combustion and Flame 131*(1), 181–197. *(p. 45, 53, 55, 56, 57, 68, 84, 85, 87, 116, 119, 148, 149)*

Chatakonda, O., E. R. Hawkes, A. J. Aspden, A. R. Kerstein, H. Kolla, and J. H. Chen (2013). On the fractal characteristics of low damköhler number flames. *Combustion and Flame 160*(11), 2422–2433. *(p. 46, 48, 50)*

Chen, Y.-C. and M. Mansour (1999). Topology of turbulent premixed flame fronts resolved by simultaneous planar imaging of lipf of oh radical and rayleigh scattering. *Experiments in Fluids 26*(4), 277–287. *(p. 48, 50, 51)*

Chen, Y.-C., N. Peters, G. Schneemann, N. Wruck, U. Renz, and M. S. Mansour (1996). The detailed flame structure of highly stretched turbulent premixed methane-air flames. *Combustion and flame 107*(3), 223–IN2.

(p. 5, 59, 60, 65, 74, 84, 85, 89, 98, 99, 100, 101, 110, 111, 112, 113, 116, 117, 179, 185)

Ciccarelli, G. and S. Dorofeev (2008). Flame acceleration and transition to detonation in ducts. *Progress in Energy and Combustion Science 34*(4), 499–550. *(p. 146)*

Cintosun, E., G. J. Smallwood, and Ö. L. Gülder (2007). Flame surface fractal characteristics in premixed turbulent combustion at high turbulence intensities. *Aiaa Journal 45*(11), 2785–2789. *(p. 77)*

Clavin, P. (1985). Dynamic behavior of premixed flame fronts in laminar and turbulent flows. *Progress in Energy and Combustion Science 11*(1), 1–59. *(p. 21, 153)*

Clavin, P. and G. Joulin (1983). Premixed flames in large scale and high intensity turbulent flow. *Journal de Physique Lettres 44*(1), 1–12. *(p. 21, 153)*

Colin, O., F. Ducros, D. Veynante, and T. Poinsot (2000). A thickened flame model for large eddy simulations of turbulent premixed combustion. *Physics of Fluids 12*(7), 1843–1863. *(p. 44, 47, 68, 72, 84, 86, 116, 118, 147, 148)*

Colin, O. and M. Rudgyard (2000). Development of high-order Taylor–Galerkin schemes for LES. *Journal of Computational Physics 162*(2), 338–371. *(p. 90, 123, 157, 164)*

Dagaut, P. and M. Cathonnet (2006). The ignition, oxidation, and combustion of kerosene: A review of experimental and kinetic modeling. *Progress in energy and combustion science 32*(1), 48–92. *(p. 39)*

Damköhler, G. (1940). Effects of reynolds number on the flame speed. *Elektrochem*. *(p. 57)*

De, A. and S. Acharya (2009). Large eddy simulation of premixed combustion with a thickened-flame approach. *Journal of Engineering for Gas Turbines and Power 131*(6), 061501. *(p. 90)*

Dem, C., M. Stöhr, C. M. Arndt, A. M. Steinberg, and W. Meier (2015). Experimental study of turbulence-chemistry interactions in perfectly and partially premixed confined swirl flames. *Zeitschrift für Physikalische Chemie 229*(4), 569–595. *(p. 117)*

Di Sarli, V., A. Di Benedetto, and G. Russo (2009). Using large eddy simulation for understanding vented gas explosions in the presence of obstacles. *Journal of hazardous materials 169*(1), 435–442. *(p. 147, 164, 175)*

Di Sarli, V., A. Di Benedetto, and G. Russo (2010). Sub-grid scale combustion models for large eddy simulation of unsteady premixed flame propagation around obstacles. *Journal of hazardous materials 180*(1), 71–78. *(p. 147, 164, 165, 175)*

Di Sarli, V., A. Di Benedetto, G. Russo, S. Jarvis, E. J. Long, and G. K. Hargrave (2009). Large eddy simulation and piv measurements of unsteady premixed flames accelerated by obstacles. *Flow, turbulence and combustion 83*(2), 227–250. *(p. 147, 164, 175)*

Dorofeev, S. B. (2011). Flame acceleration and explosion safety applications. *Proceedings of the Combustion Institute 33*(2), 2161–2175. *(p. 146)*

Driscoll, J. F. (2008). Turbulent premixed combustion: Flamelet structure and its effect on turbulent burning velocities. *Progress in Energy and Combustion Science 34*(1), 91–134. *(p. 26)*

Ducros, F., P. Comte, and M. Lesieur (1996). Large-eddy simulation of transition to turbulence in a boundary layer developing spatially over a flat plate. *Journal of Fluid Mechanics 326*, 1–36. *(p. 36, 90)*

Fairweather, M., G. Hargrave, S. Ibrahim, and D. Walker (1999). Studies of premixed flame propagation in explosion tubes. *Combustion and Flame 116*(4), 504–518. *(p. 146)*

Favre, A. (1969). Statistical equations of turbulent gases. *Problems of hydrodynamics and continuum mechanics*, 231–266. *(p. 29)*

Fiorina, B., R. Baron, O. Gicquel, D. Thevenin, S. Carpentier, N. Darabiha, et al. (2003). Modelling non-adiabatic partially premixed flames using flame-prolongation of ildm. *Combustion Theory and Modelling 7*(3), 449–470. *(p. 40)*

Fiorina, B., R. Vicquelin, P. Auzillon, N. Darabiha, O. Gicquel, and D. Veynante (2010). A filtered tabulated chemistry model for LES of premixed combustion. *Combustion and Flame 157*(3), 465–475. *(p. 85, 87, 116)*

Flohr, P. and H. Pitsch (2000). A turbulent flame speed closure model for LES of industrial burner flows. In *Proceedings of the summer program*, pp. 169–179. *(p. 47)*

Franzelli, B., E. Riber, L. Y. Gicquel, and T. Poinsot (2012). Large eddy simulation of combustion instabilities in a lean partially premixed swirled flame. *Combustion and flame 159*(2), 621–637. *(p. 117, 121, 122, 123, 134, 135, 137, 141, 179, 180, 186)*

Franzelli, B., E. Riber, M. Sanjosé, and T. Poinsot (2010). A two-step chemical scheme for kerosene–air premixed flames. *Combustion and Flame 157*(7), 1364–1373. *(p. 39, 40)*

Galpin, J., A. Naudin, L. Vervisch, C. Angelberger, O. Colin, and P. Domingo (2008). Large-eddy simulation of a fuel-lean premixed turbulent swirl-burner. *Combustion and Flame 155*(1), 247–266. *(p. 117, 121, 122)*

Garnier, E., N. Adams, and P. Sagaut (2009). *Large eddy simulation for compressible flows*. Springer. *(p. 35)*

Germano, M., U. Piomelli, P. Moin, and W. H. Cabot (1991). A dynamic subgrid-scale eddy viscosity model. *Physics of Fluids A 3*(7), 1760–1765. *(p. 36, 54, 71, 72, 84, 116, 147, 158)*

Ghosal, S. and P. Moin (1995). The basic equations for the large eddy simulation of turbulent flows in complex geometry. *Journal of Computational Physics 118*(1), 24–37. *(p. 30)*

Gicquel, L. Y., G. Staffelbach, and T. Poinsot (2012). Large eddy simulations of gaseous flames in gas turbine combustion chambers. *Progress in Energy and Combustion Science 38*(6), 782–817. *(p. 84, 146)*

Gicquel, O., N. Darabiha, and D. Thévenin (2000). Liminar premixed hydrogen/air counterflow flame simulations using flame prolongation of ILDM with differential diffusion. *Proceedings of the Combustion Institute 28*(2), 1901–1908. *(p. 40, 43)*

Giovangigli, V. (1999). Multicomponent flow modeling. modeling and simulation in science, engineering and technology. *(p. 14, 155)*

Gouldin, F. (1987). An application of fractals to modeling premixed turbulent flames. *Combustion and Flame 68*(3), 249–266. *(p. 46, 58, 76, 85, 87, 116, 119, 149)*

Gouldin, F., K. Bray, and J.-Y. Chen (1989). Chemical closure model for fractal flamelets. *Combustion and flame 77*(3), 241–259. *(p. 46, 58, 87, 119, 149)*

Gregor, M., F. Seffrin, F. Fuest, D. Geyer, and A. Dreizler (2009). Multi-scalar measurements in a premixed swirl burner using 1d raman/rayleigh scattering. *Proceedings of the Combustion Institute 32*(2), 1739–1746. *(p. 65, 85, 117)*

Gubba, S. R., S. S. Ibrahim, W. Malalasekera, and A. R. Masri (2008). LES modeling of premixed deflagrating flames in a small-scale vented explosion chamber with a series of solid obstructions. *Combustion Science and Technology 180*(10-11), 1936–1955. *(p. 147, 164)*

Gubba, S. R., S. S. Ibrahim, W. Malalasekera, and A. R. Masri (2009). An assessment of large eddy simulations of premixed flames propagating past repeated obstacles. *Combustion Theory and Modelling 13*(3), 513–540. *(p. 147, 164)*

Gubba, S. R., S. S. Ibrahim, W. Malalasekera, and A. R. Masri (2011). Measurements and LES calculations of turbulent premixed flame propagation past repeated obstacles. *Combustion and Flame 158*(12), 2465–2481. *(p. 55, 70, 71, 85, 116, 147, 148, 150, 164, 173, 176, 177)*

Gülder, Ö., G. J. Smallwood, R. Wong, D. Snelling, R. Smith, B. Deschamps, and J.-C. Sautet (2000). Flame front surface characteristics in turbulent premixed propane/air combustion. *Combustion and Flame 120*(4), 407–416. *(p. 76, 77)*

Gülder, Ö. L. (1991). Turbulent premixed combustion modelling using fractal geometry. In *Symposium (International) on Combustion*, Volume 23, pp. 835–842. Elsevier. *(p. 46, 58, 76, 85, 87, 107, 116)*

Gülder, Ö. L. and G. J. Smallwood (1995). Inner cutoff scale of flame surface wrinkling in turbulent premixed flames. *Combustion and flame 103*(1), 107–114. *(p. 46, 75, 76, 107, 119, 149, 162, 181, 187)*

Hall, R., A. Masri, P. Yaroshchyk, and S. Ibrahim (2009). Effects of position and frequency of obstacles on turbulent premixed propagating flames. *Combustion and Flame 156*(2), 439–446. *(p. 146)*

Hawkes, E. and R. Cant (2000). A flame surface density approach to large-eddy simulation of premixed turbulent combustion. *Proceedings of the Combustion Institute 28*(1), 51–58. *(p. 42, 60, 84, 110, 147)*

Herrmann, M. (2006). Numerical simulation of turbulent bunsen flames with a level set flamelet model. *Combustion and flame 145*(1), 357–375. *(p. 89)*

Hirschfelder, J. O., C. F. Curtiss, R. B. Bird, et al. (1954). *Molecular theory of gases and liquids*, Volume 26. Wiley New York. *(p. 13, 15, 86, 118)*

Ibrahim, S. S., S. R. Gubba, A. R. Masri, and W. Malalasekera (2009). Calculations of explosion deflagrating flames using a dynamic flame surface density model. *Journal of Loss Prevention in the Process Industries 22*(3), 258–264. *(p. 116, 147, 148, 150)*

Im, H. G., T. S. Lund, and J. H. Ferziger (1997). Large eddy simulation of turbulent front propagation with dynamic subgrid models. *Physics of Fluids 9*(12), 3826–3833. *(p. 55, 71, 85, 116, 148)*

International Energy Agency (2016). Key world energy statistics 2016. Technical report. *(p. 1, 2)*

Janicka, J. and A. Sadiki (2005). Large eddy simulation of turbulent combustion systems. *Proceedings of the Combustion Institute 30*(1), 537–547. *(p. 146)*

Johansen, C. and G. Ciccarelli (2013). Modeling the initial flame acceleration in an obstructed channel using large eddy simulation. *Journal of Loss Prevention in the Process Industries 26*(4), 571–585. *(p. 147)*

Jones, W. and R. Lindstedt (1988). Global reaction schemes for hydrocarbon combustion. *Combustion and flame 73*(3), 233–249. *(p. 39)*

Kader, B. (1981). Temperature and concentration profiles in fully turbulent boundary layers. *International Journal of Heat and Mass Transfer 24*(9), 1541–1544. *(p. 164, 175)*

Kamal, M. M., R. Zhou, S. Balusamy, and S. Hochgreb (2015). Favre-and reynolds-averaged velocity measurements: Interpreting piv and lda measurements in combustion. *Proceedings of the Combustion Institute 35*(3), 3803–3811. *(p. 98)*

Kaul, C. M., V. Raman, E. Knudsen, E. S. Richardson, and J. H. Chen (2013). Large eddy simulation of a lifted ethylene flame using a dynamic nonequilibrium model for subfilter scalar variance and dissipation rate. *Proceedings of the Combustion Institute 34*(1), 1289–1297. *(p. 74, 75, 85, 117)*

Kent, J., A. Masri, S. Starner, and S. Ibrahim (2005). A new chamber to study premixed flame propagation past repeated obstacles. In *5th Asia-Pacific conference on combustion*, pp. 17–20. The University of Adelaide Australia. *(p. 146)*

Kerstein, A. R., W. T. Ashurst, and F. A. Williams (1988). Field equation for interface propagation in an unsteady homogeneous flow field. *Physical Review A 37*(7), 2728. *(p. 41, 84)*

Kim, W.-W. and S. Menon (2000). Numerical modeling of turbulent premixed flames in the thin-reaction-zones regime. *Combustion Science and Technology 160*(1), 119–150. *(p. 47)*

Kim, W.-W., S. Menon, and H. C. Mongia (1999). Large-eddy simulation of a gas turbine combustor flow. *Combustion Science and Technology 143*(1-6), 25–62. *(p. 41)*

Kirkpatrick, M., S. Armfield, A. Masri, and S. Ibrahim (2003). Large eddy simulation of a propagating turbulent premixed flame. *Flow, turbulence and combustion 70*(1-4), 1–19. *(p. 147)*

Klimov, A. (1988). Laminar flame in a turbulent flow. Technical report, DTIC Document. *(p. 23)*

Knikker, R., D. Veynante, and C. Meneveau (2002). A *priori* testing of a similarity model for large eddysimulations of turbulent premixed combustion. *Proceedings of the combustion institute 29*(2), 2105–2111. *(p. 69, 85, 116)*

Knikker, R., D. Veynante, and C. Meneveau (2004). A dynamic flame surface density model for large eddy simulation of turbulent premixed combustion. *Physics of Fluids 16*(11), L91–L94. *(p. 55, 69, 70, 85, 116, 148, 150, 176)*

Knudsen, E. and H. Pitsch (2008). A dynamic model for the turbulent burning velocity for large eddy simulation of premixed combustion. *Combustion and Flame 154*(4), 740–760. *(p. 55, 73, 74, 85, 116, 148)*

Kolmogorov, A. N. (1941). The local structure of turbulence in incompressible viscous fluid for very large reynolds numbers. In *Dokl. Akad. Nauk SSSR*, Volume 30, pp. 299–303. *(p. 35)*

Kuo, K. K. (1986). *Principles of combustion*. Wiley New York et al. *(p. 17)*

Lartigue, G., U. Meier, and C. Bérat (2004). Experimental and numerical investigation of self-excited combustion oscillations in a scaled gas turbine combustor. *Applied thermal engineering 24*(11), 1583–1592. *(p. 139)*

Lax, P. D. and B. Wendroff (1964). Difference schemes for hyperbolic equations with high order of accuracy. *Communications on pure and applied mathematics 17*(3), 381–398. *(p. 157)*

Leonard, A. (1974). Energy cascade in large-eddy simulations of turbulent fluid flows. In *Turbulent diffusion in environmental pollution*, Volume 1, pp. 237–248. *(p. 29)*

Libby, P. A. and F. A. Williams (1980). Turbulent reacting flows. *Topics in Applied Physics 44*. *(p. 23)*

Lilly, D. K. (1992). A proposed modification of the germano subgrid-scale closure method. *Physics of Fluids A: Fluid Dynamics (1989-1993) 4*(3), 633–635. *(p. 36, 38)*

Lindstedt, R. and E. Vaos (2006). Transported pdf modeling of high-reynolds-number premixed turbulent flames. *Combustion and Flame 145*(3), 495–511. *(p. 90)*

Lu, T. and C. K. Law (2005). A directed relation graph method for mechanism reduction. *Proceedings of the Combustion Institute 30*(1), 1333–1341. *(p. 39)*

Lu, T. and C. K. Law (2008). A criterion based on computational singular

perturbation for the identification of quasi steady state species: A reduced mechanism for methane oxidation with no chemistry. *Combustion and Flame 154*(4), 761–774. *(p. 39)*

Luche, J., M. Reuillon, J.-C. Boettner, and M. Cathonnet (2004). Reduction of large detailed kinetic mechanisms: application to kerosene/air combustion. *Combustion science and technology 176*(11), 1935–1963. *(p. 39)*

Maas, U. and S. B. Pope (1992). Simplifying chemical kinetics: intrinsic low-dimensional manifolds in composition space. *Combustion and flame 88*(3), 239–264. *(p. 40)*

Mandelbrot, B. B. (1975). On the geometry of homogeneous turbulence, with stress on the fractal dimension of the iso-surfaces of scalars. *Journal of Fluid Mechanics 72*(03), 401–416. *(p. 46)*

Mandelbrot, B. B. (1977). *Fractals*. Wiley Online Library. *(p. 46)*

Mandelbrot, B. B. (1983). *The fractal geometry of nature*, Volume 173. Macmillan. *(p. 46, 48, 77)*

Mantzaras, J. (1992). Geometrical properties of turbulent premixed flames: comparison between computed and measured quantities. *Combustion science and technology 86*(1-6), 135–162. *(p. 76)*

Mantzaras, J., P. Felton, and F. Bracco (1989). Fractals and turbulent premixed engine flames. *Combustion and Flame 77*(3), 295–310. *(p. 77)*

Masri, A., A. AlHarbi, S. Meares, and S. Ibrahim (2012). A comparative study of turbulent premixed flames propagating past repeated obstacles. *Industrial & Engineering Chemistry Research 51*(22), 7690–7703. *(p. 5, 70, 146, 148, 150, 151, 167, 170, 173, 176, 177)*

Masri, A., S. Ibrahim, N. Nehzat, and A. Green (2000). Experimental study of premixed flame propagation over various solid obstructions. *Experimental Thermal and Fluid Science 21*(1), 109–116. *(p. 146)*

Massias, A., D. Diamantis, E. Mastorakos, and D. Goussis (1999). An algorithm for the construction of global reduced mechanisms with csp data. *Combustion and Flame 117*(4), 685–708. *(p. 39)*

Meier, W., P. Weigand, X. Duan, and R. Giezendanner-Thoben (2007). Detailed characterization of the dynamics of thermoacoustic pulsations in a lean premixed swirl flame. *Combustion and Flame 150*(1), 2–26. *(p. 5, 115, 117, 121, 128, 136, 141, 142, 179, 186)*

Mercier, R., T. Schmitt, D. Veynante, and B. Fiorina (2015). The influence of combustion sgs submodels on the resolved flame propagation. application to the LES of the cambridge stratified flames. *Proceedings of the Combustion Institute 35*(2), 1259–1267. *(p. 85, 116)*

Moureau, V., P. Domingo, and L. Vervisch (2011). From large-eddy simulation to direct numerical simulation of a lean premixed swirl flame: Filtered laminar flame-pdf modeling. *Combustion and Flame 158*(7), 1340–1357. *(p. 63, 64, 91, 117, 119, 121, 122, 130, 149)*

Moureau, V., P. Minot, H. Pitsch, and C. Bérat (2007). A ghost-fluid method for large-eddy simulations of premixed combustion in complex geometries.

Journal of Computational Physics 221(2), 600–614. *(p. 117, 121, 122)*

Mouriaux, S. (2016). *Large Eddy simulation of the turbulent spark ignition and of the flame propagation in spark ignition engines*. Ph. D. thesis, Université Paris-Saclay. *(p. 147)*

Mouriaux, S., O. Colin, and D. Veynante (2016). Adaptation of a dynamic wrinkling model to an engine configuration. *Proceedings of the Combustion Institute 36*. *(p. 55, 66, 67, 68, 103, 111, 117, 132, 148, 168)*

Murayama, M. and T. Takeno (1989). Fractal-like character of flamelets in turbulent premixed combustion. In *Symposium (International) on Combustion*, Volume 22, pp. 551–559. Elsevier. *(p. 76)*

Nicoud, F. and F. Ducros (1999). Subgrid-scale stress modelling based on the square of the velocity gradient tensor. *Flow, turbulence and Combustion 62*(3), 183–200. *(p. 38, 123, 158, 164)*

North, G. and D. Santavicca (1990). The fractal nature of premixed turbulent flames. *Combustion Science and Technology 72*(4-6), 215–232. *(p. 46, 75, 77)*

Oijen, J. v. and L. D. Goey (2000). Modelling of premixed laminar flames using flamelet-generated manifolds. *Combustion Science and Technology 161*(1), 113–137. *(p. 40, 43)*

Oran, E. S. and V. N. Gamezo (2007). Origins of the deflagration-to-detonation transition in gas-phase combustion. *Combustion and Flame 148*(1), 4–47. *(p. 146)*

O'Rourke, P. and F. Bracco (1979). Two scaling transformations for the numerical computation of multidimensional unsteady laminar flames. *Journal of Computational Physics 33*(2), 185–203. *(p. 44, 86, 118)*

Patel, S., S. Jarvis, S. Ibrahim, and G. Hargrave (2002). An experimental and numerical investigation of premixed flame deflagration in a semiconfined explosion chamber. *Proceedings of the Combustion Institute 29*(2), 1849–1854. *(p. 147)*

Peters, N. (1985). Numerical and asymptotic analysis of systematically reduced reaction schemes for hydrocarbon flames. In *Numerical simulation of combustion phenomena*, pp. 90–109. Springer. *(p. 39)*

Peters, N. (1986). Laminar flamelet concepts in turbulent combustion. In *Symposium (International) on Combustion*, Volume 21, pp. 1231–1250. Elsevier. *(p. 23, 46, 75, 76)*

Peters, N. (1999). The turbulent burning velocity for large-scale and small-scale turbulence. *Journal of Fluid Mechanics 384*, 107–132. *(p. 23, 147)*

Peters, N. (2000). *Turbulent combustion*. Cambridge university press. *(p. 73)*

Pierce, C. D. and P. Moin (1998). A dynamic model for subgrid-scale variance and dissipation rate of a conserved scalar. *Physics of Fluids 10*(12), 3041–3044. *(p. 75, 85, 117)*

Pierce, C. D. and P. Moin (2004). Progress-variable approach for large-eddy simulation of non-premixed turbulent combustion. *Journal of Fluid Mechanics 504*, 73–97. *(p. 74, 75, 85, 117)*

Pitsch, H. (2005). A consistent level set formulation for large-eddy simulation of premixed turbulent combustion. *Combustion and Flame 143*(4), 587–598. *(p. 84)*

Pitsch, H. (2006). Large-eddy simulation of turbulent combustion. *Annu. Rev. Fluid Mech. 38*, 453–482. *(p. 84, 116, 146)*

Pitsch, H. and L. D. De Lageneste (2002). Large-eddy simulation of premixed turbulent combustion using a level-set approach. *Proceedings of the Combustion Institute 29*(2), 2001–2008. *(p. 47, 90, 147)*

Poinsot, T., D. Haworth, and G. Bruneaux (1993). Direct simulation and modeling of flame-wall interaction for premixed turbulent combustion. *Combustion and Flame 95*(1), 118–132. *(p. 120)*

Poinsot, T. and D. Veynante (2011). *Theoretical and numerical combustion* (3rd ed.). www.cerfacs.fr/elearning. *(p. 3, 4, 10, 14, 23, 29, 37, 41, 84, 86, 118, 120, 146, 149)*

Poinsot, T., D. Veynante, and S. Candel (1991). Quenching processes and premixed turbulent combustion diagrams. *Journal of Fluid Mechanics 228*, 561–606. *(p. 75, 76)*

Poinsot, T. J. and S. Lele (1992). Boundary conditions for direct simulations of compressible viscous flows. *Journal of computational physics 101*(1), 104–129. *(p. 90, 123, 156, 164)*

Pope, S. B. (2000). *Turbulent flows*. Cambridge university press. *(p. 28)*

Pope, S. B. (2004). Ten questions concerning the large-eddy simulation of turbulent flows. *New journal of Physics 6*(1), 35. *(p. 28, 116, 141)*

Quillatre, P. (2014). *Simulation aux grandes échelles d'explosions en domaine semi-confiné*. Ph. D. thesis, École Doctorale Mécanique, Énergétique, Génie civil et Procédés (Toulouse); 154236012. *(p. 154)*

Quillatre, P., O. Vermorel, and T. Poinsot (2011). Large eddy simulation of turbolent premixed flames propagation in a small scale venting chamber: influence of chemistry and transport modelling. In *Seventh Mediterranean Combustion Symposium, Sardinia*. *(p. 154, 163)*

Quillatre, P., O. Vermorel, T. Poinsot, and P. Ricoux (2013). Large eddy simulation of vented deflagration. *Industrial & Engineering Chemistry Research 52*(33), 11414–11423. *(p. 147, 152, 153, 154, 156, 175)*

Ren, Z., S. B. Pope, A. Vladimirsky, and J. M. Guckenheimer (2006). The invariant constrained equilibrium edge preimage curve method for the dimension reduction of chemical kinetics. *The Journal of chemical physics 124*(11), 114111. *(p. 40)*

Renou, B. (1999). *Contribution à l'étude de la propagation d'une flamme de prémélange instationnaire dans un écoulement turbulent. Influence du nombre de Lewis*. Ph. D. thesis, Université de Rouen. *(p. 61, 85, 116)*

Réveillon, J. and L. Vervisch (1998). Subgrid-scale turbulent micromixing: Dynamic approach. *AIAA journal 36*(3), 336–341. *(p. 75, 85, 117)*

Richard, S., O. Colin, O. Vermorel, A. Benkenida, C. Angelberger, and D. Veynante (2007). Towards large eddy simulation of combustion in

spark ignition engines. *Proceedings of the Combustion Institute 31*(2), 3059–3066. *(p. 42, 46, 84, 110, 147)*

Roberts, W. L., J. F. Driscoll, M. C. Drake, and L. P. Goss (1993). Images of the quenching of a flame by a vortex-to quantify regimes of turbulent combustion. *Combustion and Flame 94*(1), 58–69. *(p. 76)*

Ronney, P. D. and V. Yakhot (1992). Flame broadening effects on premixed turbulent flame speed. *Combustion science and Technology 86*(1-6), 31–43. *(p. 77)*

Roux, S., G. Lartigue, T. Poinsot, U. Meier, and C. Bérat (2005). Studies of mean and unsteady flow in a swirled combustor using experiments, acoustic analysis, and large eddy simulations. *Combustion and Flame 141*(1), 40–54. *(p. 117, 121, 122)*

Sagaut, P. (2002). *Large eddy simulation for incompressible flows*. Springer. *(p. 28, 29, 35)*

Schmitt, T., M. Boileau, and D. Veynante (2015). Flame wrinkling factor dynamic modeling for large eddy simulations of turbulent premixed combustion. *Flow, Turbulence and Combustion 94*(1), 199–217. *(p. 55, 65, 66, 85, 87, 94, 102, 116, 117, 119, 148, 149, 179, 185)*

Schmitt, T., A. Sadiki, B. Fiorina, and D. Veynante (2013). Impact of dynamic wrinkling model on the prediction accuracy using the F-TACLES combustion model in swirling premixed turbulent flames. *Proceedings of the Combustion Institute 34*(1), 1261–1268. *(p. 55, 65, 85, 116, 117, 148)*

Schneider, C., A. Dreizler, and J. Janicka (2005). Fluid dynamical analysis of atmospheric reacting and isothermal swirling flows. *Flow, turbulence and combustion 74*(1), 103–127. *(p. 65, 85, 117)*

Schonfeld, T. and M. Rudgyard (1999). Steady and unsteady flow simulations using the hybrid flow solver avbp. *AIAA journal 37*(11), 1378–1385. *(p. 89, 123, 156)*

Selle, L., G. Lartigue, T. Poinsot, R. Koch, K.-U. Schildmacher, W. Krebs, B. Prade, P. Kaufmann, and D. Veynante (2004). Compressible large eddy simulation of turbulent combustion in complex geometry on unstructured meshes. *Combustion and Flame 137*(4), 489–505. *(p. 91, 123, 124)*

Smagorinsky, J. (1963). General circulation experiments with the primitive equations: I. the basic experiment*. *Monthly weather review 91*(3), 99–164. *(p. 36)*

Smallwood, G. J., Ö. Gülder, D. R. Snelling, B. Deschamps, and I. Gökalp (1995). Characterization of flame front surfaces in turbulent premixed methane/air combustion. *Combustion and Flame 101*(4), 461–470. *(p. 46, 48, 49)*

Smirnov, A., S. Shi, and I. Celik (2001). Random flow generation technique for large eddy simulations and particle-dynamics modeling. *Journal of Fluids Engineering 123*(2), 359–371. *(p. 89)*

Smith, G. P., D. M. Golden, M. Frenklach, N. W. Moriarty, B. Eiteneer,

M. Goldenberg, C. T. Bowman, R. K. Hanson, S. Song, W. C. Gardiner Jr, et al. (1999). Gri-mech 3.0. *(p. 38, 152)*

Spyropoulos, E. T. and G. A. Blaisdell (1996). Evaluation of the dynamic model for simulations of compressible decaying isotropic turbulence. *AIAA journal 34*(5), 990–998. *(p. 36)*

Sreenivasan, K. and C. Meneveau (1986). The fractal facets of turbulence. *Journal of Fluid Mechanics 173*, 357–386. *(p. 46)*

Steinberg, A., C. Arndt, and W. Meier (2013). Parametric study of vortex structures and their dynamics in swirl-stabilized combustion. *Proceedings of the Combustion Institute 34*(2), 3117–3125. *(p. 139)*

Sweeney, M., S. Hochgreb, and R. Barlow (2011). The structure of premixed and stratified low turbulence flames. *Combustion and Flame 158*(5), 935–948. *(p. 85)*

Sweeney, M., S. Hochgreb, M. Dunn, and R. Barlow (2011). A comparative analysis of flame surface density metrics inpremixed and stratified flames. *Proceedings of the Combustion Institute 33*(1), 1419–1427. *(p. 85)*

Tirunagari, R. R. and S. B. Pope (2016). LES/PDF for premixed combustion in the DNS limit. *Combustion Theory and Modelling 20*(5), 834–865. *(p. 98)*

Tomlin, A. S., T. Turányi, and M. J. Pilling (1997). Mathematical tools for the construction, investigation and reduction of combustion mechanisms. *Comprehensive chemical kinetics 35*, 293–437. *(p. 39)*

Trouvé, A. and T. Poinsot (1994). The evolution equation for the flame surface density in turbulent premixed combustion. *Journal of Fluid Mechanics 278*, 1–31. *(p. 42)*

Turanyi, T. (1990). Reduction of large reaction mechanisms. *New journal of chemistry 14*(11), 795–803. *(p. 39)*

van der Ven, H. (1995). A family of large eddy simulation (LES) filters with nonuniform filter widths. *Physics of Fluids 7*(5), 1171–1172. *(p. 31)*

Van Kalmthout, E. and D. Veynante (1998). Direct numerical simulations analysis of flame surface density models for nonpremixed turbulent combustion. *Physics of Fluids 10*(9), 2347–2368. *(p. 89)*

Vasilyev, O. V., T. S. Lund, and P. Moin (1998). A general class of commutative filters for LES in complex geometries. *Journal of Computational Physics 146*(1), 82–104. *(p. 31)*

Vermorel, O., P. Quillatre, and T. Poinsot (2017). LES of explosions in venting chamber: a test case for premixed turbulent combustion models. *submitted to Combustion and Flame*. *(p. 147, 156)*

Vermorel, O., S. Richard, O. Colin, C. Angelberger, A. Benkenida, and D. Veynante (2009). Towards the understanding of cyclic variability in a spark ignited engine using multi-cycle LES. *Combustion and Flame 156*(8), 1525–1541. *(p. 147)*

Vervisch, L., E. Bidaux, K. Bray, and W. Kollmann (1995). Surface density function in premixed turbulent combustion modeling, similarities be-

tween probability density function and flame surface approaches. *Physics of Fluids 7*(10), 2496–2503. *(p. 42)*

Veynante, D. and R. Knikker (2006). Comparison between LES results and experimental data in reacting flows. *Journal of Turbulence* (7). *(p. 92, 125, 128)*

Veynante, D. and V. Moureau (2015). Analysis of dynamic models for large eddy simulations of turbulent premixed combustion. *Combustion and Flame 162*(12), 4622 – 4642. *(p. 46, 55, 58, 63, 64, 65, 69, 85, 86, 87, 88, 119, 149, 162)*

Veynante, D., T. Schmitt, M. Boileau, and V. Moureau (2012). Analysis of dynamic models for turbulent premixed combustion. In *Proceedings of the Summer Program*, pp. 387. *(p. 85, 86, 87, 88, 119)*

Veynante, D. and L. Vervisch (2002). Turbulent combustion modeling. *Progress in energy and combustion science 28*(3), 193–266. *(p. 20, 21, 22, 24, 60, 87, 92)*

Volpiani, P. S., T. Schmitt, and D. Veynante (2016). A posteriori tests of a dynamic thickened flame model for large eddy simulations of turbulent premixed combustion. *Combustion and Flame 174*, 166–178. *(p. 116, 117, 120, 126, 148, 150, 162, 165)*

Volpiani, P. S., T. Schmitt, and D. Veynante (2017). Large eddy simulation of a turbulent swirling premixed flame coupling the TFLES model with a dynamic wrinkling formulation. *accepted in Combustion and Flame*. *(p. 148)*

Wang, G., M. Boileau, and D. Veynante (2011). Implementation of a dynamic thickened flame model for large eddy simulations of turbulent premixed combustion. *Combustion and Flame 158*(11), 2199–2213. *(p. 55, 57, 58, 59, 60, 64, 84, 85, 86, 87, 88, 90, 103, 116, 119, 120, 148, 179, 185)*

Wang, G., M. Boileau, D. Veynante, and K. Truffin (2012). Large eddy simulation of a growing turbulent premixed flame kernel using a dynamic flame surface density model. *Combustion and Flame 159*(8), 2742–2754. *(p. 55, 60, 61, 62, 63, 85, 87, 116, 119, 148, 149)*

Wang, P., J. Fröhlich, U. Maas, Z.-x. He, and C.-j. Wang (2016). A detailed comparison of two sub-grid scale combustion models via large eddy simulation of the preccinsta gas turbine model combustor. *Combustion and Flame 164*, 329–345. *(p. 117, 121)*

Wang, P., N. Platova, J. Fröhlich, and U. Maas (2014). Large eddy simulation of the preccinsta burner. *International Journal of Heat and Mass Transfer 70*, 486–495. *(p. 117, 121)*

Weller, H., G. Tabor, A. Gosman, and C. Fureby (1998). Application of a flame-wrinkling LES combustion model to a turbulent mixing layer. In *Symposium (International) on Combustion*, Volume 27, pp. 899–907. Elsevier. *(p. 42, 84, 110, 147)*

Williams, F. (1976). Criteria for existence of wrinkled laminar flame structure of turbulent premixed flames. *Combustion and Flame 26*, 269–270.

(p. 23)

Williams, G. (1985). *Combustion theory*. Citeseer. *(p. 11, 21, 44)*

Yoshida, A., M. Kasahara, H. Tsuji, and T. Yanagisawa (1994). Fractal geometry application in estimation of turbulent burning velocity of wrinkled laminar flame. *Combustion science and technology 103*(1-6), 207–218. *(p. 77)*

université PARIS-SACLAY

ÉCOLE DOCTORALE
Sciences mécaniques et énergétiques, matériaux et géosciences (SMEMAG)

Titre: Modèle de plissement dynamique pour la simulation aux grandes échelles de la combustion turbulente prémelangée

Mots-clés: Modèle dynamique, Combustion turbulente, Simulations aux grandes échelles

Résumé: Avec l'accroissement considérable de la puissance de calcul, les simulations aux grandes échelles (SGE) sont maintenant utilisées de façon routinière dans de nombreuses applications d'ingénierie. Les modèles de combustion usuels utilisés dans les SGE sont le plus souvent basés sur une hypothèse d'équilibre entre le mouvement des structures turbulentes et le plissement de la surface de la flamme. Ils s'écrivent alors sous forme d'expressions algébriques fonctions de grandeurs connues aux échelles résolues ainsi que de paramètres dont l'ajustement est à la charge de l'utilisateur selon la configuration étudiée et les conditions opératoires. Le modèle dynamique récemment développé ajuste automatiquement au cours du calcul les paramètres de modélisation qui peuvent alors dépendre du temps et de l'espace. Cette thèse présente une étude détaillée d'un modèle dynamique pour la simulation aux grandes échelles de la combustion turbulente prémélangée. L'objectif est de caractériser, explorer les avantages et les inconvénients, appliquer et valider le modèle dynamique dans plusieurs configurations.

Title: Dynamic wrinkling flame model for large eddy simulations of turbulent premixed combustion

Keywords: Dynamic modeling, Turbulent combustion, Large eddy simulation

Abstract: Large eddy simulation (LES) is currently applied in a wide range of engineering applications. Classical LES combustion models are based on algebraic expressions and assume equilibrium between turbulence and flame wrinkling which is generally not verified in many circumstances as the flame is laminar at early stages and progressively wrinkled by turbulent motions. In practice, this conceptual drawback has a strong consequence: every computation needs its own set of constants, i.e. any small change in the operating conditions or in the geometry requires an adjustment of model parameters. The dynamic model recently developed adjust automatically the flame wrinkling factor from the knowledge of resolved scales. Widely used to describe the unresolved turbulent transport, the dynamic approach remains underexplored in combustion despite its interesting potential. This thesis presents a detailed study of a dynamic wrinkling factor model for large eddy simulation of turbulent premixed combustion. The goal of this thesis is to characterize, unveil pros and cons, apply and validate the dynamic modeling in different flow configurations.

Université Paris-Saclay
Espace Technologique / Immeuble Discovery
Route de l'Orme aux Merisiers RD 128 / 91190 Saint-Aubin, France